



# Investigation of cardiac diffusion tensor imaging using compressed sensing

Jianping Huang

## ► To cite this version:

Jianping Huang. Investigation of cardiac diffusion tensor imaging using compressed sensing. Signal and Image processing. INSA de Lyon; Harbin Institute of Technology (Chine), 2015. English. NNT : 2015ISAL0136 . tel-01416064

HAL Id: tel-01416064

<https://theses.hal.science/tel-01416064>

Submitted on 14 Dec 2016

**HAL** is a multi-disciplinary open access archive for the deposit and dissemination of scientific research documents, whether they are published or not. The documents may come from teaching and research institutions in France or abroad, or from public or private research centers.

L'archive ouverte pluridisciplinaire **HAL**, est destinée au dépôt et à la diffusion de documents scientifiques de niveau recherche, publiés ou non, émanant des établissements d'enseignement et de recherche français ou étrangers, des laboratoires publics ou privés.

# THÈSE

*présentée devant*

**L’Institut National des Sciences Appliquées de Lyon**

*pour obtenir*

## LE GRADE DE DOCTEUR

ÉCOLE DOCTORALE: ÉLECTRONIQUE, ÉLECTROTECHNIQUE, AUTOMATIQUE  
FORMATION DOCTORALE : SCIENCES DE L’INFORMATION, DES DISPOSITIFS ET  
DES SYSTÈMES

*par*

**Jianping HUANG**

### **Etude de l'imagerie de tenseur de diffusion en utilisant l'acquisition Comprimée**

Soutenue le 13 décembre 2015

Jury :

<b>Nicole VINCENT</b>	Professeur de LIPADE	Rapporteur
<b>Jin LI</b>	Professeur d’HEU	Rapporteur
<b>Ping LI</b>	Professeur de Radiologue Hospitalier de HMU	Examinateur
<b>Isabelle E. MAGNIN</b>	Directeur de recherche INSERM	Examinateur
<b>Yue-Min ZHU</b>	Directeur de recherche CNRS	Directeur de thèse
<b>Wan-Yu LIU</b>	Professeur de HIT	Co-directeur de thèse

**INSA Direction de la Recherche - Ecoles Doctorales - Quinquennal 2011-2015**

SIGLE	ECOLE DOCTORALE	NOM ET COORDONNEES DU RESPONSABLE
CHIMIE	<b>CHIMIE DE LYON</b> <a href="http://www.edchimie-lyon.fr">http://www.edchimie-lyon.fr</a> Sec : Renée EL MELHEM Bat Blaise Pascal 3 <sup>e</sup> etage 04 72 43 80 46 Insa : R. GOURDON <a href="mailto:secretariat@edchimie-lyon.fr">secretariat@edchimie-lyon.fr</a>	<b>M. Jean Marc LANCELIN</b> Université de Lyon – Collège Doctoral Bât ESCPE 43 bd du 11 novembre 1918 69622 VILLEURBANNE Cedex Tél : 04.72.43 13 95 <a href="mailto:directeur@edchimie-lyon.fr">directeur@edchimie-lyon.fr</a>
E.E.A.	<b>ELECTRONIQUE, ELECTROTECHNIQUE, AUTOMATIQUE</b> <a href="http://edea.ec-lyon.fr">http://edea.ec-lyon.fr</a>  Sec : M.C. HAVGOUDOUKIAN <a href="mailto:Ecole-doctorale.eea@ec-lyon.fr">Ecole-doctorale.eea@ec-lyon.fr</a>	<b>M. Gérard SCORLETTI</b> Ecole Centrale de Lyon 36 avenue Guy de Collongue 69134 ECULLY Tél : 04.72.18 60.97 Fax : 04 78 43 37 17 <a href="mailto:Gerard.scorletti@ec-lyon.fr">Gerard.scorletti@ec-lyon.fr</a>
E2M2	<b>EVOLUTION, ECOSYSTEME, MICROBIOLOGIE, MODELISATION</b> <a href="http://e2m2.universite-lyon.fr">http://e2m2.universite-lyon.fr</a>  Sec : Safia AIT CHALAL Bat Atrium- UCB Lyon 1 04.72.44.83.62 Insa : S. REVERCHON <a href="mailto:Safia.ait-chalal@univ-lyon1.fr">Safia.ait-chalal@univ-lyon1.fr</a>	<b>M. Fabrice CORDEY</b> Laboratoire de Géologie de Lyon Université Claude Bernard Lyon 1 Bât Géode – Bureau 225 43 bd du 11 novembre 1918 69622 VILLEURBANNE Cédex Tél : 04.72.44.83.74 <a href="mailto:Sylvie.reverchon-pescheux@insa-lyon.fr">Sylvie.reverchon-pescheux@insa-lyon.fr</a> <a href="mailto:fabricce.cordey@univ-lyon1.fr">fabricce.cordey@univ-lyon1.fr</a>
EDISS	<b>INTERDISCIPLINAIRE SCIENCES SANTE</b> <a href="http://www.ediss-lyon.fr">http://www.ediss-lyon.fr</a> Sec : Safia AIT CHALAL Bat Atrium – UCB Lyon 1 04 72 44 83 62 Insa : <a href="mailto:Safia.ait-chalal@univ-lyon1.fr">Safia.ait-chalal@univ-lyon1.fr</a>	<b>Mme Emmanuelle CANET-SOULAS</b> INSERM U1060, CarMeN lab, Univ. Lyon 1 Bâtiment IMBL 11 avenue Jean Capelle INSA de Lyon 696621 Villeurbanne Tél : 04.72.11.90.13 <a href="mailto:Emmanuelle.canet@univ-lyon1.fr">Emmanuelle.canet@univ-lyon1.fr</a>
INFOMATHS	<b>INFORMATIQUE ET MATHEMATIQUES</b> <a href="http://infomaths.univ-lyon1.fr">http://infomaths.univ-lyon1.fr</a>  Sec : Renée EL MELHEM Bat Blaise Pascal 3 <sup>e</sup> etage <a href="mailto:infomaths@univ-lyon1.fr">infomaths@univ-lyon1.fr</a>	<b>Mme Sylvie CALABRETO</b> LIRIS – INSA de Lyon Bat Blaise Pascal 7 avenue Jean Capelle 69622 VILLEURBANNE Cedex Tél : 04.72. 43. 80. 46 Fax 04 72 43 16 87 <a href="mailto:Sylvie.calabreto@insa-lyon.fr">Sylvie.calabreto@insa-lyon.fr</a>
Matériaux	<b>MATERIAUX DE LYON</b> <a href="http://ed34.universite-lyon.fr">http://ed34.universite-lyon.fr</a>  Sec : M. LABOUNE PM : 71.70 -Fax : 87.12 Bat. Direction 1 <sup>er</sup> et. <a href="mailto:Ed.materiaux@insa-lyon.fr">Ed.materiaux@insa-lyon.fr</a>	<b>M. Jean-Yves BUFFIERE</b> INSA de Lyon MATEIS Bâtiment Saint Exupéry 7 avenue Jean Capelle 69621 VILLEURBANNE Cedex Tél : 04.72.43 71.70 Fax 04 72 43 85 28 <a href="mailto:Ed.materiaux@insa-lyon.fr">Ed.materiaux@insa-lyon.fr</a>
MEGA	<b>MECANIQUE, ENERGETIQUE, GENIE CIVIL, ACOUSTIQUE</b> <a href="http://mega.universite-lyon.fr">http://mega.universite-lyon.fr</a>  Sec : M. LABOUNE PM : 71.70 -Fax : 87.12 Bat. Direction 1 <sup>er</sup> et. <a href="mailto:mega@insa-lyon.fr">mega@insa-lyon.fr</a>	<b>M. Philippe BOISSE</b> INSA de Lyon Laboratoire LAMCOS Bâtiment Jacquard 25 bis avenue Jean Capelle 69621 VILLEURBANNE Cedex Tél : 04.72.43.71.70 Fax : 04 72 43 72 37 <a href="mailto:Philippe.boisse@insa-lyon.fr">Philippe.boisse@insa-lyon.fr</a>
ScSo	<b>ScSo*</b> <a href="http://recherche.univ-lyon2.fr/scso/">http://recherche.univ-lyon2.fr/scso/</a>  Sec : Viviane POLSINELLI Brigitte DUBOIS Insa : J.Y. TOUSSAINT <a href="mailto:viviane.polsinelli@univ-lyon2.fr">viviane.polsinelli@univ-lyon2.fr</a>	<b>Mme Isabelle VON BUELZINGLOEWEN</b> Université Lyon 2 86 rue Pasteur 69365 LYON Cedex 07 Tél : 04.78.77.23.86 Fax : 04.37.28.04.48 <a href="mailto:isavonb@dbmail.com">isavonb@dbmail.com</a>

\*ScSo : Histoire, Géographie, Aménagement, Urbanisme, Archéologie, Science politique, Sociologie, Anthropologie

# **Investigation of Cardiac Diffusion Tensor Imaging Using Compressed Sensing**

## **Abstract**

The investigation of the micro fiber structures of the heart provides a new approach to explaining heart disease and investigating effective therapy means. Diffusion tensor magnetic resonance (DTMR) imaging or diffusion tensor imaging (DTI) currently provides a unique tool to image the three-dimensional (3D) fiber structures of the heart *in vivo*. However, DTI is known to suffer from long acquisition time, which greatly limits its practical and clinical use. Classical acquisition and reconstruction methods do not allow coping with the problem. The main motivation of this thesis is then to investigate fast imaging techniques by reconstructing high-quality images from highly undersampled data. The methodology adopted is based on the recent theory of compressed sensing (CS). More precisely, we address the use of CS for magnetic resonance imaging (MRI) and cardiac DTI.

First, we formulate the magnetic resonance (MR) image reconstruction as a problem of optimization with data-driven tight frame (TF) and total generalized variation (TGV) constraints in the framework of CS, in which the data-driven TF is used to adaptively learn a set of filters from the highly under-sampled data itself to provide a better sparse approximation of images and the TGV is devoted to regularizing adaptively image regions and thus suppressing staircase effects. Second, we propose a new CS method that employs joint sparsity and rank deficiency prior to reconstruct cardiac DTMR images from highly undersampled k-space data. Then, always in the framework of CS theory, we introduce low rank constraint and total variation (TV) regularizations in the CS reconstruction formulation, to reconstruct cardiac DTI images from highly undersampled k-space data. Two TV regularizations are considered: local TV (i.e. classical TV) and nonlocal TV (NLTV). Finally, we propose two randomly perturbed radial undersampling schemes (golden-angle and random angle) and the optimization with low rank constraint and TV regularizations to deal with highly undersampled k-space acquisitions in cardiac DTI, and compare the proposed CS-based DTI with existing radial undersampling strategies such as uniformity-angle, randomly perturbed uniformity-angle, golden-angle, and random angle.

# **Etude de l'imagerie de tenseur de diffusion en utilisant l'acquisition Comprimée**

## **Résumé**

L'étude de la structure microscopique des fibres du cœur offre une nouvelle approche pour expliquer les maladies du cœur et pour trouver des moyens de thérapie efficaces. L'imagerie de tenseur de diffusion par résonance magnétique (DTMR) ou l'imagerie de tenseur de diffusion (DTI) fournit actuellement un outil unique pour étudier les structures tridimensionnelles (3D) de fibres cardiaques *in vivo*. Cependant, DTI est connu pour souffrir des temps d'acquisition longs, ce qui limite considérablement son application pratique et clinique. Les méthodes traditionnelles pour l'acquisition et la reconstruction de l'image ne peuvent pas résoudre ce problème. La motivation principale de cette thèse est alors d'étudier des techniques d'imagerie rapide en reconstruisant des images de haute qualité à partir des données fortement sous-échantillonnées. La méthode adoptée est basée sur la nouvelle théorie de l'acquisition compressée (CS). Plus précisément, nous étudions l'utilisation de la théorie de CS pour l'imagerie par résonance magnétique (IRM) et DTI cardiaque.

Tout d'abord, nous formulons la reconstruction de l'image par résonance magnétique (MR) comme un problème d'optimisation avec les contraintes de trames ajustées guidées par les données (TF) et de variation totale généralisée (TGV) dans le cadre de CS, dans lequel, le TF guidé par les données est utilisé pour apprendre de manière adaptative un ensemble de filtres à partir des données fortement sous-échantillonnées afin d'obtenir une meilleure approximation parcimonieuse des images, et le TGV est dédié à régulariser de façon adaptative les régions d'image et à réduire ainsi les effets d'escalier. Ensuite, nous proposons une nouvelle méthode CS qui emploie conjointement la parcimonie et la déficience de rang pour reconstruire des images de DTMR cardiaques à partir des données de l'espace  $k$  fortement sous-échantillonnées. Puis, toujours dans le cadre de la théorie CS, nous introduisons la contrainte de rang faible et la régularisation de variation totale (TV) dans la formulation de la reconstruction par CS. Deux régularisations TV sont considérées: TV locale (i.e. TV classique) et TV non locale (NLTV). Enfin, nous proposons deux schémas de sous-échantillonnage radial aléatoire (angle d'or et angle aléatoire) et une méthode d'optimisation avec la contrainte de faible rang et la régularisation TV pour traiter des données espace  $k$  fortement sous-échantillonnées en DTI cardiaque. Enfin, nous comparons nos méthodes avec des stratégies existantes de sous-échantillonnage radial telles que l'angle uniforme, l'angle uniforme perturbé aléatoirement, l'angle d'or et l'angle aléatoire.

## Acknowledgments

I would like to take this opportunity to thank all the people who helped and supported me during my thesis, and without whom the finish of this dissertation would not have been possible.

First and foremost, I would like to express my sincere gratitude to my supervisor, Professor Yuemin Zhu. He gave me valuable advices for solving the numerous problems of this thesis in detail, provided me many insightful ideas for this work and helped me on all aspects during the entire period of my PhD. He is more like a friend than a supervisor, his open-minded and optimistic character deeply affected me. The things I learnt from him would make me benefit in all my life. It has been an absolute pleasure and honor to be his student, and I want to thank him from the bottom of my heart.

I would like also to express my deepest gratitude to my co-supervisor, Professor Wanyu Liu, for giving me this great opportunity to pursue my doctoral degree in Laboratory Creatis in France. I am grateful for him to bring me to the world of medical image processing, his unselfish help, pertinent advice, confidence and encouragement throughout my doctoral studies, which helped me to finally finish this doctoral research journey. I am immensely grateful to him for everything.

I express my gratitude to the members of my thesis committee, especially the reviewers of my thesis, Professor Nicole VINCENT and Jin LI, thank you for agreeing to be my thesis reviewers and for consuming your valuable time to read and comment this work. Your pertinent and detailed comments make a great improvement to this thesis and provide me more idea for the future work. Thank you also for being very kind and patient to me during the defense. I also like to thank the Professor Isabelle E. Magnin and Professor Ping LI for agreeing to be part of my thesis committee, thank you for your advices and kindness.

I also want to express my deep gratitude especially for those who always help me and support me during my thesis. Thanks to Lihui Wang for her support and help during my PhD study, and I appreciate very much the valuable discussion with Shengfu Li, Yanli Zhang and Chunyu Chu, thanks to all of you for your suggestions to my work. I would also like to thank my laboratory colleagues and my friends, their names are not mentioned here, without whom, my PhD life would not have been filled with happy memories and full of joys.

Lastly, I would like to give my deepest gratitude to my family members: my mother and father, thank them for giving me selfishness support, patient listening, constant encouragement and deep love throughout my life. Many thanks to my sisters and brothers for their consistent love and support. I would also like to thank especially my dear wife for her unending love, patience and encouragement during my entire study, and thank you for giving me such a beautiful baby girl, who was born while I was working on this thesis.

# Contents

Abstract .....	I
Résumé .....	II
Acknowledgments .....	III
Contents .....	IV
Content of Figures .....	VII
Introduction Générale .....	1
General Introduction .....	15
1 Heart function and disease .....	19
Résumé en français .....	20
Abstract .....	21
1.1 Introduction .....	22
1.2 Heart anatomy .....	22
1.2.1 <i>Heart structure</i> .....	22
1.2.2 <i>Myocardium structure</i> .....	25
1.3 Heart diseases .....	28
1.4 Relation between fiber structure and heart function .....	30
1.5 Conclusion .....	30
2 Diffusion tensor imaging (DTI) and compressed sensing (CS) theory .....	31
Résumé en français .....	32
Abstract .....	33
2.1 Magnetic Resonance Imaging .....	34
2.1.1 <i>Basic physics</i> .....	34
2.1.2 <i>Signal spatial encoding</i> .....	37
2.1.3 <i>k-space</i> .....	40
2.1.4 <i>MR pulse sequences</i> .....	41
2.2 Cardiac diffusion tensor imaging (DTI) .....	43
2.2.1 <i>Diffusion physics</i> .....	43
2.2.2 <i>Diffusion signal</i> .....	45
2.2.3 <i>Diffusion Tensor Imaging (DTI)</i> .....	47
2.3 Compressed Sensing .....	49
2.3.1 <i>Shannon theory</i> .....	50
2.3.2 <i>Sparsity</i> .....	54
2.3.3 <i>Incoherence</i> .....	55
2.3.4 <i>Sensing</i> .....	56
2.3.5 <i>Recovery</i> .....	57
2.4 Conclusion .....	57
3 Compressed sensing MRI via data-driven tight frame and total generalized variation(TGV) ..	59
Résumé en français .....	60
Abstract .....	61
3.1 Introduction .....	62
3.2 Methodology .....	63
3.2.1 <i>Preliminaries</i> .....	63
3.2.2 <i>Proposed model</i> .....	65
3.3 Experiments and results .....	67
3.3.1 <i>Experimental setup</i> .....	67

3.3.2	<i>Visual comparison</i> .....	69
3.3.3	<i>Effects of sampling rates</i> .....	72
3.3.4	<i>Effects of filter size</i> .....	72
3.3.5	<i>Computation time</i> .....	75
3.4	Conclusion.....	76
4	Accelerated cardiac DTI based on CS using joint sparsity and low rank approximation .....	77
	Résumé en français.....	78
	Abstract .....	79
4.1	Introduction .....	80
4.2	Proposed method .....	81
4.3	Experimental Results.....	84
4.3.1	<i>Simulated and real data</i> .....	84
4.3.2	<i>Evaluation criteria</i> .....	84
4.3.3	<i>Comparison with existing techniques</i> .....	85
4.3.4	<i>Simulation results</i> .....	85
4.3.5	<i>Real data</i> .....	87
4.3.6	<i>Compared with the repetition-reduced method</i> .....	90
4.4	Discussion.....	92
4.5	Conclusion.....	93
5	Accelerated cardiac DTI based on CS using low-rank and non-local TV constraint .....	94
	Résumé en français.....	95
	Abstract .....	96
5.1	Introduction .....	97
5.2	Methods.....	98
5.2.1	<i>Non local TV</i> .....	98
5.2.2	<i>CS-MRI reconstruction using NLTV</i> .....	99
5.2.3	<i>CS DT-MR image reconstruction using low rank and TV model</i> .....	103
5.3	Experimental Results.....	105
5.3.1	<i>Data and sampling pattern</i> .....	105
5.3.2	<i>Evaluation criteria</i> .....	106
5.3.3	<i>Comparison with existing techniques</i> .....	107
5.3.4	<i>Effects of sampling rates</i> .....	107
5.3.5	<i>Maps of FA and MD</i> .....	108
5.3.6	<i>Tensor fields visualization</i> .....	109
5.3.7	<i>Effects of regularization parameters</i> .....	109
5.4	Conclusion.....	110
6	The influence of radial undersampling schemes on compressed sensing cardiac DTI.....	111
	Résumé en français.....	112
	Abstract .....	113
6.1	Introduction .....	114
6.2	Experimental method.....	115
6.2.1	<i>Cardiac datasets and Evaluation criteria</i> .....	115
6.2.2	<i>Sampling schemes</i> .....	116
6.3	Experimental results .....	117
6.3.1	<i>Effects of sampling rates</i> .....	117
6.3.2	<i>Maps of FA and MD</i> .....	117
6.3.3	<i>Tensor fields visualization</i> .....	120
6.4	Conclusion.....	122
7	General conclusions and perspectives .....	124

7.1 Contributions .....	125
7.2 Discussion and perspectives .....	126
7.3 Author's publications .....	126
Bibliographies .....	127
FOLIO ADMINISTRATIF .....	142

# Content of Figures

Fig. 1.1 Heart anatomical structure. (From Texas Heart Institute Heart Information Center, <a href="http://www.texasheartinstitute.org/hic/anatomy/anatomy2.cfm">http://www.texasheartinstitute.org/hic/anatomy/anatomy2.cfm</a> ) .....	23
Fig. 1.2 Heart Valves (From: <a href="http://www.webmd.com/heart-disease/guide/heart-valve-disease">http://www.webmd.com/heart-disease/guide/heart-valve-disease</a> ) .....	24
Fig. 1.3 Heart wall structure (From: <a href="http://encyclopedia.lubopitko-bg.com/Structure_of_the_Heart.html">http://encyclopedia.lubopitko-bg.com/Structure_of_the_Heart.html</a> ) .....	25
Fig. 1.4 Helical rope model of myocardium (From: [Kocica <i>et al.</i> , 2006]).....	26
Fig. 1.5 Torrent-Guasp's myocardial band model (From: [Buckberg <i>et al.</i> , 2008]).....	26
Fig. 1.6 Geodesic model (From: [Jouk <i>et al.</i> , 2007]).....	27
Fig. 1.7 An extension of geodesic model: pretzel model. Like the pretzel cookies, two joined torus form a pretzel in this model. For better understanding the further deformations, a lattice was drawn, where the lines in red are parallel to the surface of revolution, and those in blue are the meridians, as shown in subfigure (A). Four special positions are defined: lower left aperture (lla), lower right aperture (lra), upper left aperture (ula) and upper right aperture (ura). For mimicking the right ventricle structure, the torus on the left was bent in such a way that the lower aperture comes up to the upper aperture. However, for the left ventricle, it is mimicked by shrinking the lower right aperture into a point, as shown in subfigure (B). In subfigure (C), it explains how LV and RV could nest together and form a pretzel model, where the green lines represent the geodesic on the nested pretzels (From: [Jouk <i>et al.</i> , 2007]). .....	27
Fig. 1.8 Schematic of laminar structure model for cardiac fiber (From: [Legrice <i>et al.</i> , 1995]) .....	28
Fig. 1.9 Dilated Cardiomyopathy(from: <a href="https://en.wikipedia.org/wiki/Dilated_cardiomyopathy">https://en.wikipedia.org/wiki/Dilated_cardiomyopathy</a> ) .....	29
Fig. 1.10 Hypertrophic cardiomyopathy (from: <a href="http://www.nlm.nih.gov/medlineplus/ency/article/000192.htm">http://www.nlm.nih.gov/medlineplus/ency/article/000192.htm</a> ) .....	29
Fig. 1.11 Restrictive cardiomyopathy (From: <a href="http://trialx.com/curebyte/2011/08/28/photos-related-to-restrictive-cardiomyopathy">http://trialx.com/curebyte/2011/08/28/photos-related-to-restrictive-cardiomyopathy</a> ).....	30
Fig. 2.1 Spin and precession of protons (From: [Blink, 2004]) .....	35
Fig. 2.2 RF excitation (a) and relaxation (b).....	35
Fig. 2.3 Schema for T1 and T2 relaxation (GM: gray matter, WM: white matter) (From: [Elmaoḡlu <i>et al.</i> , 2011]) .....	36
Fig. 2.4 When the $B_1$ RF-pulse is applied, total magnetization $M_0$ is tilted from z -axis to xy-plane and it continues to precess in xy-plane at Larmor frequency. When a coil is positioned perpendicular to magnetization $M_{xy}$ , a current (MR signal) is inducted based on Faraday's principle on the coil.(From: [Elmaoḡlu <i>et al.</i> , 2011]) .....	37
Fig. 2.5 magnetic field gradients for spatial encoding (From: <a href="https://www.imaios.com/en/e-Courses/e-MRI">https://www.imaios.com/en/e-Courses/e-MRI</a> ).....	37
Fig. 2.6 Diagram for MRI Slice selection (From: [McRobbie <i>et al.</i> , 2006]) .....	38
Fig. 2.7 Diagram for MRI phase encoding (From: [Hornak, 2008]) .....	39
Fig. 2.8 Diagram for frequency or readout encoding (From: [Hornak, 2008]).....	40
Fig. 2.9 k-space .....	40
Fig. 2.10 The effects of removing the portion of k-space data on the reconstructed image. ....	41
Fig. 2.11 The k-space filled by uses straight lines from a Cartesian grid.....	41
Fig. 2.12 Diagram of SE sequence and its principle (From: [Wang, 2013]) .....	42
Fig. 2.13 Gradient echo sequence and its principle (From: [Wang, 2013]) .....	42
Fig. 2.14 The schematic of the molecular diffusion trajectory of a single water molecule (From: [Wang, 2013])......	44
Fig. 2.15 Illustration of the difference between restricted and hindered diffusion [Wang, 2013]. .....	45
Fig. 2.16 Stejskal-Tanner diffusion magnetic resonance imaging sequence (From: [Perrin <i>et al.</i> , 2005]) .....	46

Fig. 2.17 The example of sampling the analog signals in time domain (a analog signal (red line) and the equidistant sampling points (marked blue circle )).....	51
Fig. 2.18 Diagram of the sampling process. ....	52
Fig. 2.19 Frequency interpretation of the sampling theorem, the sample frequency of analog input signal $f_s$ is (a) more than Nyquist rate; (b) equal to Nyquist rate; (c) less than Nyquist rate (From: <a href="http://www.onmyphd.com/?p=aliasing">http://www.onmyphd.com/?p=aliasing</a> ) .....	53
Fig. 2.20 The analog signal is reconstructed by ideal low-pass filtering. (a) a perfect recovery is possible provided that the sample frequency is satisfied with Nyquist criterion; (b) ruining the possibility of exact recovery that the sample frequency is not satisfied with Nyquist criterion (From: <a href="http://www.onmyphd.com/?p=aliasing">http://www.onmyphd.com/?p=aliasing</a> ). ....	53
Fig. 2.21 An example of sparse signal in transform domain. ....	55
Fig. 2.22 Sparse representation and approximation of an image. (a) Original image. (b) multi-scale wavelet representation (large coefficients are represented by light pixels, while small coefficients are represented by dark pixels). (c) wavelet transform coefficients (arranged in order for enhanced visibility). (d) approximation of image (a) obtained by zeroing out all the wavelet coefficients but keeping only the largest 10% of the coefficients. ....	55
Fig. 3.1 Illustration the data-driven TF filters constructed with two different sizes. (a) the filter (atom) size $8 \times 8$ . (b) the filter (atom) size $16 \times 16$ .....	65
Fig. 3.2 k-space undersampling mask and MR images. (a) k-space sampling mask; (b) Coronal brain; (c) Cardiac; (d) Shoulder; (e) Renal arteries. ....	68
Fig. 3.3 Results of reconstruction on the coronal brain MR image using different methods with 15% sampling. (a) Original MR images. images reconstructed by (b) SparseMRI [Lustig <i>et al.</i> , 2007]; (c). FCSA [Huang <i>et al.</i> , 2011b]; (d) Framelet+NLTV [Gopi <i>et al.</i> , 2014]; (e) Shearlet+TGV [Guo <i>et al.</i> , 2014]; (f) data-driven TF+TGV (proposed). .....	69
Fig. 3.4 Results of reconstruction on the cardiac MR image using different methods with 15% sampling. (a) Original MR images; images reconstructed using (b) SparseMRI [Lustig <i>et al.</i> , 2007]; (c). FCSA [Huang <i>et al.</i> , 2011b]; (d) Framelet+NLTV [Gopi <i>et al.</i> , 2014]; (e) Shearlet+TGV [Guo <i>et al.</i> , 2014]; (f) data-driven TF+TGV (proposed). .....	70
Fig. 3.5 Results of reconstruction on the shoulder MR image using different methods with 15% sampling. (a) Original MR images; images reconstructed using (b) SparseMRI [Lustig <i>et al.</i> , 2007]; (c). FCSA [Huang <i>et al.</i> , 2011b]; (d) Framelet+NLTV [Gopi <i>et al.</i> , 2014]; (e) Shearlet+TGV [Guo <i>et al.</i> , 2014]; (f) data-driven TF+TGV (proposed). .....	70
Fig. 3.6 Results of reconstruction on the renal arteries MR image using different methods with 15% sampling. (a) Original MR images; images reconstructed using (b) SparseMRI [Lustig <i>et al.</i> , 2007]; (c). FCSA [Huang <i>et al.</i> , 2011b]; (d) Framelet+NLTV [Gopi <i>et al.</i> , 2014]; (e) Shearlet+TGV [Guo <i>et al.</i> , 2014]; (f) data-driven TF+TGV (proposed). .....	71
Fig. 3.7 Comparison of PSNR as a function of sampling rate on different MR images. (a) Coronal brain image. (b) Cardiac image. (c) Shoulder image. (d) Renal arteries image. ....	72
Fig. 3.8 Comparison of RLNE as a function of sampling rate on different MR images. (a) Coronal brain image. (b) Cardiac image. (c) Shoulder image. (d) Renal arteries image. ....	73
Fig. 3.9 Comparison of MSSIM as a function of sampling rate on different MR images. (a) Coronal brain image, (b) Cardiac image; (c) Shoulder image. (d) Renal arteries image.....	73
Fig. 3.10 Comparison of PSNR curves with different filters size. (a) Coronal brain image, (b) Cardiac image, (c) Shoulder image. (d) Renal arteries image.....	74
Fig. 3.11 Comparison of RLNE curves with different filters size. (a) Coronal brain image, (b) Cardiac image, (c) Shoulder image. (d) Renal arteries image.....	74
Fig. 3.12 Comparison of MSSIM curves with different filters size. (a) Coronal brain image. (b) Cardiac image. (c) Shoulder image. (d) Renal arteries image.....	75
Fig. 4.1 Illustration the principle of the proposed approach. ....	82
Fig. 4.2 Performance comparisons on simulated human heart data with ISNR 20dB. RMSE of (a) FA; (b) MD. ....	85

Fig. 4.3 Maps of FA (first row) and MD (second row) of the simulated human heart data with the sampling rate of 25% and ISNR 20dB. (a) Reconstruction from the complete k-space data; Reconstructions from undersampled k-space using (b) basis CS; (c) joint sparsity and (d) the proposed methods.....	86
Fig. 4.4 RMSE of FA and MD of reconstructions from undersampled simulated human heart data using the proposed method with varied ISNRs and sampling ratio (R). (a) RMSE of FA; (b) RMSE of MD.....	86
Fig. 4.5 Performance comparisons on real human heart data with different sampling rates and ISNR 0dB. (a) mean RMSE of FA; (b) mean RMSE of MD; (c) mean RMSE of TA; (d) mean RMSE of HA.....	87
Fig. 4.6 Performance comparisons on real human heart data with different sampling rates and ISNR 30dB. (a) mean RMSE of FA; (b) mean RMSE of MD; (c) mean RMSE of TA; (d) mean RMSE of HA.....	88
Fig. 4.7 The reconstruction tensor fields on real human heart data for slice 4 with sampling rates 15% and ISNR 30dB using the different methods. (a) Reconstruction from the complete k-space data with repeated 6 times; Reconstructions from undersampled k-space using (b) basis CS, (c) joint sparsity and (d) the proposed methods.....	88
Fig. 4.8 Maps of FA (first row), MD (second row), TA(three row) and HA(four row) of the real human heart data on slice 4 with the sampling rate of 25% and ISNR 0dB. (a) Reconstruction from the complete k-space data (column one). Reconstructions from undersampled k-space using (b) basis CS (column two); (c) joint sparsity (column three) and (d) the proposed methods (column four). .....	89
Fig. 4.9 Maps of FA (first row), MD (second row), TA(three row) and HA(four row) of the real human heart data on slice 4 with the sampling rate of 25% and ISNR 30dB. (a) Reconstruction from the complete k-space data (column one). Reconstructions from undersampled k-space using (b) basis CS (column two); (c) joint sparsity (column three) and (d) the proposed methods (column four). .....	90
Fig. 4.10 Maps of TA (row first, second) and HA (row three, four) on the real human heart data for slice 4 with the ISNR 0dB. (a) Reconstruction from the complete k-space data with repeated 6 times (column one); (b)-(d) in second and four row is Reconstructions from undersampled k-space using with sampling ratio 15%, 30% and 50%, respectively; (b)-(d) in first and three row is reconstruction from complete k-space data with repeated 1, 2 and 3 times .....	91
Fig. 4.11 The reconstruction tensor fields using the proposed and the repetition-reduced methods at varied acceleration factors. (a) Reconstruction from the complete k-space data with repeated 6 times; (b)-(d) Reconstruction from the complete k-space data with repeated 1, 2 and 3 times, respectively. Reconstructions from undersampled k-space with the sampling ratio 15%, 30% and 50%, respectively; (e)-(g) the ISNR 0dB; (h)-(j) the ISNR 30dB.....	92
Fig. 5.1 The image gradient is calculated in (a) conventional TV regularization; and (b) NLTV regularization.....	99
Fig. 5.2 Results of reconstruction on MR images using different methods. (a): k-space sampling mask. (b) and (c): Original MR images of brain and chest respectively. From (d) to (f): brain image reconstructed using FCSA, NLTV_FSCA and the proposed method respectively. From (g) to (i): chest image reconstructed using FCSA, NLTV_FSCA and the proposed method respectively..	101
Fig. 5.3 Curve of PSNR (a), MSSIM (b) and MSE (c) versus different sampling rates for the MR images of brain reconstructed with FCSA, NLTV_FCSA, and NLTV_FCSA_TV methods respectively.....	102
Fig. 5.4 Reference human cardiac DW images in one diffusion direction. (a) Simulated data; (b) real data .....	106
Fig. 5.5 Performance comparisons on simulated heart data with ISNR 30dB. (a) RMSE of FA; (b) RMSE of MD.....	107
Fig. 5.6 Performance comparisons on real human heart data with ISNR 30dB. (a) RMSE of FA; (b) RMSE of MD.....	107

Fig. 5.7 Maps of FA (first row) and MD (second row) of the simulated human heart data with the sampling rate of 25% and ISNR 30dB. (a) Reconstruction from the complete k-space data; Reconstructions from undersampled k-space using (b) joint sparsity with TV; (c) low rank with TV; and (d) the low rank with NLTV methods. ....	108
Fig. 5.8 Maps of FA (first row) and MD (second row) of the real human heart data with the sampling rate of 25% and ISNR 30dB. (a) Reconstruction from the complete k-space data; Reconstructions from undersampled k-space using (b) joint sparsity with TV; (c) low rank with TV; and (d) the low rank with NLTV methods. ....	108
Fig. 5.9 The reconstruction tensor fields on simulated human heart data with sampling rates 15% and ISNR 30dB using the different methods. (a) Reconstruction from the complete k-space data; Reconstructions from undersampled k-space using (b) joint sparsity with TV; (c) low rank with TV; and (d) the low rank with NLTV methods. ....	109
Fig. 5.10 The reconstruction tensor fields on real human heart data with sampling rates 15% and ISNR 30dB using the different methods. (a) Reconstruction from the complete k-space data; Reconstructions from undersampled k-space using (b) joint sparsity with TV; (c) low rank with TV; and (d) the low rank with NLTV methods. ....	109
Fig. 5.11 Effects of regularization parameters. (a) RMSE of FA on simulated data; (b) RMSE of MD on simulated data. ....	110
Fig. 6.1 Reference human cardiac DW images. (a) Simulated data; (b) real data. ....	115
Fig. 6.2 Demonstrate the randomly perturbed radial lines. ....	116
Fig. 6.3 Reference k-space sampling masks in one diffusion direction with sampling rate of 20%. (a) uniform-angle; (b) golden-angle; (c) random-angle; (d)-(f) randomly perturbed (a)-(c), respectively. ....	117
Fig. 6.4 Performance comparisons on simulated data with different sampling rates (RP is the abbreviation of randomly perturbed). (a) RMSE of FA; (b) RMSE of MD. ....	118
Fig. 6.5 Performance comparisons on real data with different sampling rates (RP is the abbreviation of randomly perturbed). (a) RMSE of FA; (b) RMSE of MD. ....	118
Fig. 6.6 Maps of FA of the simulated human heart data with 25% sampling rates. (a) Reconstruction from the complete k-space data. Reconstructions from undersampled k-space using (b) uniform-angle radial, (c) golden-angle radial, (d) random-angle radial, and (e)-(g) the corresponding randomly perturbed radial sampling of (b)-(d). ....	119
Fig. 6.7 Maps of MD of the simulated human heart data with 25% sampling rates. (a) Reconstruction from the complete k-space data. Reconstructions from undersampled k-space using (b) uniform-angle radial, (c) golden-angle radial, (d) random-angle radial, and (e)-(g) the corresponding randomly perturbed radial sampling of (b)-(d). ....	119
Fig. 6.8 Maps of FA of the real human heart data with 25% sampling rates. (a) Reconstruction from the complete k-space data. Reconstructions from undersampled k-space using (b) uniform-angle radial, (c) golden-angle radial, (d) random-angle radial, and (e)-(g) the corresponding randomly perturbed radial sampling of (b)-(d). ....	120
Fig. 6.9 Maps of MD of the real human heart data with 25% sampling rates. (a) Reconstruction from the complete k-space data. Reconstructions from undersampled k-space using (b) uniform-angle radial, (c) golden-angle radial, (d) random-angle radial, and (e)-(g) the corresponding randomly perturbed radial sampling of (b)-(d). ....	120
Fig. 6.10 The reconstruction tensor fields on simulated human heart data with sampling rates 25% and ISNR 30dB (Diffusion tensor field represented by arrows and ellipsoid. In order to enhance the orientation of the cardiac fibers, the tensor image is sampled with a ratio of 3 to1, and shown on the top right corner of the each sub-figure). (a) Reconstruction from the complete k-space data. Reconstructions from undersampled k-space using (b) uniform-angle radial, (c) golden-angle radial, (d) random-angle radial, and (e)-(g) the corresponding randomly perturbed radial sampling of (b)-(d). ....	121
Fig. 6.11 The reconstruction tensor fields on real human heart data with sampling rates 25% and ISNR 30dB (Diffusion tensor field represented by arrows. In order to enhance the orientation of the	

cardiac fibers, the tensor image is sampled with a ratio of 3 to1, and shown on the top right corner of the each sub-figure). (a) Reconstruction from the complete k-space data. Reconstructions from undersampled k-space using (b) uniform-angle radial, (c) golden-angle radial, (d) random-angle radial, and (e)-(g) the corresponding randomly perturbed radial sampling of (b)-(d)..... 121

## Introduction Générale

Le cœur est l'un des principaux organes du corps humain, qui pompe sans cesse le sang contenant de l'oxygène et les nutriments nécessaires à d'autres parties du corps pour maintenir la vie. Les maladies cardiaques ou les maladies plus généralement cardiovasculaires (cardiovascular disease—CVD) est la principale cause de décès dans le monde, représentant environ 30% (plus de 17.3 millions de décès) de tous les décès dans le monde entier [Christodoulou *et al.*, 2014, Go *et al.*, 2014, Mozaffarian *et al.*, 2015]. Chaque année, les CVD provoquent 47% de tous les décès (plus de 4 millions de décès) en Europe et 40% (plus de 1,9 millions de décès) dans l'Union européenne [Nichols *et al.*]. D'autre part, les CVD ont des coûts aussi bien économiques que humains importants pour l'Europe. Globalement, la dépense pour les CVD dans l'Union européenne est près de € 196 000 000 000 par an. De ce coût total des maladies cardiovasculaires dans l'Union européenne, environ 54% sont dûs à des coûts de soins de santé directs, 24% en raison de pertes de productivité et 22% en raison de la prestation de soins informels de personnes atteintes de maladies cardiovasculaires [Nichols *et al.*].

Par conséquent, d'un point de vue de la santé et de l'économie, il est très important d'étudier la structure microscopique du cœur afin d'expliquer les symptômes de la maladie de ce dernier et les moyens thérapeutiques efficaces. La microstructure du cœur est complexe, en particulier son architecture de fibres, qui est fondamentale pour maintenir les fonctions mécaniques et électrophysiologies cardiaques. Connaître l'architecture des fibres cardiaques en trois dimensions (3D) permettra d'obtenir une nouvelle façon de comprendre comment la structure des fibres du cœur influence ses fonctions électriques et mécaniques et d'étudier les maladies cardiaques sous-jacentes.

La première compréhension de l'architecture des fibres cardiaques est issue des mesures histologiques sur des régions du tissu sélectionnées [Ross *et al.*, 1979]. Ces techniques histologiques sont connues de souffrir certaines limites, telles que la résolution spatiale, la distorsion et le désalignement. D'ailleurs, elles ne sont pas tridimensionnelles par essence. Afin de résoudre ces problèmes, l'imagerie en lumière polarisée (Polarized Light Imaging-PLI, en anglais) a été proposée pour obtenir les orientations des fibres dans des cœurs ex vivo [Jouk *et al.*, 1995, Jouk *et al.*, 2007]. Cette technique permet pour la première fois de mesurer physiquement les orientations 3D des fibres d'un cœur entier avec une haute résolution spatiale ( $0.1 \text{ mm} \times 0.1 \text{ mm} \times 0.5 \text{ mm}$ ). Par rapport aux méthodes de dissection et histologiques, elle est plus objective, car elle n'implique aucune opération humaine durant le processus de mesure. Cependant, les deux techniques histologiques et PLI sont ex vivo et ne peuvent pas être utilisées pour étudier l'architecture des fibres in vivo du cœur humain.

Plus récemment, l'imagerie par résonance magnétique de diffusion (IRMd), qui comprend l'imagerie du tenseur de diffusion (DTI) et l'imagerie de diffusion en haute résolution angulaire (HARDI), a émergé comme une technique nouvelle et prometteuse pour analyser la structure des fibres des tissus en 3D. L'imagerie de tenseur de diffusion par résonance magnétique (DTMRI), appelée également l'imagerie du tenseur de diffusion (DTI), est une technique IRMd permettant de caractériser quantitativement la géométrie et l'organisation des microstructures tissulaires [Basser *et al.*, 1994a;1994b]. C'est un outil puissant et actuellement le seul moyen d'étudier de manière non-invasive l'architecture des fibres du cœur humain [Hsu *et al.*, 2001, Le Bihan *et al.*, 2001, Helm *et al.*, 2005b, Wu *et al.*, 2006,

Toussaint *et al.*, 2010, Tournier *et al.*, 2011, Wei *et al.*, 2013, Froeling *et al.*, 2014, Naumova *et al.*, 2014, Wei *et al.*, 2015].

Cependant, en IRMd, l'un des principaux problèmes est le mouvement cardiaque qui provoque le flou et la perte du signal [Nielles-Vallespin *et al.*, 2013, Wei *et al.*, 2013]. Afin de minimiser les artefacts de mouvement cardiaques, il est important de garder le temps d'acquisition des images DT le plus court possible à chaque battement du cœur. D'autre part, la résolution de DTI cardiaque *in vivo* est encore trop faible (2,6 mm dans le plan et l'épaisseur de 6-7 mm). Ainsi, il est important de développer la technique d'acquisition afin d'obtenir des données de DTI avec une résolution plus élevée. Une résolution spatiale plus élevée signifie que nous pouvons obtenir des faisceaux de fibres qui pourraient être plus cohérents avec les études histologiques *ex vivo*. Ce problème peut être amélioré par l'acquisition rapide de données. En outre, il est bien connu que l'acquisition de l'image pondérée en diffusion est souvent altérée par du bruit important et l'intensité des signaux DW est plus faible que celle de signaux par résonance magnétique classiques [Bao *et al.*, 2013, Zhang *et al.*, 2013]. En pratique, faire la moyenne du signal en répétant l'acquisition est généralement considéré comme un bon moyen d'augmenter le rapport signal sur bruit (SNR), mais qui prolonge la durée d'acquisition. En résumé, le DTI est connu pour souffrir du temps d'acquisition long afin d'obtenir des données de haute qualité (y compris les résolutions temporelle et spatiale, SNR), ce qui limite considérablement son utilisation pratique et clinique pour l'imagerie du cœur humain [Dou *et al.*, 2002, Dou *et al.*, 2003, Helm *et al.*, 2005b, Wu *et al.*, 2006].

Traditionnellement, de nombreuses tentatives ont été faites afin d'accélérer l'acquisition des données, de réduire la quantité de données acquises et d'améliorer le SNR de signaux de diffusion autant que possible, comme l'imagerie parallèle [Bammer *et al.*, 2001, Bammer *et al.*, 2002, Jaermann *et al.*, 2004, Holdsworth *et al.*, 2009], l'imagerie multi-coupe simultanée [Filli *et al.*, 2015, Lau *et al.*, 2015], la reconstruction k-espace partiel [Luo *et al.*, 2012], et la projection-reconstruction avec l'encodage filtrée réduite [Jiang *et al.*, 2005]. Mais, ces méthodes ne sont pas très appropriées pour les données k-espace fortement sous-échantillonnées.

Au cours des dernières années, l'acquisition comprimée (compressed sensing—CS en anglais) a émergé comme une nouvelle théorie qui combine le schéma d'acquisition des données et la reconstruction des images de haute qualité à partir des mesures fortement sous-échantillonnées (par rapport au théorème Shannon-Nyquist d'échantillonnage traditionnel [Candes *et al.*, 2006a, Candes *et al.*, 2006c, Donoho, 2006]). Le CS exploite la parcimonie ou la compressibilité de signaux dans un certain domaine (pixel ou un domaine transformé), et combine l'échantillonnage et la compression dans un cadre unifié. À ce jour, le CS a été appliqué avec succès à l'imagerie biomédicale et a montré un grand potentiel [Wang *et al.*, 2011], pour l'IRM [Lustig *et al.*, 2007, Lustig *et al.*, 2008] et l'IRM dynamique [Bilen, 2013].

La motivation principale de cette thèse est alors d'étudier les techniques d'imagerie rapide en reconstruisant des images de haute qualité à partir des données fortement sous-échantillonnées. La méthode adoptée est basée sur la théorie récente de CS. Plus précisément, nous abordons l'utilisation du CS pour l'imagerie par résonance magnétique (IRM) et DTI cardiaque. Ce mémoire de thèse est organisé comme suit.

La première partie de ce manuscrit, qui décrit le contexte nécessaire pour les chapitres suivants, est comme suit:

**Chapitre 1** *Fonction et maladie cardiaques.* Ce chapitre décrit l'anatomie du cœur humain, sa fonction et sa maladie. On aborde plus particulièrement la relation entre la structure des fibres cardiaques, la fonction cardiaque et les maladies cardiaques.

**Chapitre 2** *Imagerie de tenseur de diffusion (DTI) et théorie d'acquisition comprimée (CS).* Ce chapitre introduit le principe de l'imagerie par résonance magnétique (IRM) et de l'IRM de diffusion (IRMd), y compris la formation de l'image MR, la reconstruction de l'image et l'imagerie du tenseur de diffusion (DTI) cardiaque. Il décrit également la théorie de CS, les algorithmes de reconstruction et leurs applications.

La deuxième partie est dédiée à la reconstruction de l'IRM et DTI cardiaque basée sur CS:

**Chapitre 3** *Acquisition comprimée via trames ajustées guidées par les données et variation totale généralisée.* Ce chapitre propose une méthode améliorée pour reconstruire des images MR dans le cadre de CS en combinant la contrainte de trames ajustées guidées par les données (TF data-driven) et la régularisation de variation totale généralisée (TGV). Le TF data-driven est utilisé pour apprendre de manière adaptative un ensemble de filtres à partir des données sous-échantillonées pour fournir une meilleure approximation parcimonieuse d'images. Le TGV est une généralisation de la théorie de TV, qui régularise sélectivement des régions d'image à différents niveaux et donc réduit l'effet d'escalier. Les expériences ont été réalisées sur les images par résonance magnétique de différents organes afin d'estimer l'efficacité de notre algorithme. Les résultats démontrent que l'approche proposée améliore les performances de reconstruction de différents types d'images MR. Certains résultats ont fait l'objet de [Huang *et al.*, 2015b].

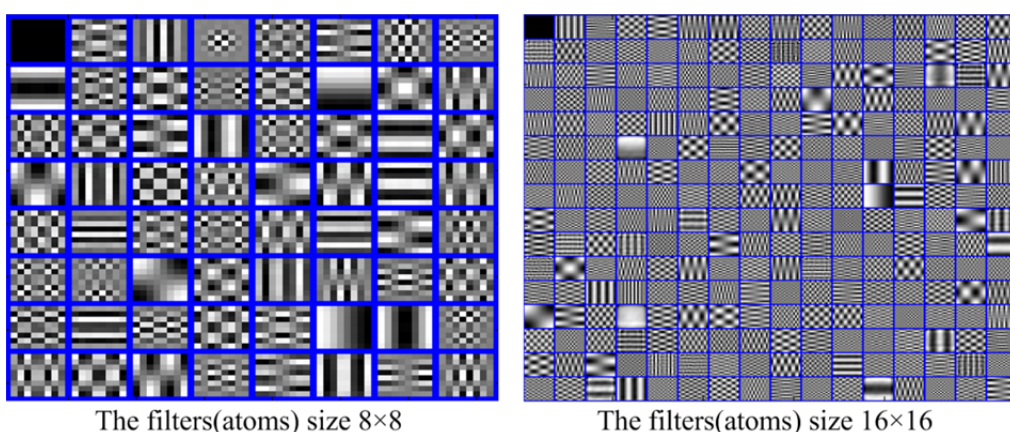
La méthode proposée pour reconstruire les images MR à partir des données espace k fortement sous-échantillonées consiste à résoudre le problème d'optimisation suivant

$$\hat{x} = \arg \min_x \left\{ \frac{1}{2} \|F_u x - b\| + \lambda \cdot \|\Psi x\|_1 + \beta \cdot \text{TGV}_\alpha^2(x) \right\}.$$

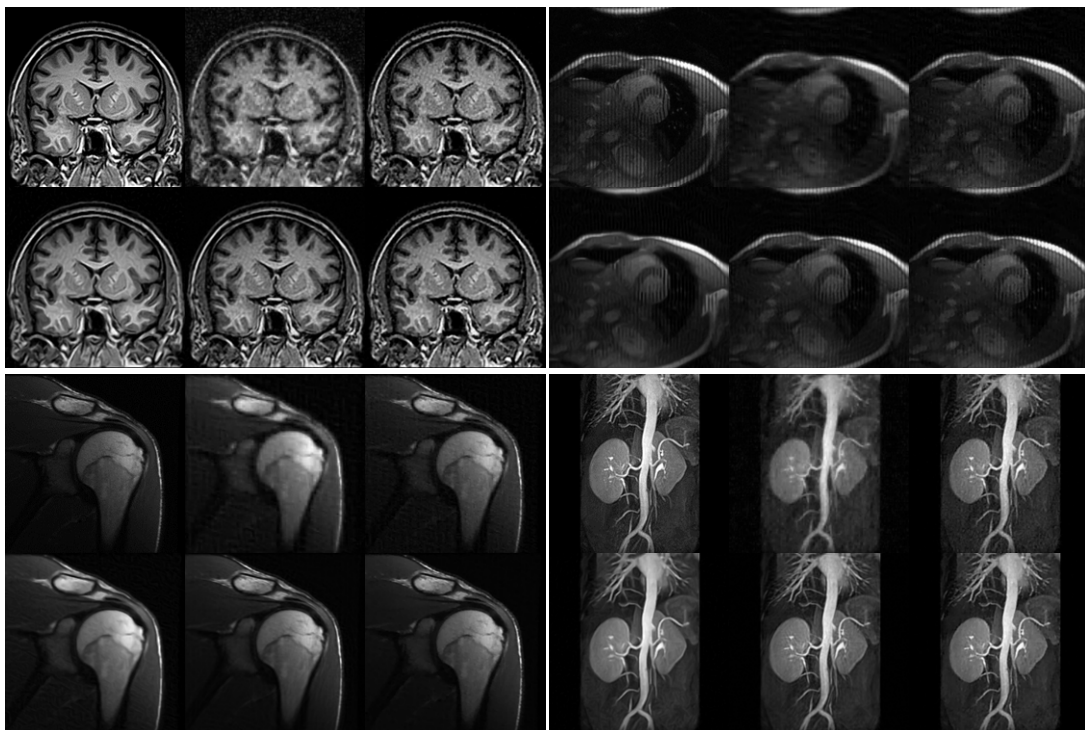
Le TF data-driven est une technique d'apprentissage de dictionnaires, qui vise à construire des trames ajustées à partir des images d'entrée afin de représenter de manière parcimonieuse les données en question en résolvant le problème de minimisation suivant

$$\min_{v, \Psi} \|v - \Psi x\|_2^2 + \gamma \cdot \|v\|_0, \quad \text{subject to } \Psi^T \Psi = I.$$

Les figures suivantes illustrent les filtres de TF data-driven, qui sont construits avec deux tailles différentes (chaque petit bloc de l'image représente un filter).

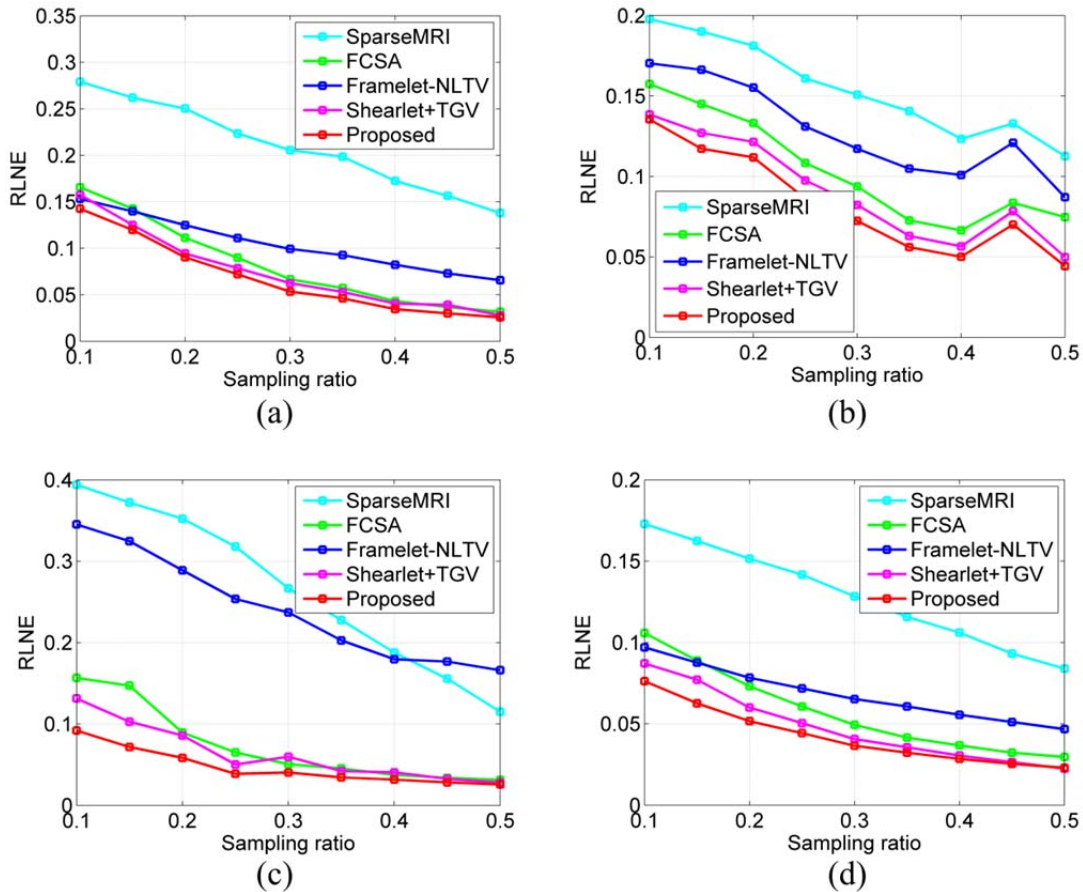


Les résultats de reconstruction sur différentes images MR à l'aide de la méthode développée sont illustrés ci-dessous, la comparaison avec des méthodes récentes étant également donnée.



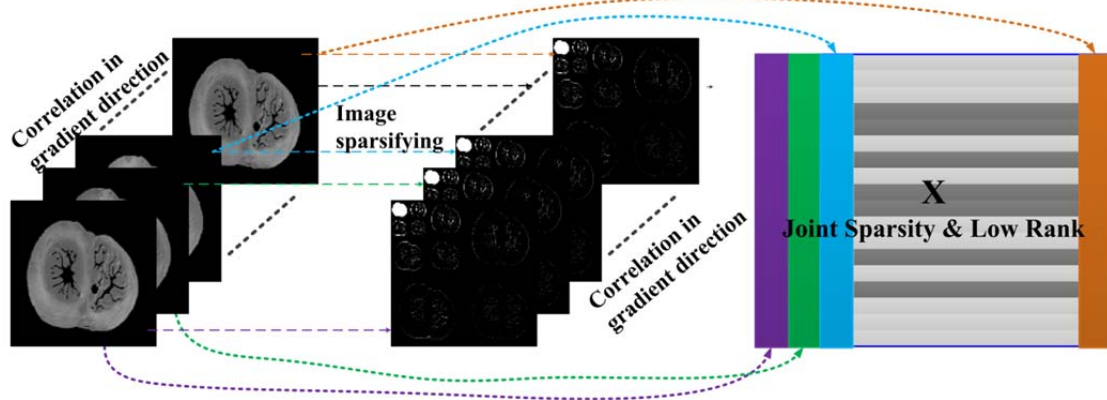
Résultats de reconstruction (un taux d'échantillonnage de 15%) correspondant à 4 organes. De gauche à droite et de haut en bas : images cérébrales coronales; images cardiaques; images d'épaule, et images artérielles rénales. Pour chaque organe, les 6 images correspondent aux 6 méthodes suivantes (de gauche à droite et de haut en bas) : Original MR images; images reconstructed by (b) SparseMRI [[Lustig et al., 2007](#)]; (c). FCSA [[Huang et al., 2011b](#)]; (d) Framelet+NLTV [[Gopi et al., 2014](#)]; (e) Shearlet+TGV [[Guo et al., 2014](#)]; (f) data-driven TF+TGV (proposée).

Les courbes suivantes illustrent la performance de la méthode proposée en termes de l'erreur de norme  $l_2$  relative (relative  $l_2$  norm error—RLNE) en fonction du taux d'échantillonnage. Les 4 figures correspondent respectivement aux images MR des 4 organes suivants : (a) images cérébrales coronales; (b) images cardiaques; (c) images d'épaule et (d) images artérielles rénales.



**Chapitre 4** *DTI cardiaque accéléré basé sur l’acquisition comprimée en utilisant conjointement la parcimonie et l’approximation de rang faible.* Ce chapitre présente un nouvel algorithme de reconstruction basée sur l’acquisition comprimée en utilisant conjointement la parcimonie et la déficience de rang pour reconstruire des images de DTMR cardiaques à partir des données espace k sous-échantillonnées. La parcimonie et la déficience de rang sont incorporées dans le cadre de la reconstruction CS. Le problème d’optimisation sous contrainte est résolu par une méthode rapide de premier ordre. Les expériences ont été réalisées à la fois sur les DTMR images cardiaques simulées et réelles. Les résultats démontrent que l’approche proposée présente une meilleure reconstruction que des méthodes existantes en termes des indices DTI tels que l’anisotropie fractionnelle (FA), la diffusivité moyenne (MD), l’angle transversal et l’angle d’hélice. Ces résultats ont été retranscrits dans [Huang et al., 2015a].

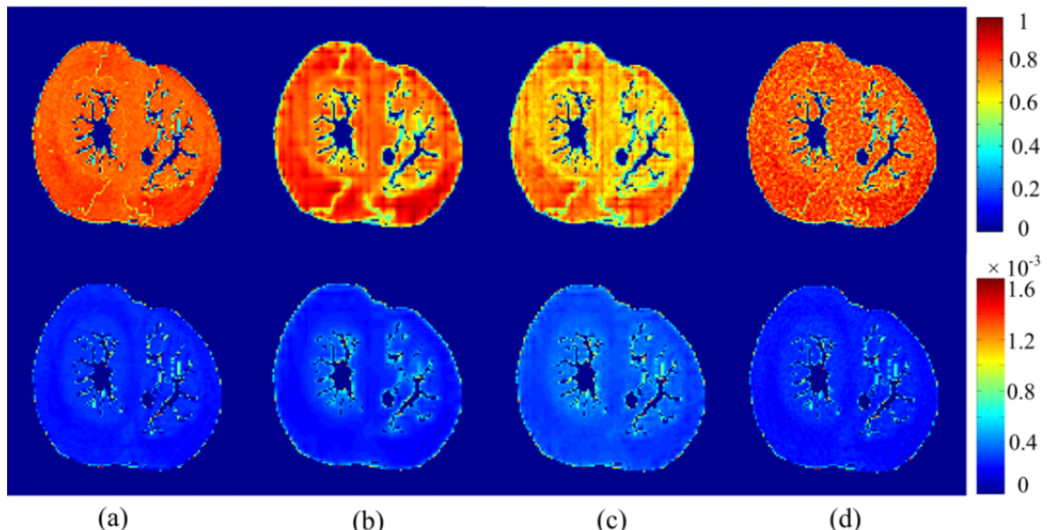
Les images pondérées en diffusion (diffusion weighted—DW) peuvent être parcimonieuses dans un domaine transformé convenable. En plus, les images DW acquises dans différentes directions de gradient de diffusion sont corrélées. Tout cela signifie que si l’on arrange ces images (ou leur coefficients transformés) dans une matrice  $X$  comme vecteurs de colonne, la matrice ainsi résultante sera parcimonieuse en ligne (row-sparse) et aura un faible rang (low rank). La figure ci-dessous illustre ce principe.



La reconstruction des images DW peut être formulée comme le problème d'optimisation suivant:

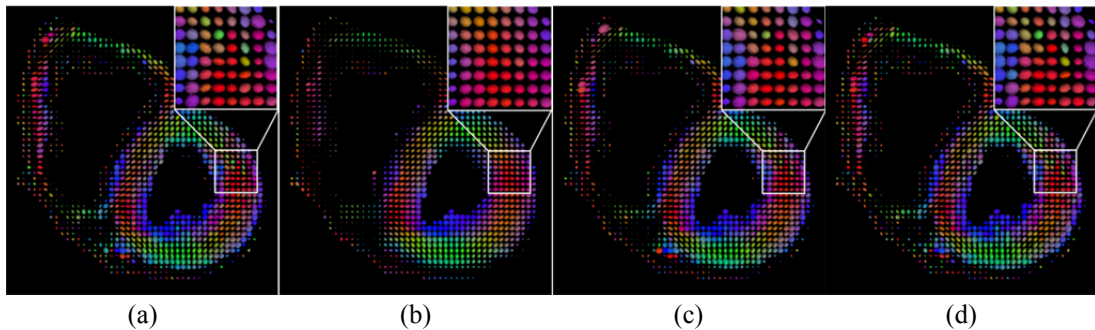
$$\widehat{X} = \arg \min_X \left\{ \frac{1}{2} \|F^u X - b\|_2^2 + \alpha \cdot \|X\|_* + \beta \cdot \|\Phi X\|_{2,1} \right\}$$

La figure ci-dessous illustre les cartographies de FA (première ligne) et de MD (deuxième ligne) calculées à partir des images DW simulées.



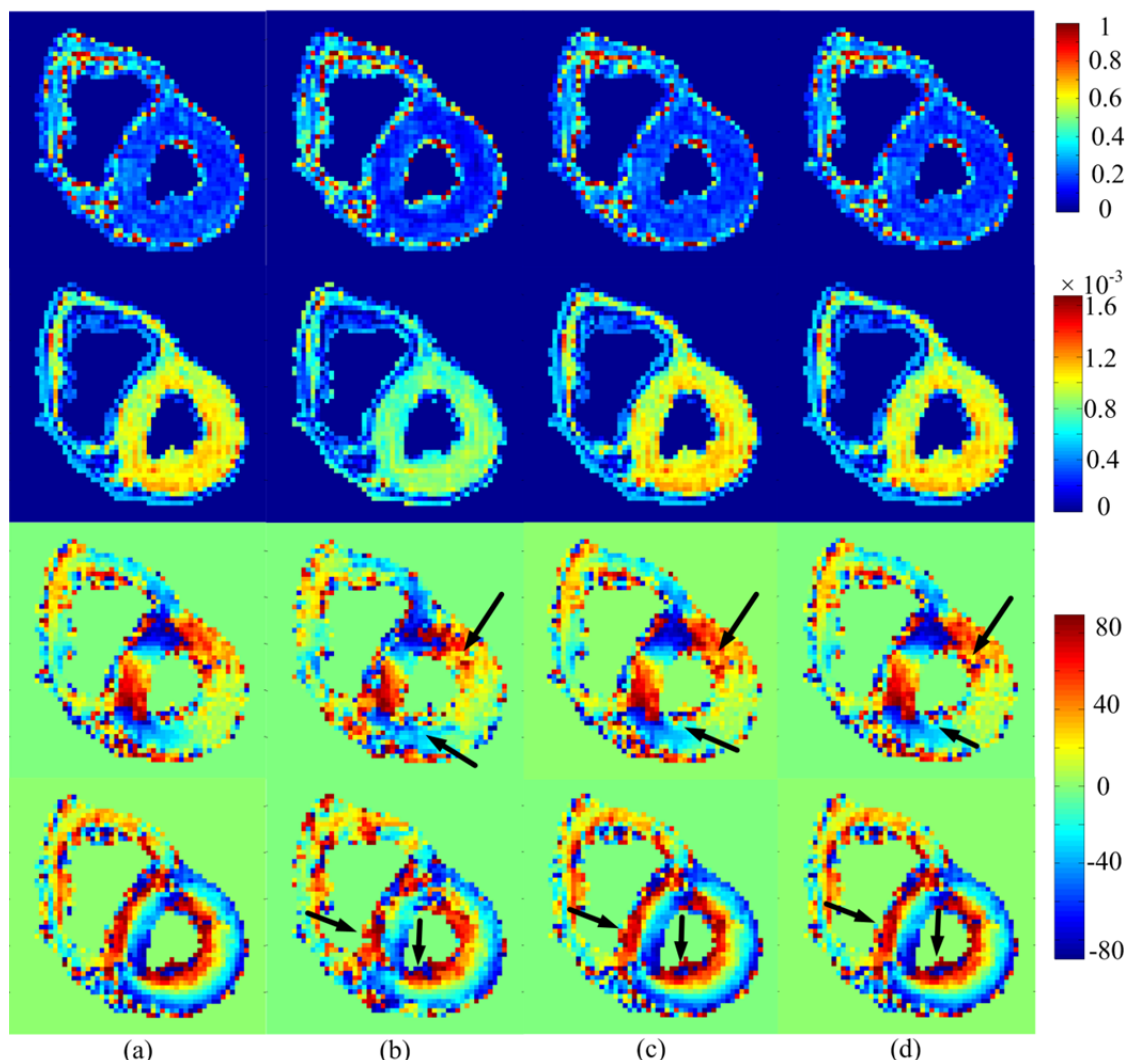
Cartographies de FA (première ligne) et de MD (deuxième ligne) calculées à partir des images DW simulées. Reconstruction en utilisant (a) l'espace k complet, (b) basis CS, (c) joint sparsity, et (d) la méthode proposée.

La figure ci-dessous illustre les champs de tenseurs sur des données réelles du cœur humain en utilisant différentes méthodes avec un taux d'échantillonnage de 15%. (a) Reconstruction from the complete k-space data; Reconstructions from undersampled k-space using (b) basis CS, (c) joint sparsity and (d) the proposed methods.



Résultats de reconstruction des champs de tenseur. (a) Reconstruction à partir de l'espace  $k$  complet. Reconstructions à partir de l'espace  $k$  sous-échantillonné en utilisant (b) basis CS, (c) joint sparsity, et (d) la méthode proposée.

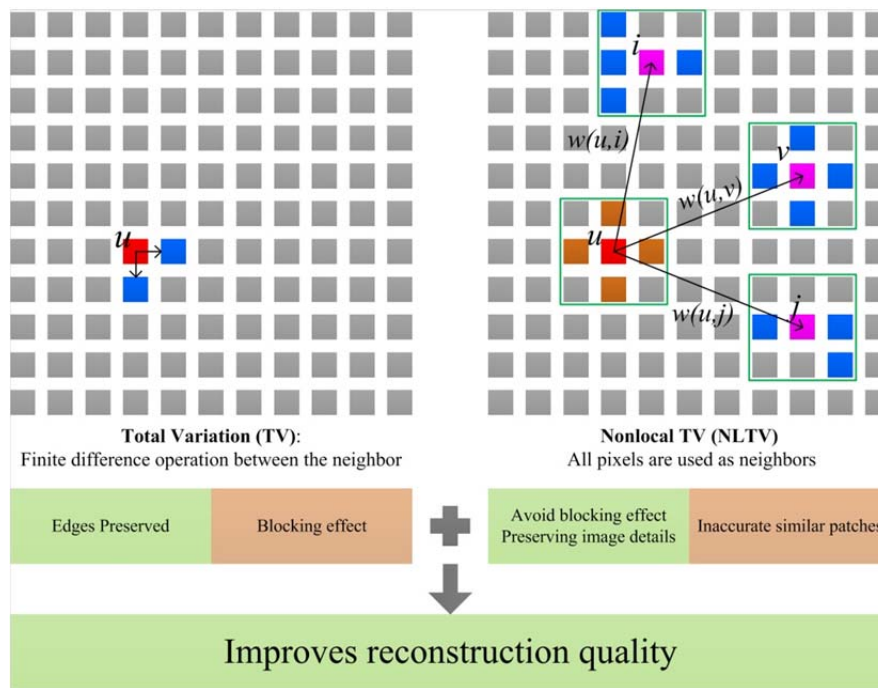
La figure ci-dessous montre les cartographies de FA (première ligne), MD (deuxième ligne), TA (troisième ligne—angle transverse) et HA(quatrième ligne—angle d'hélice d'un cœur humain ex vivo. Le taux d'échantillonnage est 25%.



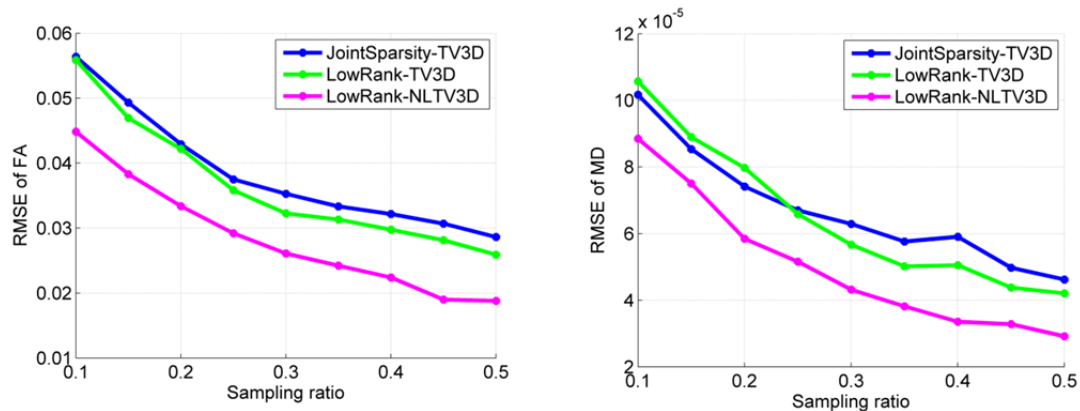
Résultats de reconstruction des cartographies. (a) Reconstruction à partir de l'espace  $k$  complet (colonne 1). Reconstructions à partir de l'espace  $k$  sous-échantillonné en utilisant (b) basis CS (colonne 2); (c) joint sparsity (colonne 3), et (d) la méthode proposée (colonne 4).

**Chapitre 5** DTI cardiaque accéléré basé sur l'acquisition comprimée en utilisant de l'approximation de rang faible et la contrainte de TV non locale. Ce chapitre présente une nouvelle méthode de reconstruction en utilisant la théorie d'acquisition comprimée (compressed sensing—CS) avec la contrainte de rang faible et la régularisation par variation totale (TV) afin de reconstruire des images DTI cardiaques à partir des données k-espace fortement sous-échantillonnées. Deux régularisations TV sont considérées: TV locale (i.e. TV classique) et TV non locale (NLTv). Le problème d'optimisation sous contrainte est résolu par une méthode rapide d'ordre premier. Les expérimentations sont effectuées sur des images pondérées en diffusion simulées et réelles. Les résultats montrent que les erreurs de reconstruction avec nos approches sont inférieures à celles produites par des méthodes de reconstruction CS-DTI existantes, en termes des indices du tenseur de diffusion, tels que l'anisotropie fractionnelle (FA) et diffusivité moyenne (MD). Certains des résultats présentés dans ce chapitre ont été publiés dans ISBI 2014 [Huang *et al.*, 2014].

La contrainte TV permet une élimination efficace des artefacts de sous-échantillonnage ainsi qu'un débruitage avec préservation de bords de l'image. Toutefois, le modèle TV favorise des structures de l'image constante par morceaux, rend des détails flous et provoque l'effet de bloc avec des structures fines perdues, bien que les bords soient préservés dans la reconstruction. La méthode de régularisation de variation totale non locale (NLTv) étend la TV classique à une variante non locale de cette dernière. Dans la NLTv, le gradient est calculé en faisant intervenir des pixels appartenant à toute image au lieu des plus proches pixels voisins. La différence entre la TV et la NLTv est illustrée par la figure suivante.

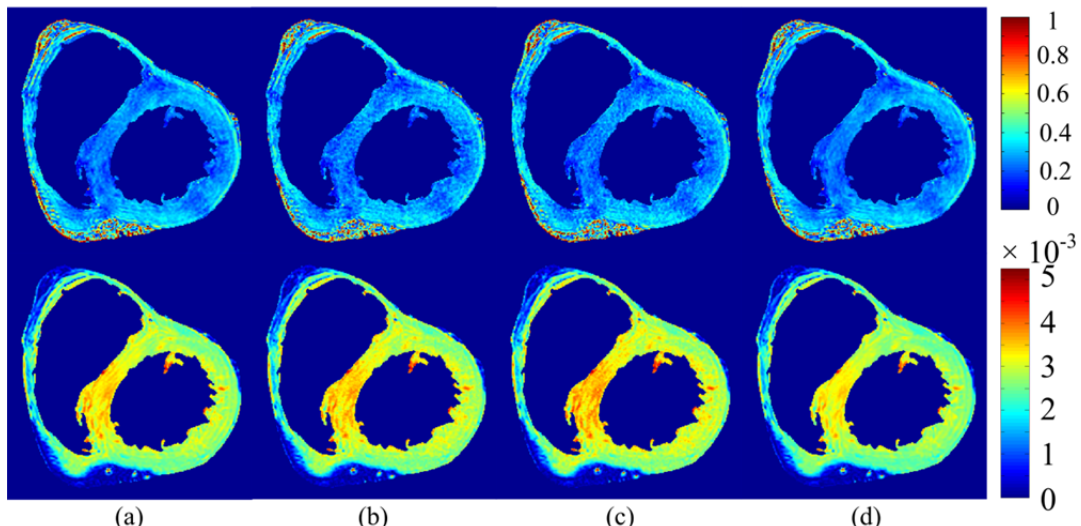


Les résultats expérimentaux démontrent que les modèles TV et NLTv sont complémentaires, ce qui rend la méthode proposée particulièrement efficace pour réduire le bruit et préserver les bords et les détails de l'image. Par conséquent, la méthode de reconstruction proposée produit des images de haute qualité, comme l'illustrent les courbes dans la figure ci-dessous.



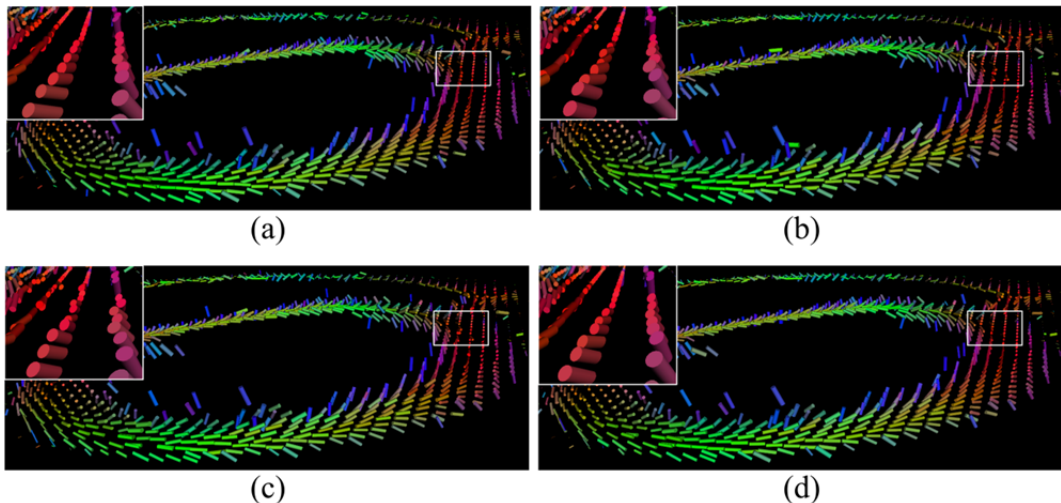
La figure ci-dessous montre les cartographies de FA (gauche) et de MD (droite) d'un cœur humain ex vivo avec un taux d'échantillonnage de 25%.

Illustrated the maps of FA (first row) and MD (second row) of the real human heart data with the sampling rate of 25%. (a) Reconstruction from the complete k-space data; Reconstructions from undersampled k-space using (b) joint sparsity with TV; (c) low rank with TV; and (d) the low rank with NLTV methods.



Résultats de reconstruction des cartographies de FA et MD. (a) Reconstruction à partir de l'espace k complet. Reconstructions à partir de l'espace k sous-échantillonné en utilisant (b) joint sparsity with TV; (c) low rank with TV; and (d) the low rank with NLTV methods.

La reconstruction des champs de tenseurs sur des coeurs humains ex vivo en utilisant différentes méthodes (avec un taux d'échantillonnage de 15%) est montrée dans la figure ci-dessous.

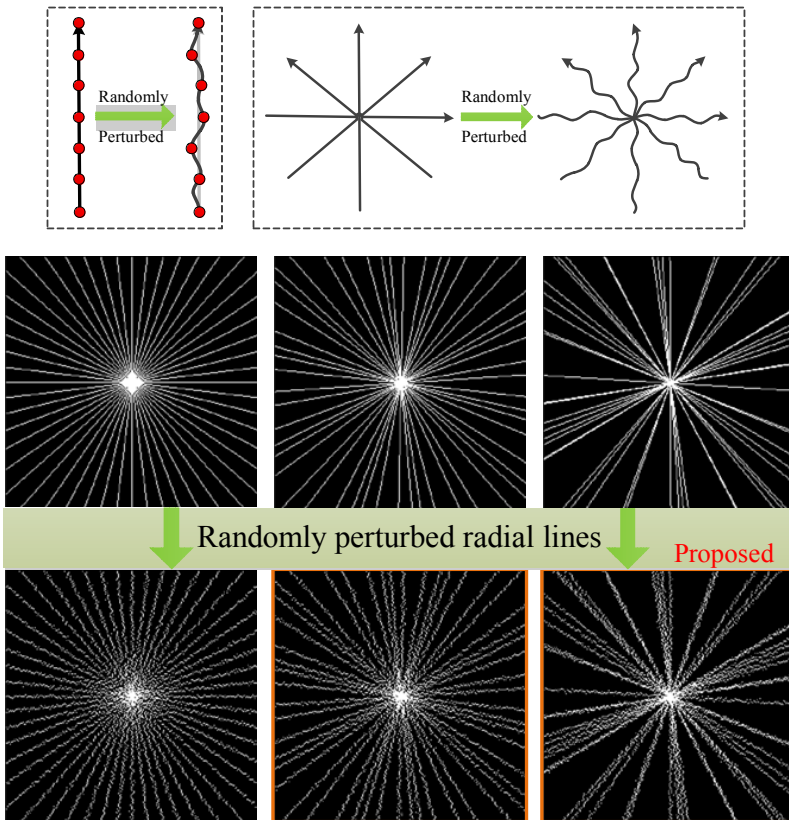


Résultats de reconstruction des champs de tenseurs. (a) Reconstruction à partir de l'espace  $k$  complet. Reconstructions à partir de l'espace  $k$  sous-échantillonné en utilisant (b) joint sparsity with TV; (c) low rank with TV; and (d) the low rank with NLTV methods.

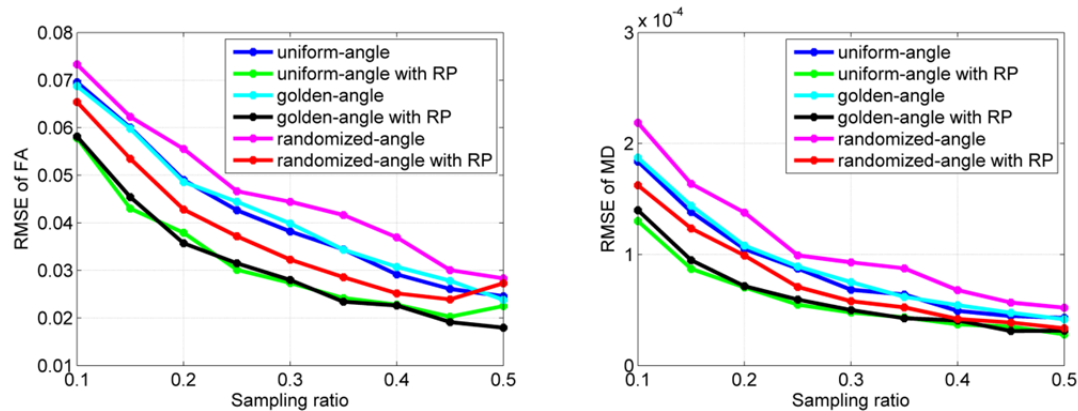
**Chapitre 6** *Influence des schémas de sous-échantillonnage radial sur le DTI cardiaque basé sur CS.* Ce chapitre s'intéresse à l'impact des schémas de sous-échantillonnage radial sur le DTI cardiaque basé sur CS. Le sous-échantillonnage de l'espace  $k$  fournit un moyen efficace de réduire la quantité de données à acquérir tout en maintenant la qualité de l'image. L'échantillonnage purement aléatoire de l'espace  $k$  est généralement impossible en raison des considérations physiologiques et matériel. Le sous-échantillonnage radial est l'un des schémas les plus populaires d'échantillonnage de l'espace  $k$  non-cartésien, parce qu'il est relativement moins sensible au mouvement que les trajectoires cartésiennes. Les artefacts de reconstruction linéaire ressemblent plus au bruit. Pour ces raisons, l'imagerie radiale est une stratégie prometteuse de sous-échantillonnage pour accélérer les acquisitions. Dans ce chapitre, nous proposons deux schémas de sous-échantillonnage radial perturbés aléatoirement: angle d'or et angle aléatoire. Les méthodes proposées sont comparées avec les méthodes existantes, y compris l'angle uniforme, l'angle uniforme perturbé aléatoirement, l'angle d'or et l'angle aléatoire. Les méthodes ont été évaluées sur des images aussi bien simulées que réelles du cœur.

- **Angle uniforme:** L'angle entre les échantillons sur les rayons voisins est incrémenté par un incrément d'angle constant  $\Delta\phi = \frac{180}{K}$ , où  $K$  est le nombre de rayons.
- **Angle d'or:** Les projections radiales sont successivement incrémentées avec l'angle d'or  $\Delta\phi = \frac{\sqrt{5}-1}{2} \cdot 180 \approx 111.25^\circ$ .
- **Angle aléatoire:** dans ce cas, les rayons sont générés à partir des angles aléatoires qui sont uniformément distribués.

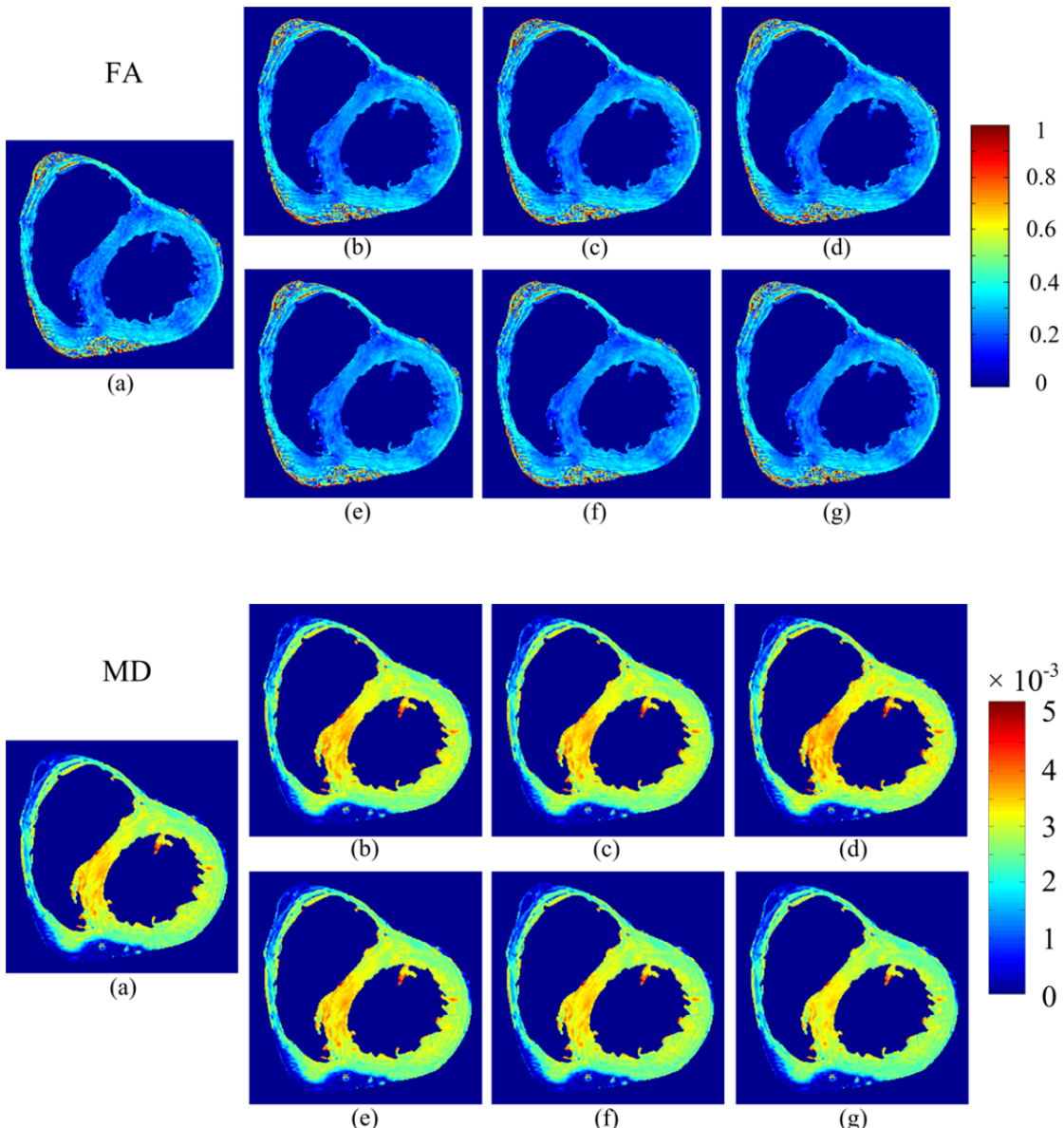
La figure suivante illustre comment perturber les lignes radiales en ajoutant de légères déviations aléatoires selon la loi gaussienne avec des moyennes nulles et des variances variables.



Les courbes suivantes montrent que pour la même quantité de données espace k, échantillonner aléatoirement autour d'une ligne radiale produit une meilleure reconstruction en termes de FA et MD, et que le sous-échantillonnage avec l'angle d'or aléatoirement perturbé conduit aux meilleurs résultats pour la reconstruction CS-DTMR cardiaque. La comparaison de performance a été effectuée en termes de RMSE de FA et MD sur des données réelles et en fonction du taux d'échantillonnage (RP est l'abréviation du terme Randomly Perturbed).

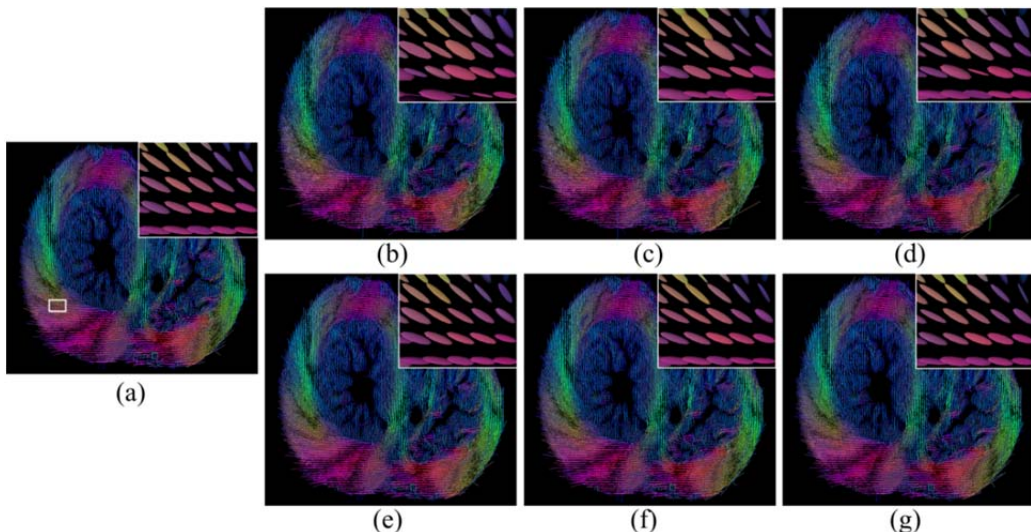


Les cartographies de FA et de MD d'un cœur humain ex vivo obtenues avec un taux d'échantillonnage de 25% sont données ci-dessous.



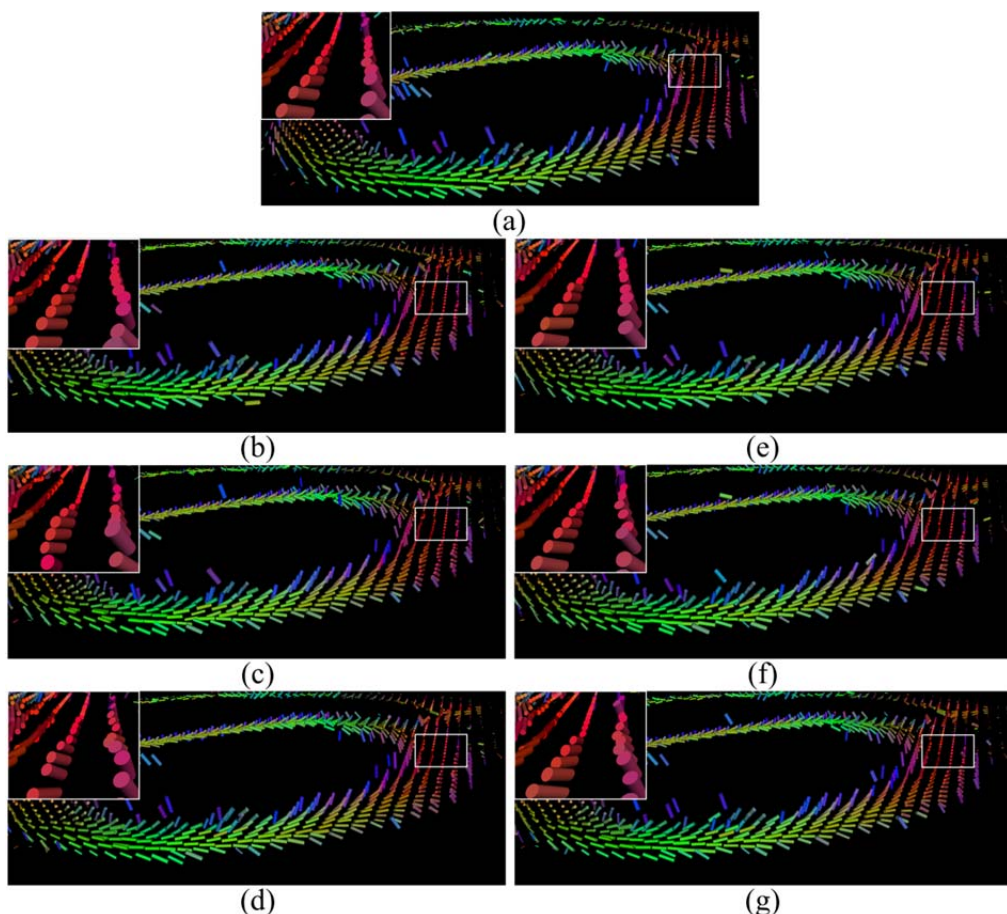
Cartographies de FA et MD obtenues avec un taux d'échantillonnage de 25%. (a) Reconstruction à partir de l'espace k complet. Reconstructions à partir de l'espace k sous-échantilloné en utilisant (b) uniform-angle radial, (c) golden-angle radial, (d) random-angle radial, et (e)-(g) the corresponding randomly perturbed radial sampling of (b)-(d).

La reconstruction des champs de tenseurs sur des images cardiaques simulées est montrée dans la figure ci-dessous (avec un taux d'échantillonnage de 25%). Les tenseurs sont représentés par des ellipsoïdes. Afin de mieux visualiser l'orientation des fibres cardiaques, les images de tenseurs sont sous-échantillonées avec un taux de 3 en prenant un tenseur sur 3.



Champs de tenseurs reconstruits avec différentes stratégies de sous-échantillonnage. (a) Reconstruction à partir de l'espace  $k$  complet. Reconstructions à partir de l'espace  $k$  sous-échantilloné en utilisant (b) uniform-angle radial, (c) golden-angle radial, (d) random-angle radial, et (e)-(g) the corresponding randomly perturbed radial sampling of (b)-(d).

Un exemple de reconstruction de champs de tenseurs sur coeurs humains réels est donné dans la figure ci-dessous. Le taux d'échantillonnage est 25%. Comme dans l'exemple illustré ci-dessus, les tenseurs sont représentés par des ellipsoïdes, et afin de mieux visualiser l'orientation des fibres cardiaques, les images de tenseurs sont sous-échantillonées avec un taux de 3 en prenant un tenseur sur 3.



Exemple de reconstruction de champs de tenseurs sur un cœur humain réel, obtenus avec différentes stratégies de sous-échantillonnage. (a) Reconstruction à partir de l'espace k complet. Reconstructions à partir de l'espace k sous-échantillonné en utilisant (b) uniform-angle radial, (c) golden-angle radial, (d) random-angle radial, et (e)-(g) the corresponding randomly perturbed radial sampling of (b)-(d).

**Chapitre 7** *Conclusions générales et perspectives.* Il résume les contributions et les perspectives des travaux de recherche présentés dans cette thèse.

Le présent travail a proposé plusieurs méthodes efficaces pour reconstruire des images IRM et plus spécifiquement des images MR de tenseurs de diffusion (DTMR) cardiaques à partir de l'espace k fortement sous-échantillonné. Nous avons étudié plus particulièrement deux schémas de sous-échantillonnage radial pour DTMR cardiaque basée sur la théorie CS. Les expériences menées ont démontré l'efficacité de nos méthodes. À la lumière de ces résultats, un certain nombre de points intéressants peuvent être formulés pour les travaux futurs. Tout d'abord, les résultats présentés dans cette thèse étant sur le coeur ex vivo, il serait intéressant d'appliquer les méthodes au DTI cardiaque in vivo. Ensuite, étant donné que la technique d'imagerie parallèle permet l'obtention de facteurs d'accélération plus élevées, il serait envisageable de combiner le CS, l'imagerie parallèle et des trajectoires non cartésiennes afin d'accélérer encore plus l'acquisition de données et de réduire les artefacts de mouvement cardiaques pour le DTI du cœur humain. Enfin, l'imagerie de diffusion à haute résolution angulaire (HARDI) ayant récemment reçu l'attention intensive, il serait intéressant d'étendre les méthodes proposées à HARDI.

## General Introduction

The heart is one of the most vital organs of the human body, which pumps continually blood containing oxygen and nutrients needed by the other parts of the body to maintain life. The heart diseases or more generally cardiovascular diseases (CVD) is the leading cause of death in the world, representing an estimated 30% (over 17.3 million deaths) of all deaths across the globe [Christodoulou *et al.*, 2014, Go *et al.*, 2014, Mozaffarian *et al.*, 2015]. Each year CVD causes 47% of all deaths (over 4 million deaths) in Europe and 40% (over 1.9 million deaths) in the European Union [Nichols *et al.*]. On the other hand, CVD has major economic costs as well as human costs for Europe. Overall CVD is estimated to cost the European Union economy almost €196 billion a year. Of the total cost of CVD in the European Union, around 54% is due to direct health care costs, 24% due to productivity losses and 22% due to the informal care of people with CVD [Nichols *et al.*].

Therefore, from the point of view of health and economic opportunities, it is very critical to study the microstructure of the heart for both explaining the heart disease symptoms and investigating the effective therapy means. The microstructure of the heart is complex, and in particular cardiac fiber architecture is fundamental in electrophysiological and mechanical functions of the heart. Obtaining cardiac three-dimensional (3D) fiber architecture will provide a new way to understand how the fiber structure of the heart influences its electrical and mechanical functions and study the underlying disease of the heart.

The first understanding of cardiac fiber architectures was achieved using histological analysis of selected tissue regions [Ross *et al.*, 1979]. Such techniques are known to suffer from many problems such as spatial resolution, distortion and misalignment. In addition, they are not by essence 3D. To get rid of these problems, polarized light imaging (PLI) was developed to investigate 3D fiber orientations of ex vivo human hearts [Jouk *et al.*, 1995, Jouk *et al.*, 2007]. This technique provides for the first time a mean to physically measure 3D orientations of myocardial fibers of an entire heart, with a high spatial resolution of  $0.1\text{mm} \times 0.1\text{mm} \times 0.5\text{mm}$ . Compared with dissection and histological techniques, PLI is more objective since it does not involve any human operation during the measurement process. However, both histological and PLI techniques are only limited to ex vivo hearts and cannot be used for imaging in vivo human hearts.

More recently, Diffusion Magnetic Resonance Imaging (dMRI), which includes Diffusion Tensor Imaging (DTI) and High Angular Resolution Diffusion Imaging (HARDI), has emerged as a new and promising technique for analyzing the 3D fibrous structure of tissues. dMRI allows quantitative characterization of the shape and organization of tissue microstructures [Basser *et al.*, 1994a;1994b]. It is a powerful tool and is currently the only means to noninvasively investigate fiber architectures of the human heart [Hsu *et al.*, 2001, Le Bihan *et al.*, 2001, Helm *et al.*, 2005b, Wu *et al.*, 2006, Toussaint *et al.*, 2010, Tournier *et al.*, 2011, Wei *et al.*, 2013, Froeling *et al.*, 2014, Naumova *et al.*, 2014, Wei *et al.*, 2015].

However, one of the most difficult problems in cardiac dMRI is cardiac motion, which causes blurring or signal losses [Nielles-Vallespin *et al.*, 2013, Wei *et al.*, 2013]. In order to minimize cardiac motion artefacts, it is important to keep DT image acquisition time as short as possible in each heartbeat. On the other hand, the spatial resolution of in vivo cardiac DTI is still too low (2.6mm in the plane and 6-7mm thickness). Therefore, one important work is to develop acquisition techniques to obtain higher resolution DTI data. With higher spatial

resolution, we can obtain fiber tracts that could be much coherent with ex vivo histological studies. This can be achieved by faster collection of data. In addition, it is well known that the acquisition of diffusion weighted (DW) images is often corrupted by high-level noise (signal-to-noise ratio—SNR) and the intensity of DW signals is weaker than that of classical magnetic resonance signals [Bao *et al.*, 2013, Zhang *et al.*, 2013]. In practice, the additional signal averaging through acquisition repetition is generally a good way to increase SNR, but it further lengthens scan time. In summary, DTI is known to suffer from long acquisition time to obtain high quality data (temporal and spatial resolution, SNR), which greatly limits its practical and clinical use for human heart imaging [Dou *et al.*, 2002, Dou *et al.*, 2003, Helm *et al.*, 2005b, Wu *et al.*, 2006].

Conventionally, many attempts have been made in order to speed up data acquisition, reduce the amount of data required and improve the SNR of diffusion signals as much as possible, including parallel imaging [Bammer *et al.*, 2001, Bammer *et al.*, 2002, Jaermann *et al.*, 2004, Holdsworth *et al.*, 2009], simultaneous multislice imaging [Filli *et al.*, 2015, Lau *et al.*, 2015], partial k-space reconstruction [Luo *et al.*, 2012], and filtered reduced-encoding projection-reconstruction [Jiang *et al.*, 2005]. But, these methods are not very suitable for highly undersampled k-space data.

In recent years, Compressed Sensing (CS) has emerged as a new framework for both acquiring data and reconstructing signals with high quality from highly undersampled measurements (with respect to the traditional Shannon-Nyquist sampling theorem required [Candes *et al.*, 2006a, Candes *et al.*, 2006c, Donoho, 2006]). CS exploits sparsity or compressibility of signals in certain domain (pixel or transform domain), and combines the sampling and compression into a unified framework. To date, CS has been successfully applied in biomedical imaging and has shown great potential [Wang *et al.*, 2011], such as MRI [Lustig *et al.*, 2007, Lustig *et al.*, 2008] and dynamic MRI [Bilen, 2013].

The main motivation of this research is to investigate fast imaging techniques by reconstructing high-quality images from highly undersampled data. The methodology adopted is based on the recent theory of CS. More precisely, we address the use of CS for magnetic resonance imaging (MRI) and cardiac DTI.

The research work presented in this thesis is organized as follows.

The first part of this manuscript describes the necessary background for the subsequent chapters:

**Chapter 1** “*Heart function and disease*” describes the human heart anatomy, cardiac function and disease. we describe the relation between cardiac fiber structure and heart function and diseases.

**Chapter 2** “*Diffusion Tensor Imaging (DTI) and Compressed Sensing (CS) Theory*” introduces the principles of Magnetic Resonance Imaging (MRI) and diffusion MRI (dMRI), covering MR image formation, image reconstruction and cardiac diffusion tensor imaging (DTI). It also describes the CS theory, reconstruction algorithms and their applications.

The second part is dedicated to the reconstruction MRI and cardiac DTI based on CS:

**Chapter 3** “*Compressed Sensing MRI via Data-driven tight frame and Total Generalized Variation*” addresses the proposed method for MR image reconstruction with data-driven tight frame and total generalized variation(TGV) constraints. The data-driven TF is used to adaptively learn a set of filters from the under-sampled data itself to provide a better sparse approximation of images. The TGV is a generalization of the total variation (TV) theory, which “selectively regularizes” different image regions at different levels and thus leads to suppression of the staircase effect. The proposed methods are evaluated on different MR

images with varying content. The experimental results demonstrate that the proposed approach improves reconstruction quality compared to state of the art CS-MRI reconstruction methods [Huang *et al.*, 2015b].

**Chapter 4** “*Accelerated Cardiac DTI Based on CS Using Joint Sparsity and Low Rank Approximation*” presents a new CS reconstruction method that employs joint sparsity and rank deficiency prior to reconstruct cardiac DTMR images from highly undersampled k-space data. The sparsity and rank deficiency are incorporated into the CS reconstruction framework. The underlying constrained optimization problem is solved by the first-order fast method. The experiments were carried out on both simulation and real human cardiac DTMR images. The results demonstrate that the proposed approach has lower reconstruction errors in terms of DTI indices, including fractional anisotropy (FA), mean diffusivity (MD), transverse angle and helix angle, compared to existing CS-DTMR image reconstruction techniques. Some of the results mentioned in this chapter were reported in [Huang *et al.*, 2015a].

**Chapter 5** “*Accelerated cardiac DTI based on CS using low-rank approximation and non-local TV constraint*” proposes to apply the CS scheme with the low rank constraint and total variation (TV) regularizations to reconstruct cardiac DTI images from highly undersampled k-space data. Two TV regularizations are considered: local TV (i.e. classical TV) and nonlocal TV (NLTv). The experiments are carried out on both simulated and real human cardiac diffusion weighted (DW) images. The results demonstrate that the proposed approach presents lower reconstruction errors compared to existing CS-DTMR images reconstruction techniques. Some of the results presented in this chapter were reported in ISBI 2014 [Huang *et al.*, 2014].

**Chapter 6** “*The influence of radial undersampling schemes on compressed sensing cardiac DTI*” studies the impact of the radial undersampling schemes on CS-based cardiac DTI. In this chapter, we propose two randomly perturbed radial undersampling schemes: golden-angle and random angle. The proposed methods are compared with existing radial undersampling methods: uniformity-angle, randomly perturbed uniformity-angle, golden-angle, random angle. The experiments were carried out on both simulation and real human heart DTI data.

**Chapter 7** “*General conclusions and perspectives*” summarizes the contributions followed by the perspectives of the research work presented in this thesis.

# **Part I**

---

---

## **Medical and methodological background**

---

---

# Chapter 1

## Heart function and disease

### Contents

---

Résumé en français.....	20
Abstract .....	21
1.1    Introduction.....	22
1.2    Heart anatomy.....	22
1.2.1 <i>Heart structure</i> .....	22
1.2.1.1    Chambers .....	22
1.2.1.2    Valves .....	23
1.2.1.3    Cardiac wall .....	24
1.2.2 <i>Myocardium structure</i> .....	25
1.2.2.1    Myocardial band model .....	25
1.2.2.2    Geodesic model.....	26
1.2.2.3    Laminar structure model.....	28
1.3    Heart diseases .....	28
1.4    Relation between fiber structure and heart function .....	30
1.5    Conclusion .....	30

---

## Résumé en français

Le cœur est l'un des organes les plus vitaux du corps humain, qui pompe sans cesse le sang contenant de l'oxygène et les nutriments nécessaires à d'autres parties du corps pour maintenir la vie. Les maladies cardiaques ou plus généralement les maladies cardiovasculaires (MCV) sont la principale cause de décès dans le monde. L'étude de la structure microscopique des fibres du cœur offre une nouvelle approche pour expliquer les maladies du cœur et trouver des moyens efficaces de thérapie. Dans ce chapitre, nous décrivons d'abord les structures cardiaques, puis nous citons certaines maladies cardiaques liées à la structure du muscle cardiaque. Enfin, nous exposons la relation entre la structure de fibres cardiaques et la fonction et la maladie du cœur.

**Abstract**

The heart is one of the most vital organs of the human body, which pumps non-stop blood containing oxygen and nutrients needed by the other parts of the body to maintain life. The heart diseases or more generally cardiovascular diseases (CVD) is the leading cause of death in the world. The investigation of the micro fiber structures of the heart provides a new approach to explaining heart disease and investigating effective therapy means. In this chapter, we first illustrate the heart structures from the view of the anatomy, and then present some cardiac diseases related to the cardiac fiber structure. At last, we describe the relation between cardiac fiber structure and heart function and diseases.

## 1.1 Introduction

The heart is one of the most vital organs of the human body, which pumps non-stop blood containing oxygen and nutrients needed by the other parts of the body to maintain life. The heart diseases or more generally cardiovascular diseases (CVD) is the leading cause of death in the world, representing an estimated 30% (over 15.616 million deaths) of all deaths across the globe [Christodoulou *et al.*, 2014, Go *et al.*, 2014, Nicholas *et al.*, 2015]. Each year CVD causes 47% of all deaths (over 4 million deaths) in Europe and 40% (over 1.9 million deaths) in the European Union [Nichols *et al.*]. On the other hand, CVD has major economic costs as well as human costs for Europe. Overall CVD is estimated to cost the European Union economy almost €196 billion a year. Of the total cost of CVD in the European Union, around 54% is due to direct health care costs, 24% due to productivity losses and 22% due to the informal care of people with CVD [Nichols *et al.*]. The heart has been extensively studied due to its importance to the human health. Therefore, from the point of view of health and economic opportunities, it is very critical to learn about the heart structure and its functions for both explaining the heart disease symptoms and investigating the effective therapy means.

## 1.2 Heart anatomy

Generally, the heart is located between the lungs in the middle of the chest, behind and slightly to the left of the breastbone. It is well known that the heart has approximatively the size of a fist and lies in the thoracic cavity. Usually, the heart can be divided mainly into four chambers (shown in Fig. 1.1): the two upper chambers of the heart are receiving chambers, and are called atriums; the bottom chambers are discharging chambers, and are called ventricles. The two right chambers, the right atrium (RA) and the right ventricle (RV), together are referred to as the right heart, and the two left chambers, the left atrium (LA) and left ventricle (LV), as the left heart. Each ventricle has a inlet valve and an outlet valve. These four valves ensure that blood flow travels through the heart only in one direction.

### 1.2.1 Heart structure

#### 1.2.1.1 Chambers

The whole human heart contains 4 chambers and is divided into right and left sides. There are the right atrium, left atrium, right ventricle, and left ventricle. Each side has an upper chamber called the atrium and a lower chamber called the ventricle. These four chambers constitute the blood circulation system of the body, where the chambers in the right side pump the deoxygenated blood and those in the left side pump the oxygenated blood.

**Right atrium:** It situates in the upper right section of the heart, receiving the de-oxygenated blood from the other parts of the body though two major veins, the superior vena cava and the inferior vena cava. The superior vena cava returns de-oxygenated blood mainly from the head, neck, arm and chest regions of the body to the right atrium. The inferior vena cava returns de-oxygenated blood from the lower body regions such as legs, back, abdomen and pelvis to the right atrium. The right atrium also pumps blood through the tricuspid valve into the right ventricle situated below.

**Right ventricle:** Located below the right atrium, this chamber has a form of triangle and extends from right atrium to near the apex of the heart. It receives blood from the right atrium and pumps it to the main pulmonary artery. The main pulmonary artery extends from the right ventricle and branches into left and right pulmonary arteries, which extend to the lungs. Here oxygen-poor blood picks up oxygen and is returned to the heart via the pulmonary veins.

**Left atrium:** This chamber sits opposite to the right atrium. The blood that goes through the lung becomes oxygenated; it returns into the left atrium via the right and left pulmonary veins and then the left atrium pumps this oxygen-rich blood into the left ventricle through the bicuspid valve or mitral valve.

**Left ventricle:** It is the lower part of the heart in the left side. Compared with the right ventricle, it is much longer and looks like a cone. It receives oxygen-rich blood from the left atrium above it, and pumps it through the aortic valve such that it is distributed throughout the entire body via the aorta, including the heart muscle itself through the coronary arteries. The left side of the heart is thicker than the right one because of the requirement to pump blood from the left side throughout the body, as opposed to the right side pumping only through the lungs.

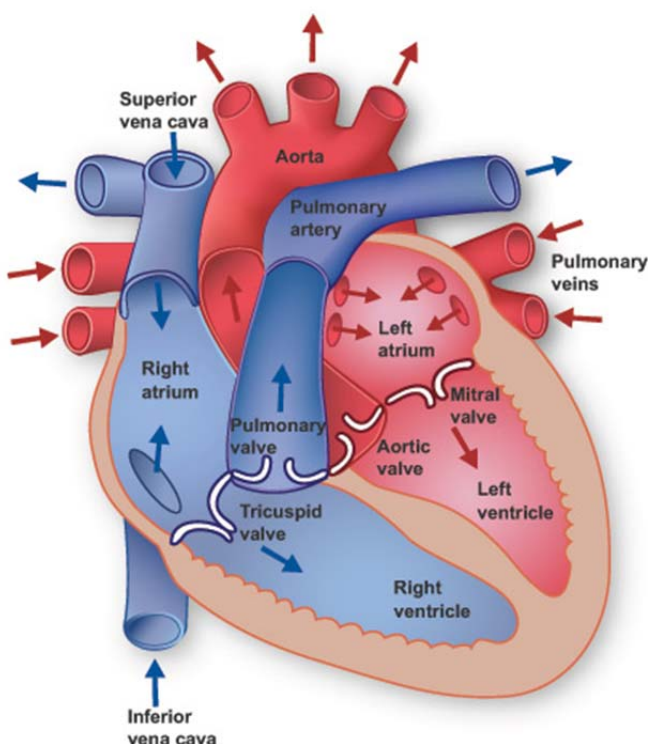


Fig. 1.1 Heart anatomical structure. (From Texas Heart Institute Heart Information Center, <http://www.texasheartinstitute.org/hic/anatomy/anatomy2.cfm>)

### 1.2.1.2 Valves

The blood circulating in the heart must flow in the correct direction: this is guaranteed by the heart valves. Four main valves determine the pathway of blood flow and allow the chambers of the heart to carry out their functions efficiently. These four valves can be classified into two groups, one is the atrioventricular valves and the other is semilunar valves, as shown in Fig. 1.2.

#### Atrioventricular valves

The valves that allow the blood to flow from the atria to the ventricles are called atrioventricular valves, which keep the blood from returning to the atrium. They are located between the atria and the ventricles. Named after the left and right side, atrioventricular valves can be divided into two types: tricuspid valve and mitral valve. The tricuspid valve is located between the right atrium and the right ventricle. The purpose of this valve is to open when the right atrium is in systole phase, thereby forcing any additional de-oxygenated blood

into the ventricle. The mitral valve is located between the left atrium and the left ventricle. Similar to the tricuspid valve, during the atrium's systole phase, the valve is forced open to allow the oxygenated blood from the lungs to enter into the left ventricle.

### Semilunar valves

There are two kinds of semilunar valves, one is pulmonary valve, which sits between the right ventricle and the pulmonary artery, the other is aortic valve which is located at the exit of the aorta and the left ventricle. Either of two valves opens and closes to allow the unidirectional flow of blood out of the heart, while preventing the blood flowing back into the ventricles.

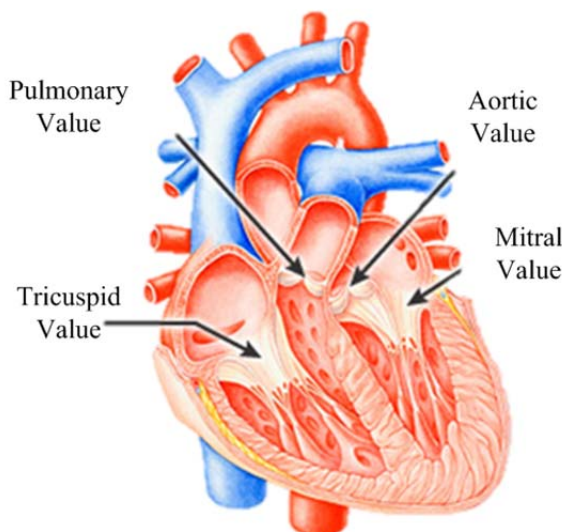


Fig. 1.2 Heart Valves (From: <http://www.webmd.com/heart-disease/guide/heart-valve-disease>)

#### 1.2.1.3 Cardiac wall

Generally, the cardiac wall consists of three tissues layers: epicardium, myocardium and endocardium, shown as in Fig. 1.3. Each layer is specialized in its structure and function. Thus, all three layers function together to ensure proper functioning of the heart and to ensure that it pumps blood properly to all organs in the body. Given below are details about the structures and functions of these three layers.

#### Epicardium

Epicardium describes the outer layer of heart tissue, when considered as a part of pericardium, it is the inner layer and called visceral pericardium. It is composed of a single sheet of squamous epithelial cells overlying delicate connective tissue. Epicardium serves as a protection layer because it can produce a pericardial fluid, which lubricates motion between the inner and outer layer of pericardium.

#### Myocardium

The myocardium is the basic muscle that makes up the heart. This muscle is involuntary and, this is striated in nature. The cardiac muscle structure consists of basic units of cardiac muscle cells known as myocyte. Coordinated contraction of the cardiac muscles is what makes the heart propel blood to various parts of the body. It is the function of the coronary arteries to supply blood and oxygen to the cardiac muscles. This is the thickest of all the layers. As is common knowledge, the cardiac muscle function is to ensure that the heart beats

around 72 times per minute. Thus, the cardiac muscles cannot afford to rest even for a single second. Therefore, it is essential that these muscles get blood supply and nutrition continuously, as any kind of disruption in the blood and nutrition supply to these muscles can result in death of a part of the cardiac muscle, which is known as myocardial infarction or heart attack. This could in turn lead to a complete cessation of functioning of the heart muscles, known as cardiac arrest.

### Endocardium

The endocardium is the innermost, thin and smooth layer of epithelial tissue that lines the inner surface of all the heart chambers and valves, which is responsible for prolonging myocardial contraction.

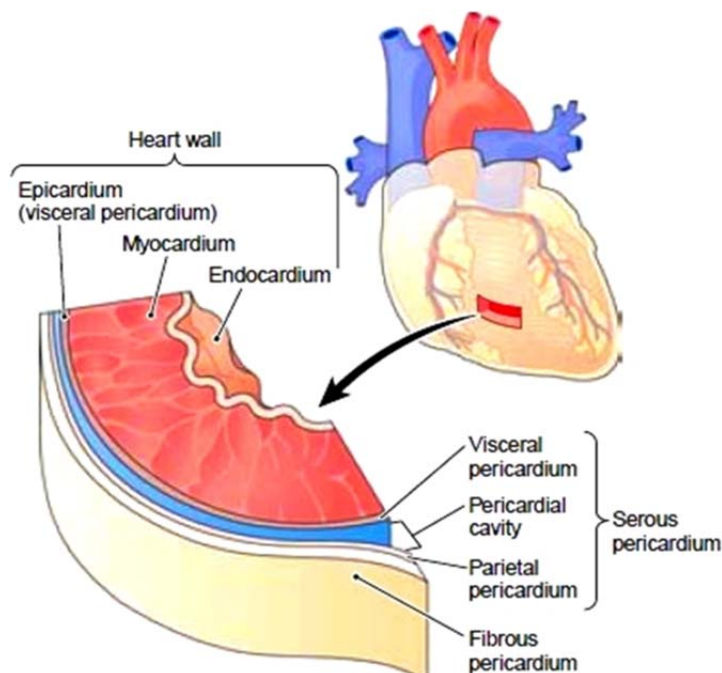


Fig. 1.3 Heart wall structure (From: [http://encyclopedia.lubopitko-bg.com/Structure\\_of\\_the\\_Heart.html](http://encyclopedia.lubopitko-bg.com/Structure_of_the_Heart.html))

### 1.2.2 Myocardium structure

In the three layers of the heart wall, the myocardium layer is the most important one for maintaining the heart normal functions. There are numerous models describing the structure of myocardium; here we present several well-known ones.

#### 1.2.2.1 Myocardial band model

The helical ventricular myocardial band (HVMB) concept, proposed in 1972 by the Spanish scientist Francisco Torrent-Guasp [Torrent-Guasp, 1973], brings a new viewpoint on the architecture of ventricular myocardium. This idea is of helical rope model, which considers the configuration of myocardium as shown in Fig. 1.4.

This model describes the myocardium structure as helical ropes whose length varies with the position in the base-apex direction. However, the major weakness of this model is that it does not exhibit visible branching connections between rope bundles. In order to deal with this problem, the HVMB model [Torrent-Guasp *et al.*, 2001, Corno *et al.*, 2006] was proposed. HVMB considers the myocardium as a muscular band twisted and curled in two helical loops: the basal loop (from the root of the pulmonary artery to the beginning of the central fold) and

the apical loop (from the beginning of central fold to the root of aorta). Each of these two loops is further divided into two segments, in which the basal loop is categorized in the right segment (RS) that coincides with the RV wall and the left segment (LS) that coincides with the LV wall. The apical loop is divided into descendent (DS) and ascendant segments (AS), as shown in Fig. 1.5.

HVMB gives a visual recognition about the myocardium muscular trajectories and some reasonable explanations about the heart electrical and mechanical properties and functions. It is however very important to investigate other means for characterizing myocardium muscle orientations.

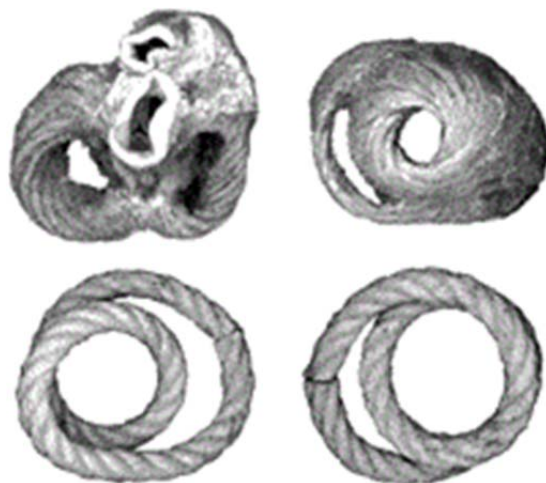


Fig. 1.4 Helical rope model of myocardium (From: [Kocica *et al.*, 2006])

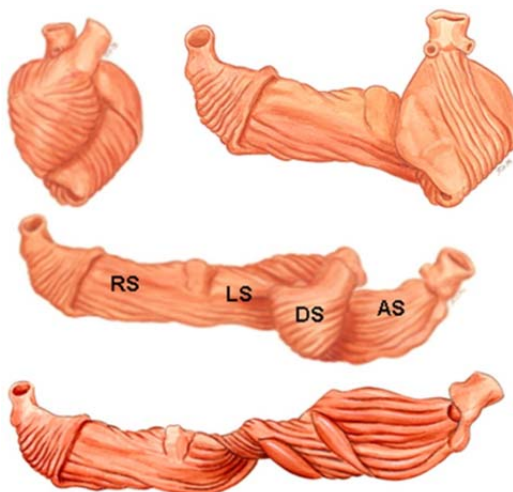


Fig. 1.5 Torrent-Guasp's myocardial band model (From: [Buckberg *et al.*, 2008])

### 1.2.2.2 Geodesic model

Geodesic cardiac fiber model was initially proposed by Streeter [Streeter, 1979], who stated that the myocardial fibers run like geodesics on a nested set of toroidal bodies of revolution. This mathematical expression being a little obscure for anatomist and cardiologist, Jouk [Jouk *et al.*, 2007] made a clearer explanation about this model using the Fig. 1.6.

One can explain the model by taking a piece of paper and drawing saying three parallel lines, which could be considered as the geodesics of the plane surface. Then, we roll the paper

by making the superior border against the inferior border and form a cylinder. The drawn lines in the first step become the geodesics of the cylinder. Finally, we bend the cylinder until the left end touches the right end, thus generating a torus. The lines are still geodesics. According to Streeter, from inner to outer, the myocardial muscle is nested by the elongated tori like Russian dolls, as shown in Fig. 1.6 (d).

Streeter's model only giving the cardiac fiber map of LV, Jouk extended Streeter's conjecture by proposing the pretzel model [Jouk et al., 2007] which describes the fiber architecture of the whole ventricular mass as illustrated in Fig. 1.7.

Compared to the Streeter's model, this model gives not only the same description for the LV myocardial structure, but also provides a new recognition about the fiber arrangement of the RV. The upper left aperture would correspond to the tricuspid orifice and the lower left aperture to the pulmonary orifice. Between these apertures is the supraventricular crest. In this representation, it is given by the narrow part of the nested bent tori, while the wide part of the bent tori corresponds to the septal and lateral walls of the right ventricle. Up to now, this model still requires the mathematical and experimental validations.

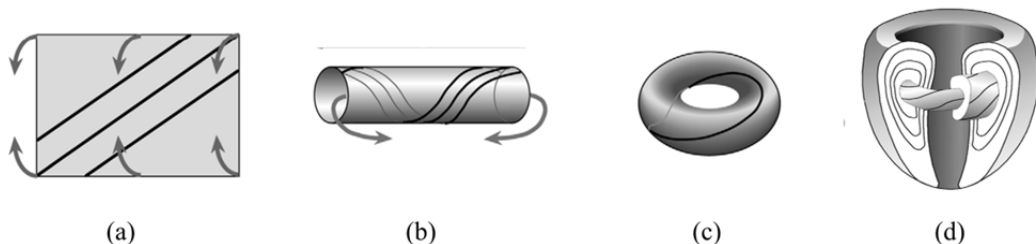


Fig. 1.6 Geodesic model (From: [Jouk et al., 2007])

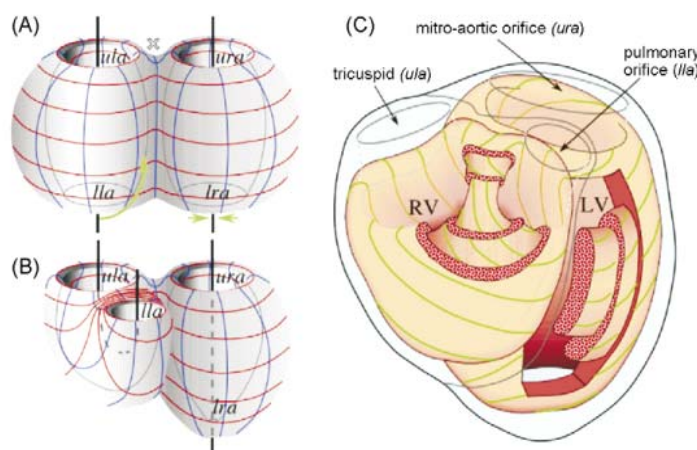


Fig. 1.7 An extension of geodesic model: pretzel model. Like the pretzel cookies, two joined torus form a pretzel in this model. For better understanding the further deformations, a lattice was drawn, where the lines in red are parallel to the surface of revolution, and those in blue are the meridians, as shown in subfigure (A). Four special positions are defined: lower left aperture (lla), lower right aperture (lra), upper left aperture (ula) and upper right aperture (ura). For mimicking the right ventricle structure, the torus on the left was bent in such a way that the lower aperture comes up to the upper aperture. However, for the left ventricle, it is mimicked by shrinking the lower right aperture into a point, as shown in subfigure (B). In subfigure (C), it explains how LV and RV could nest together and form a pretzel model, where the green lines represent the geodesic on the nested pretzels (From: [Jouk et al., 2007]).

### 1.2.2.3 Laminar structure model

The two models above is a sort of continuum model which assumed that the material properties of ventricular myocardium are transversely isotropic with respect to the myofiber axis, supporting the view that neighboring myocytes are uniformly coupled. However, LeGrice and coworkers [LeGrice *et al.*, 1997] demonstrated that ventricular myocardium is structurally orthotropic, with myocytes arranged in layers that are typically four cells thick, as shown in Fig. 1.8. Adjacent layers are separated by cleavage planes that have a characteristic radial orientation in base-apex ventricular section and are significant in extent, particularly in the LV mid-wall. Therefore, at any point within the ventricle, it is possible to define three material axes: (i) the fiber orientation, (ii) perpendicular to fiber orientation within a muscle layer, and (iii) normal to the muscle layer.

Using these three axes to represent the cardiac fiber orientation of dog and pig, the results conform to the anatomy structure [Legrice *et al.*, 1995].

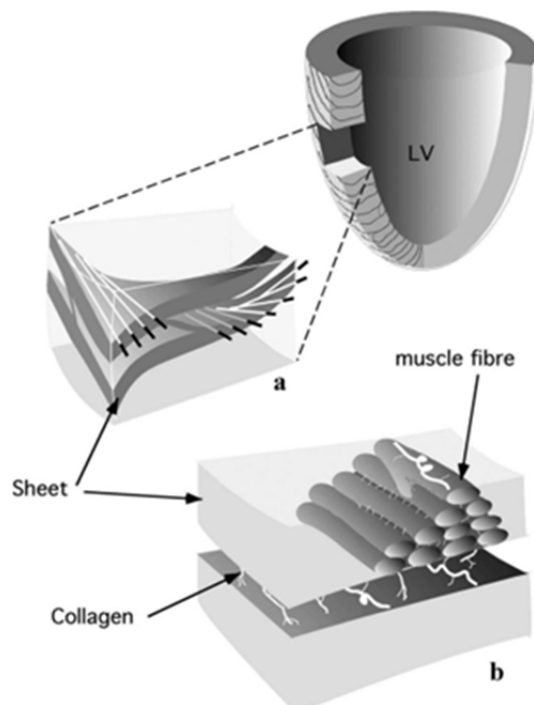


Fig. 1.8 Schematic of laminar structure model for cardiac fiber (From: [Legrice *et al.*, 1995])

## 1.3 Heart diseases

The heart can be regarded as a pump that is made of muscle tissue. The presence of the four chambers keeps oxygen-rich blood from mixing with oxygen-poor blood, and the return of oxygen-poor blood after circulating the body to the heart.

Many different types of heart disease can occur, depending on their causes. We can cite coronary artery disease, heart attack, heart failure, and heart valve disease. Heart muscle disease, also known as cardiomyopathy, is a type of progressive heart disease. It refers to a group of disorders that directly damage the muscle of the heart walls. In these disorders, the heart is abnormally enlarged, thickened, and/or stiffened, and all the chambers of the heart are affected. Depending on the nature of the injury or the abnormality in the heart muscle, the structure of the heart chambers can change. As a result, the ability of the heart muscle to pump blood is weakened, often causing heart failure and the backup of blood into the lungs or rest of the body. The disease can also cause abnormal heart rhythms. Among many possible

types of cardiomyopathy, we describe three main types: dilated cardiomyopathy, hypertrophic cardiomyopathy and restrictive cardiomyopathy.

### Dilated cardiomyopathy

This is the most common heart muscle disease type. It is also called congestive cardiomyopathy. This type of disease damages the heart muscle fibers, weakening the chamber walls of the heart [Jefferies *et al.*, 2010], as shown in Fig. 1.9. It may be caused by reduced blood flow to the heart (ischemic heart disease), infections, toxins and certain drugs. It also may be inherited from a parent. It usually enlarges (dilates) the left ventricle.

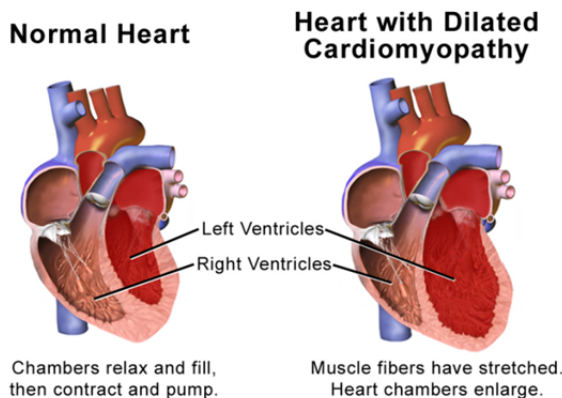


Fig. 1.9 Dilated Cardiomyopathy (from: [https://en.wikipedia.org/wiki/Dilated\\_cardiomyopathy](https://en.wikipedia.org/wiki/Dilated_cardiomyopathy))

### Hypertrophic cardiomyopathy

This disease is relatively rare, but is the second most common type of cardiomyopathy. Hypertrophic cardiomyopathy (HCM) [Dominguez-Rodriguez *et al.*, 2013, Ker, 2014] is also known as idiopathic hypertrophic subaortic stenosis (IHSS) or asymmetric septal hypertrophy (ASH). It is characterized by a disorderly growth of heart muscle fibers, which causes the heart chambers to become thick-walled and bulky (Fig. 1.10). The thickening can make it harder for blood to leave the heart, forcing the heart to work harder to pump blood. It also can make it harder for the heart to relax and fill with blood.

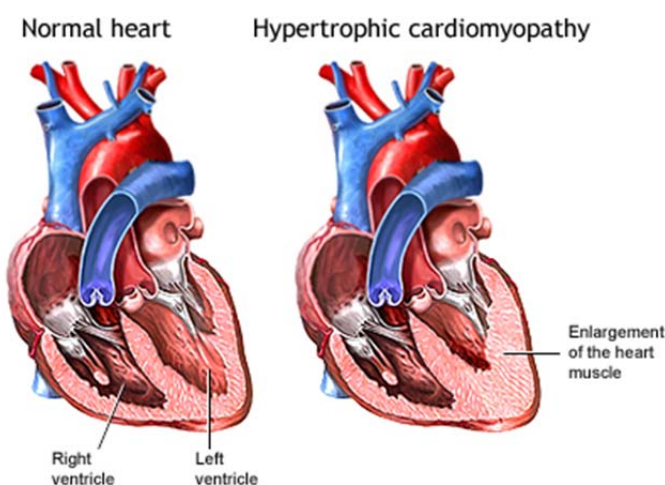


Fig. 1.10 Hypertrophic cardiomyopathy (from: <http://www.nlm.nih.gov/medlineplus/ency/article/000192.htm>)

## Restrictive cardiomyopathy

Restrictive cardiomyopathy is very rare. In this type of heart muscle disease, abnormal cells, proteins, or scar tissue infiltrate the muscle and structures of the heart, causing the chambers to become stiff and bulky [Zangwill *et al.*, 2009, Gupta *et al.*, 2012]. The heart may initially contract normally, but the rigid chambers restrict the return of blood to the heart. As a result, high pressures are needed to fill the heart chambers, forcing the blood back into various tissues and organs such as the lungs, abdomen, arms, and legs. The heart muscle can also be damaged and contractions be impaired.

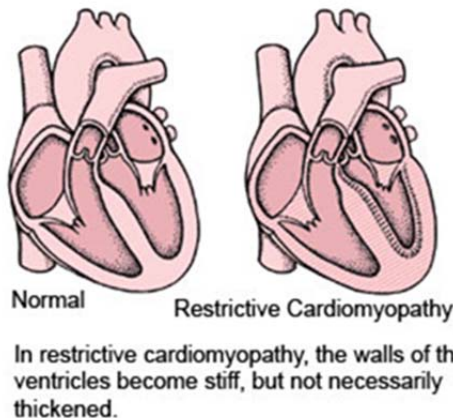


Fig. 1.11 Restrictive cardiomyopathy (From:<http://trialx.com/curebyte/2011/08/28/photos-related-to-restrictive-cardiomyopathy>)

## 1.4 Relation between fiber structure and heart function

The extension, thickening and radial reorientation of the myofiber structure are the basis of contraction and relaxation of the myocardium and allow the latter to function as a pump. But the exact mechanism is not yet clear. By compensating for cardiac motion, cardiac DTI data have been successfully acquired both at systole and diastole. Recent results obtained by Nielles and co-workers [Nielles-Vallespin *et al.*, 2013] have shown that there is a reorganization of cardiac fibers, namely the variation in orientation of diffusion tensors over cardiac cycles. The ability to map myocardial fiber structure and its dynamics, especially combined with myocardial strain imaging techniques, could provide novel insights into the structure-function relation in the heart.

## 1.5 Conclusion

In this chapter, we have described the heart structures, especially, the architecture of heart wall and the cardiac fiber arrangement patterns. We observe that most cardiomyopathies affect the structure of ventricles, especially the left ventricle. In this sense, the investigation of the cardiac fiber architecture in the left ventricle before and after heart disease would be very interesting for the clinical diagnosis and treatment.

## Chapter 2

# Diffusion tensor imaging (DTI) and compressed sensing (CS) theory

## Contents

---

Résumé en français.....	32
Abstract .....	33
2.1 Magnetic Resonance Imaging.....	34
2.1.1 <i>Basic physics</i> .....	34
2.1.2 <i>Signal spatial encoding</i> .....	37
2.1.3 <i>k-space</i> .....	40
2.1.4 <i>MR pulse sequences</i> .....	41
2.2 Cardiac diffusion tensor imaging (DTI) .....	43
2.2.1 <i>Diffusion physics</i> .....	43
2.2.2 <i>Diffusion signal</i> .....	45
2.2.3 <i>Diffusion Tensor Imaging (DTI)</i> .....	47
2.2.3.1 DTI model description .....	47
2.2.3.2 Tensor estimation .....	47
2.2.3.3 Diffusion characteristics extraction.....	48
2.3 Compressed Sensing.....	49
2.3.1 <i>Shannon theory</i> .....	50
2.3.2 <i>Sparsity</i> .....	54
2.3.3 <i>Incoherence</i> .....	55
2.3.4 <i>Sensing</i> .....	56
2.3.5 <i>Recovery</i> .....	57
2.4 Conclusion .....	57

---

## Résumé en français

Dans ce chapitre, nous introduisons les éléments de base en imagerie par résonance magnétique (IRM) nécessaires pour mieux comprendre les chapitres suivants du manuscrit. Le chapitre est organisé comme suit. Section 2.1 présente brièvement les principes de l'IRM et l'IRM de diffusion, y compris la génération et l'acquisition des signaux, le codage spatial, et les séquences d'impulsions. Section 2.2 décrit certaines techniques d'imagerie cardiaque les plus courantes et leur principes physiques, plus particulièrement le DTI cardiaque. Finalement, une introduction concise de la théorie d'acquisition comprimée (CS) est présentée dans la section 2.3.

## Abstract

In this chapter, we introduce the background of magnetic resonance imaging (MRI) necessary for the better understanding of the subsequent chapters of the manuscript. The chapter is organized as follows. Section 2.1 briefly introduces the principles of MRI and diffusion MRI, including signal generation and detection, spatial encoding, and MR pulse sequences. Section 2.2 describes some most common cardiac imaging techniques and their physical principles, in particular cardiac DTI. Finally, a concise introduction of the compressed sensing (CS) theory is presented in Section 2.3.

## 2.1 Magnetic Resonance Imaging

Magnetic resonance imaging (MRI) is a non-invasive medical imaging technique widely used to investigate the anatomy and physiology of the body in clinical diagnosis. Unlike Computed Tomography (CT) or X-ray imaging, MRI does not use ionizing radiation and also does not require the introduction of a radioactive agent that is employed in Positron Emission Tomography (PET). In this section, we briefly introduce the principle and concepts of MRI concisely. The detailed information about this technique can be found in [Haacke *et al.*, 1999, Liang *et al.*, 2000, Elmaoġlu *et al.*, 2011, Westbrook *et al.*, 2011, Foltz *et al.*, 2012, Brown *et al.*, 2014, Constantinides, 2014]. There exist also a number of e-books or online courses, such as <https://www.imaios.com/en/e-Courses/e-MRI> and <http://www.cis.rit.edu/htbooks/mri/>, in which are elaborated the development history, physical phenomena, principles and applications.

### 2.1.1 Basic physics

It is well known that the human body tissues contain a lot of water and thus hydrogen nuclei (protons  $^1\text{H}$ ). These slightly positive electrical charged proton have magnetic properties and behave like tiny rotating magnets, like the earth. A proton is constantly turning around an axis, which is called *nuclear spin* as shown in Fig. 2.1(a). The spinning of the protons will generate a lot of tiny magnets; the sum of all the tiny magnetic fields of the spins is called net magnetization or macroscopic magnetization. In our body, these tiny bar magnets are ordered randomly. Thus, the sum of all the spin magnetic forces equalizes, namely a *null net magnetization*. However, when we put these protons under a large external magnetic field  $B_0$ , some interesting things happen: the proton not only rotates about its own axis but also “wobbles” about the axis of  $B_0$ . As a result, all the protons align with the external magnetic field, some of the spins align with the field (parallel) and some align against the field (anti-parallel). Meanwhile, they precess or wobble due to the magnetic momentum of the atom, as illustrated in Fig. 2.1(b). This is called *precession*. The precession frequency (resonance frequency)  $\omega_0$  (MHz) is called *Larmor frequency* or *precessional frequency*, which is determined by the strength of the main magnetic field  $B_0$  (T) and the gyromagnetic ratio  $\gamma$  (MHz/T) of proton  $^1\text{H}$ .

$$\omega_0 = \gamma B_0 \quad (2.1)$$

#### Resonance

Because within the  $B_0$  magnetic field, there are more spins aligned with the field (parallel) than spins aligned against the field (anti-parallel), a *magnetization*  $M_0$  is generated that results from the sum of all magnetic fields and points in the same direction as the main magnetic field  $B_0$ . However, compared with  $B_0$ ,  $M_0$  is too small to be detected. Therefore, in order to observe the variation of  $M_0$ , a new dynamic and short duration magnetic field  $B_1$ , often referred as a *RF pulse*, is applied to move out of alignment away from  $B_0$ . This is called *RF excitation*. The angle to which the  $M_0$  moves relative to  $B_0$  is called *flip angle*. The magnitude of the flip angle depends on the amplitude and duration of the RF pulse. During

excitation, longitudinal magnetization  $M_0$  decreases and a transverse magnetization  $M_{xy}$  appears.

If the RF radiation is of sufficient magnitude and duration and is applied at a right angle to the  $B_0$  field, the net magnetization vector can be made to precess until it reaches the transverse plane ( $x - y$  plan), and then *resonance* occurs, which makes that the longitudinal magnetization  $M_0$  is completely transferred into the transverse magnetization  $M_{xy}$  (all spins are in phase: complete phase coherence). Such a pulse of radiation is called a  $90^\circ$  *RF pulse*, and the RF pulse frequency matches the precession frequency of the protons (Larmor frequency). Now, the protons are processing in phase in the transverse plane as shown in Fig. 2.2(b).

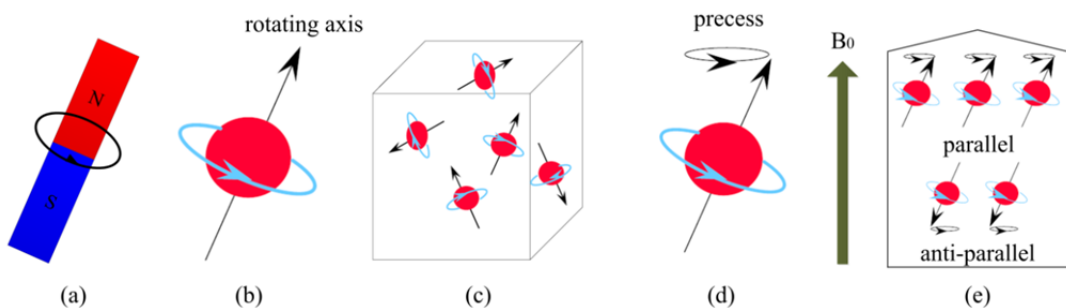


Fig. 2.1 Spin and precession of protons (From: [Blink, 2004])

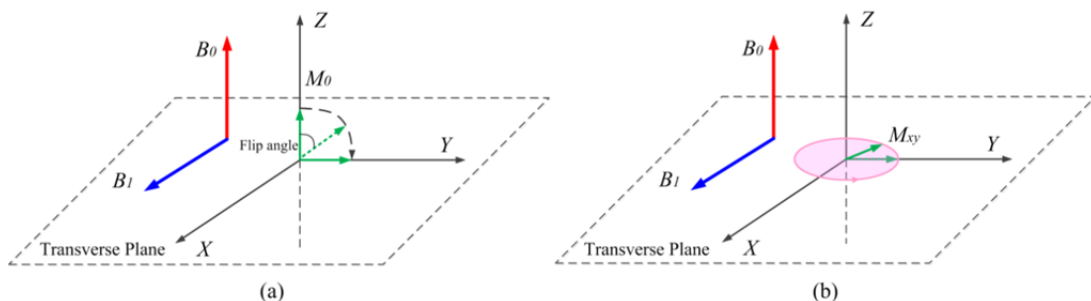


Fig. 2.2 RF excitation (a) and relaxation (b)

## Relaxation

After resonance, the protons are processing in phase in the transverse plane, in a temporary manner. If the  $90^\circ$ RF pulse is switched off, the water protons will again return to their initial state. In this case, the magnetization will again be influenced by  $B_0$  and tries to realign with the latter. To this end, the magnetization must lose the energy given by the RF pulse, and its return to the equilibrium of net magnetization is a process called *relaxation*. The time needed for the amount of magnetization to return to completely longitudinal plane after the application of the  $90^\circ$  RF pulse is defined as *T1 relaxation*. The rate of this return to equilibrium is an exponential process, whose time constant is defined as  $T_1$ . At the same time but independently, the amount of magnetization in the transverse plane gradually decreases according to an exponential law, producing a so-called *T2 decay*. So, the T2 relaxation time of a tissue is its time constant to decay. After time T1, longitudinal magnetization is returned to 63% of its final value, and after time T2, transverse magnetization has lost 63 % of its original value, as shown in Fig. 2.3. Since the relaxation time is crucial for MRI, the relaxation determines signal intensity as well as image contrast [Gossuin *et al.*, 2010].

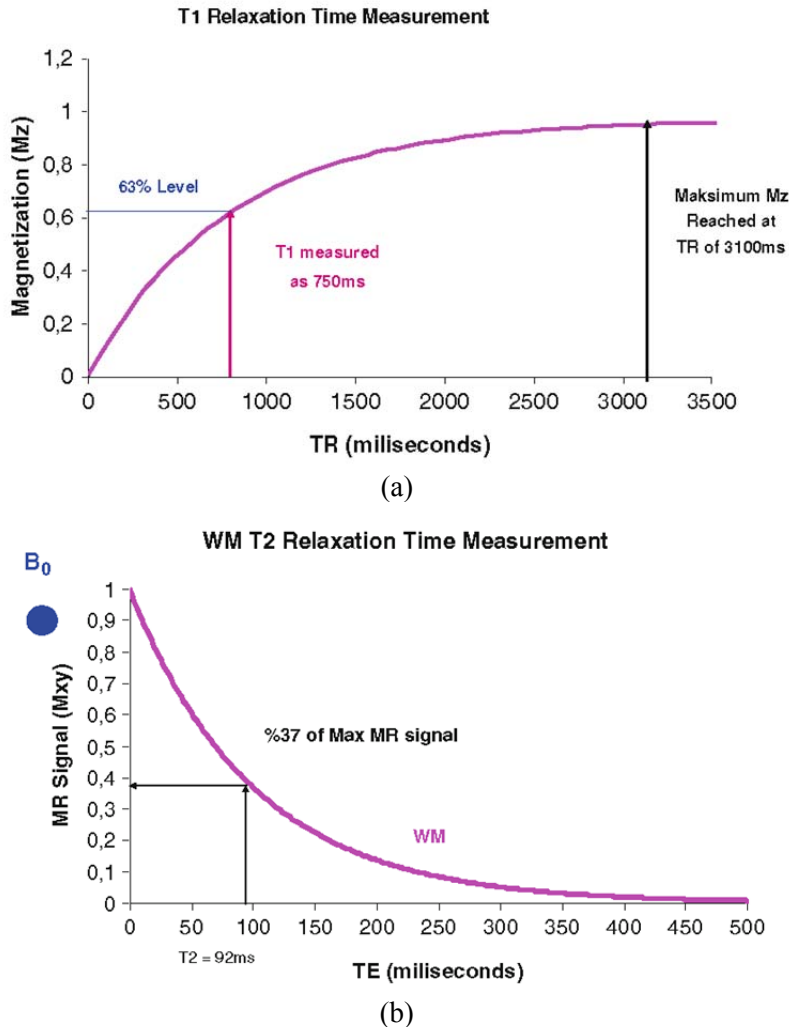


Fig. 2.3 Schema for T1 and T2 relaxation (GM: gray matter, WM: white matter) (From: [Elmaoğlu *et al.*, 2011])

### MR signal

Once the RF pulse is turned off, relaxation happens. If we place a receiver coil in the transverse plane and the coil is positioned perpendicular to magnetization  $M_{xy}$ . The variation of magnetization will produce magnetic field fluctuations inside the coil and consequently will induce a current (*MR signal*), following the well-known Faraday's principle on the coil. This current constitutes the MR signal that relates to the three properties of a tissue, namely proton density, T1 and T2. The magnetization variation is described by Bloch equation [Bloch, 1946]

$$\frac{dM}{dt} = M \times \gamma B_0 + \frac{M_0 - M_z}{T_1} + \frac{M_{xy}}{T_2} \quad (2.2)$$

where  $M_z$  and  $M_{xy}$  are the longitudinal and transverse magnetizations, respectively.

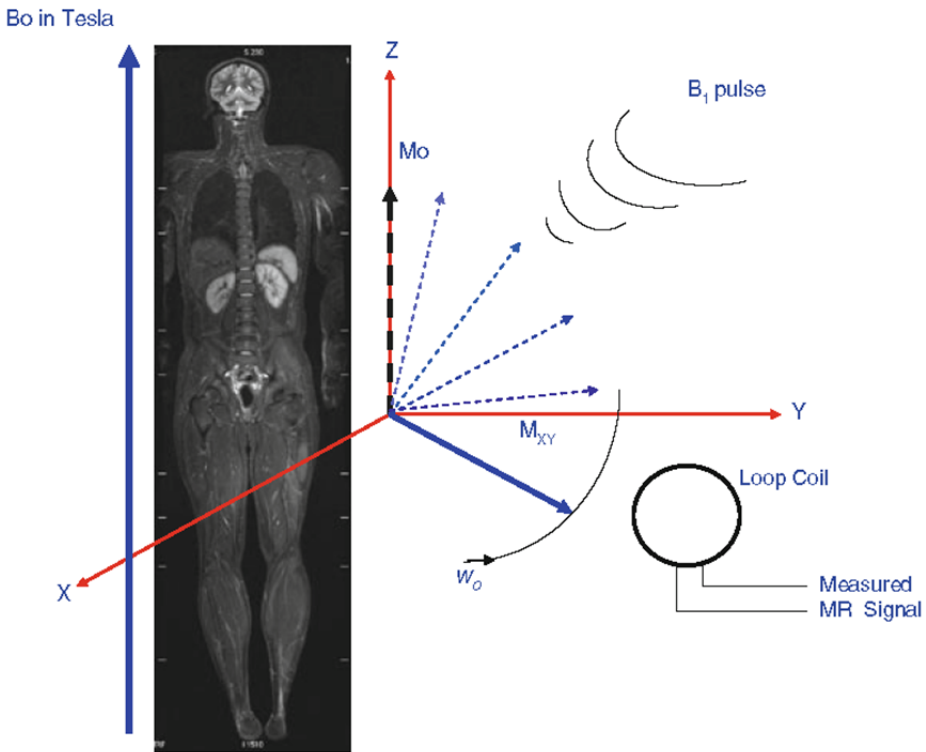


Fig. 2.4 When the  $B_1$  RF-pulse is applied, total magnetization  $M_0$  is tilted from  $z$ -axis to  $xy$ -plane and it continues to precess in  $xy$ -plane at Larmor frequency. When a coil is positioned perpendicular to magnetization  $M_{xy}$ , a current (MR signal) is induced based on Faraday's principle on the coil.(From: [Elmaoğlu et al., 2011])

### 2.1.2 Signal spatial encoding

Now we know how MRI works and how to create and acquire an MR signal at the coil, but we still cannot determine where the signal is coming from. To localize the voxels (single volume elements containing protons) spatially from MR signal in three dimensions, three steps are required to encode spatial information. There are the slice selection, the encoding of spatial information along the rows and the encoding of spatial information along the columns. Spatial encoding relies on successively applying magnetic field gradients, as shown in Fig. 2.5.

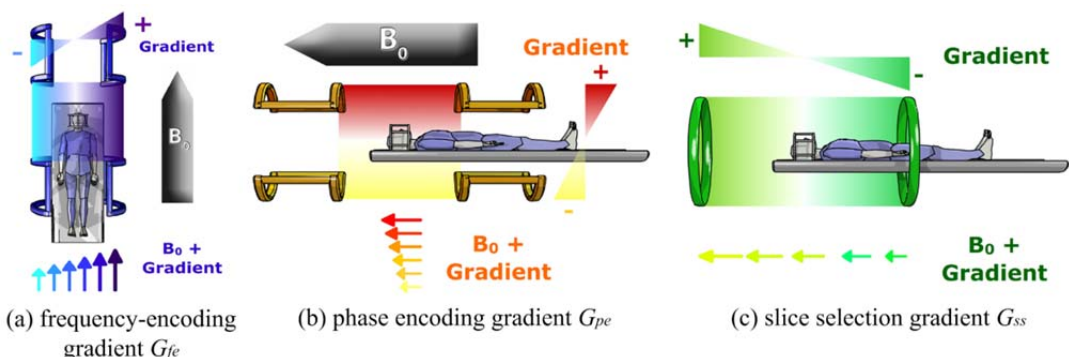


Fig. 2.5 magnetic field gradients for spatial encoding (From: <https://www.imaios.com/en/e-Courses/e-MRI>)

## Slice selection

During the switched on of RF pulse, if the magnetic field is homogenous through the patient body, all the protons will resonate with the same precession frequency and contribute to the MRI signal. In this situation, we would have no clue where the signal comes from in the body. Therefore, the first step of spatial encoding is to apply a magnetic field gradient to select the slice plane, as shown in Fig. 2.5(c). This operation is called *slice selection*, with the *Slice Selection Gradient (G<sub>ss</sub>)*  $G_{ss}$  that is applied perpendicularly to the desired slice plane. As mentioned earlier, excitation of spins only happens when the RF pulse is applied at the Larmor frequency of those spins. In the presence of a gradient, the Larmor frequency changes along the direction of the gradient, therefore only the spins located at a given thin slice perpendicular to the gradient direction can be in resonance and emit a signal. The RF wave associated with the slice selection gradient and the adapted resonance frequency is called the *selective pulse*. The RF pulse frequency can be changed to acquire multiple slices at different positions in the body, as illustrated in Fig. 2.6.

The slice thickness  $th$  depends both on the frequency bandwidth of the selective RF pulse  $\Delta\omega$  and on the strength of the slice selection gradient  $G_{ss}$ . It is given by

$$th = \frac{\Delta\omega}{\gamma G_{ss}} \quad (2.3)$$

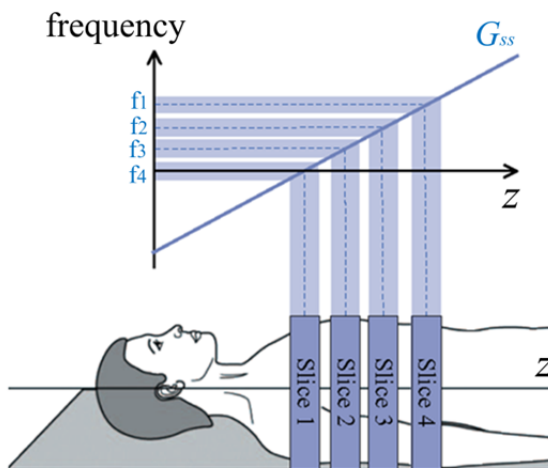


Fig. 2.6 Diagram for MRI Slice selection (From: [McRobbie *et al.*, 2006])

## Phase encoding

A big improvement is that we now know the MRI signal coming from the single slice in the body. But, within the one slice there are still an awful lot of protons, and we still don't know from where the signal is coming from in the slice. It must be located along both the axes of this slice to further encode spatial information. This is realized by phase and frequency encoding. Before applying phase encoding gradient, all the spins in the slice precess with the same frequency and they are *in phase*. When the phase encoding gradient is applied, the magnetic field strength and therefore the precessional frequency of spins along the axis of the phase gradient is altered. Since the precession speed of the spins changes, so does the accumulated phase of magnetic moments along their precession path, which is illustrated in Fig. 2.7.

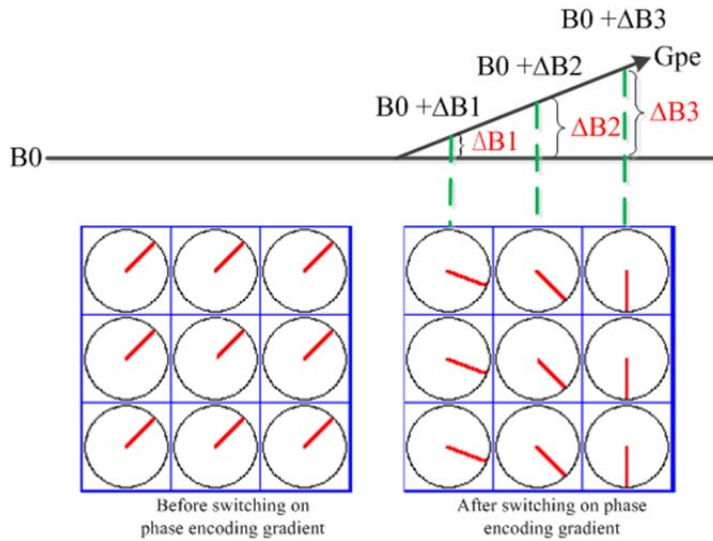


Fig. 2.7 Diagram for MRI phase encoding (From: [Hornak, 2008])

When the phase encoding gradient  $G_{pe}$  is turned off, the magnetic field strength returns to the main field strength, and all the spins within the slice return to the same frequency (Larmor frequency), but in different phases. This difference in phase between the spins is used to encode the spins' position along the phase encoding direction. This process is called *phase encoding*.

The spatial resolution  $res_{pe}$  along the phase encoding direction is determined by the field of view ( $FOV_{pe}$ ) along this direction, the phase encoding steps number  $n_{pe}$ , the encoding gradient strength changes  $\Delta G_{pe}$  between two steps, and the gradient duration  $\delta_{Gpe}$ . It is expressed as

$$res_{pe} = \frac{FOV_{pe}}{n_{pe}} = \frac{1}{\gamma \Delta G_{pe} \delta_{Gpe} n_{pe}} \quad (2.4)$$

### Frequency encoding

Before second encoding process, we know that the MR signal comes from a slice and contains a number of RF waves. The RF waves have the same frequency, but have different phases. The signal must now be located along the other axis of the slice, and this is achieved by *frequency encoding*. Using the same principle as for phase encoding, the application of the frequency encoding gradient will alter the magnetic field strength and thus the precessional frequency of spins. Thus, the frequency difference between the spins is produced, and the signal can be identified according to its frequency along the frequency gradient direction, see Fig. 2.8.

Frequency encoding gradient is usually turned on when receiving the signal. Therefore, it is also called the readout gradient. The steepness of the slope of the frequency encoding gradient determines the size of field of view ( $FOV_{ro}$ ) and also the spatial resolution  $res_{ro}$  in this direction [Westbrook *et al.*, 2011]:

$$res_{ro} = \frac{FOV_{ro}}{n_{ro}} = \frac{BW}{\gamma G_{ro} n_{ro}} \quad (2.5)$$

where  $BW$  is the bandwidth of the receive digitizer,  $G_{ro}$  is the strength of the frequency encoding gradient, and  $n_{ro}$  is the acquisition number.

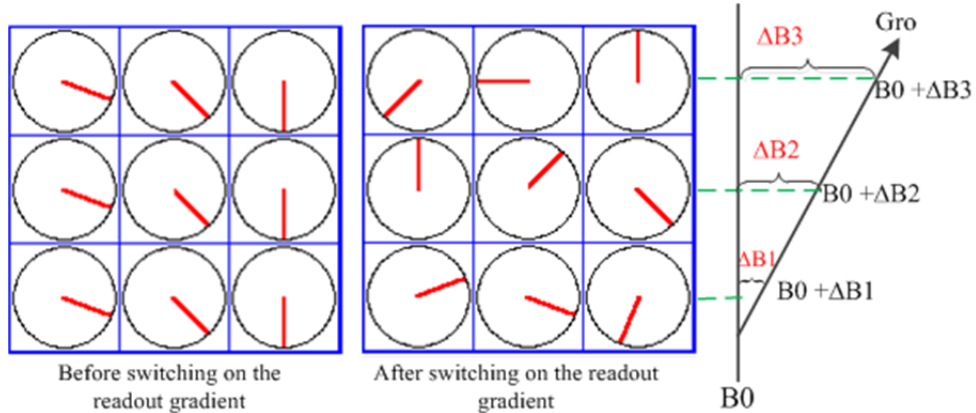


Fig. 2.8 Diagram for frequency or readout encoding (From: [Hornak, 2008])

### 2.1.3 k-space

The readout MR signal is a mix of RF waves containing spatial information with different amplitudes, frequencies and phases. This MR signals is digitized and raw data are written into a data matrix during data acquisition called *k*-space. The *k*-space is derived from the data space with axes ( $k_x$  and  $k_y$ ) referred to as spatial frequencies. The data space is an “analog” version of *k*-space. The *k*-space data are equivalent to a Fourier plane and then the MR image can be obtained by means of a 2D inverse Fourier Transform from *k*-space data, as shown in Fig. 2.9(b) and (c). The data in the center of *k*-space contains the maximum signal and contributes to the signal-to-noise and contrast information for the image, and the periphery of *k*-space data provides information regarding the fine detail information (edges and boundaries) of the image. As shown in Fig. 2.10, we can see that if we take a set of raw data and reconstruct just the center of the *k*-space, we will in this case remove fine details of the image (second column). If we reconstruct just the outside (third column) of the *k*-space, we will in this case preserve high frequency components or morphological details of the image, compared to the image reconstructed from the complete *k*-sapce data (first column).

The process of filling the *k*-space is determined by specific MRI sequences that combine RF pulses and encoding gradients in a given order. A most commonly used trajectory in clinical imaging is to fill the *k*-space line by line in a Cartesian grid, as shown in Fig. 2.11.

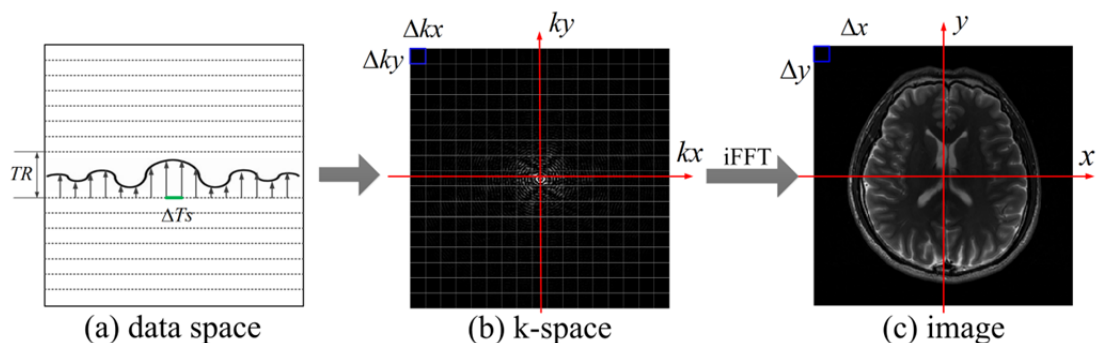


Fig. 2.9 k-space

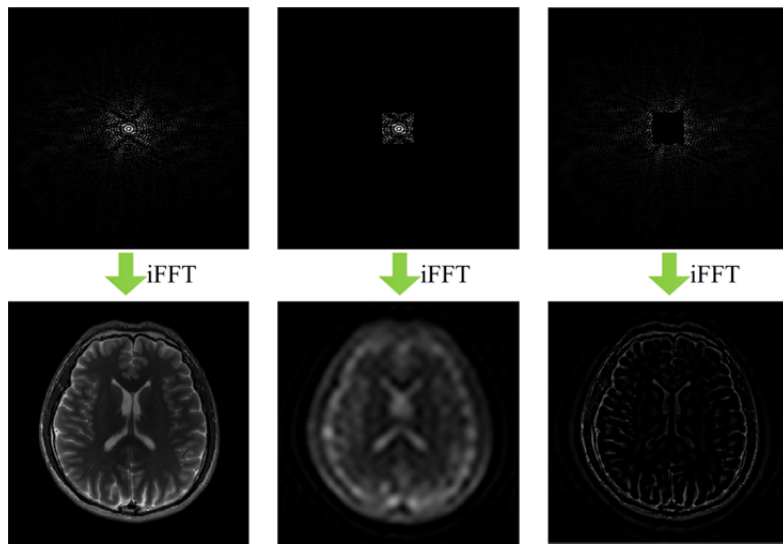


Fig. 2.10 The effects of removing the portion of k-space data on the reconstructed image.

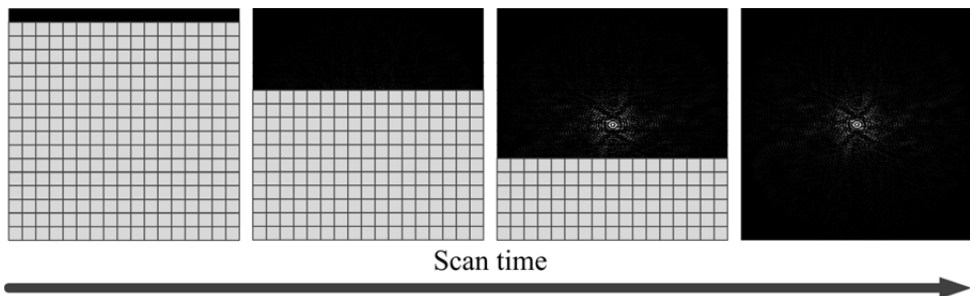


Fig. 2.11 The k-space filled by uses straight lines from a Cartesian grid.

### 2.1.4 MR pulse sequences

MR pulse sequences is the heart of MRI, which are the computer software executing a series of commands and allow us to control the way in which the system applies pulses, gradients, data sampling windows, etc., in a predefined timing window. There are over a hundred different sequences and each sequence is designed to favor the signal of a particular tissue (contrast), at varying rates (speeds), whereas limiting the artifacts and keeping sufficient the signal-to-noise ratio [Haacke *et al.*, 1999, Bernstein *et al.*, 2004, Brown *et al.*, 2014]. This subsection discusses two most commonly and important used pulse sequences: spin echo and gradient echo.

#### Spin echo sequence

The spin echo (SE) sequence is frequently used in MRI experiments because of its versatility and good imaging quality. It uses a  $90^\circ$  excitation RF pulse followed by one or a series of  $180^\circ$  rephasing RF pulses to generate a spin echo, as shown in Fig. 2.12. After the  $90^\circ$  excitation pulse, the magnetization is flipped into the transverse plane, and immediately starts to dephase due to T2 relaxation caused by the difference in speed of spins. A  $180^\circ$  pulse is then applied to flip the spin vectors so that the previously slower vectors are effectively precessing ahead of the previously faster ones. After a further time delay (equal to TE/2), a spin echo is formed.

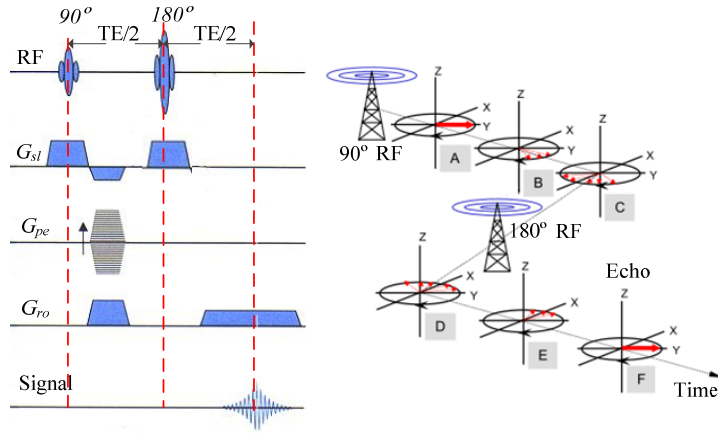


Fig. 2.12 Diagram of SE sequence and its principle (From: [Wang, 2013])

In most MRI sequences, after slice selection gradient is often applied a gradient with half amplitude strength of  $G_{sl}$ , which is used to compensate the dephasing effects caused by the inhomogeneity of the gradient. For the same reason, before 180° RF pulse, a gradient is applied along the reading out direction.

Owing to the spatial encoding with the gradients, the intensity of each voxel in the image only depends on the proton density, T1 and T2 values. Changing the sequence parameters will lead to the images with different contrasts. The SE sequence has a higher SNR and few artifacts, and is the best one to obtain T2 contrast image, but it needs longer acquisition time.

### Gradient echo sequence

The gradient echo sequence (GE) is similar to the SE sequence with the exception that it forms the echo using a gradient polarity reversal (Fig. 2.13). It starts with an excitation RF pulse with flip angle of  $\alpha^\circ$  that depends on the magnetization flipped into the transverse plane. Because of T2 relaxation, spins are dephasing, until the polarity is changed. After that, the spins begin to rephase until it is in phase again. GE sequence does not compensate the inhomogeneity of the magnetic field, and therefore has an increased sensitivity to T2\* decay caused by the lack of a 180° refocusing pulse. But this shortens acquisition time, which is useful when fast scan is required.

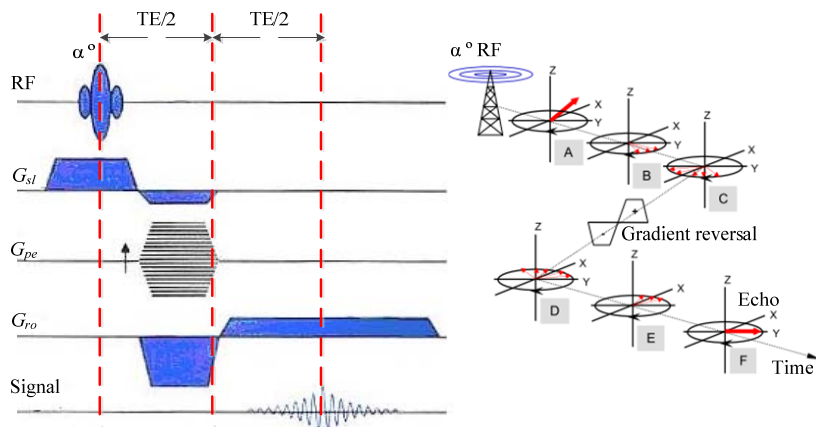


Fig. 2.13 Gradient echo sequence and its principle (From: [Wang, 2013])

## 2.2 Cardiac diffusion tensor imaging (DTI)

Conventionally, the histological measurements of selected tissue regions were used to obtain the cardiac fiber architecture [Ross *et al.*, 1979]. But, it is well known that such techniques suffer from distortion and misalignment, and they do not allow the 3D reconstruction of fiber structures. The polarized light imaging (PLI) was proposed to detect fiber orientations in ex vivo human hearts to overcome these problems [Jouk *et al.*, 1995, Jouk *et al.*, 2007]. However, both histological and PLI techniques are ex vivo and cannot be used for in vivo studies of the human heart.

Recently, Diffusion Magnetic Resonance Imaging (dMRI) [Jones, 2011, Johansen-Berg *et al.*, 2013] has emerged as a new and promising noninvasive technique for analyzing the 3D fibrous structure of tissues in vivo [Jones, 2011]. This technique has been widespread used for the human brain [Luna *et al.*, 2012], but only a few studies have been applied to the heart [Hsu *et al.*, 2001, Helm *et al.*, 2005b, Wu *et al.*, 2006, Toussaint *et al.*, 2010, Naumova *et al.*, 2014]. dMRI determines the diffusion properties of water molecules in biological tissues via estimating the average displacement of water particles from the phase change occurring and thus inferring the microstructure of the diffusion environment. This average displacement can be accurately described at the scale of a voxel by the Ensemble Average Propagator (EAP), which represents the full 3D displacement of water molecule diffusion [Merlet *et al.*, 2013]. Using dMRI to infer the EAP requires acquiring number of diffusion images at different diffusion gradient directions in the sampling space. Instead of computing a complete EAP, the diffusion process is described by a simpler model in the case of isotropic diffusion, namely the Apparent Diffusion Coefficient (ADC) [Le Bihan, 2013]. However, in the presence of diffusion anisotropy, diffusion can no longer be characterized by a single ADC. A common and well known assumption is to consider that water molecule diffusion has a Gaussian distribution, thus, the concept of diffusion tensor  $D$  was introduced into dMRI to describe the EAP, thus leading to diffusion tensor MRI (DT-MRI) or simply diffusion tensor imaging (DTI) that was developed in the mid 1990s [Basser *et al.*, 1994a]. DTI is the first MRI technique and perhaps the only noninvasive technique that allows studying cardiac fiber architecture in vivo and become increasingly popular among clinicians and researchers [Stejskal *et al.*, 1965, Basser *et al.*, 1994a, Nielles-Valdespin *et al.*, 2013, Soares *et al.*, 2013, Wei *et al.*, 2013, Naumova *et al.*, 2014]. In addition to these, other new techniques have also been developed to further characterize the features of the diffusion displacement profile [Assemal *et al.*, 2011, Tournier *et al.*, 2011, Fernandez-Miranda, 2013], such as diffusion spectrum imaging (DSI) [Weden *et al.*, 2005], high angular resolution diffusion imaging (HARDI) [Tuch *et al.*, 1999, Frank, 2001;2002], Q-ball MRI [Tuch, 2004], and diffusion orientation transform (DOT) [Ozarslan *et al.*, 2006]. Some detailed description on these techniques and their applications can be found in [Jones, 2011].

This thesis focuses on DTI of the heart, and more specially on the diffusion tensor model in cardiac DTI. In this section, we first explain the principle of diffusion MRI briefly, then we introduce briefly the concept of DTI models.

### 2.2.1 Diffusion physics

#### Brownian motion

Diffusion is a natural phenomenon, which refers to the net movement of molecules or atoms from a region of high concentration to a region of low concentration without requiring bulk motion. Molecules at 0°K (-273°C) experience a random motion called *Brownian*

*movement.* The Brownian motion is usually described by the random walk model [Goel *et al.*, 2013] which not only gives the trajectory of molecular diffusion, but also the diffusion displacement during a given time interval, as shown in Fig. 2.14. “Diffusion” in biological tissues usually refers to the random motion of water molecules when they are agitated by thermal energy.

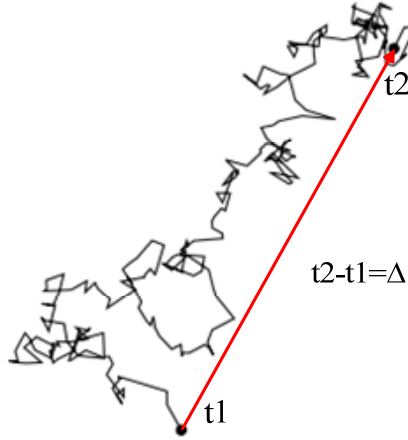


Fig. 2.14 The schematic of the molecular diffusion trajectory of a single water molecule (From: [Wang, 2013])

In Fig. 2.14, the red vector represents the molecular displacement during the diffusion time interval  $\Delta$ , between  $t_1$  and  $t_2$ . The displacement traveled by one molecule is determined by several factors such as the diffusion time interval  $\Delta$ , the diffusion coefficient of the medium, and the diffusion types (free, hindered, or restricted diffusion). Diffusion is a random process, which means that a molecule beginning at the same position and diffusing during the same time would probably end at different locations. Therefore, to better describe diffusion phenomenon, the concept of diffusion displacement distribution, also known as the displacement probability density function (PDF), was introduced [Callaghan, 1993]. In the present thesis, PDF is written as  $P(\bar{x}_\Delta | \bar{x}_0, \Delta)$ , which describes the probability of a water molecule located at position  $\bar{x}_0$  moving to the position  $\bar{x}_\Delta$  after the time interval  $\Delta$ .

In the case of isotropic diffusion in a homogeneous medium, following the central limit theorem, the PDF is Gaussian. For a 3D system it can be expressed as:

$$P(\bar{x}, \Delta) = \frac{1}{\sqrt{|D|(4\pi\Delta)^3}} \exp\left(-\frac{(\bar{x}^T D^{-1} \bar{x})/2}{4\Delta}\right) \quad (2.6)$$

with  $\bar{x} = \bar{x}_\Delta - \bar{x}_0$ . The variance of  $\bar{x}$  is proportional to the diffusion time  $\Delta$ :

$$\langle |\bar{x}|^2 \rangle = 6D\Delta \quad (2.7)$$

Eq.(2.7) is the famous Einstein equation [Einstein, 1956].

### Restricted diffusion

In the free diffusion, water molecules move freely in all spatial directions (e.g. cerebrospinal fluid). However, in biological tissues, the motion of water molecules inevitably encounters obstacles (structured tissues, vascular structures, nerve fibers, etc.). Therefore, the diffusion of water molecules is often anisotropic and is restricted in certain spatial directions,

depending on the environment. Usually, the random motion of water molecules can be summarized into other two different types, called as “hindered” and “restricted” diffusion, as shown in Fig. 2.15 where the difference between the “hindered” and “restricted” diffusion can be clearly seen.

The PDF of restricted and hindered diffusion is complex. It depends on diffusion time, diffusion coefficient, and most importantly diffusion environment structures. Therefore, the variation of the PDF can reveal the tissue structure and the physical property changes.

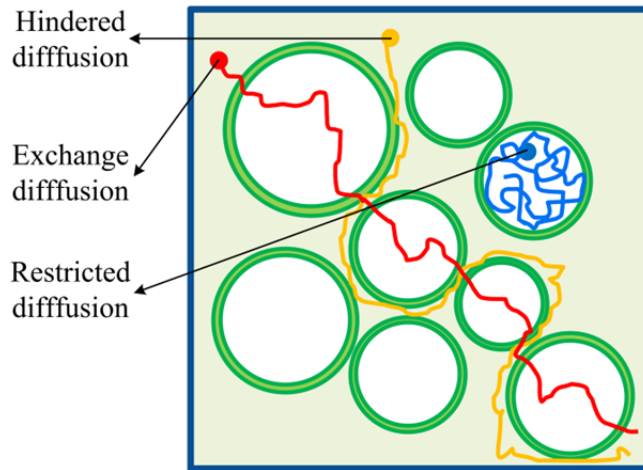


Fig. 2.15 Illustration of the difference between restricted and hindered diffusion [Wang, 2013].

## 2.2.2 Diffusion signal

The effect of diffusion on the MRI signal was first noticed by Hahn in 1950 [Hahn, 1950]. A few years later, Torrey [Torrey, 1956] generalized the Bloch equations in incorporating the elements of molecular diffusion. He shows that in the presence of molecular diffusion, the transverse magnetization variation is given by

$$\frac{d\overline{\mathbf{M}}}{dt} = \gamma \overline{\mathbf{M}} \times \overline{\mathbf{B}_0} + \begin{pmatrix} \frac{M_x}{T_2} \\ \frac{M_y}{T_2} \\ \frac{M_0 - M_z}{T_1} \end{pmatrix} + D \nabla^2 \overline{\mathbf{M}} \quad (2.8)$$

where  $\nabla^2$  designates the Laplace operator. The first two terms of the right-hand side of Eq.(2.8) correspond to the original Bloch equation, and the third term describes molecular diffusion. This equation is also known as *Bloch-Torrey equation*. In order to detect molecular diffusion information, the original MRI pulse sequence was altered, leading to a new imaging modality, called the diffusion weighted magnetic resonance imaging (DW-MRI) [Mori *et al.*, 1999].

In principle, all MRI pulse sequences are to some extent sensitive to molecular motion and diffusion. In 1965, an MRI sequence sensitive to Brownian water motion was introduced by Stejskal and Tanner in order to extract diffusion information for in vivo applications [Stejskal *et al.*, 1965]. This sequence is based on a SE sequence, with the addition of a symmetric pair of diffusion-weighted gradients to the two sides of the refocusing 180° RF pulse in each encoding directions (slice selection, phase and frequency encoding), as illustrated in Fig. 2.16.

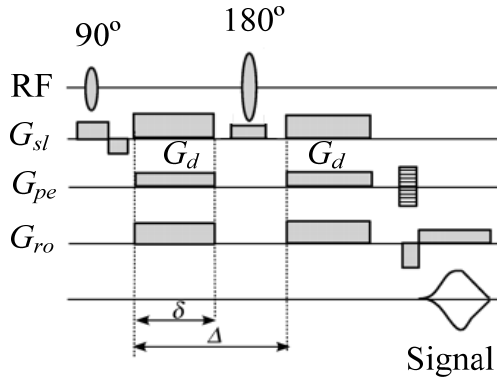


Fig. 2.16 Stejskal-Tanner diffusion magnetic resonance imaging sequence (From: [Perrin *et al.*, 2005])

Different magnitudes of the diffusion-weighted gradients in the three encoding directions provide a specific diffusion-weighted direction corresponding to the encoding coordinate system. The first of these gradients offsets the phase of the spins by an amount that depends on their location, the second provides equal and opposite (due to 180° pulse) rephasing if the spins have not moved during the diffusion time  $\Delta$ , which is the time between the application of the two gradients. Because the spins move randomly due to diffusion, the rephasing effects of 180° will disappear. The more spins diffuse during the diffusion time, the less perfect the rephasing and the smaller the amplitude of the final signal. More diffusion is thus reflected by a more attenuated signal.

The diffusion signal detected by this sequence is

$$S(b) = M_0 \exp\left(-\frac{t}{T_2}\right) \exp(-bD) \quad (2.9)$$

where  $b$  is defined by

$$b = \gamma^2 \int_0^{TE} \left( \int_0^t G_d(t') dt' \right)^2 dt \quad (2.10)$$

For the sequence in Fig. 2.16, the b-value is given by

$$b = \gamma^2 \delta^2 (\Delta - \delta/3) G_d^2 \quad (2.11)$$

b-value ( $\text{s/mm}^2$ ) is a diffusion-weighting factor that accounts for the relevant characteristics of the diffusion gradient such as the diffusion gradient amplitude  $G_d$ , the duration and the time interval between two diffusion gradients. In the absence of diffusion gradients, the b-value is 0 and the signal detected by MRI scanner is reduced to:

$$S_0 = M_0 \exp\left(-\frac{t}{T_2}\right) \quad (2.12)$$

Eq.(2.9) then becomes

$$S(b) = S_0 \exp(-bD) \quad (2.13)$$

Then the diffusion coefficient along the direction of the applied diffusion gradients can be measured by comparing the MRI signal with and without diffusion-weighted gradients. However, Eq.(2.13) is derived by assuming that the diffusion has a Gaussian profile. Therefore, it is only valid under the situation that the effect of diffusion during the application

of the diffusion gradients is negligible. It is also assumed that the dephasing due to the application of the imaging gradients can be neglected.

The diffusion process in biological tissues is no longer free, but hindered and modulated by many mechanisms, such as the restriction due to the cell membrane, tortuosity around the obstacles, the influence of perfusion caused by the blood flow, etc. [Kopf *et al.*, 1996, Beaulieu, 2002]. Therefore, the diffusion coefficient in this case is usually smaller than that of free diffusion, and it is often called the apparent diffusion coefficient (ADC) [Lebihan *et al.*, 1986].

### 2.2.3 Diffusion Tensor Imaging (DTI)

In the traditional DW-MRI, the diffusion process is simply described by a single scalar parameter, the Apparent Diffusion Coefficient (ADC). However in the presence of diffusion anisotropy, diffusion can no longer be characterized by a single ADC, but needs to be described at different spatial directions. This leads to the introduction of the concept of diffusion tensor imaging (DTI) [Basser *et al.*, 1994a] and leading to DTI.

#### 2.2.3.1 DTI model description

In DTI, the diffusion magnetic resonance signal is expressed by [Le Bihan *et al.*, 2001]:

$$E(b) = S_0 \exp(-b\mathcal{D}) \quad (2.14)$$

where  $b$  characterizes the gradient pulses used in the MRI sequence including the gradient amplitude  $G$ , the gradient impulse duration  $\delta$  and the diffusion time  $\Delta$ ,  $S_0$  the magnetic resonance signal intensity, and  $\mathcal{D}$  the diffusion tensor defined by:

$$\mathcal{D} = \begin{pmatrix} D_{xx} & D_{xy} & D_{xz} \\ D_{yx} & D_{yy} & D_{yz} \\ D_{zx} & D_{zy} & D_{zz} \end{pmatrix} \quad (2.15)$$

In the spin echo sequence [Stejskal *et al.*, 1965], the b-value is calculated by means of

$$b = (\gamma \bar{G} \delta)^2 (\Delta - \delta / 3) \quad (2.16)$$

with  $\gamma$  denoting the gyromagnetic ratio of 1H proton,

According to the thermodynamic laws [Groot *et al.*, 1963], the diffusion tensor of water molecules is thought to be symmetrical ( $D_{ij} = D_{ji}$ , with  $i, j = x, y, z$ ).

#### 2.2.3.2 Tensor estimation

Because the diffusion tensor  $D$  is symmetric, the diffusion signal in Eq.(2.14) becomes:

$$E = S_0 \exp(-b_{xx}D_{xx} - b_{yy}D_{yy} - b_{zz}D_{zz} - 2b_{xy}D_{xy} - 2b_{xz}D_{xz} - 2b_{yz}D_{yz}) \quad (2.17)$$

The logarithm of the diffusion signal  $E$  is

$$\ln(E) = \ln(S_0) - b_{xx}D_{xx} - b_{yy}D_{yy} - b_{zz}D_{zz} - 2b_{xy}D_{xy} - 2b_{xz}D_{xz} - 2b_{yz}D_{yz} \quad (2.18)$$

For simplicity, the right-hand side of Eq.(2.18) can be written as

$$\ln(E) = BX \quad (2.19)$$

with

$$B = (-b_{xx}, -b_{yy}, -b_{zz}, -2b_{xy}, -2b_{xz}, -2b_{yz}, 1) \quad (2.20)$$

$$X = [D_{xx}, D_{yy}, D_{zz}, D_{xy}, D_{xz}, D_{yz}, \ln(S_0)]^T \quad (2.21)$$

In order to obtain the six components of the diffusion tensor, the diffusion signal should be measured in at least six different diffusion angles (projections) corresponding to six different gradient directions. It follows that

$$\ln(E_i) = B_i X \quad (2.22)$$

where  $i = 1, 2, \dots, M$  with  $M \geq 6$ . When  $M = 6$ , the diffusion tensor can be calculated directly through the following equation.

$$X = B_i^{-1} \ln(E_i) \quad (2.23)$$

When the number of acquisition directions is more than six, there is no true inverse  $B_i^{-1}$ , but Eq.(2.22) can still be solved by calculating a pseudo inverse matrix  $B^\psi$ :

$$B^\psi = (B^T B)^{-1} B^T \quad (2.24)$$

Consequently, the components of the diffusion tensor are obtained from:

$$X = (B_i^T B_i)^{-1} B_i^T \ln(E_i) \quad (2.25)$$

### 2.2.3.3 Diffusion characteristics extraction

Once the diffusion tensor is calculated, diffusion characteristics can be extracted for describing the structures of the diffusion environment. Generally, concerning diffusion in biological tissues, especially in the cardiac tissue, we mostly care about the main direction of diffusion, the local mean diffusivity and the diffusion anisotropy.

#### Main direction of the diffusion

Mathematically, a tensor is often represented by an ellipsoid [Basser, 1995] with its three main axes represented by eigenvectors. Each eigenvector has an eigenvalue, denoted by  $\lambda$ . It is assumed that the direction of the eigenvector associated with the largest eigenvalue of the tensor corresponds to the local orientation of the tissue. The diffusion orientation extracted from DTI is commonly used for doing fiber tracking in the brain [Mori *et al.*, 2002, Le Bihan, 2003, Huppi *et al.*, 2006, Assaf *et al.*, 2008], sometimes in the heart muscle [Zhukov *et al.*, 2003, Sosnovik *et al.*, 2009, Zhang *et al.*, 2010a] and some other tissues. Up to now, it is the unique method to observe the “in vivo” cerebral connectivity non-invasively.

#### Mean Diffusivity (MD)

Mean diffusivity (MD) is a metric often used in DTI. It represents the overall mean-squared displacement of the water molecules and gives information about the overall presence or not of obstacles to the diffusion in one voxel or one region. It is defined by the average of the three ADCs respectively measured along the three axes of the tensor. Assuming that the tensor axes are respectively aligned along x, y and z, then the MD is defined by

$$MD = \frac{ADC_x + ADC_y + ADC_z}{3} \quad (2.26)$$

From the mathematical point of view, the MD can also be calculated from the eigenvalues of the tensor

$$MD = \frac{\lambda_1 + \lambda_2 + \lambda_3}{3} \quad (2.27)$$

### Fractional Anisotropy (FA)

The fractional anisotropy (FA) describes the spatial heterogeneity of water molecules displacements, which is related to the presence of orientated structures [Pierpaoli *et al.*, 1996]. It is defined as:

$$FA = \sqrt{\frac{3}{2}} \sqrt{\frac{(\lambda_1 - MD)^2 + (\lambda_2 - MD)^2 + (\lambda_3 - MD)^2}{(\lambda_1^2 + \lambda_2^2 + \lambda_3^2)}} \quad (2.28)$$

## 2.3 Compressed Sensing

Most physical (real world) signals are analog, but most modern signal processing systems are digital. To process these signals in modern signal processing systems efficiently, a process called *sampling* is required in order to convert a signal from analog to "digital" form. In general, it is impossible to perfectly reconstruct a signal from a series of sampling measurements without prior knowledge or assumptions about the signal. Over time, engineers have improved their understanding of which assumptions are practical and how they can be generalized. A breakthrough in signal processing field was the Shannon-Nyquist Sampling Theorem, and the theoretical foundation of this revolution is the pioneering work of Kotelnikov, Nyquist, Shannon, and Whittaker [WIITAKER, 1915, Nyquist, 1928, Kotelnikov, 1933, Shannon, 1949]. The theorem states that for the continuous-time band-limited signals, if the *sampling rate* (also called *Nyquist rate*) is more than twice of the signal's highest frequency, then the signal can be recovered perfectly. It is a fundamental bridge between analog signals (often called "continuous-time signals") and digital signals (often called "discrete-time signals"), and provides the sufficient (but not necessary) conditions for the sampling and reconstructing a band-limited signal without lost actual information. The Shannon-Nyquist sampling theory can be generalized for non-uniform samples as opposed to equally spaced samples in time and was developed in 1967 by Landau [Landau, 1967]. In this cases, perfectly reconstructing a band-limited signal may still be possible if the average sampling rate satisfies the Nyquist condition [Marvasti, 2000]. Unfortunately, firstly, in some cases, the signal bandwidth is unknown in advance. Secondly, in many important and emerging applications, the conventional Nyquist rate of sampling is too high to implement (for example, the analog-to-digital conversion (ADC) technology based on uniform sampling by limited to within the high frequency signal (less than 1GHz)). Otherwise, we often compress the data soon after sensing to address the logistical and computational challenges involved in dealing with such high-dimensional data; this is wasteful of valuable sensing resources.

Most recently, a complete theory called Compressed Sensing (CS, also referred to: compressive sensing, compressive sampling, and sketching/heavy-hitters in the literature) was developed as a new theory framework for both acquiring data and reconstructing signals with high quality from highly undersampled measurements (with respect to the traditional Shannon-Nyquist sampling theorem required). The fundamental idea and main motivation of CS is rather than first sampling at a high rate and then compressing the sampled data, we

would like to directly sense the data in a compressed form (i.e., at a lower sampling rate) and the signal can be reconstructed perfectly. The seminal papers were developed by E. Candès, J. Romberg, T. Tao [Candes et al., 2006a, Candes et al., 2006b, Candes et al., 2006c] and by D. Donoho [Donoho, 2006]. However, the hints in this direction have been traced back much further [Beurling, 1938, Santosa et al., 1986, Donoho et al., 1989, Gorodnitsky et al., 1992, Rudin et al., 1992a, Gorodnitsky et al., 1995, Feng, 1997, Gorodnitsky et al., 1997, Rao et al., 1998, Vetterli et al., 2002], while the idea of CS has only recently gained significant attraction in the signal processing community.

CS differs from classical sampling in three important respects. First, sampling theory typically considers finite length and continuous-time signals. In contrast, CS is a mathematical theory focused on measuring finite-dimensional vectors in  $\mathbb{R}^n$ . Second, rather than sampling the signal at specific points in time, CS systems typically acquire measurements in the form of inner products between the signal and more general test functions. This is in fact in the spirit of modern sampling methods that similarly acquire signals by more general linear measurements [Unser, 2000, Eldar et al., 2009, Tropp et al., 2010a], more specifically, the randomness often plays a key role in the design of these test functions. Thirdly, the two frameworks differ in the manner in which they deal with signal recovery, i.e., the problem of recovering the original signal from samples. In the Nyquist-Shannon framework, signal recovery is achieved through sinc interpolation—a linear process that requires little computation and has a simple interpretation. However, signal recovery in CS is typically achieved using highly nonlinear methods and the survey in [Rubinstein et al., 2010, Tropp et al., 2010b] for an overview of these techniques.

CS is an exciting and rapidly growing field, attracting considerable attention in many research areas such as applied mathematics, computer science and electrical engineering, and a series of papers have come out [Baraniuk, 2007, Candes et al., 2008, Lustig et al., 2008, Strohmer, 2012, Duarte et al., 2013, Qaisar et al., 2013, Rivenson et al., 2013, Graff et al., 2015]. First monograph in the literature to provide an up-to-date comprehensive survey of some of the important results in CS was published [Eldar et al., 2012]. Other supplementary textbook for courses on computer vision, coding theory and signal processing [Foucart et al., 2013, Vishal M. Patel et al., 2013, Carmi et al., 2014]. In addition, there are a lot of valuable resources on the internet for researchers, graduate students and practitioners wanting to learn and join this exciting research area, such as compressive sensing resources DISP\_RICE (<http://dsp.rice.edu/cs>), compressive sensing the big picture (<http://sites.google.com/site/igorcarron2/cs>) and Nuit Blanche compressive sensing blog (<http://nuit-blanche.blogspot.com/search/label/CS>).

Although most natural phenomena are analog, in this thesis, our discuss will focus on discrete and finite-length signal because the conceptually simpler and the available discrete CS theory is far more developed. The development of the classical CS theory framework for continuous time/space signals can be found in [Eldar, 2009, Duarte et al., 2011].

### 2.3.1 Shannon theory

Sampling procedure is necessary for converting analog signals to digital signals. Before introducing the Shannon-Nyquist sampling paradigm, let us start with an example, as shown in Fig. 2.17, a analog signal (red line) and the equidistant sampling points (marked blue circle ) are shown in the time domain. It can be seen that when the uniform sampling interval is too large, the sampled signal looks like very different compared with the original signal (red line).

In other words, if the sampling frequency is too low, the sampled signal appears to have a different frequency.

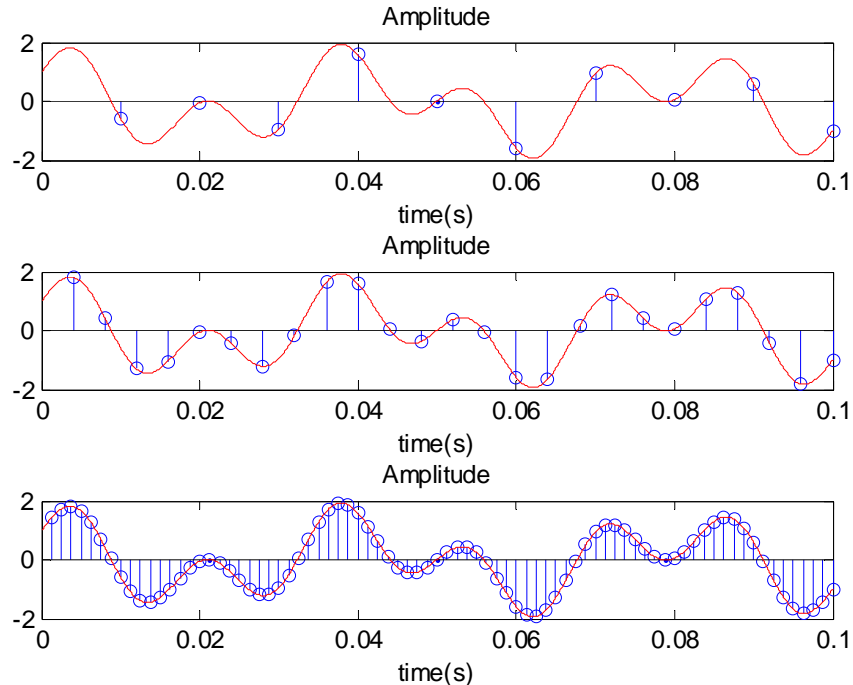


Fig. 2.17 The example of sampling the analog signals in time domain (a analog signal (red line) and the equidistant sampling points (marked blue circle )).

Although it is easy to understand what happens to a signal in the time domain after sampling, it is not so clear what happens in the frequency domain. Without the loss of generality, let  $x(t)$  denote a band-limited continuous-time signal with frequency smaller than  $B$  (in Hz) and is sampled uniformly at  $t = nT_s$ , with  $T_s = \frac{1}{f_s}$  denoting the sampling period in seconds (in this case  $f_s$  is the sampling frequency). The sampling process provides uniformly spaced pointwise samples of the analog input , as depicted in Fig. 2.18.

Sampling can be seen as multiplying a signal  $x(t)$  by a train of Dirac impulses  $s(t)$  equally spaced by  $T_s$  .

$$\begin{aligned} x_s(t) &= x(t) \sum_{k=-\infty}^{\infty} \delta(t - kT_s) \\ &= \sum_{k=-\infty}^{\infty} x(kT_s) \delta(t - kT_s) \end{aligned} \quad (2.29)$$

The transform of the train of Dirac impulses is:

$$F \left\{ \sum_{k=-\infty}^{\infty} \delta(t - kT_s) \right\} = \frac{1}{T_s} \sum_{k=-\infty}^{\infty} \delta(f - kf_s) \quad (2.30)$$

From this, it can be seen that the Fourier transform of the train of impulses is also a train of impulses. According to the convolution theorem, two functions multiplication in the time domain is equal to the convolution in the frequency domain, the spectrum of the sampled signal  $X_s(f)$  is then given by:

$$\begin{aligned}
 X_s(f) &= X(f) * \left[ \frac{1}{T_s} \sum_{k=-\infty}^{\infty} \delta(f - kf_s) \right] \\
 &= \int_{-\infty}^{\infty} X(s) \frac{1}{T_s} \sum_{k=-\infty}^{\infty} \delta(f - s - kf_s) ds \\
 &= \frac{1}{T_s} \sum_{k=-\infty}^{\infty} \int_{-\infty}^{\infty} X(s) \delta(f - s - kf_s) ds \\
 &= \frac{1}{T_s} \sum_{k=-\infty}^{\infty} X(f - kf_s)
 \end{aligned} \tag{2.31}$$

This result tells us that the spectrum of the sampled signal consists of periodically repeated copies of the spectrum  $X(f)$  of the original signal, namely sampling the temporal signal amounts for replicating its spectrum at frequency points that are multiple of  $f_s$ , as shown in Fig. 2.19.

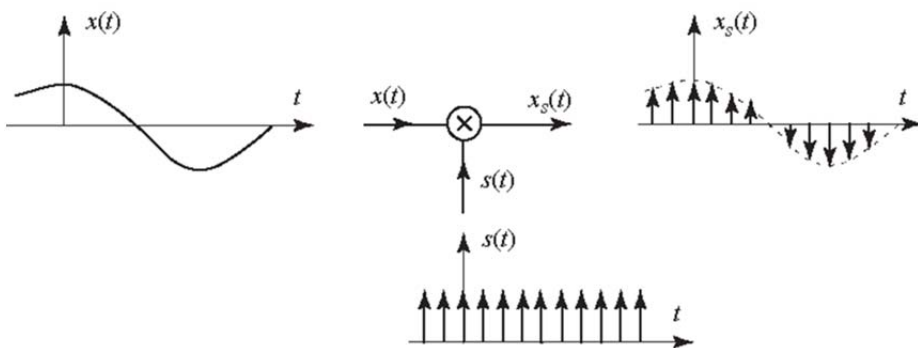


Fig. 2.18 Diagram of the sampling process.

The Shannon-Nyquist sampling paradigm [Shannon, 1949] is a classical theory and plays a fundamental role in signal processing and communications. It tells us how to convert an analog signal into a sequence of numbers and at what frequency we should sample a signal in order to reconstruct it exactly. Consider a continuous-time signal  $x(t)$  is band-limited signal with frequency smaller than  $B$  (in Hz), the samples rate is  $f_s = \frac{1}{T_s}$ . The Shannon-Nyquist sampling theorem says:

**Theorem [Shannon]:** *If a function  $x(t)$  contains no frequencies higher than  $B$  (in Hertz), it is completely determined by giving its ordinates at a series of points spaced  $T_s = \frac{1}{2B}$  seconds apart.*

Therefore, if the minimum sampling rate  $f_s$  is more than twice of the signal's highest frequency  $B$ , then the signal  $x(t)$  can be reconstructed perfectly from its samples without aliasing. This condition is known as *Nyquist criterion*, and the frequency  $2B$  is called the *Nyquist rate*.

The Shannon-Nyquist sampling theorem and its corresponding reconstruction formula are best understood in the frequency domain, as illustrated in Fig. 2.19.

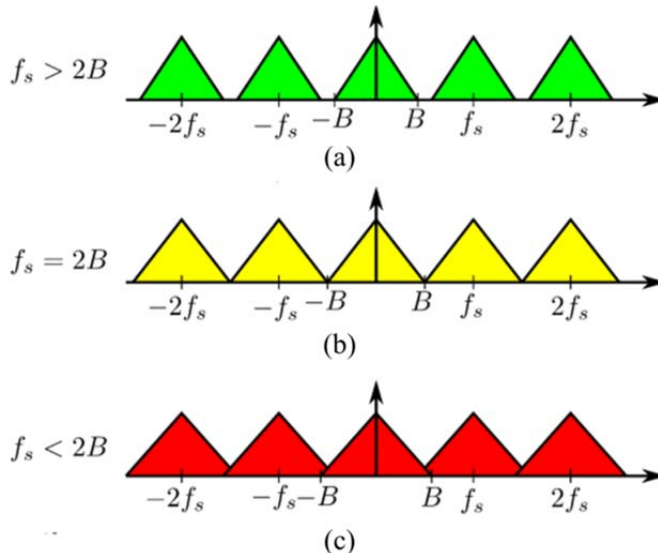


Fig. 2.19 Frequency interpretation of the sampling theorem, the sample frequency of analog input signal  $f_s$  is (a) more than Nyquist rate; (b) equal to Nyquist rate; (c) less than Nyquist rate (From: <http://www.onmyphd.com/?p=aliasing>)

From the previous description, we have seen that the sampling process is making an infinite copies of the spectrum of the signal around multiples of the sampling frequency. If the sampling frequency meets the Nyquist criterion, none of these copies will overlap with each other. Consequently, the continuous-time signal  $x(t)$  can be reconstructed by lowpass filtering, as illustrated in Fig. 2.20(a). Otherwise, if the sample frequency is not satisfied with Nyquist criterion, the copies will overlap and a certain band of frequencies in the baseband will be contaminated with components of adjacent copies (see Fig. 2.20(b)), thereby ruining the possibility of exact recovery.

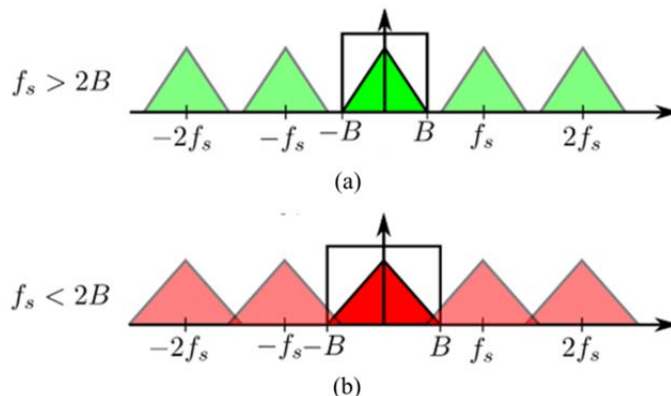


Fig. 2.20 The analog signal is reconstructed by ideal low-pass filtering. (a) a perfect recovery is possible provided that the sample frequency is satisfied with Nyquist criterion; (b) ruining the possibility of exact recovery that the sample frequency is not satisfied with Nyquist criterion (From: <http://www.onmyphd.com/?p=aliasing>).

Usually, real-world signals of interest are most time band-limited, and also often contaminated by the components of higher frequencies, such as noise and interferences. If sampling frequency is satisfied just with the Nyquist criterion (not over-sampled), the unwanted components would get aliased to the baseband and contaminate the sampled signal. To avoid that, the signal is filtered before sampling with a cut-off frequency matching the bandwidth of the signal of interest. Higher frequencies are eliminated or greatly reduced and their aliasing becomes negligible. This processing scheme is achieved by anti-aliasing filters.

### 2.3.2 Sparsity

Sparsity (or compressibility) and incoherence are two fundamental premises under which recovery is possible in the development of current CS theory. The sparsity requires the signal to be sparse in some domain. Sparsity has largely been exploited in signal processing and approximation theory for tasks such as compression [Pennebaker *et al.*, 1993, DeVore, 1998, Taubman *et al.*, 2002] and denoising [Rudin *et al.*, 1992a, Donoho, 1995].

Many natural signals often have concise representations or can be well-approximated using just a few elements in a proper basis or dictionary. Mathematically, a discrete signal  $x \in R^n$  is said to be  $k$ -sparse, if it has at most  $k$  nonzeros entries, i.e.,  $\|x\|_0 \leq k$ ,  $k \ll n$ .

Let us take as an example a signal  $x$  in time domain defined by  $x(t) = \sin\left(2\pi \frac{29}{1024}t\right) + \sin\left(2\pi \frac{100}{1024}t\right)$  with  $0 \leq t < 1024$ . In time domain,  $x(t)$  is non-sparse as shows in Fig. 2.21(a) and Fig. 2.21(b) shows the sparsity of the same signal in the Fourier domain.

However, in practice, few real-world signals are truly sparse but often *compressible*. Compressible signals have few significant coefficients and the coefficients decay as a power law. It means that a compressible signal can be well-approximated by a sparse signal. One can easily show that the thresholding strategy (keeping only the  $k$  ( $k \ll n$ ) largest coefficients) results in the optimal approximation. Compressibility can be quantified by calculating the error induced when approximating a signal  $x$ , which can be expressed as:

$$\varepsilon = \|x - x_k\| \quad (2.32)$$

Generally, the signals are not themselves sparse, but which admit a sparse representation in some basis (transform domain). This implies that the described signals can be expressed as linear combinations of a few basis functions from a pre-specified basis or dictionary. In general, the choice of a proper dictionary can be done using one of two ways [Chen *et al.*, 2001, Rubinstein *et al.*, 2010]: ① building a sparsifying dictionary based on a mathematical model of the data, such as Fourier, wavelet, or ② learning a dictionary to best perform on a training set. In this case we will still refer to  $x$  as being  $k$ -sparse, with the understanding that we can express  $x$  as:

$$x = \Psi c = \sum_{i=1}^n c_i \psi_i \quad (2.33)$$

where  $c_i = \langle x, \psi_i \rangle$  are the transform coefficients of  $x$  with respect to the basis or dictionary  $\Psi$  with vectors  $\{\psi_i\}$  as columns (called atoms), and  $\|c\|_0 \leq k$ .

Fig. 2.22 gives an example of an image and its best  $k$ -term approximation. The original image with size of  $256 \times 256$  is shown in Fig. 2.22(a) and its wavelet transform coefficients are shown in Fig. 2.22(b) (Note: light pixels represent larger coefficients and dark pixels smaller coefficients). It can be seen that although nearly all the image pixels have nonzero values, the most wavelet coefficients are very small. It means that the relatively few large wavelet coefficients contain most of the information. Hence, we can set the small wavelet coefficients to zero to obtain a good approximation (or representation) of the image and the difference with the original image is hardly noticeable. For example, we can approximate the original image obtained by zeroing out all the wavelet coefficients except ng only the largest 10% of

the coefficients, as illustrated in Fig. 2.22(d). This explains why compression techniques such as JPEG, MPEG, or MP3 work so well in practice.

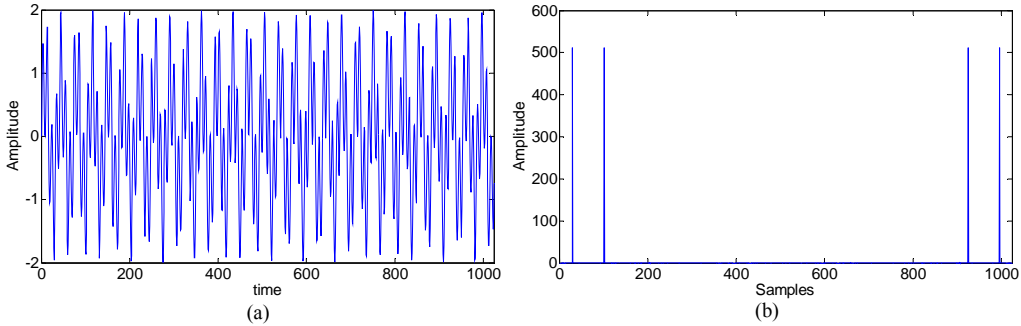


Fig. 2.21 An example of sparse signal in transform domain.

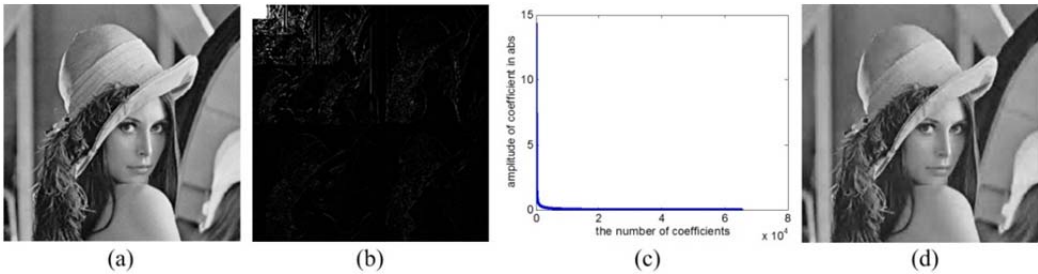


Fig. 2.22 Sparse representation and approximation of an image. (a) Original image. (b) multi-scale wavelet representation (large coefficients are represented by light pixels, while small coefficients are represented by dark pixels). (c) wavelet transform coefficients (arranged in order for enhanced visibility). (d) approximation of image (a) obtained by zeroing out all the wavelet coefficients but keeping only the largest 10% of the coefficients.

### 2.3.3 Incoherence

In addition to the sparsity, the incoherence is another fundamental premise underlying CS. For notation and treatment simplicity, here we consider a pair  $(\Phi, \Psi)$  of orthobases of  $\mathbb{R}^n$ , but it is not essential. The basis  $\Phi$  and  $\Psi$  are used for sensing and sparsely representing the signal  $x$ , respectively. The coherence (also known as mutual coherence) between the sensing basis  $\Phi$  and the sparsifying basis  $\Psi$  is defined as [Donoho *et al.*, 2001]:

$$\mu(\Phi, \Psi) = \sqrt{n} \cdot \max_{1 \leq k, j \leq n} |\langle \varphi_k, \psi_j \rangle| \quad (2.34)$$

where  $\varphi_k$  and  $\psi_j$  are the  $k$ th and  $j$ th column of  $\Phi$  and  $\Psi$ , respectively.

Clearly, the  $\mu(\Phi, \Psi)$  measure the largest correlation between any two elements of basis  $\Phi$  and basis  $\Psi$ . According to linear algebra, the coherence measure  $\mu$  is in the range  $[1, \sqrt{n}]$ , see [Donoho *et al.*, 2001]. In CS, we are mainly concerned with low coherence pairs where the two bases are *incoherent*. The incoherence requires that the rows  $\{\varphi_k\}$  of sensing basis cannot sparsely represent the columns  $\{\psi_j\}$  of sparse basis (and vice versa). The random matrices with independent identically distributed (i.i.d.) entries, e.g., Gaussian or  $\pm 1$  binary entries, exhibit largely a very low coherence with any fixed  $\Psi$ . There are many other low coherence pairs [Jacques *et al.*, 2010]:

- $\mu(I, F) = 1$ , here  $\Phi$  is the canonical or spike basis and  $\Psi$  is the Fourier basis;
- $\mu(I, \widehat{H}_n)$ , here  $\Phi$  is the canonical or spike basis and  $\Psi = \widehat{H}_n = \frac{H_n}{\sqrt{n}}$ ,  $H_n$  is the Hadamard-Walsh matrix.
- $\mu(\Phi, \Psi) = 1.5 \sim 3.0$ , here  $\Phi$  is noiselets [Coifman et al., 2001] and  $\Psi$  wavelets bases (such as Haar, Daubechies wavelets).

### 2.3.4 Sensing

Let  $x \in \mathbb{R}^n$  represent the signal to be sensed, then the information about signal  $x$  is obtained by linear functionals recording the values in standard setup:

$$y_k = \langle x, \varphi_k \rangle, \quad k = 1, 2, \dots, m. \quad (2.35)$$

where  $\varphi_k$  is the sensing waveforms.

If the sensing waveforms are Dirac delta functions (spikes), then  $y$  is a vector of sampled values of  $x$  in the time or space domain. If the sensing waveforms are indicator functions of pixels, then  $y$  is the image data typically collected by sensors in a digital camera. If the sensing waveforms are sinusoids, then  $y$  is a vector of Fourier coefficients; this is the sensing modality used in magnetic resonance imaging (MRI).

The sensing process using matrix notation can be expressed as:

$$y = \Phi x \quad (2.36)$$

where  $\Phi \in \mathbb{R}^{m \times n}$  denote the sensing matrix and  $y \in \mathbb{R}^m$  is the obtained signal.

Under conventional sensing paradigm ' $m$ ' must be at least equal to ' $n$ ' (the sensing waveforms are Dirac delta functions—spikes). However, in CS, the matrix  $\Phi$  represents a dimensionality reduction, i.e., it maps  $\mathbb{R}^n$  into  $\mathbb{R}^m$ , where  $n$  is generally large and  $m$  is typically much smaller than  $n$ . Obviously, this is a highly underdetermined problem (too few equations and too many unknowns). So, there are two main theoretical questions. First, how to choose the type of sensing matrix  $\Phi$  for the purpose of sensing to ensure that it preserves the information in the signal  $x$ ? Second, how many measurements  $y$  should be collected to ensure that these measurements will be sufficient to recover the original signal  $x$  from measurements  $y$ .

The robustness of the CS relies heavily on a notion called *restricted isometry property (RIP)* which was first introduced and studied in [Candes et al., 2005].

**Definition [Candes et al., 2005]:** A matrix  $\Phi$  satisfies the restricted isometry property (RIP) of order  $k$  if there exists a  $\delta_k \in (0, 1)$  such that

$$(1 - \delta_k) \|x\|_2^2 \leq \|\Phi x\|_2^2 \leq (1 + \delta_k) \|x\|_2^2 \quad (2.37)$$

holds for all  $x \in \sum_k$ .

If a matrix  $\Phi$  satisfies the RIP, then this is sufficient for a variety of algorithms to be able to successfully recover a sparse signal from noisy measurements. Recently, a natural generalization of the well-known RIP was proposed [Candes et al., 2011], which introduces a condition on the measurement/sensing matrix which is a natural generalization of the well-

known restricted isometry property, called D-RIP. The D-RIP guarantees accurate recovery of signals that are nearly sparse in (possibly) highly overcomplete and coherent dictionaries.

On the other hand, the following theorem addresses explicitly the second question:

**Theorem [Candes, 2008]:** *Given  $x \in \mathbb{R}^n$  and suppose  $x$  is  $s$ -sparse in basis  $\Psi$ . Select  $m$  measurements in the  $\Phi$  domain uniformly at random. If*

$$m \geq C \cdot \mu^2(\Phi, \Psi) \cdot s \cdot \log(n) \quad (2.38)$$

for some positive constant  $C$ , then signal  $x$  can be exactly reconstructed with overwhelming probability.

### 2.3.5 Recovery

Given an observation vector  $y$  and the sensing matrix  $\Phi$ , the aim is to recover the sparse signal  $x$  with  $y = \Phi x$  by solving an optimization problem of the form:

$$\min_{x \in \mathbb{R}^n} \|x\|_0 \quad \text{subject to } y = \Phi x \quad (2.39)$$

However, this problem involves the  $l_0$  norm which requires combinatorial optimization. Fortunately, it is shown that it is possible to replace the  $l_0$  norm by the  $l_1$  norm that represents the sum of absolute values of each element in a vector for equivalently finding the solution of Eq.(2.39) if  $x$  is sufficiently sparse [Donoho, 2006]. This  $l_1$  minimization problem is expressed as:

$$\min_{x \in \mathbb{R}^n} \|x\|_1 \quad \text{subject to } y = \Phi x \quad (2.40)$$

Many algorithms can be used to find the solution of Eq.(2.39) and (2.40) to recovery the original signal from its compressed measurements, such as Matching Pursuit/Greedy [Mallat et al., 1993, Pati et al., 1993, Tropp et al., 2007], Basis Pursuit/Linear Programming [Chen et al., 2001, Donoho, 2006], Iterative Thresholding [Fornasier et al., 2008], Proximal [Parikh et al., 2013], and many others [Tropp et al., 2010b, Nesterov, 2013, Nesterov et al., 2013].

Proximal-Gradient Methods are particularly suitable for inverse problems involving large-scale data sets. In a recent work [Beck et al., 2009b] by Beck and Teboulle, some early work of Nesterov [Nesterov, 1983] was extended in developing a fast iterative shrinkage-thresholding algorithm (FISTA) for general convex problem. Motivated by the effective acceleration scheme in FISTA, the composite splitting algorithm (CSA) and its accelerated version (FCSA) are proposed in [Huang et al., 2011a, Huang et al., 2011b] to solve the composite regularization problem.

## 2.4 Conclusion

In this chapter, we introduce some elements necessary for a better understanding of the subsequent chapters of the manuscript. First, we introduced the principle of Magnetic Resonance Imaging (MRI), including the magnetization process of  $^1\text{H}$ , precession, excitation, relaxation, and signal detection, spatial encoding technique. All of these make it clear how MRI works. Next, the physical process of molecular diffusion was presented, and by combining the principle of MRI and the process of diffusion, the principle of DTI was elaborated. Finally, the compressed sensing (CS) theory was described, including classic Shannon theory, sensing matrix and reconstruction algorithms.

## **PART II**

---

---

### **Contributions**

---

---

## Chapter 3

# Compressed sensing MRI via data-driven tight frame and total generalized variation(TGV)

## Contents

---

Résumé en français.....	60
Abstract .....	61
3.1    Introduction.....	62
3.2    Methodology .....	63
3.2.1 <i>Preliminaries</i> .....	63
3.2.2 <i>Proposed model</i> .....	65
3.3    Experiments and results .....	67
3.3.1 <i>Experimental setup</i> .....	67
3.3.2 <i>Visual comparison</i> .....	69
3.3.3 <i>Effects of sampling rates</i> .....	72
3.3.4 <i>Effects of filter size</i> .....	72
3.3.5 <i>Computation time</i> .....	75
3.4    Conclusion .....	76

---

## Résumé en français

Sous-échantillonner les données k-espace est un moyen efficace pour réduire le temps d'acquisition en imagerie par résonance magnétique (IRM). L'acquisition comprimée (CS) a un grand potentiel pour accélérer l'IRM tout en maintenant une haute qualité d'image. La parcimonie ou compressibilité est une prémissse fondamentale de l'acquisition comprimée. Les transformées prédéfinies, telles que la transformée en ondelettes discrète (DWT), les framelets et le shearlet, ont été largement utilisées pour fournir des représentations parcimonieuses des images par résonance magnétique (MR). Ce chapitre propose une méthode améliorée pour reconstruire des images MR dans le cadre de CS en combinant la contrainte de trames ajustées guidées par les données (TF data-driven) et la régularisation de variation totale généralisée (TGV). Le TF data-driven est utilisé pour apprendre de manière adaptative un ensemble de filtres à partir des données sous-échantillonnées pour fournir une meilleure approximation parcimonieuse de l'image. Ainsi, l'algorithme de reconstruction CS basé sur le TF data-driven peut produire de meilleurs résultats pour la plupart des images MR. Contrairement à la régularisation de variation totale (TV), qui préserve des bords ou contours mais brouille des détails et provoque l'effet de bloc avec des structures fines perdues, le TGV est une généralisation de la théorie de TV, qui régularise sélectivement des régions d'image à des niveaux différents et donc réduit l'effet d'escalier. La reconstruction proposée est réalisée par l'utilisation d'un algorithme rapide dit composition-décomposition (fast composite splitting algorithm—FCSA) afin d'accélérer le calcul. La méthode proposée est évaluée sur des images MR de différents organes. Les résultats démontrent que l'approche proposée améliore la reconstruction et préserve caractéristiques diverses de l'image telles que les bords et les textures en comparaison avec d'autres transformées parcimonieuses souvent utilisées dans l'acquisition comprimée en l'IRM.

## Abstract

Under-sampling k-space data is an efficient way to reduce the acquisition time of magnetic resonance imaging (MRI). Compressed sensing has shown great potential for accelerating MRI process while maintaining high image quality. Sparsity or compressibility is a fundamental premise underlying compressed sensing. The predefined transforms, such as the discrete wavelet transform (DWT), the framelets and the shearlet, have been widely used to provide sparse representations for limited types of magnetic resonance (MR) images. This chapter proposes an improved CS reconstruction method for MR images by combining data-driven tight frame (data-driven TF) constraint and Total generalized variation (TGV) regularization together. The data-driven TF is used to adaptively learn a set of filters from the under-sampled data itself to provide a better sparse approximation of images. Hence, compressed sensing MRI (CS-MRI) reconstruction method based on the data-driven TF can produce better reconstruction results for a broader range of MR images. Unlike the total variation (TV) regularization, which preserves sharp edges but it blurs some details and causes blocking effect with fine structures lost, the TGV is a generalization of the TV theory, which “selectively regularizes” different image regions at different levels and thus leads to suppression of the staircase effect. The proposed reconstruction problem is solved by Fast Composite Splitting Algorithm (FCSA) in order to improve computational efficiency. We conducted experiments to estimate the effectiveness of our algorithm on different MR images with varying content. The experimental results demonstrate that the proposed approach improves the reconstruction performance, and preserves various image features (including edges and textures) in comparison with other commonly used sparsifying transforms for CS-MRI.

### 3.1 Introduction

Magnetic resonance imaging (MRI) is a non-invasive medical imaging technique widely used to investigate the anatomy and function of the body in clinical diagnosis. However, the imaging speed of MRI is often limited because of the important quantity of k-space data to acquire. Reducing the acquisition time of MRI therefore remains a great challenge for clinical applications. Numerous efforts have been dedicated to designing fast acquisition sequences and reducing the amount of data required as much as possible while maintaining reconstruction quality [McGibney *et al.*, 1993, Pruessmann *et al.*, 1999, Blaimer *et al.*, 2004, Luo *et al.*, 2012, Tsao *et al.*, 2012]. Among them, parallel imaging (PI) emerged as the most widely used technique in clinical routine [Larkman *et al.*, 2007]. There are a variety of PI methods such as simultaneous acquisition of spatial harmonics (SMASH) [Sodickson *et al.*, 1997], sensitivity encoding (SENSE) [Pruessmann *et al.*, 1999], generalized autocalibrating partially parallel acquisitions (GRAPPA) [Griswold *et al.*, 2002], and iterative self-consistent parallel imaging reconstruction (SPIRiT) [Lustig *et al.*, 2010]. However, the PI techniques are typically limited by Nyquist sampling rate and the achieved acceleration is limited to low factor values [Kieren Grant, 2015].

Recently, the emergence of compressed sensing (CS) [Candes *et al.*, 2006a, Donoho, 2006] methods provides a new approach to reconstructing magnetic resonance (MR) images with high quality from significantly under-sampled k-space data, called the CS-MRI, which assumes that MR images have a sparse representation in certain domain (image or transform domain). CS-MRI exploits the sparsity of signals or images to reconstruct the MR images from far fewer samples than conventional methods, and consequently, it allows reducing MRI scanning time efficiently without degrading image quality [Lustig *et al.*, 2007, Lustig *et al.*, 2008, Kieren Grant, 2015].

Sparsity or compressibility is a fundamental premise underlying CS-MRI. The first CS-MRI reconstruction method was proposed in [Lustig *et al.*, 2007], which achieved reconstruction by combining total variation (TV) and wavelets as sparsifying transforms. However, since the TV model favours piecewise constant image structures, such TV model-based methods blur details and cause blocking effect with fine structures lost, although the edges are preserved in reconstruction. To overcome the intrinsic drawback of the TV model, various extensions of this model have been proposed for CS-MRI image reconstruction, such as nonlocal total variation (NLTV) [Elmoataz *et al.*, 2008, Gilboa *et al.*, 2008, Lou *et al.*, 2010, Liang *et al.*, 2011, Junzhou *et al.*, 2012, Gopi *et al.*, 2014] and total generalized variation (TGV) [Bredies *et al.*, 2010, Knoll *et al.*, 2010, Knoll *et al.*, 2011a, Knoll *et al.*, 2011b, Knoll *et al.*, 2012, Guo *et al.*, 2014, Zhao *et al.*, 2014]. These methods can avoid the staircase artifacts that are common to TV and wavelet regularizations, while better preserving image edges and details.

Another common sparsity used for CS-MRI reconstruction is based on the discrete wavelet transform (DWT) [Lustig *et al.*, 2007, He *et al.*, 2009, Yang *et al.*, 2010, Huang *et al.*, 2011b]. It is well known that traditional wavelets transform appropriately point-like singularities, but generally lack performance when dealing with singularities in higher dimension, such as edges, contours or regular textures in two-dimensional (2D) images [Jacques *et al.*, 2011]. To overcome the limitation, multi-scale geometric analysis method is introduced into CS-MRI in order to more sparsely represent piecewise smooth images containing rich geometric information (e.g. edges, curves, etc.), such as contourlets [Gho *et al.*, 2010, Qu *et al.*, 2010], framelets [Compton *et al.*, 2012, Gopi *et al.*, 2014], and shearlet [Jing *et al.*, 2013, Guo *et al.*, 2014].

Data adaptive transforms can sparsify images better than those explored in various image-processing problems in recent years. Instead of predefined transforms, Hong et al [Hong *et al.*, 2011] proposed a data-adaptive sparsifying transform using singular value decomposition (SVD) for CS-MRI image reconstruction. This method can be applied to a broader range of MR images to improve image reconstruction quality effectively. In [Cai *et al.*, 2014], an adaptive data-driven tight frame (data-driven TF) was proposed to solve image restoration problems, and has been successfully applied to image denoising and seismic data restoration problems [Liang *et al.*, 2014]. Dictionary learning approaches learn a dictionary as a sparse basis from the elemental patches of particular image instance or class of images to achieve better sparsity of the input image in CS-MRI [Chen *et al.*, 2010, Akcakaya *et al.*, 2011, Ravishankar *et al.*, 2011, Huang *et al.*, 2015c]. However, these methods ignored the relationship between image patches in dictionary learning and sparse coding. Meanwhile, an adaptive nonlocal processing was also introduced for image restoration [Buades *et al.*, 2005, Dabov *et al.*, 2007, Bao *et al.*, 2013, Zhang *et al.*, 2014]. By combining the notion of patches and nonlocal processing, a patch-based nonlocal operator was introduced for CS-MR image reconstruction [Qu *et al.*, 2014]. This kind of methods is based on grouping similar 2-D image patches into 3-D data arrays, and then 3-D transforming the data arrays to obtain sparsity. Since the methods exploit the nonlocal self-similarity of images, it becomes possible to achieve lower reconstruction errors and higher visual quality, compared with the conventional CS-MRI reconstruction methods.

In this chapter, we propose a CS method for reconstructing MR images from highly undersampled k-space data. The method is based on the combined use of data-driven tight frame (TF) and total generalized variation (TGV) regularization. The data-driven TF is used to adaptively learn a set of filters from the under-sampled data to provide a better sparse approximation of images. The TGV allows selectively regularizing different image regions to avoid staircase effect. The proposed reconstruction problem is solved by Fast Composite Splitting Algorithm (FCSA).

The rest of the chapter is organized as follows. The proposed CS-MRI reconstruction method is detailed in Section 3.2. The experiments and results are presented in Section 3.3, followed by conclusion in Section 3.4.

## 3.2 Methodology

### 3.2.1 Preliminaries

**Tight Frame(TF)** [Daubechies *et al.*, 2003, Cai *et al.*, 2010]: The *frame* is a generalized concept of the *basis* formed of linearly dependent vectors. Specifically, a set of vectors  $\{\varphi_i\}_i^n \subset H$  is a frame in Hilbert space  $H$ , if there exist two positive constants  $A$  and  $B$ , such that for any vector  $x \in R^d$ :

$$A\|x\|_2^2 \leq \sum_n |\langle \varphi_i, x \rangle|^2 \leq B\|x\|_2^2 \quad (3.1)$$

When the constants  $A = B = 1$ , the frame  $\{\varphi_i\}_i^n$  is called the *tight frame (TF)*.

For a given frame  $\{\varphi_i\}_i^n$ , two associated operators can be defined: the analysis operator  $\Psi$  defined by

$$\Psi : x \in H \rightarrow \{\langle x, \varphi_i \rangle\} \in l^2(\mathbb{N}) \quad (3.2)$$

and the synthesis operator (adjoint operator of the analysis operator):

$$\Psi^T : \{c_i\} \in l^2(\mathbb{N}) \rightarrow \sum_n c_i \varphi_i \in H \quad (3.3)$$

The sequence  $\{\varphi_i\}_i^n$  forms a tight frame if and only if  $\Psi^T \Psi = I$  with  $I$  designating the identity operator.

A tight frame can be constructed from a set of filters based on the Unitary Extension Principle (UEP) proposed in [Ron *et al.*, 1997]. Given a set of filters  $\{a_i\}_i^n$ , the analysis operator  $\Psi$  can be defined as:

$$\Psi = \left[ S_{a_1}^T, S_{a_2}^T, \dots, S_{a_n}^T \right]^T \quad (3.4)$$

and its adjoint operator (synthesis operator)  $\Psi^T$  by:

$$\Psi^T = \left[ S_{a_1}, S_{a_2}, \dots, S_{a_n} \right] \quad (3.5)$$

Here,  $S_a$  refers to the linear convolution operator. For a filter with finite support, the convolution operation can be represented by a block-wise Toeplitz matrix under Neumann boundary conditions [Chan *et al.*, 2004]. For example, the discrete wavelet tight frame is one of the widely used tight frames, which is generated by a set of filters called framelet filter  $h_i$  (corresponding to  $a_i$ ).

**Data-driven TF** [Cai *et al.*, 2014]: A tight frame simply constructed from predefined filters can sparsely represent certain classes of data. However, it is not efficient when the image structure is complex (for example for complex geometric structures, rich textures, etc.). The data-driven TF is then proposed that is constructed from a set of filters adaptively learned from the input data itself to sparsely represent the given data. Given an image  $x$ , a set of filters  $\{a_i\}_i^n$  (the size of  $a_i$  is  $\sqrt{n} \times \sqrt{n}$ ) can be learned by solving the following minimization problem [Cai *et al.*, 2014]:

$$\min_{v, \Psi} \|v - \Psi x\|_2^2 + \gamma \cdot \|v\|_0, \quad \text{subject to } \Psi^T \Psi = I \quad (3.6)$$

where  $v$  is the coefficient vector that sparsely approximates the tight frame coefficients  $\Psi x$ ,  $\Psi$  the analysis operator,  $\Psi^T$  the synthesis operator, and  $\gamma > 0$  a regularization parameter. The detail and complete description of the data-driven TF construction scheme and numerical solver can be found in [Cai *et al.*, 2014]. An example of the data-driven TF filters constructed with two different sizes is shown in Fig. 3.1 (a small image block represents a filter).

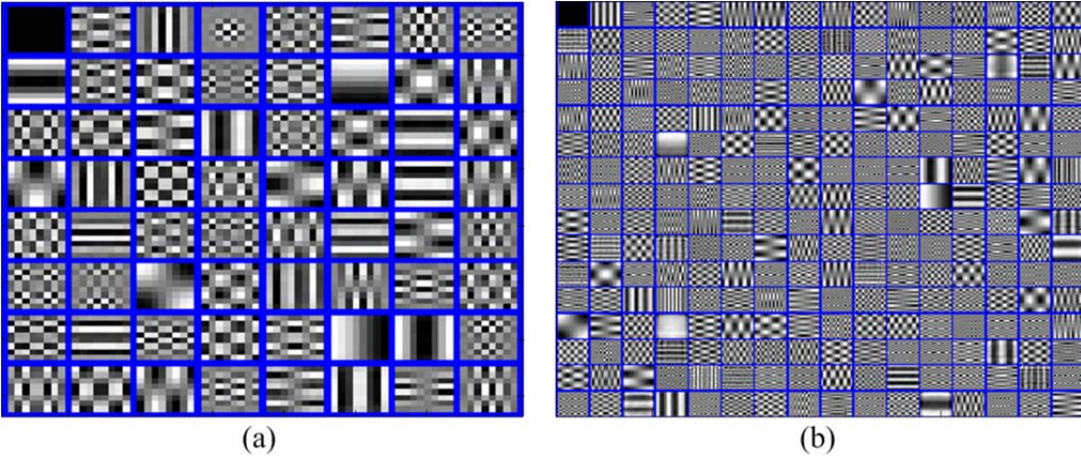


Fig. 3.1 Illustration the data-driven TF filters constructed with two different sizes. (a) the filter (atom) size  $8 \times 8$ . (b) the filter (atom) size  $16 \times 16$ .

**Total generalized variation (TGV)** [Bredies et al., 2010]: Unlike TV regularization, which preserves sharp edges but blurs some details and causes blocking effect with fine structures lost, the TGV is a direct extension of the classical TV semi-norm and the regularization term is convex. The TGV “selectively regularizes” different image regions at different levels and thus leads to better performance by preserving edges and suppressing the staircase effect [Bredies et al., 2010, Knoll et al., 2011a]. The discrete TGV of second-order formulated by [Knoll et al., 2011a] is:

$$\text{TGV}_\alpha^2(u) = \min_{\Omega} \alpha_1 \int_{\Omega} |\nabla u - v| dx + \alpha_0 \int_{\Omega} |\varepsilon(v)| dx \quad (3.7)$$

where  $\varepsilon(v) = \frac{1}{2}(\nabla v + \nabla v^T)$  denotes the symmetrized derivative,  $\alpha_0$  and  $\alpha_1$  are the positive weights.

### 3.2.2 Proposed model

Assuming that  $x$  is a MR image and  $F_u$  is a partial Fourier transform which can be expressed by  $F_u = P \cdot F$ , with  $F$  the Fourier transform and  $P$  the common under-sampling pattern (mask). The under-sampled measurements  $b$  of the image  $x$  with an unknown observation noise  $\varepsilon$  in k-space is then defined as [Lustig et al., 2008]:

$$b = F_u \cdot x + \varepsilon \quad (3.8)$$

For the under-sampling case, Eq.(3.8) is highly underdetermined and has therefore an infinity of solutions. In order to find the optimal solution to this problem, additional constraints are introduced into the CS framework according to some prior knowledge. Thus, the CS-MRI reconstruction can be formulated as the following optimization problem:

$$\hat{x} = \arg \min_x \|F_u x - b\|_2^2 + \lambda \cdot J(x) \quad (3.9)$$

where  $J(x)$  is a regularizing functional and  $\lambda > 0$  denotes a balancing parameter.

Now, by introducing the above-stated data-driven TF and TGV regularization, we can formulate the CS-MRI reconstruction as the following optimization problem:

$$\hat{x} = \arg \min_x \left\{ \frac{1}{2} \|F_u x - b\| + \lambda \cdot \|\Psi x\|_1 + \beta \cdot \text{TGV}_\alpha^2(x) \right\} \quad (3.10)$$

In the formula, the first term  $\|F_u x - b\|$  is a data fidelity term, the second term  $\|\Psi x\|_1$  and the third term  $\text{TGV}_\alpha^2(x)$  are regularization terms, and  $\lambda$  and  $\beta$  are the regularization parameters.  $\Psi$  is the data-driven TF described above,  $\text{TGV}_\alpha^2(x)$  refers to the second-order TGV of the image  $x$ , where, according to [Knoll et al., 2011a], the weights  $\alpha_0$  and  $\alpha_1$  appearing in Eq.(3.7) do not need to be tuned and are set to 2 and 1, respectively.

The proposed optimization problem (Eq.(3.10)) can be solved by the Fast Composite Splitting Algorithm (FCSA) proposed in [Huang et al., 2011b]. Let  $f(x) = \frac{1}{2} \|F_u x - b\|_2^2$ , which is a convex and smooth function with Lipschitz constant  $L$ , and  $g(x) = \lambda \cdot \|\Psi x\|_1 + \beta \cdot \text{TGV}_\alpha^2(x)$  denoted as a regularizing functional. According to the FCSA algorithm framework, the  $g(x)$  problem can be divided into two sub-problems: the regularization of  $l_1$ -norm and TGV. Thus,  $g(x)$  can be expressed as  $g(x) = g_1(x) + g_2(x)$ , where  $g_1(x) = \lambda \cdot \|\Psi x\|_1$  and  $g_2(x) = \beta \cdot \text{TGV}_\alpha^2(x)$ . Each sub-problem is actually a convex function which can be solved by a proximal mapping operation. Given a continuous convex function  $\varphi(x)$ , the proximal map is described as [Beck et al., 2009a;b]:

$$\text{prox}_\rho(\varphi)(x) = \arg \min_u \left\{ \varphi(u) + \frac{1}{2\rho} \|u - x\|_2^2 \right\} \quad (3.11)$$

where scalar  $\rho > 0$  is the inverse of the Lipschitz constant  $L$  of  $\nabla f$  defined [Beck et al., 2009a] by  $\nabla f = \left( \frac{1}{2} \|F_u x - b\|_2^2 \right)' = F_u^T (F_u x - b)$ , with  $F_u^T$  denotes the inverse partial Fourier transform.

Then, the regularization of  $l_1$ -norm sub-problem is achieved via solving the following minimization

$$\text{prox}_\rho(g_1)(x) = \arg \min_u \left\{ \frac{1}{2\rho} \|u - x\|_2^2 + 2\lambda \cdot \|\Psi u\|_1 \right\} \quad (3.12)$$

Eq.(3.12) is solved using an iteration thresholding algorithm under a tight frame [Cai et al., 2014].

The TGV regularization sub-problem is formulated as:

$$\text{prox}_\rho(g_2)(x) = \arg \min_u \left\{ \frac{1}{2\rho} \|u - x\|_2^2 + 2\beta \cdot \text{TGV}_\alpha^2(u) \right\} \quad (3.13)$$

Eq.(3.13) can be solved using the first-order primal-dual algorithm. More details about this algorithm can be found in [Knoll et al., 2011a].

The proposed algorithm is outlined as follow:

---

**INPUT:**

$K$  : the maximum number of iterations;  
 $n$  : the filter size of data-driven TF;  
 $\lambda, \beta$  : the regularization parameters;  
 $\eta$  : the tolerance parameter;

**INIT:** Set  $\rho = 1/L, t^1 = 1, x^0 = r^1 = 0, k = 0$ ;

**OUTPUT:**

$x$  : reconstructed image.

---

**REPEAT**

$k = k + 1$ ;

Generate the analysis operator  $\Psi^k$  according to Eq. (3.6);

$$x_g = r^k - \rho \nabla f(r^k);$$

$$x_1 = prox_\rho(2\lambda \|\Psi^k x\|_1)(x_g);$$

$$x_2 = prox_\rho(2\beta \cdot TGV_\alpha^2(x))(x_g);$$

$$x^k = \frac{x_1 + x_2}{2};$$

$$t^{k+1} = \frac{1 + \sqrt{1 + 4(t^k)^2}}{2};$$

$$r^{k+1} = x^k + \frac{t^k - 1}{t^{k+1}}(x^k - x^{k-1});$$

**UNTIL**  $k > K$  **OR**  $\frac{\|x^{k-1} - x^k\|_2}{\|x^k\|_2} < \eta$

---

### 3.3 Experiments and results

#### 3.3.1 Experimental setup

To evaluate the performance of the proposed method, the MR images of size  $256 \times 256$  from [Huang *et al.*, 2011b, Chen *et al.*, 2014] were used, as shown in Fig. 3.2 (b)-(e). In Fig. 3.2 (a), is shown the k-space sampling mask where the k-space data is sampled with a rate of 15% (i.e. keeping 15% of the complete k-space data) using variable density undersampling pattern [Lustig *et al.*, 2007]. The proposed method was also compared with existing state of the art CS-MRI methods based on the commonly used sparsifying transforms, including the SparseMRI [Lustig *et al.*, 2007], FCSA [Huang *et al.*, 2011b], Framelet+NLT [Gopi *et al.*, 2014], Shearlet+TGV [Guo *et al.*, 2014]. For fair comparisons, all codes were downloaded from the authors' website and the corresponding experimental setup was carefully followed.

The observation measurement  $b$  was modeled as  $b = F_u x + \varepsilon$ , where  $\varepsilon$  represents complex Gaussian white noise with standard deviation  $\sigma_n$ . The associated input SNR (ISNR) [Carrillo *et al.*, 2012] is defined as  $ISNR = 20 \log_{10} \left( \frac{\sigma_x}{\sigma_n} \right)$ , with  $\sigma_x$  denoting the standard deviation of the original image. In the proposed method, the filter size of data-driven TF was set as  $8 \times 8$ ,

the regularization parameter  $\lambda$  in the soft-thresholding operator as  $0.1 \times \sigma_n$ , the regularization parameter  $\beta$  as 0.05, and the ISNR as 30 dB. Note that, in the proposed method, since the filter size of data-driven TF has non negligible influence on computation time, to assess the influence of filter size on reconstruction results, several filter sizes were tested, including  $2 \times 2$ ,  $4 \times 4$ ,  $8 \times 8$ ,  $10 \times 10$ ,  $16 \times 16$ .

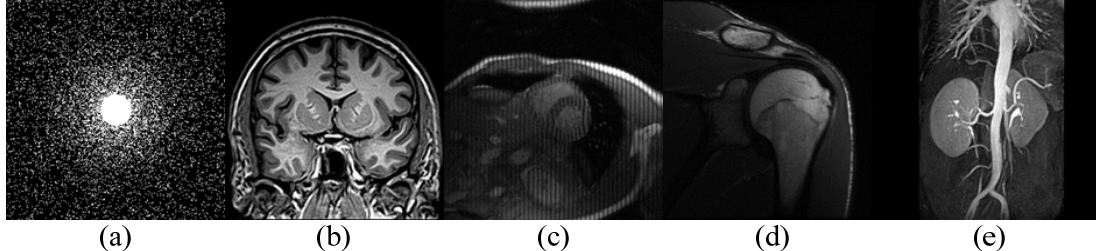


Fig. 3.2 k-space undersampling mask and MR images. (a) k-space sampling mask; (b) Coronal brain; (c) Cardiac; (d) Shoulder; (e) Renal arteries.

In addition to the visual assessment, three quantitative indices were calculated for the MR images reconstructed with different methods. They are the peak-signal-to-noise ratio (PSNR), relative l2 norm error (RLNE) [Qu *et al.*, 2012] and mean structural similarity (MSSIM) [Wang *et al.*, 2004]. PSNR and RLNE are widely used for measuring reconstruction accuracy, and MSSIM is used for evaluating the structural similarity between reconstructed and reference images.

The PSNR is defined as:

$$\text{PSNR} = 20 \log_{10} \left( \frac{\text{MAX}_x}{\sqrt{\text{MSE}}} \right) \quad (3.14)$$

here,  $\text{MSE} = \frac{1}{M \times N} \sum_{i=0}^{M-1} \sum_{j=1}^{N-1} [x_{ref}(i, j) - x_{rec}(i, j)]^2$ ,  $\text{MAX}_x$  is the maximum possible pixel value of the image, which is set to be 1 or 255.

The RLNE is given by:

$$\text{RLNE} = \frac{\|x_{ref} - x_{rec}\|_2}{\|x_{ref}\|_2} \quad (3.15)$$

where  $x_{ref}$  and  $x_{rec}$  denote the images reconstructed from respectively full and partial k-spaces.

The SSIM is defined as [Wang *et al.*, 2004]:

$$\text{SSIM}(x, y) = \frac{(2\mu_x\mu_y + C_1)(2\sigma_{xy} + C_2)}{(\mu_x^2 + \mu_y^2 + C_1)(\sigma_x^2 + \sigma_y^2 + C_2)} \quad (3.16)$$

where the parameters  $C_1$  and  $C_2$  are constants that avoid instability when the local means  $\mu_x$ ,  $\mu_y$  and local standard deviations  $\sigma_x$ ,  $\sigma_y$  are close to zero. The mean SSIM (MSSIM) is a single value that represents an overall quality measure of the entire image. The MSSIM values exhibit much better consistency with qualitative visual appearance [Wang *et al.*, 2004].

The experiments were performed on a PC computer with Intel (R) Core (TM) i5-2400 3.1GHz CPU, 4.00GB memory and Windows 7 SP1, MATLAB Version 7 platform.

### 3.3.2 Visual comparison

Fig. 3.3 to Fig. 3.6 show the visual comparison of the MR images reconstructed using different methods. The sampling ratio was set to be approximately 15%. It is seen that the proposed method provides more satisfying results with clear contours, sharp edges and fine image details.

More quantitatively, the PSNR, RLNE and MSSIM indices calculated for the MR images reconstructed with the different methods are given in Table 3-1 to Table 3-3. It can be observed that the proposed method improves the reconstruction performance in comparison with existing methods, by providing higher PSNRs, smaller RLNEs, and greater MSSIMs.

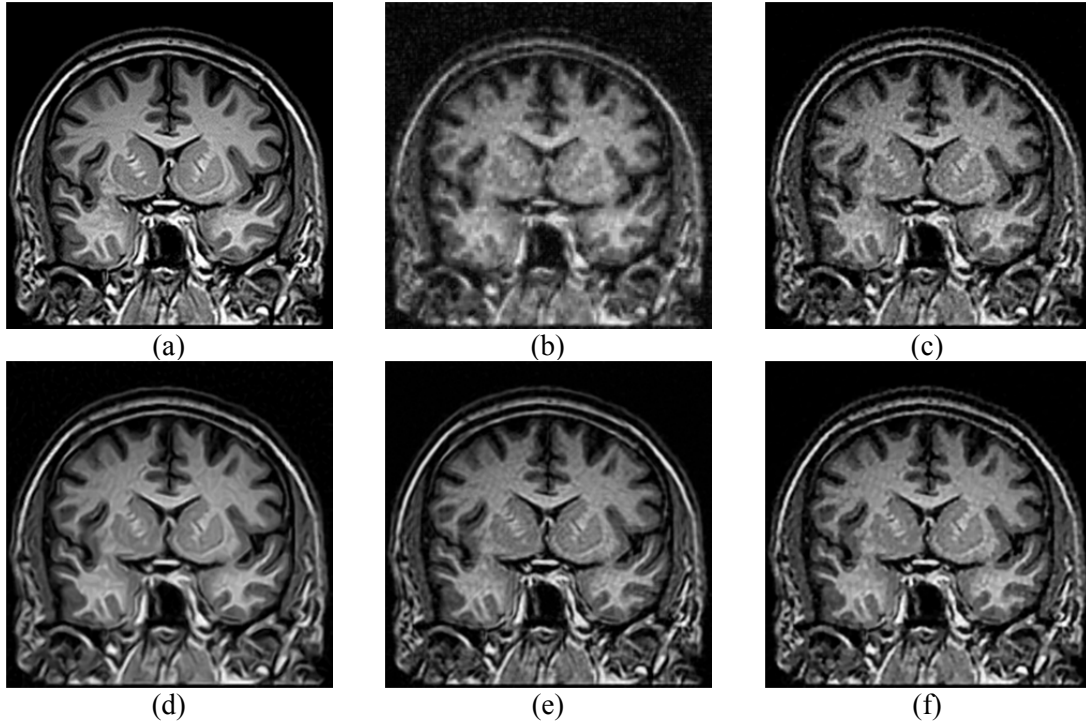


Fig. 3.3 Results of reconstruction on the coronal brain MR image using different methods with 15% sampling. (a) Original MR images. images reconstructed by (b) SparseMRI [Lustig *et al.*, 2007]; (c). FCSA [Huang *et al.*, 2011b]; (d) Framelet+NLTV [Gopi *et al.*, 2014]; (e) Shearlet+TGV [Guo *et al.*, 2014]; (f) data-driven TF+TGV (proposed).

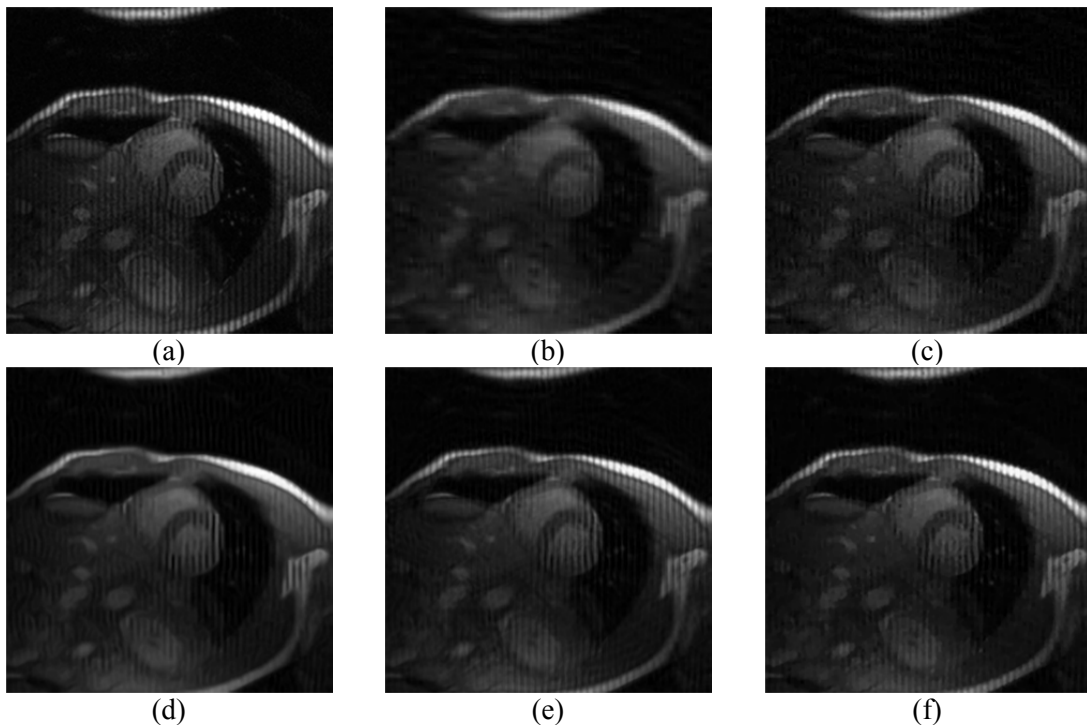


Fig. 3.4 Results of reconstruction on the cardiac MR image using different methods with 15% sampling. (a) Original MR images; images reconstructed using (b) SparseMRI [Lustig *et al.*, 2007]; (c). FCSA [Huang *et al.*, 2011b]; (d) Framelet+NLTV [Gopi *et al.*, 2014]; (e) Shearlet+TGV [Guo *et al.*, 2014]; (f) data-driven TF+TGV (proposed).

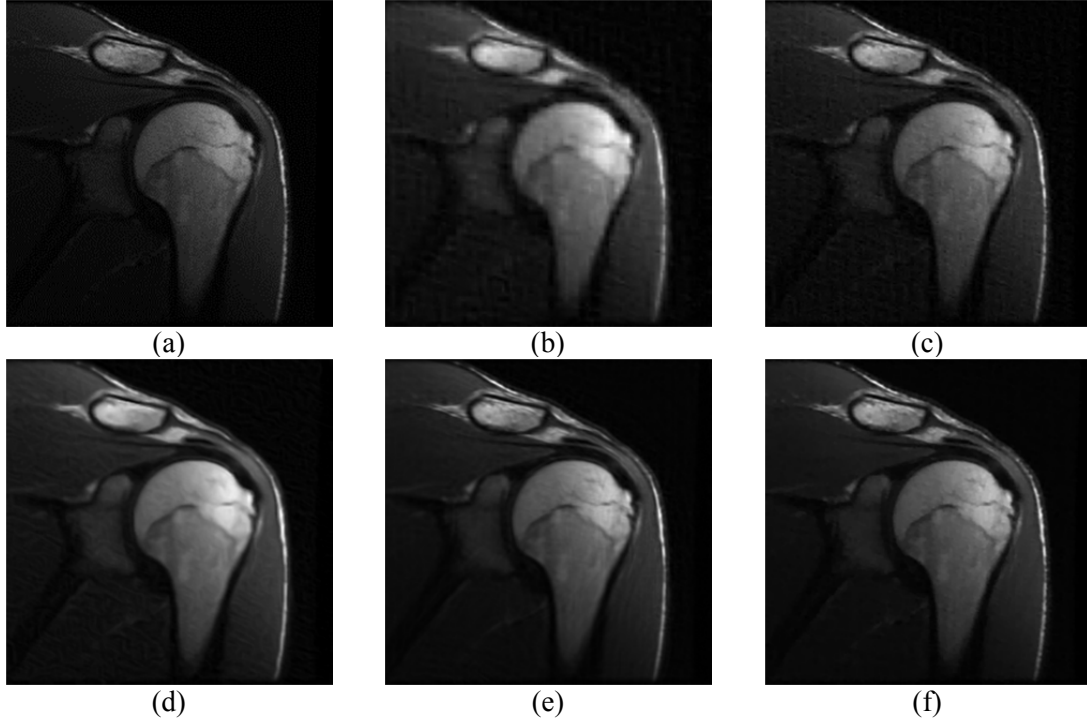


Fig. 3.5 Results of reconstruction on the shoulder MR image using different methods with 15% sampling. (a) Original MR images; images reconstructed using (b) SparseMRI [Lustig *et al.*, 2007]; (c). FCSA [Huang *et al.*, 2011b]; (d) Framelet+NLTV [Gopi *et al.*, 2014]; (e) Shearlet+TGV [Guo *et al.*, 2014]; (f) data-driven TF+TGV (proposed).

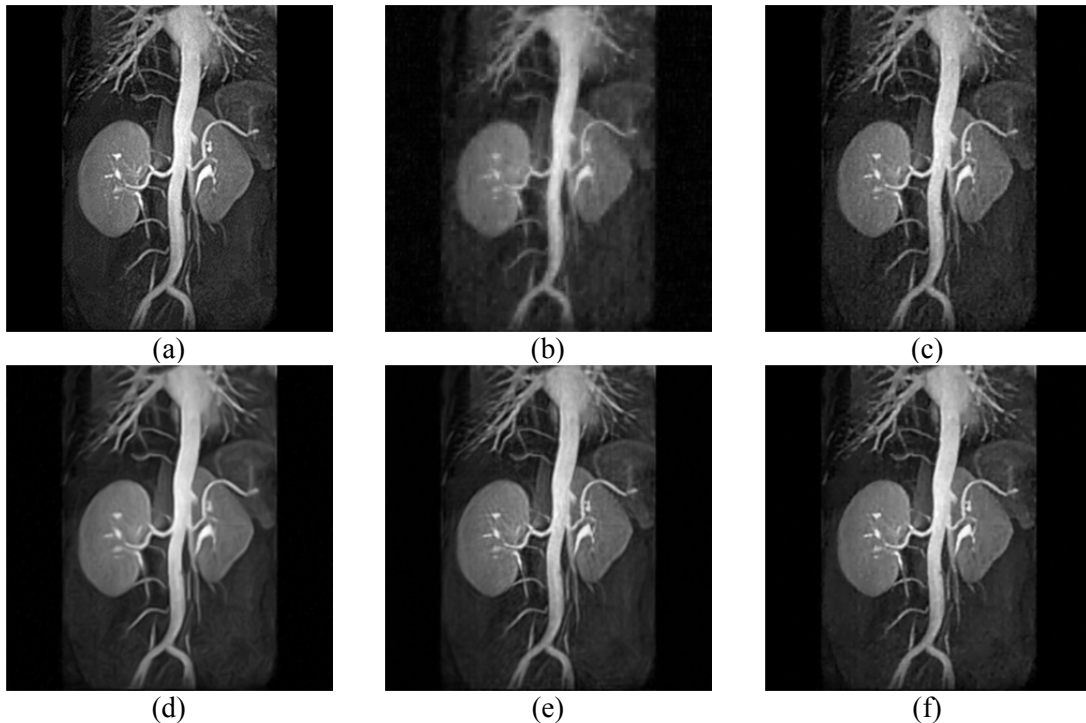


Fig. 3.6 Results of reconstruction on the renal arteries MR image using different methods with 15% sampling. (a) Original MR images; images reconstructed using (b) SparseMRI [Lustig *et al.*, 2007]; (c). FCSA [Huang *et al.*, 2011b]; (d) Framelet+NLTV [Gopi *et al.*, 2014]; (e) Shearlet+TGV [Guo *et al.*, 2014]; (f) data-driven TF+TGV (proposed).

Table 3-1 PSNR of reconstruction on MR images using different methods with 15% sampling.

	SparseMRI	FCSA	Framelet+NLTV	Shearlet+TGV	Proposed
Coronal Brain	20.79	26.07	26.25	27.21	<b>27.59</b>
Cardiac	30.08	32.44	31.25	33.60	<b>34.30</b>
shoulder	23.86	31.94	25.05	35.08	<b>38.27</b>
Renal arteries	26.97	32.21	32.34	33.46	<b>35.28</b>

Table 3-2 RLNE of reconstruction on MR images using different methods with 15% sampling.

	SparseMRI	FCSA	Framelet+NLTV	Shearlet+TGV	Proposed
Coronal Brain	0.26	0.14	0.14	0.13	<b>0.12</b>
Cardiac	0.19	0.15	0.17	0.13	<b>0.12</b>
shoulder	0.37	0.15	0.32	0.10	<b>0.07</b>
Renal arteries	0.16	0.09	0.09	0.08	<b>0.06</b>

Table 3-3 MSSIM of reconstruction on MR images using different methods with 15% sampling.

	SparseMRI	FCSA	Framelet+NLTV	Shearlet+TGV	Proposed
Coronal Brain	0.53	0.84	0.85	0.87	<b>0.88</b>
Cardiac	0.75	0.80	0.79	0.84	<b>0.86</b>
shoulder	0.82	0.89	0.89	0.96	<b>0.97</b>
Renal arteries	0.58	0.88	0.88	0.89	<b>0.93</b>

### 3.3.3 Effects of sampling rates

In order to investigate the effects of sampling rate on MR image reconstruction, experiments were also performed with sampling rate varying from 10% to 50% (corresponding to 0.1~0.5 on the x-axis in the figures). The curves of PSNR, RLNE and MSSIM versus different sampling rates for all the MR images reconstructed with different methods are shown in Fig. 3.7 to Fig. 3.9. It can be seen that the proposed method almost always outperforms SparseMRI, FCSA, Framelet+NLTV and Shearlet+TGV for different MR image and different sampling rates. For example, as illustrated in Fig. 3.7 (a), Fig. 3.8 (a), and Fig. 3.9 (a) on the coronal brain MR image, the proposed method delivers higher PSNR and MSSIM and lower RLNE than the other methods. These results also imply that, for the same image reconstruction quality, the proposed method requires even fewer samples and as a result allows further shortening acquisition time.

### 3.3.4 Effects of filter size

The influence of filter size on reconstruction results are illustrated in Fig. 3.10 to Fig. 3.12. We observe that the reconstruction performance (PSNR, RLNE and MSSIM) of the proposed method on different images changed little when the filters size was larger than  $2 \times 2$ . This means that the proposed method is little sensitive to the filter size.

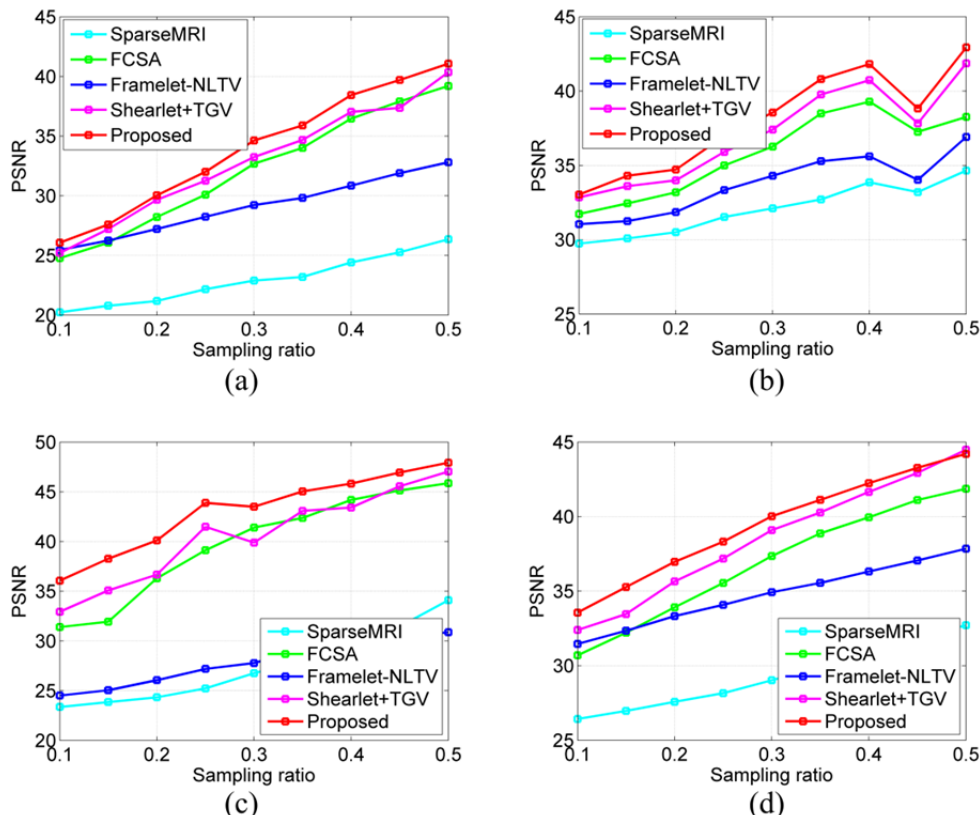


Fig. 3.7 Comparison of PSNR as a function of sampling rate on different MR images. (a) Coronal brain image. (b) Cardiac image. (c) Shoulder image. (d) Renal arteries image.

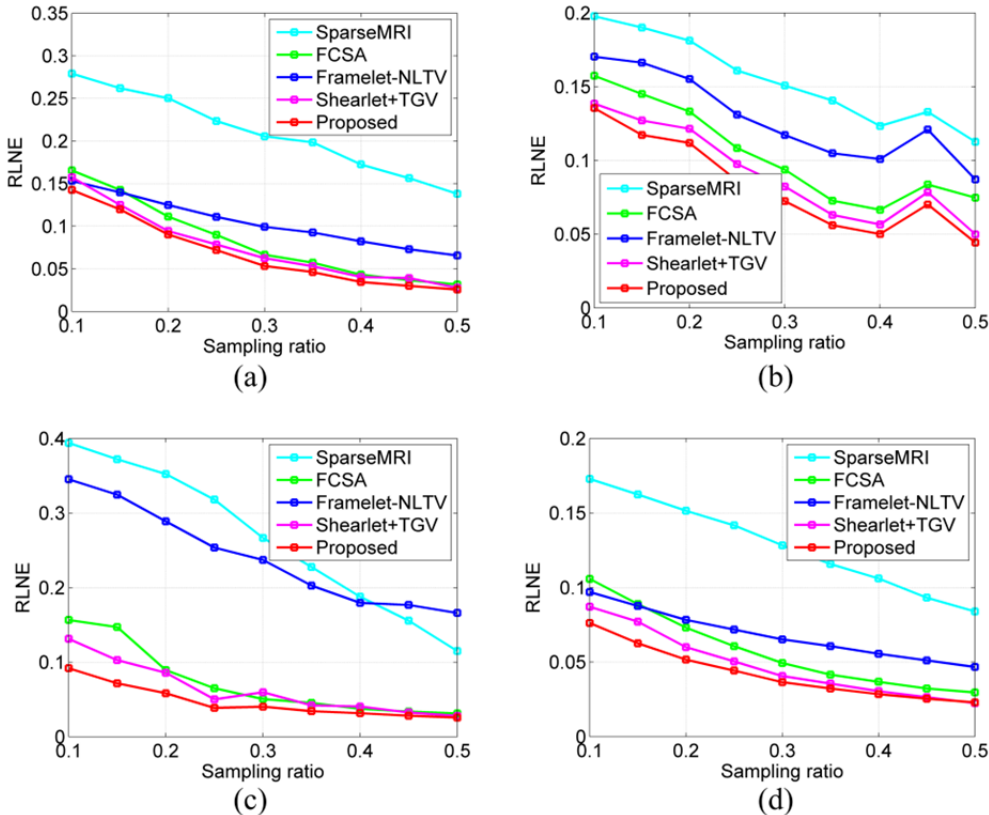


Fig. 3.8 Comparison of RLNE as a function of sampling rate on different MR images. (a) Coronal brain image. (b) Cardiac image. (c) Shoulder image. (d) Renal arteries image.

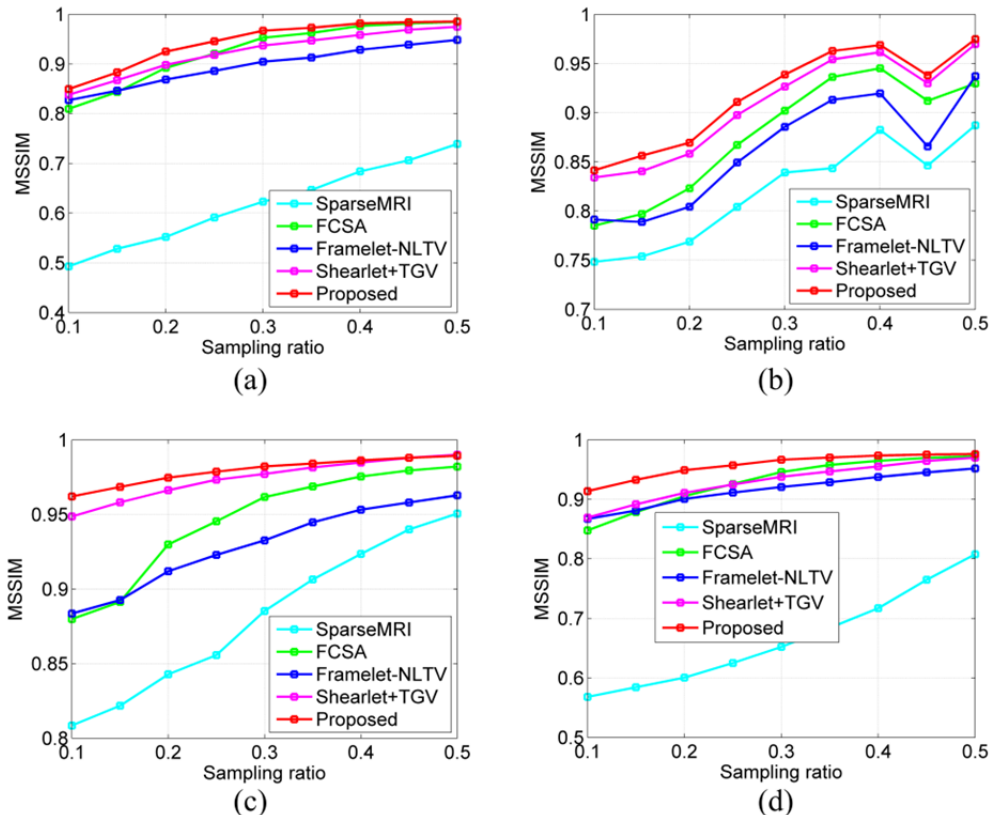


Fig. 3.9 Comparison of MSSIM as a function of sampling rate on different MR images. (a) Coronal brain image, (b) Cardiac image; (c) Shoulder image. (d) Renal arteries image.

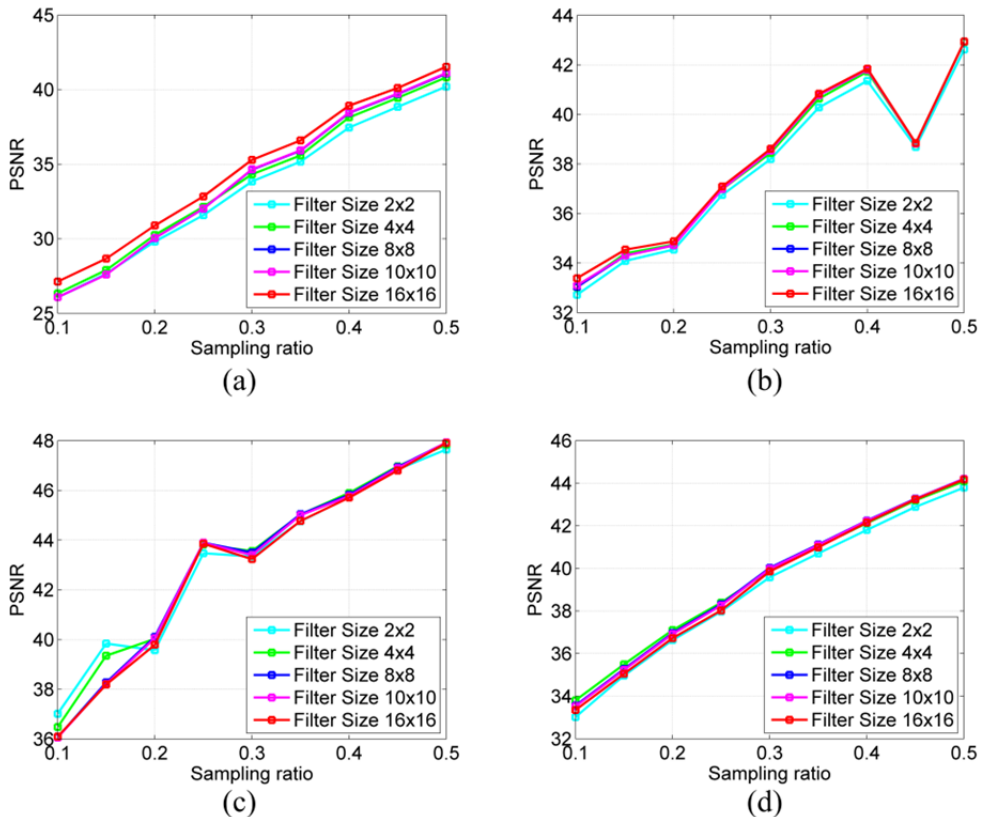


Fig. 3.10 Comparison of PSNR curves with different filters size. (a) Coronal brain image, (b) Cardiac image, (c) Shoulder image. (d) Renal arteries image.

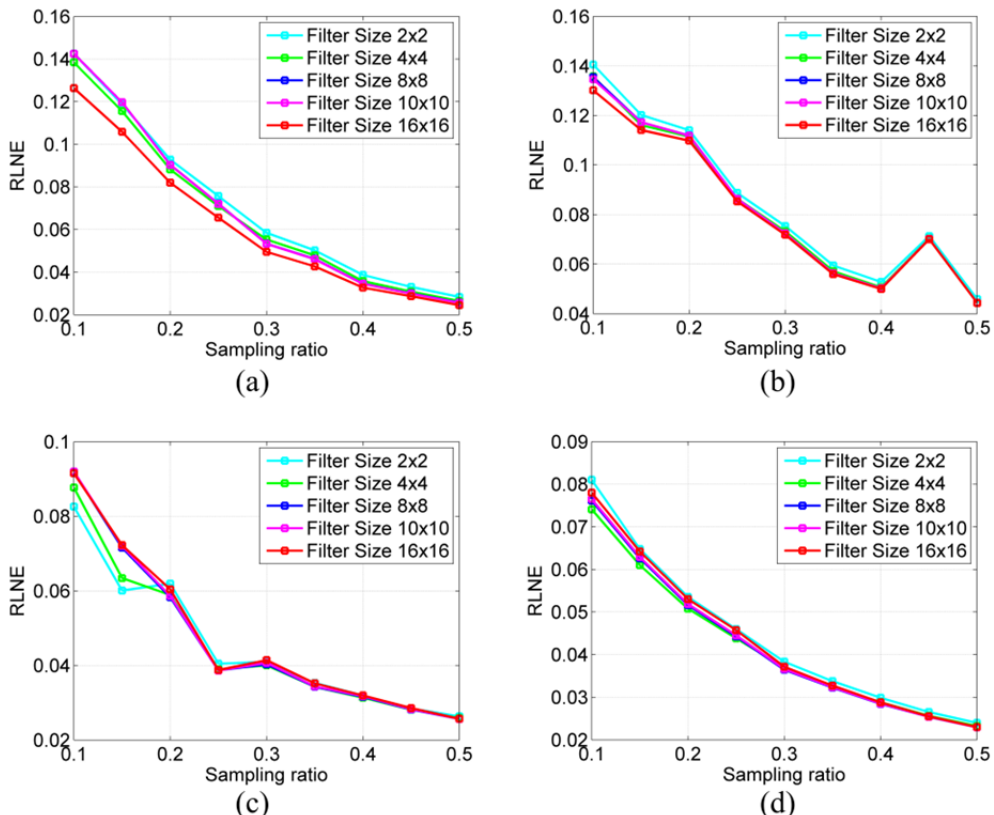


Fig. 3.11 Comparison of RLNE curves with different filters size. (a) Coronal brain image, (b) Cardiac image, (c) Shoulder image. (d) Renal arteries image.

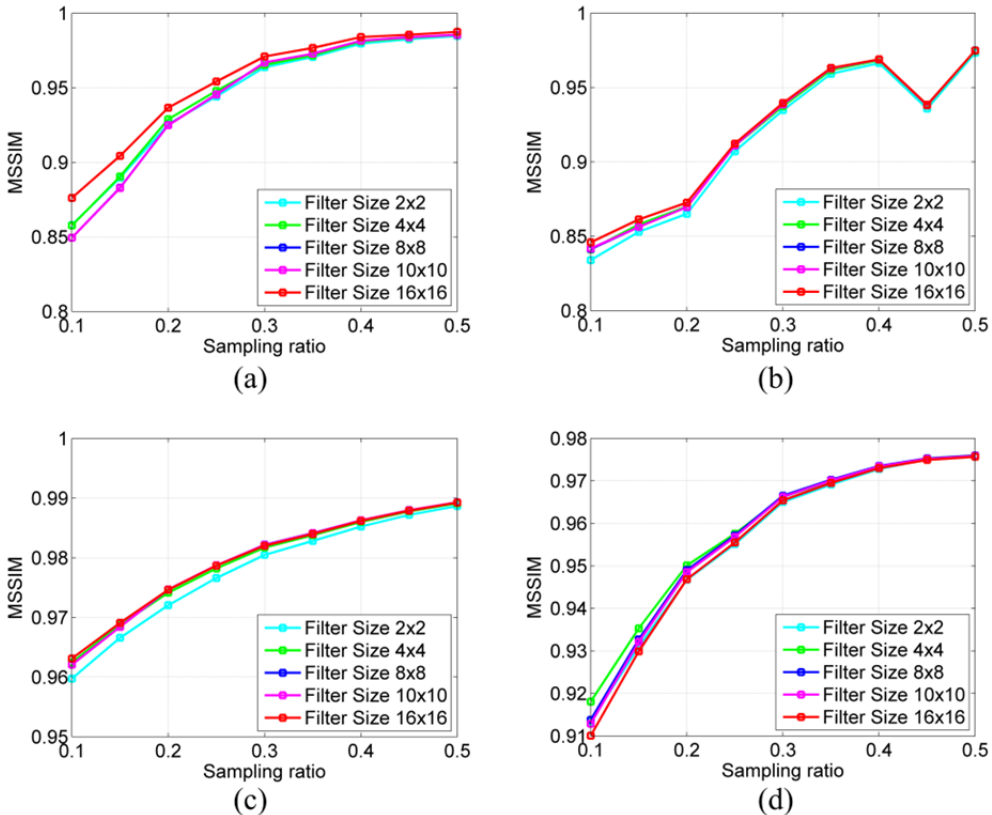


Fig. 3.12 Comparison of MSSIM curves with different filters size. (a) Coronal brain image. (b) Cardiac image. (c) Shoulder image. (d) Renal arteries image.

### 3.3.5 Computation time

Concerning computation time, the comparison between the proposed method and the other methods is given in Table 3-4 with a sampling ratio of 10%. It can be clearly seen that the FCSA method is the fastest among the four methods, and the proposed method takes the longest time. Moreover, the computation time of the proposed method increases with the increase of the filter size.

Table 3-4 Comparison of computation time (in second) of different methods on different images with a sampling ratio of 10%

methods \ image	Coronal brain	Cardiac	Shoulder	Renal arteries
methods				
FCSA	6.2	5.9	5.9	5.2
SparseMRI	16.7	20.1	19.9	18.1
Shearlet+TGV	87.2	88.6	100.3	58.9
Framelet+NLT	291.0	288.7	291.8	292.3
Proposed (filters size 2×2)	491.2	491.3	491.4	490.1
Proposed (filters size 4×4)	1559.9	1565.5	1564.2	1567.8
Proposed (filters size 8×8)	6158.6	6172.6	6157.3	6153.0
Proposed (filters size 10×10)	9638.6	9662.9	9653.6	9639.6

### 3.4 Conclusion

We have proposed a CS method for reconstructing various types of MR images from highly undersampled k-space data. The method presents the particularity of combining the data-driven TF and TGV to form a new regularization approach, which has enabled us to adaptively generate a set of filters from the undersampled data, obtain a better sparse approximation of MR images, and avoid staircase effects commonly present in TV regularization. The experimental results demonstrated that the proposed method presents better performance than existing state of the art CS-MRI methods for various MR images by preserving edges, suppressing under-sampling artifacts, delivering higher PSNR and MSSIM and lower RLNE at a wide range of sampling rates from 10% to 50%. In the future work, it would be interesting to work on how to accelerate the computation time of the proposed method.

## Chapter 4

# Accelerated cardiac DTI based on CS using joint sparsity and low rank approximation

## Contents

---

Résumé en français.....	78
Abstract .....	79
4.1 Introduction.....	80
4.2 Proposed method .....	81
4.3 Experimental Results .....	84
4.3.1 <i>Simulated and real data</i> .....	84
4.3.2 <i>Evaluation criteria</i> .....	84
4.3.3 <i>Comparison with existing techniques</i> .....	85
4.3.4 <i>Simulation results</i> .....	85
4.3.5 <i>Real data</i> .....	87
4.3.6 <i>Compared with the repetition-reduced method</i> .....	90
4.4 Discussion .....	92
4.5 Conclusion .....	93

---

## Résumé en français

L'imagerie du tenseur de diffusion par résonance magnétique (DTMR), appelée également imagerie du tenseur de diffusion (DTI), a été largement utilisée pour étudier de manière nondestructive les structures de fibres des tissus biologiques. Cependant, DTI est connu pour souffrir du temps d'acquisition long, ce qui limite considérablement son application pratique et clinique. Ce chapitre propose un nouvel algorithme de reconstruction par acquisition comprimée (compressed sensing—CS) en utilisant conjointement la parcimonie et la déficience de rang pour reconstruire des images DTMR cardiaques à partir des données espace k fortement sous-échantillonnées. Les images pondérées en diffusion dans différentes directions sont tout d'abord empilées en colonnes pour former une matrice. Cette matrice est parcimonieuse dans la direction de ligne dans le domaine transformé et a un faible rang. Ces deux propriétés sont ensuite incorporées dans le cadre de la reconstruction CS. Le problème d'optimisation sous contrainte est résolu par une méthode rapide d'ordre premier. La méthode a été évaluée sur des images DTMR cardiaques à la fois simulées et réelles. Les résultats démontrent que l'approche proposée présente des erreurs de reconstruction plus faibles par rapport aux techniques de reconstruction existantes en termes des indices de DTI, tels que l'anisotropie fractionnelle (FA), la diffusivité moyenne (MD), l'angle transversal et l'angle d'hélice,

## Abstract

Diffusion tensor magnetic resonance (DTMR) imaging or diffusion tensor imaging (DTI) has been widely used to probe invasively biological tissue structures. However, DTI is known to suffer from long acquisition time, which greatly limits its practical and clinical use. This chapter proposes a new Compressed Sensing (CS) reconstruction method that employs joint sparsity and rank deficiency prior to reconstruct cardiac DTMR images from the undersampled k-space data. Diffusion weighted images acquired in different diffusion directions are firstly stacked as columns to form the matrix. Such matrix is row sparse in transform domain and also has a low rank. These two properties are then incorporated into the CS reconstruction framework. The underlying constrained optimization problem is finally solved by the first-order fast method. The experiments were carried out on both simulation and real human cardiac DTMR images. The results demonstrate that the proposed approach has lower reconstruction errors for DTI indices, including fractional anisotropy (FA), mean diffusivities (MD), transverse angle and helix angle, compared to the existing CS-DTMR image reconstruction techniques.

## 4.1 Introduction

The heart is one of the most important organ in the human body, which pumps blood and supplying oxygen and nutrients needed by the other parts of the body to maintain life. Cardiovascular diseases are still the leading cause of death worldwide, accounting for an estimated 30% of all deaths across the globe [Christodoulou *et al.*, 2014, Go *et al.*, 2014]. Thus, it is very critical to probe the micro-structure of the heart for both explaining the heart disease symptoms and investigating the effective therapy means. Diffusion tensor magnetic resonance (DTMR) imaging or diffusion tensor imaging (DTI) is an MRI technique that allows quantitative characterization of the geometry and organization of tissue microstructures [Basser *et al.*, 1994a;1994b]. It appears currently as a powerful tool and the only means to investigate noninvasively fiber architectures of the human heart [Le Bihan *et al.*, 2001, Tournier *et al.*, 2011, Froeling *et al.*, 2014, Naumova *et al.*, 2014]. However, DTI is known to suffer from long acquisition time to obtain high quality data (temporal and spatial resolution, signal-to-noise ratio (SNR)), which greatly limits its practical and clinical use for human heart imaging [Dou *et al.*, 2002, Dou *et al.*, 2003, Helm *et al.*, 2005b, Wu *et al.*, 2006]. Many attempts have been made in order to reduce the amount of data required and improve the SNR of diffusion signals as much as possible [Jiang *et al.*, 2005], like SNR enhancing joint reconstruction [Halder *et al.*, 2013] and parallel imaging [Bammer *et al.*, 2001, Bammer *et al.*, 2002, Jaermann *et al.*, 2004, Holdsworth *et al.*, 2009].

In recent years, Compressed Sensing (CS) has emerged as a new framework for reconstructing signals with high quality from less measurements than the traditional Shannon-Nyquist sampling theorem required [Candes *et al.*, 2006a, Candes *et al.*, 2006c, Donoho, 2006]. CS exploits sparsity or compressibility of signals in certain domain (pixel or transform domain), and combines the sampling and compression into a unified framework. To date, compressed sensing has been successfully applied in Biomedical Imaging and has shown great potential [Wang *et al.*, 2011], such as MRI [Lustig *et al.*, 2007, Lustig *et al.*, 2008], dynamic MRI [Bilen, 2013].

Inspired by the principles of CS, a constrained reconstruction technique based on a regularization framework to jointly reconstruct sparse sets of cardiac DTI data is proposed [Adluru *et al.*, 2007]. Rather than reconstructing images one by one and by taking into account the fact that the diffusion weighted (DW) images obtained at different gradient directions are often correlated, a distributed compressed sensing-based method was proposed in [Wu *et al.*, 2014], which exploits the joint sparsity property among DW images to obtain better reconstruction quality. Utilizing the inter-image correlation of DW images, combination of compressed sensing and parallel imaging can further improve acquisition efficiency [Shi *et al.*, 2014]. In addition, the DW images are stacked as column vectors of a matrix; the resulting matrix is rank-deficient as well. CS-DTMR image reconstruction from undersampled k-space is then formulated as a low-rank matrix approximation problem [Hao Gao *et al.*, 2013]. Considering the situation that drastic phase changes across the DW directions, a phase-constrained low-rank (PCLR) approach was developed [Gao *et al.*, 2014]. On the other hand, model-based CS method for DTI was proposed in [Yanjie *et al.*, 2012, Welsh *et al.*, 2013], which uses the signal intensity model to directly estimate diffusion tensor fields from undersampled k-space data.

This chapter proposes a new CS reconstruction method that employs joint sparsity and rank deficiency prior for cardiac DTMR images reconstruction. DW images acquired at different gradient directions are firstly stacked as columns to form the matrix; such matrix is row

sparse in transform domain and also has a low rank. These two properties are then incorporated into the CS reconstruction framework. The underlying optimization problem is finally solved by the first-order fast method.

This chapter is organized as follows. Section 4.2 presents the proposed reconstruction method. The performance of the proposed method is assessed in Section 4.3 using both simulation and real human cardiac datasets. The discussions are presented in Section 4.4. Finally the conclusion is drawn in Section 4.5.

## 4.2 Proposed method

Assuming that  $x_l$  is a DW image with size  $m \times n$  and  $F_l^u$  is a partial Fourier transform for  $l$ th direction. Then the undersampled k-space data  $b_l$  of the DW image for each direction in k-space can be formulated as:

$$b_l = F_l^u x_l + \varepsilon_l \quad (4.1)$$

where,  $\varepsilon$  is the noise level, and diffusion direction  $l = 1, 2, \dots, L$ .

Since the DW images are correlated across the diffusion directions, each image  $x_l$  shares the same sparse support in the pixel or transform domain with other images. This means that when the different images are stacked as column vectors of matrix  $X$  (as shown in Eq.(4.2) ), the resulting matrix is row-sparse. Better reconstruction accuracy can be obtained when the joint sparsity property along diffusion directions is exploited [Wu *et al.*, 2014], which is to solve the optimization problem as shown in Eq.(4.3).

$$X_{mn \times L} = [x_1, x_2, \dots, x_L] = \begin{bmatrix} x_{1,1} & x_{1,2} & \cdots & x_{1,L} \\ x_{2,1} & x_{2,2} & \cdots & x_{2,L} \\ \vdots & \vdots & \ddots & \vdots \\ x_{mn,1} & x_{mn,2} & \cdots & x_{mn,L} \end{bmatrix} \quad (4.2)$$

$$\min \sum_{i=1}^N \|(\Phi X)_i\|_2 \quad \text{s.t.} \quad \|F^u X - b\|_2 \leq \varepsilon \quad (4.3)$$

where  $i$  refers to the the  $i$ th row of coefficients matrix  $\Phi X$ , and

$$\begin{bmatrix} b_1 \\ \vdots \\ b_l \\ \vdots \\ b_L \end{bmatrix} = \begin{bmatrix} F_1^u & 0 & 0 & 0 & 0 \\ 0 & \ddots & 0 & 0 & 0 \\ 0 & 0 & F_l^u & 0 & 0 \\ 0 & 0 & 0 & \ddots & 0 \\ 0 & 0 & 0 & 0 & F_L^u \end{bmatrix} \begin{bmatrix} x_1 \\ \vdots \\ x_l \\ \vdots \\ x_L \end{bmatrix} \quad (4.4)$$

The Diffusion Weighted (DW) images are sparse/compressible in suitable domain, and also the DW images acquired at different gradient directions are correlated. In this study, we confirm that the data matrix  $X$  is not only row sparse but also is low-rank. The matrix  $X$  is low rank means that  $\text{rank}(X) \leq \min(mn, L)$ . The principle of the proposed approach as illustrated in Fig. 4.1.

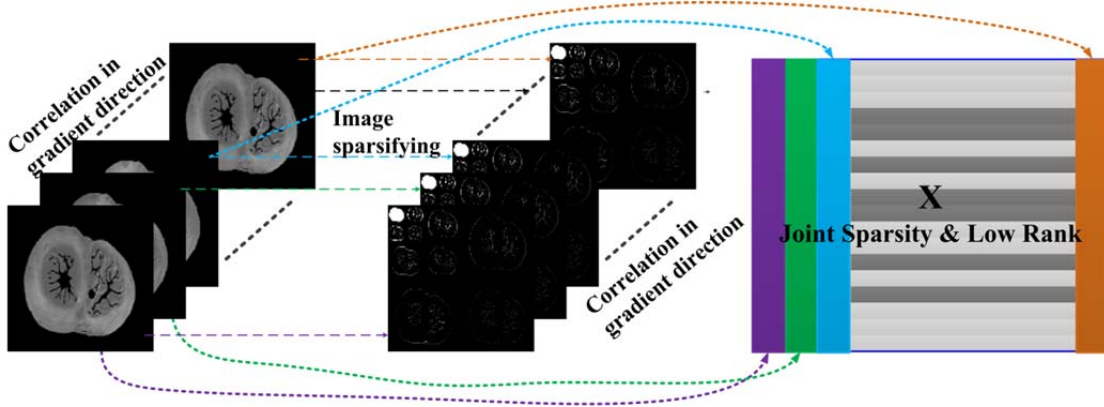


Fig. 4.1 Illustration the principle of the proposed approach.

This chapter proposes a new reconstruction method for DW images by combining row sparse and low rank prior properties of the data matrix  $X$  together. Consequently, the reconstruction can be described as the following optimization problem:

$$\hat{X} = \arg \min_{X} \left\{ \frac{1}{2} \|F^u X - b\|_2^2 + \alpha \cdot \|X\|_* + \beta \cdot \|\Phi X\|_{2,1} \right\} \quad (4.5)$$

here,  $\Phi$  is a sparsity transform, such as wavelet transform;  $\|\bullet\|_*$  is the nuclear norm, which is the best convex approximation of the rank function;  $\|\bullet\|_{2,1}$  refers to the  $l21$  norm of matrix  $\Phi X$ , which is the  $l2$  norm computed over the rows and then applying the  $l1$  norm to the resulting vector;  $\alpha > 0$  and  $\beta > 0$  are two positive regularization parameters, respectively.

The Eq.(4.5) can be solved by the variable splitting and alternating minimization scheme. An auxiliary variable  $S$  is introduced and let  $S = \Phi X$ ; then, the Eq.(4.5) can be rewritten as:

$$\hat{X} = \arg \min_{X} \left\{ \frac{1}{2} \|F^u X - b\|_2^2 + \alpha \cdot \|X\|_* + \beta \cdot \sum_{i=1}^{mn} \|S_i\|_2 + \gamma \|S - \Phi X\|_2^2 \right\} \quad (4.6)$$

where  $S_i$  is the  $i$ th row of coefficients matrix.

This optimization problem can be solved using alternating minimization scheme, namely solve  $S$ -subproblem and  $X$ -subproblem, respectively.

First, for a fixed  $X$ , solve:

$$\begin{aligned} \hat{S} &= \arg \min_S \left\{ \beta \cdot \sum_{i=1}^{mn} \|S_i\|_2 + \gamma \|S - \Phi X\|_2^2 \right\} \\ &= \arg \min_S \left\{ \frac{1}{2} \|S - \Phi X\|_2^2 + \frac{\beta}{2\gamma} \cdot \sum_{i=1}^{mn} \|S_i\|_2 \right\} \end{aligned} \quad (4.7)$$

the optimal solution of this sub-problem can be obtained through the proximal operator with  $l21$  norm [Kowalski *et al.*, 2013].

Then, solve  $X$ -subproblem as follow:

$$\hat{X} = \arg \min_X \left\{ \frac{1}{2} \|F^u X - b\|_2^2 + \alpha \cdot \|X\|_* + \gamma \|S - \Phi X\|_2^2 \right\} \quad (4.8)$$

This problem can be effectively solved using the Fast Iterative Shrinkage Thresholding Algorithm (FISTA) introduced in [Beck *et al.*, 2009b]. Specifically, let

$f(X) = \frac{1}{2} \|F^u X - b\|_2^2 + \gamma \|S - \Phi X\|_2^2$ , which is a convex and smooth function with the Lipschitz constant  $L_f$ ,  $g(X) = \alpha \cdot \|X\|_*$  is convex but non-smooth functions. Then, the  $X$  subproblem can be solved by a proximal mapping operation according to FISTA:

$$\text{prox}_\rho(\phi)(x) = \arg \min_u \left\{ \phi(u) + \frac{1}{2\rho} \|u - x\|_2^2 \right\} \quad (4.9)$$

where  $\rho$  is the inverse of the Lipschitz constant  $L_f$  of  $\nabla f$ , and  $\nabla f$  is denoted as [Beck et al., 2009b]:

$$\begin{aligned} \nabla f &= \left( \frac{1}{2} \|F^u X - b\|_2^2 + \gamma \|S - \Phi X\|_2^2 \right)' \\ &= (F^u)^T (F^u X - b) + \frac{\gamma}{2} \Phi^T (\Phi X - S) \end{aligned} \quad (4.10)$$

where  $(F^u)^T$  indicating the inverse partial Fourier transform.

The outline of the proposed method for problem (4.5) is detailed as follows.

**INPUT:**

$K$  : the maximum number of iterations;

$\alpha, \beta, \gamma$  : the regularization parameters;

$tol$  : the tolerance parameter.

**INIT:**  $\rho = 1/L, t^1 = 1, X^0 = r^1 = 0, k = 0$ ;

**OUTPUT:**

$\widehat{X}$  : the reconstructed DW images.

**REPEAT:**

$k = k + 1$ ;

$S^k = \text{prox}_\rho(2\beta \|\Phi X\|_{2,1})(x_g)$ ;

$x_g = r^k - \rho \nabla f(r^k)$ ;

$X^k = \text{prox}_\rho(2\alpha \|X\|_*)(x_g)$ ;

$t^{k+1} = \frac{1 + \sqrt{1 + 4(t^k)^2}}{2}$ ;

$r^{k+1} = X^k + \frac{t^k - 1}{t^{k+1}} (X^k - X^{k-1})$ ;

**UNTIL**  $k > K$  **OR**  $\frac{\|X^{k-1} - X^k\|_2}{\|X^k\|_2} < tol$ .

## 4.3 Experimental Results

### 4.3.1 Simulated and real data

The experiments were carried out on both simulated and real human cardiac DTMR datasets. Simulated DW images were generated as proposed in [Wang *et al.*, 2012], which using physical measurements from polarized light imaging (PLI) to generate realistic DW images at different diffusion gradient directions. Simulated DTI data were obtained with diffusion gradient directions applied in 42 directions. The real data concerns human heart and acquired with an image resolution of  $2.0 \times 2.0 \times 2.0 \text{ mm}^3$ , 12 diffusion gradient directions, slices 6, and repeated 6 times for averaging to enhance SNR. The simulated and real DW images were obtained with diffusion sensitivity  $b = 1000 \text{ s/mm}^2$ , and the image size of  $128 \times 128$ . The k-space was undersampled using the variable density undersampling pattern [Lustig *et al.*, 2007].

### 4.3.2 Evaluation criteria

In DTI, the diffusion tensor  $D$  was used to describe the diffusion properties in each voxel, which is a  $3 \times 3$  symmetric and positive definite matrix. There are many measure indices derived from the diffusion tensor  $D$  to characterizing the water molecule diffusion quantitatively [Basser *et al.*, 1996, Pierpaoli *et al.*, 1996]. Mean diffusivity (MD) and Fractional anisotropy (FA) are two quantitative parameters commonly used in a clinical setting to assessing tissue microstructure, which characterize the mean diffusivity and regarding the diffusion anisotropy, respectively. The FA and MD are defined as follow:

$$\text{MD} = \frac{\lambda_1 + \lambda_2 + \lambda_3}{3} \quad (4.11)$$

$$\text{FA} = \sqrt{\frac{3 \cdot [(\lambda_1 - \text{MD})^2 + (\lambda_2 - \text{MD})^2 + (\lambda_3 - \text{MD})^2]}{2 \cdot (\lambda_1^2 + \lambda_2^2 + \lambda_3^2)}} \quad (4.12)$$

On the other hand, for determin the orientation of a fiber, the helix angle (HA) (also called the inclination angle or fiber angle) and the transverse angle (TA) are among the most widely used, which can be derived from the eigensystem of diffusion tensor  $D$ . The HA was defined as the angle between the projection of the primary eigenvector onto the tangent plane and the imaging plane, and the TA was defined as the angle between the projection of the primary eigenvector onto the imaging plane and the tangent plane [Streeter *et al.*, 1969, Scollan *et al.*, 1998, Chen *et al.*, 2003].

In this chapter, the root mean square errors (RMSE) of FA, MD, TA and HA were calculated to evaluate and compare the reconstruction performance. The RMSE defined as:

$$\text{RMSE} = \sqrt{\frac{\|\text{vec}(x_{\text{rec}}) - \text{vec}(x_{\text{ref}})\|_2^2}{N}} \quad (4.13)$$

where,  $x_{\text{rec}}$  and  $x_{\text{ref}}$  denoted the reconstructed signal and reference signal,  $N$  is the total number of signal.

### 4.3.3 Comparison with existing techniques

To evaluate the performance of the proposed method, comparison was performed with several state of the art reconstruction methods, including the basic CS method [Huang *et al.*, 2011b] and joint sparsity method [Wu *et al.*, 2014]. Note that, the basis CS method was chosen total variation (TV) and discrete wavelet transform (DWT) regularization, which are widely used as sparsifying transforms for CS-MR image reconstruction [Lustig *et al.*, 2007, Huang *et al.*, 2011b]. The DW images were reconstructed one by one from the same undersampled data.

The observation measurement  $b$  is corrupted by complex Gaussian white noise  $\varepsilon$  with standard deviation  $\sigma_n$ . The latter is derived from the associated input SNR (ISNR) [Carrillo *et al.*, 2012], which is defined as:  $\text{ISNR} = 20 \log_{10} \left( \frac{\sigma_x}{\sigma_n} \right)$ , where  $\sigma_x$  denotes the standard deviation of the DW images.

The Daubechies wavelets with four decomposition levels are used; the regularization parameter  $\alpha$ ,  $\beta$ , and  $\gamma$  are set to 0.001, 0.0035 and 0.01, respectively.

### 4.3.4 Simulation results

Comparisons of the reconstruction performance between the four methods with sampling rates of 10%~50% for simulated human cardiac data are illustrated in Fig. 4.2. From the figures, it can be seen that the proposed method achieves better reconstructions with lower RMSE of FA and MD compared with other methods.

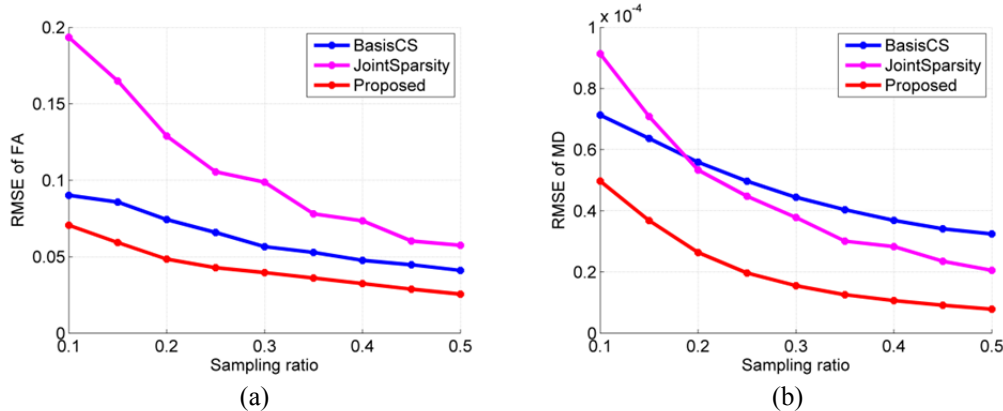


Fig. 4.2 Performance comparisons on simulated human heart data with ISNR 20dB. RMSE of (a) FA; (b) MD.

Table 4-1 qualitatively gives the RMSE of FA and MD using different methods on simulated human cardiac data with the sampling ratio of 25% (corresponds to the acceleration factor of 4) and ISNR 20dB.

Table 4-1 RMSE of FA and MD on simulated human cardiac data with sampling ratio 25% and ISNR 20dB (The unit of MD is  $\times 10^{-3} \text{ mm}^2/\text{s}$ ).

Methods	FA	MD
Basis CS	0.066	0.050
Joint Sparsity	0.105	0.045
Proposed	0.043	0.020

Fig. 4.3 shows the maps of FA and MD on simulated heart data with the sampling rate of 25% and ISNR 20dB. In these calculations, the involved diffusion tensors corresponding to the complete k-space were taken as the references. As shown in Fig. 4.3, the FA and MD maps with the proposed method are visually better than those obtained with other methods.

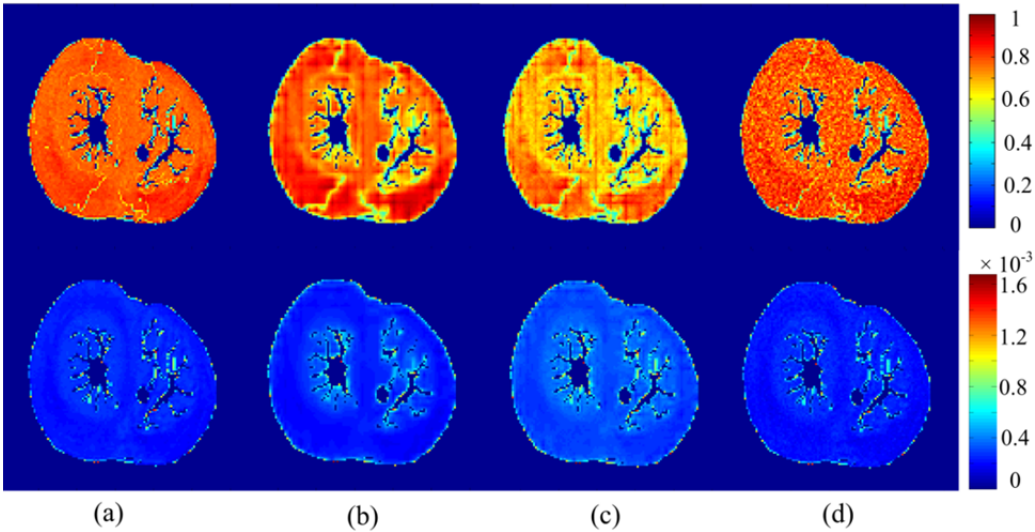


Fig. 4.3 Maps of FA (first row) and MD (second row) of the simulated human heart data with the sampling rate of 25% and ISNR 20dB. (a) Reconstruction from the complete k-space data; Reconstructions from undersampled k-space using (b) basis CS; (c) joint sparsity and (d) the proposed methods.

In Fig. 4.4, the RMSE of FA and MD of reconstructions from undersampled simulated DTI data using the proposed method with varied ISNRs and sampling ratio (R), are given. As illustrated in Fig. 4.4, the reconstruction performance of RMSE of FA and MD changing with the sampling ratio and ISNR. Increasing sampling ratio will reduce the reconstruction error RMSEs and reduce ISNR will increase the reconstruction error RMSEs. Fixed a sampling ratio, such as 25%, a better reconstruction performance can be obtained with higher ISNR.

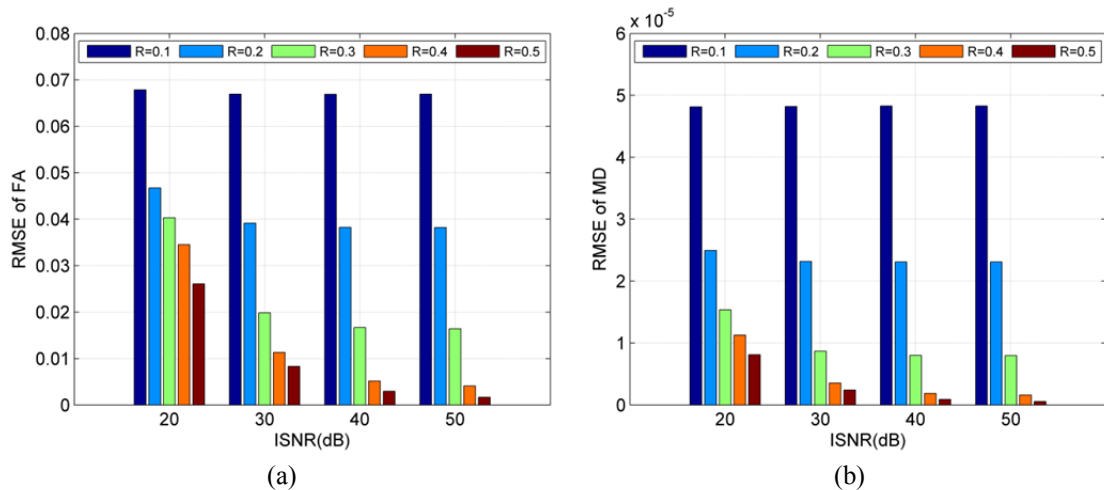


Fig. 4.4 RMSE of FA and MD of reconstructions from undersampled simulated human heart data using the proposed method with varied ISNRs and sampling ratio (R). (a) RMSE of FA; (b) RMSE of MD.

### 4.3.5 Real data

Fig. 4.5 and Fig. 4.6 shows the reconstruction errors (the mean RMSE of FA, MD, TA and HA) as a function of the sampling ratio (10%~50%) using three methods on real human cardiac data with ISNR 0dB and 30dB, respectively. From the figures, it can be observed that the proposed method achieves better reconstruction accuracy with lower mean RMSE of FA, MD, TA and HA compared with other methods on both ISNR 0dB and 30dB situation.

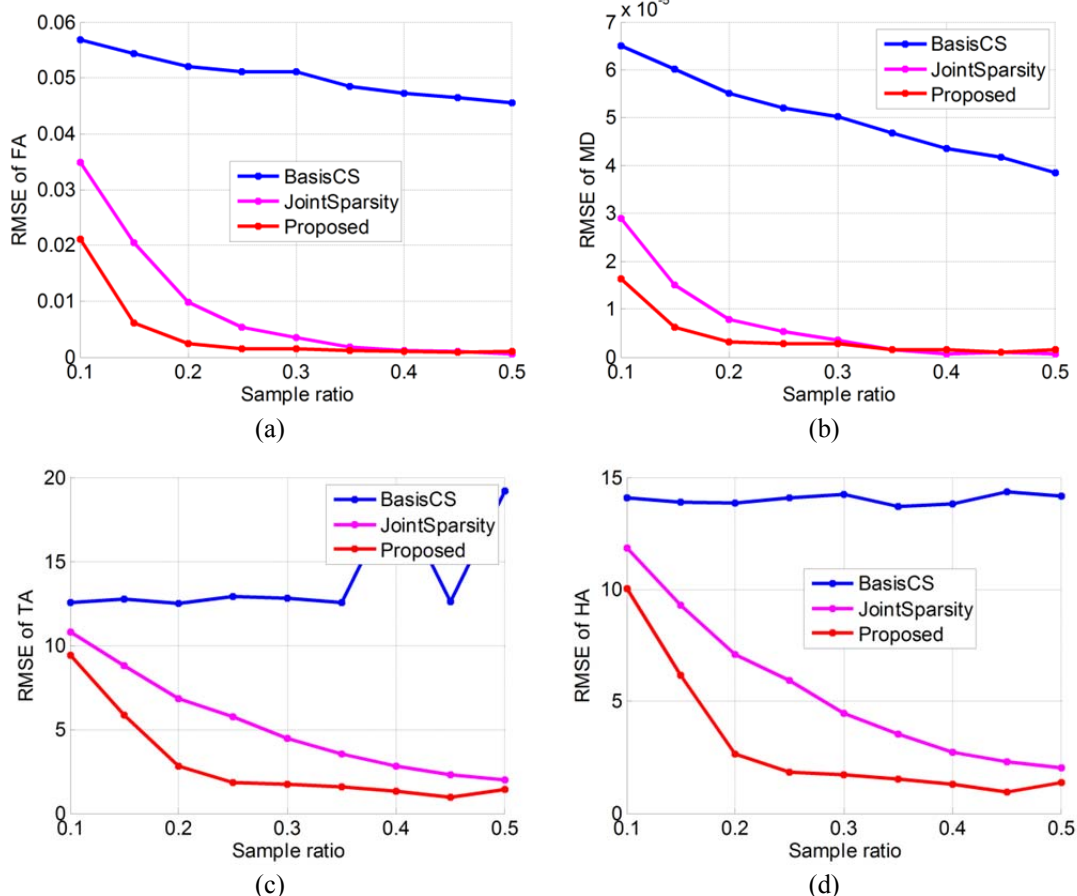
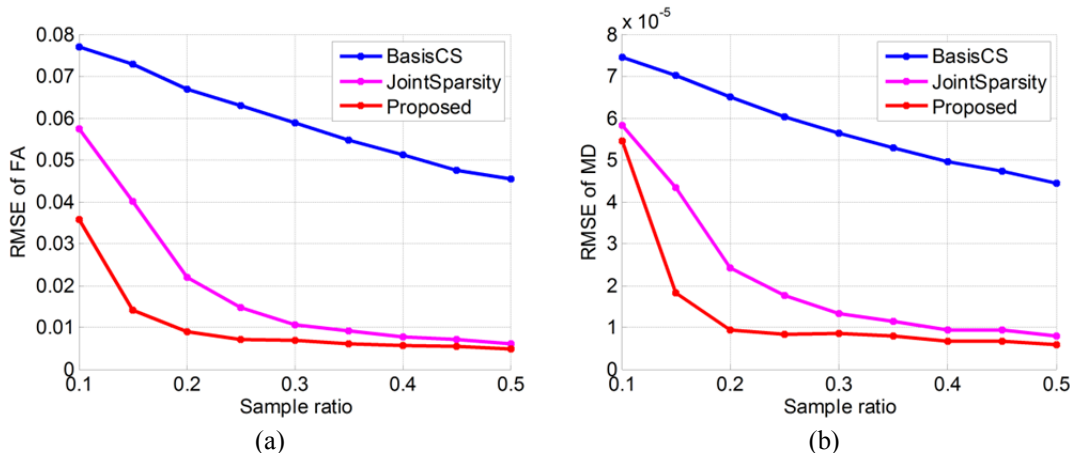


Fig. 4.5 Performance comparisons on real human heart data with different sampling rates and ISNR 0dB. (a) mean RMSE of FA; (b) mean RMSE of MD; (c) mean RMSE of TA; (d) mean RMSE of HA.



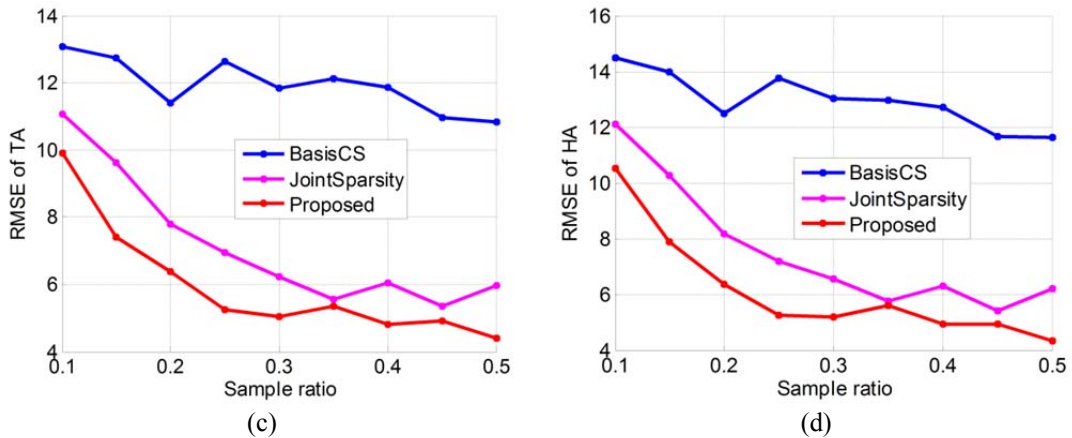


Fig. 4.6 Performance comparisons on real human heart data with different sampling rates and ISNR 30dB. (a) mean RMSE of FA; (b) mean RMSE of MD; (c) mean RMSE of TA; (d) mean RMSE of HA.

Table 4-2 quantitatively compares the mean RMSE of FA, MD, TA and HA using different methods on real human cardiac data with the sampling ratio of 25% and ISNR 0dB and 30dB, respectively.

Table 4-2 Comparative reconstruction performance of DTI indices (mean RMSE of FA, MD, TA and HA) on real human heart data with sampling ratio 25% (The unit of MD is  $\times 10^3 \text{ mm}^2/\text{s}$ ).

	ISNR = 0dB				ISNR = 30dB			
	FA	MD	TA( $^\circ$ )	HA( $^\circ$ )	FA	MD	TA( $^\circ$ )	HA( $^\circ$ )
Basis CS	0.051	0.052	12.894	14.083	0.063	0.060	12.635	13.761
Joint Sparsity	0.005	0.005	5.766	5.935	0.015	0.018	6.955	7.203
Proposed	0.001	0.003	1.832	1.826	0.007	0.008	5.249	5.240

Fig. 4.7 illustrated the reconstructed tensor fields obtained using the four methods (the basisCS, LowRank, JointSparsity and the Proposed) on real human cardiac data for slice 4 with sampling rates of 15% (approximation acceleration factors 6) and ISNR 30dB. The tensor fields are displayed as ellipsoids and colored according to the direction of their principal eigenvectors via DTI tensor viewer [Toussaint *et al.*, 2007].

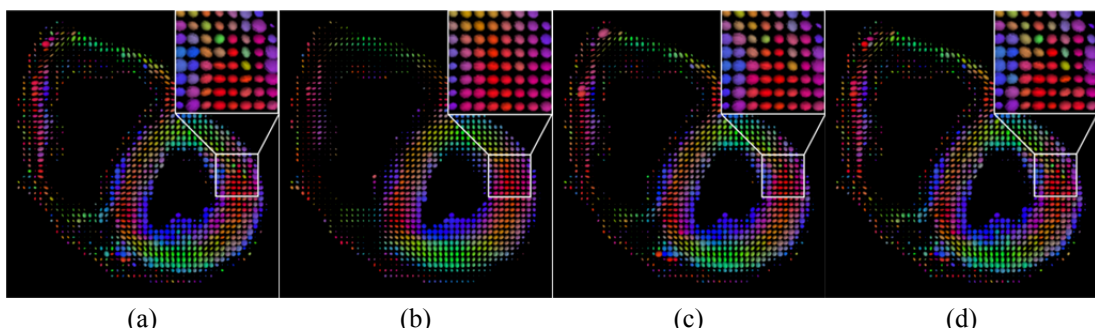


Fig. 4.7 The reconstruction tensor fields on real human heart data for slice 4 with sampling rates 15% and ISNR 30dB using the different methods. (a) Reconstruction from the complete k-space data with repeated 6 times; Reconstructions from undersampled k-space using (b) basis CS, (c) joint sparsity and (d) the proposed methods.

Obviously, the reconstructed tensor fields of the proposed method gives greater the visual effects and visually comparable with the references. The visual comparison show that the performance of the proposed method outperforms the other method.

Fig. 4.8 and Fig. 4.9 show the maps of FA, MD, TA and HA on real human heart data for slice 4 with the sampling rate of 25% and ISNR 0dB and 30dB, respectively. The diffusion tensors corresponding derived from the complete k-space were taken as the references (first column). From the figures, it can be seen that the reconstructed maps of DTI indices (FA, MD, TA and HA) with the proposed method are visually better than those obtained with other methods.

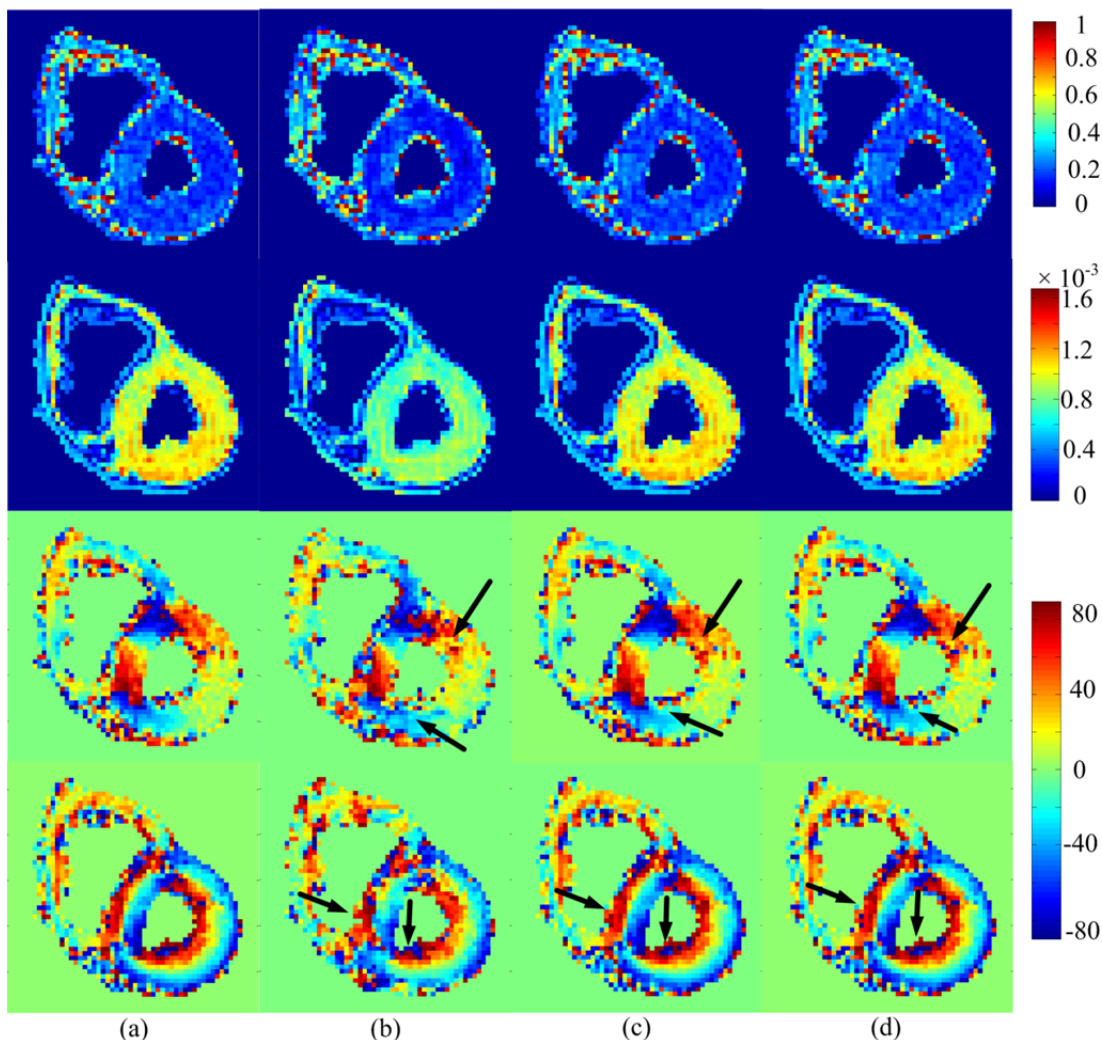


Fig. 4.8 Maps of FA (first row), MD (second row), TA(three row) and HA(four row) of the real human heart data on slice 4 with the sampling rate of 25% and ISNR 0dB. (a) Reconstruction from the complete k-space data (column one). Reconstructions from undersampled k-space using (b) basis CS (column two); (c) joint sparsity (column three) and (d) the proposed methods (column four).

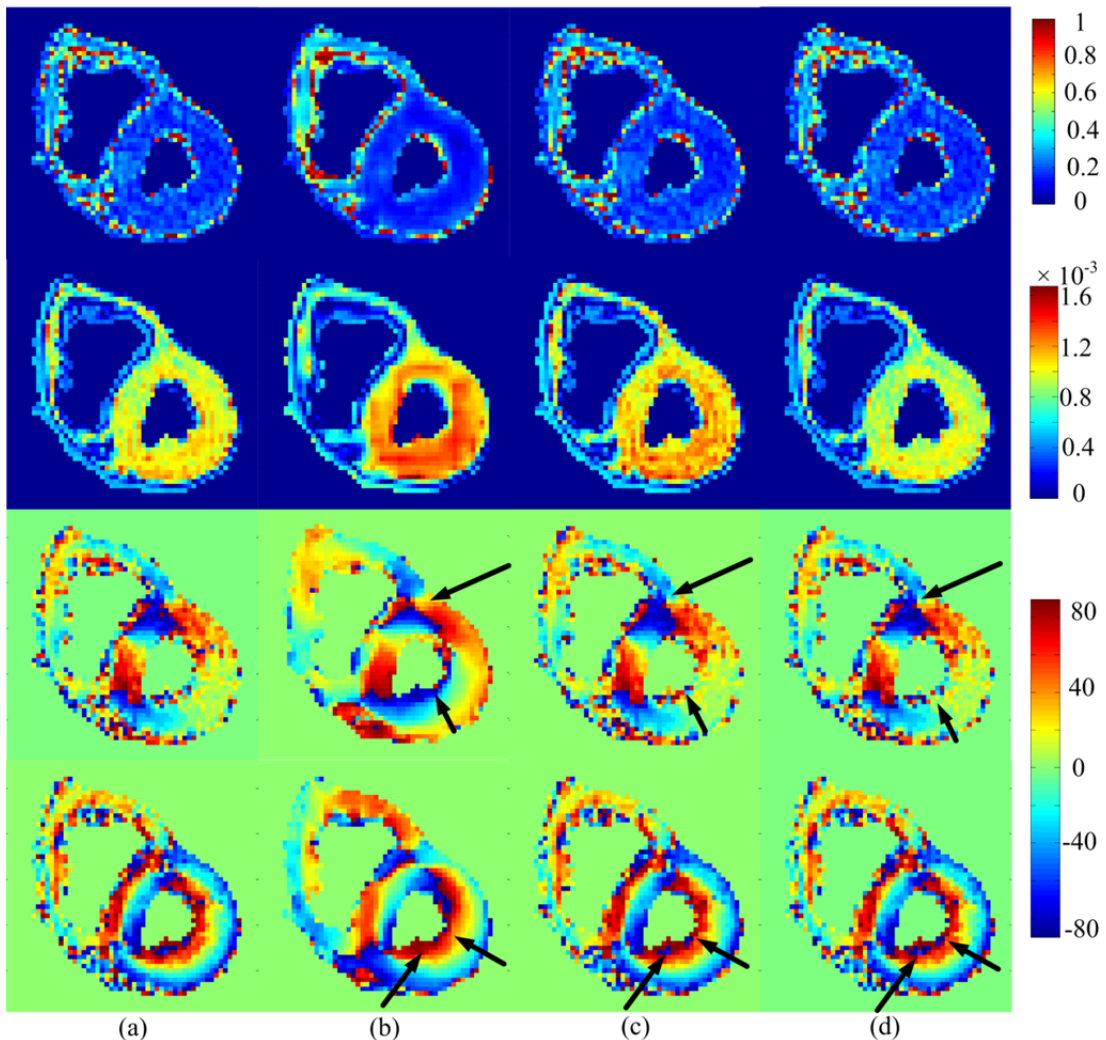


Fig. 4.9 Maps of FA (first row), MD (second row), TA(three row) and HA(four row) of the real human heart data on slice 4 with the sampling rate of 25% and ISNR 30dB. (a) Reconstruction from the complete k-space data (column one). Reconstructions from undersampled k-space using (b) basis CS (column two); (c) joint sparsity (column three) and (d) the proposed methods (column four).

#### 4.3.6 Compared with the repetition-reduced method

In Table 4-3 the reconstruction performance between the proposed and the repetition-reduced methods at varied acceleration factors with the ISNR 0dB and 30dB, are compared. The reconstruction using complete k-space and scan repeated 6 times data were taken as the gold standards. The table is revealing in several ways. First, the reconstruction accuracy increases with the reduce acceleration factor for proposed and scan repetition methods; second, the proposed method provides the better performance (RMSE of FA, MD, TA and HA) than the scan repetition-reduced method at different acceleration factor; last, the reconstruction accuracy of proposed method decreases with the reduce ISNR value (sample noise).

Fig. 4.10 gives a visual comparisons of results on maps of TA and HA.

Table 4-3 the RMSE of FA, MD, TA and HA, reconstruction using proposed method and scan repetition-reduced at different acceleration factors.

acceleration factor		ISNR = 0dB				ISNR = 30dB			
		FA	MD	TA(°)	HA(°)	FA	MD	TA(°)	HA(°)
Sampling ratio = 15%	≈6	0.006	0.006	5.860	6.159	0.014	0.018	7.418	7.895
Sampling ratio = 30%	≈3	0.001	0.003	1.729	1.720	0.007	0.008	5.055	5.204
Sampling ratio = 50%	≈2	0.001	0.002	1.393	1.385	0.005	0.006	4.388	4.329
Repetition = 1	≈6	0.053	0.043	16.148	17.020	0.053	0.043	16.148	17.020
Repetition = 2	≈3	0.036	0.026	15.545	16.265	0.036	0.026	15.545	16.265
Repetition = 3	≈2	0.026	0.018	15.108	15.441	0.026	0.018	15.108	15.441

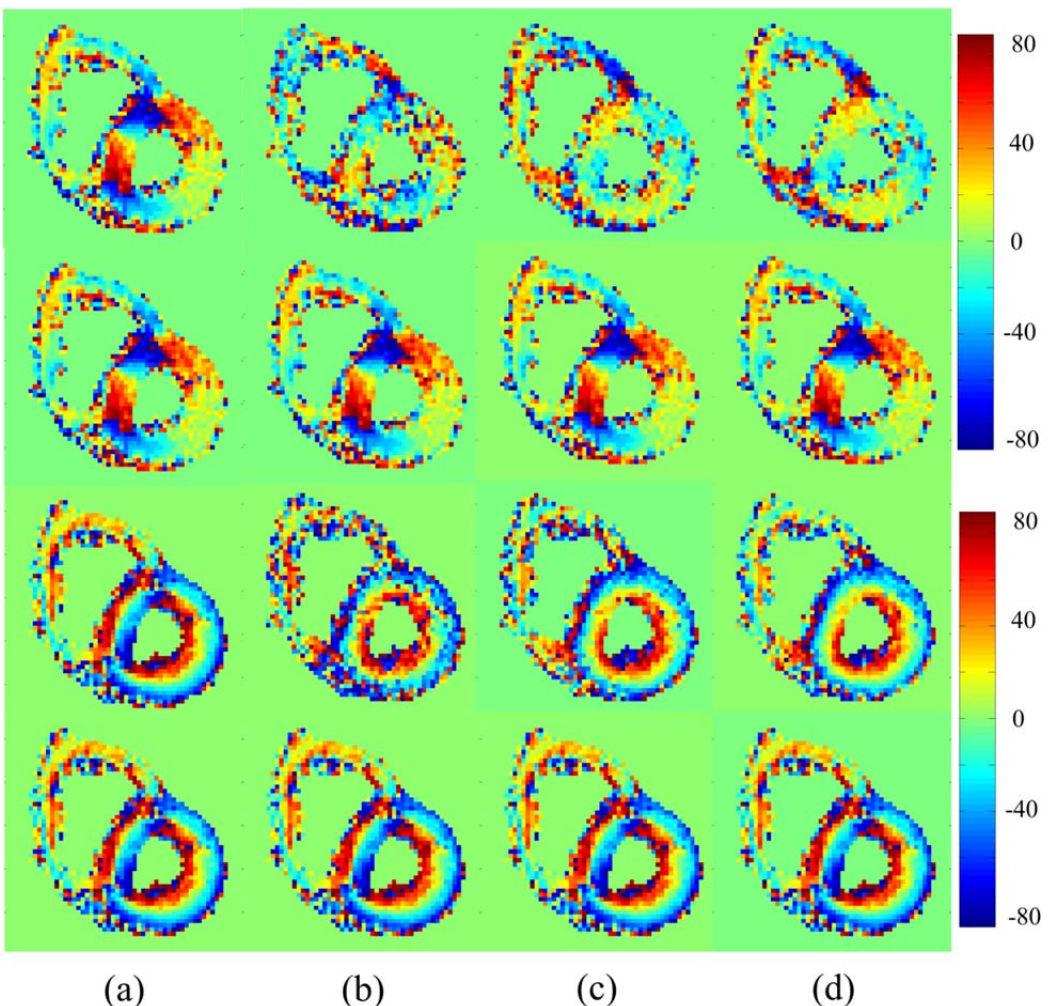


Fig. 4.10 Maps of TA (row first, second) and HA (row three, four) on the real human heart data for slice 4 with the ISNR 0dB. (a) Reconstruction from the complete k-space data with repeated 6 times (column one); (b)-(d) in second and fourth row is Reconstructions from undersampled k-space using with sampling ratio 15%, 30% and 50%, respectively; (b)-(d) in first and third row is reconstruction from complete k-space data with repeated 1, 2 and 3 times

Fig. 4.11 illustrated the reconstructed tensor fields using the proposed and the repetition-reduced methods at varied acceleration factors. The tensor fields are displayed as ellipsoids and colored according to the direction of their principal eigenvectors using DTI tensor viewer [Toussaint *et al.*, 2007]. The reconstructed tensor fields of the proposed method always obtains greater the visual effects on all acceleration factors and visually comparable with the references. At acceleration factors 6 (as shown in Fig. 4.11 (b), (e) and (h)), the tensor field of the repetition-reduced method is not arranged in order and is far worse than the references, whereas the proposed method can make the disordered tensor field more regular and the ellipsoids show shapes and colors more close to the reference on both ISNR 0dB and 30 dB.

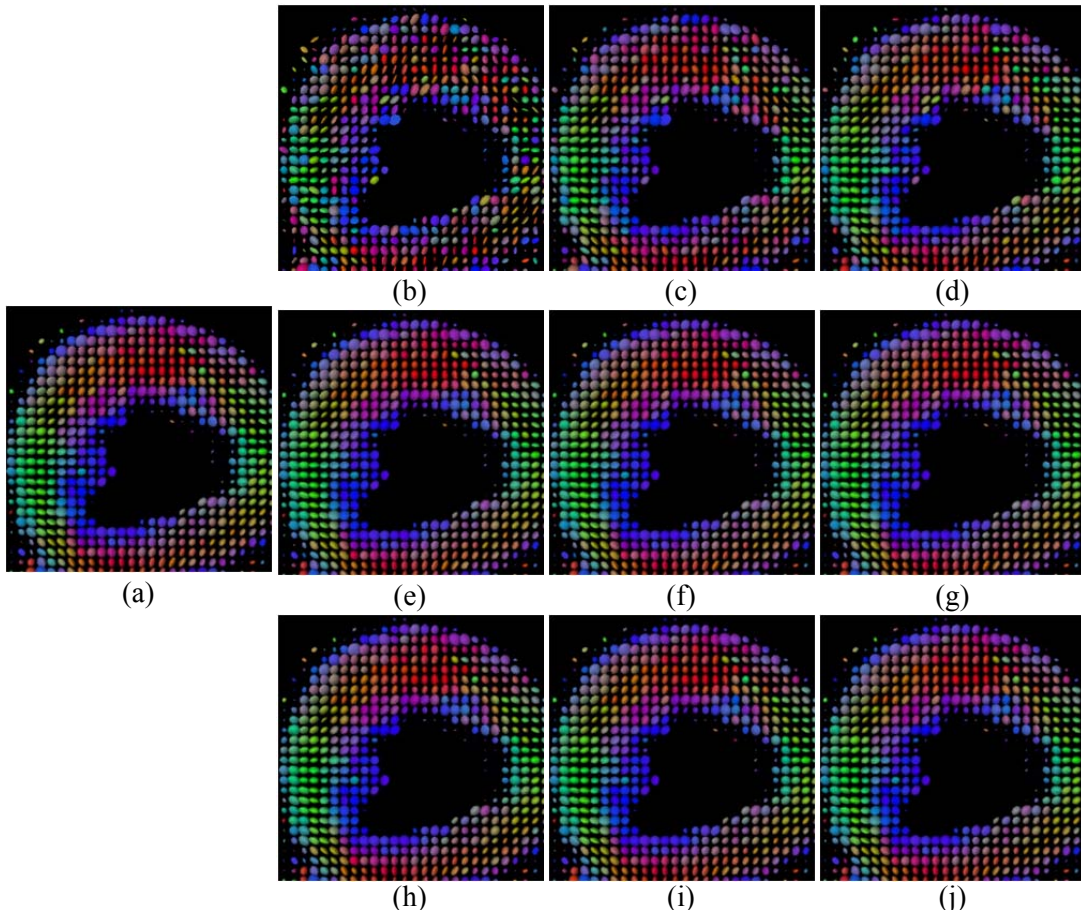


Fig. 4.11 The reconstruction tensor fields using the proposed and the repetition-reduced methods at varied acceleration factors. (a) Reconstruction from the complete k-space data with repeated 6 times; (b)-(d) Reconstruction from the complete k-space data with repeated 1, 2 and 3 times, respectively. Reconstructions from undersampled k-space with the sampling ratio 15%, 30% and 50%, respectively; (e)-(g) the ISNR 0dB; (h)-(j) the ISNR 30dB.

#### 4.4 Discussion

Simultaneous exploiting the joint sparsity and low rank properties among DW images gives better reconstruction quality for human heart diffusion tensor reconstruction. The experimental results show that the reconstruction accuracy (RMSE of DTI indices) of proposed method yields considerably superior results in comparison with the state-of-the-art reconstruction techniques. In this study, reconstruction performance was demonstrated with the different ISNR and sampling ratio. The reconstruction performance of proposed method decreases with the reduce measurement noise (ISNR), and increases with the sampling ratio (reduce acceleration factors).

As known, low signal-to noise ratio (SNR) is one of the most important issues in DTI. In practice, the additional signal averaging in forms of acquisition repetition is generally as a good way to increasing SNR. In Table 4-4, the reconstruction performance comparisons between the CS and the repetition-reduced methods are given. It is shown that the undersampling methods give better results. For a fixed acceleration factor, one way is to reduce repetition times while increasing the sampling ratio and another way is to increase repetition times while reducing sampling ratio. Table 4-4 gives some quantitative results at acceleration factors 6 estimated from the CS and the repetition-reduced or combination of both. These results demonstrated that increasing repetition times while reducing sampling ratio is a good way to achieve more accurate reconstruction for accelerating DTI.

Table 4-4 RMSE of FA, MD, TA and HA estimated from the proposed method and the scan repetition-reduced at acceleration factors 6

	ISNR = 0dB				ISNR = 30dB			
	FA	MD	TA(°)	HA(°)	FA	MD	TA	HA(°)
Repetition = 1 and Sampling ratio = 100%	0.053	0.043	16.148	17.020	0.053	0.043	16.148	17.020
Repetition = 2 and Sampling ratio = 50%	0.036	0.026	11.784	12.852	0.036	0.026	11.726	12.814
Repetition = 3 and Sampling ratio = 30%	0.026	0.018	10.381	11.345	0.026	0.019	10.400	11.420
Repetition = 6 and Sampling ratio = 15%	0.006	0.006	5.860	6.159	0.014	0.018	7.418	7.895

In this chapter, the regularization parameter  $\alpha$  and  $\beta$  was empirically chosen, it is not optimal. Many approaches have been introduced for optimal selection of the regularization parameter, such as the L-curve method [Hansen *et al.*, 1993]. In the future work, we will utilizes this method to estimate the optimized parameters. Although this method only for one parameter, but we can use an alternate strategy to select sub-optimal parameters.

## 4.5 Conclusion

This chapter proposed an efficient method for reconstructing DTMR images from undersampled k-space data using the compressed sensing. Based on the combined use of joint sparsity and low rank regularization together, the proposed method exploits simultaneously intra-image spatial redundancy and inter-image correlation across diffusion directions. The results on both simulated and real human cardiac DW images showed that the proposed method provides more accurate reconstructions and more accurate DTI indices compared with the state-of-the-art CS DTMR image reconstruction techniques.

## Chapter 5

### Accelerated cardiac DTI based on CS using low-rank and non-local TV constraint

#### Contents

---

Résumé en français.....	95
Abstract .....	96
5.1    Introduction.....	97
5.2    Methods .....	98
5.2.1 <i>Non local TV</i> .....	98
5.2.2 <i>CS-MRI reconstruction using NLTV</i> .....	99
5.2.3 <i>CS DT-MR image reconstruction using low rank and TV model</i> .....	103
5.3    Experimental Results .....	105
5.3.1 <i>Data and sampling pattern</i> .....	105
5.3.2 <i>Evaluation criteria</i> .....	106
5.3.3 <i>Comparison with existing techniques</i> .....	107
5.3.4 <i>Effects of sampling rates</i> .....	107
5.3.5 <i>Maps of FA and MD</i> .....	108
5.3.6 <i>Tensor fields visualization</i> .....	109
5.3.7 <i>Effects of regularization parameters</i> .....	109
5.4    Conclusion .....	110

---

## Résumé en français

L'imagerie du tenseur de diffusion (DTI) est une technique prometteuse pour étudier de manière invasive la structure des fibres du cœur. Cependant, le temps d'acquisition de cette technique est long. Afin de résoudre ce problème, nous proposons d'utiliser la théorie d'acquisition comprimée (compressed sensing—CS) avec la contrainte de rang faible et la régularisation par variation totale (TV) afin de reconstruire des images DTI cardiaques à partir des données k-espace fortement sous-échantillonnées. Deux régularisations TV sont considérées: TV locale (i.e. TV classique) et TV non locale (NLTВ). Le problème d'optimisation sous contrainte est résolu par une méthode rapide d'ordre premier. Les expérimentations sont effectuées sur des images pondérées en diffusion simulées et réelles. Les résultats montrent que les erreurs de reconstruction avec nos approches sont inférieures à celles produites par des méthodes de reconstruction CS-DTI existantes, en termes des indices du tenseur de diffusion, tels que l'anisotropie fractionnelle (FA) et diffusivité moyenne (MD).

## Abstract

Diffusion tensor imaging (DTI) is a promising imaging technique to investigate invasively the micro fiber structure of the heart. However, a great challenge of the technique is the long acquisition time. To cope with the problem, we propose to apply the compressed sensing (CS) scheme with the low rank constraint and total variation (TV) regularizations to reconstruct cardiac DTI images from highly undersampled k-space data. Two TV regularizations are considered: local TV (i.e. classical TV) and nonlocal TV (NLTV). The subsequent constrained optimization problem is solved by the first-order fast method. The experiments are carried out on both simulated and real human cardiac diffusion weighted (DW) images. The results demonstrate that the proposed approaches present lower reconstruction errors compared to existing CS-DTI images reconstruction techniques, in terms of DTI indices such as fractional anisotropy (FA) and mean diffusivities (MD).

## 5.1 Introduction

As mentioned in the preceding chapter, DTI is known to suffer from long acquisition time and worse image quality (spatial resolution, signal-to-noise ratio—SNR), which greatly limits its practical and clinical use for human heart imaging [Dou *et al.*, 2002, Dou *et al.*, 2003, Helm *et al.*, 2005b, Wu *et al.*, 2006]. Classical efforts of reducing the required amount of data and improving the SNR of diffusion signals include parallel imaging [Bammer *et al.*, 2001, Bammer *et al.*, 2002, Jaermann *et al.*, 2004, Holdsworth *et al.*, 2009], simultaneous multislice imaging [Filli *et al.*, 2015, Lau *et al.*, 2015], partial k-space reconstruction [Luo *et al.*, 2012], and filtered reduced-encoding projection-reconstruction [Jiang *et al.*, 2005]. But, these methods are not very suitable for highly undersampled k-space data.

In recent years, Compressed Sensing (CS) has emerged as a new framework for reconstructing signals with high quality from few measurements highly undersampled with respect to the traditional Shannon-Nyquist sampling theorem [Candes *et al.*, 2006a, Candes *et al.*, 2006c, Donoho, 2006]. CS exploits sparsity or compressibility of signals in certain domain (pixel or transform domain), and combines the sampling and compression into a unified framework. To date, CS has been successfully applied to conventional magnetic resonance (MR) images, such as anatomical MRI [Lustig *et al.*, 2007, Lustig *et al.*, 2008], diffusion MRI [Hao Gao *et al.*, 2013] and dynamic MRI [Bilen, 2013], and has shown great potential [Wang *et al.*, 2011]. But, relatively little work can be found in the use of CS approaches for DTI, and even less on human cardiac DTI.

Inspired by the principles of CS, a constrained reconstruction technique based on a regularization framework to jointly reconstruct sparse sets of cardiac DTI data is proposed [Adluru *et al.*, 2007]. Rather than reconstructing images one by one and by taking into account the fact that the diffusion weighted (DW) images obtained at different gradient directions are often correlated, a distributed compressed sensing-based method was proposed in [Wu *et al.*, 2014], which exploits the joint sparsity property among DW images to obtain better reconstruction quality. Utilizing the inter-image correlation of DW images, combination of compressed sensing and parallel imaging can be further improve acquisition efficiency [Shi *et al.*, 2014]. Considering the situation that drastic phase changes across the DW directions, a phase-constrained low-rank (PCLR) approach was developed [Gao *et al.*, 2014]. On the other hand, model-based CS method for DTI was proposed in [Yanjie *et al.*, 2012, Welsh *et al.*, 2013], which uses the signal intensity model to directly estimate diffusion tensor fields from undersampled k-space data.

This chapter proposes a new CS reconstruction method that employs rank deficiency prior and total variation (TV) constraint for cardiac DTI images reconstruction. Two TV regularizations are considered: local TV (i.e. classical TV) and nonlocal TV (NLTV). The local TV constraint allows for effective removal of undersampling artifacts and edge-preserving denoising, whereas the NLTV allows avoiding detail blurring, blocking effect and fine structures lossing. The subsequent constrained optimization problem is solved by the first-order fast method. The experiments are carried out on both simulated and real human cardiac diffusion weighted (DW) images. This chapter is organized as follows: section 5.2 presents the proposed reconstruction method; section 5.3 analyzes the method's performance using simulation and real human cardiac datasets; Finally the conclusion is drawn in Section 5.4.

## 5.2 Methods

### 5.2.1 Non local TV

Undersampling k-space data is an efficient way to reduce the acquisition time of magnetic resonance imaging (MRI) technique. As a promising signal recovery method, compressed sensing (CS) is able to reconstruct magnetic resonance images using a few samples and therefore has great potential in speeding up MRI process. CS relies on the empirical observation that many types of signal or images can be well approximated by a sparse expansion in terms of a suitable basis, that is, by only a small number of non-zero coefficients.

A common and popular regularization is total variation (TV) to preserve image edges, initially presented by Rudin et al. in 1992 for denoising applications [Rudin et al., 1992b]. it has been successfully employed in the many applications of image processing. The TV-based constraint  $\|x\|_{TV}$  defined as:

$$\|x\|_{TV} = \sum_{i=1}^M \sum_{j=1}^N \|D_{ij}x\|_2 \quad (5.1)$$

where  $D_{ij}$  represents the finite difference operation between the neighbor pixels  $i$  and  $j$ .

The TV constraint yields an effective removal of undersampling artifacts as well as an edge-preserving denoising of the image. However, the TV model favours the piecewise constant image structures, such method only makes use of local image information. Consequently, it blurs some details and causes blocking effect with fine structures lost, although the edges preserved in reconstruction. To overcome the intrinsic drawback of the TV model, NLTВ reconstruction methods were proposed to overcome the intrinsic drawback of the TV model [Zhang et al., 2010b], somewhat as nonlocal (NL) means filter for denoising [Buades et al., 2005, Coupe et al., 2008], and CS-MRI [Liang et al., 2011, Junzhou et al., 2012]. These methods can avoid blocking effects effectively but not unable to find similar patches accurately since structural information has been seriously degraded by the undersampled k-space reconstruction. The nonlocal total variation (NLTВ) regularization method extends the conventional TV norm to a nonlocal version. In NLTВ, the gradient is calculated using the pixels belonging to the whole image instead of the nearest neighboring pixels. Fig. 5.1 illustrates difference between TV and NLTВ about the calculate of image gradient.

The NLTВ-based constraint defined as:

$$\|x\|_{NLTВ} = \sum_u \sqrt{\sum_v [x(u) - x(v)]^2 w(u, v)} \quad (5.2)$$

where  $x(u)$  and  $x(v)$  are the image values at the coordinate of  $u$  and  $v$ ,  $w(u, v)$  is the graph weight function defined as:

$$w(u, v) = \begin{cases} \frac{1}{Z_x} \exp(-\frac{\|q_x(u) - q_x(v)\|_2^2}{2h^2}) & \text{if } \|u - v\|_2 \leq \frac{\delta}{2} \\ 0 & \text{otherwise} \end{cases} \quad (5.3)$$

In Eq.(5.3),  $q_x(u)$  and  $q_x(v)$  represent a small patch centering at the coordinates  $u$  and  $v$  respectively,  $Z_x$  signifies a normalization factor,  $h$  denotes a scale parameter which is

related to the patch size and the standard deviation of noise, it controls to what extent similarity between patches is enforced, and  $\delta$  is a positive value used to control the nonlocality of the method and to speed up computation, which means that only the neighbors in a window  $\delta$  around the target pixel are considered when calculating the nonlocal image gradient [Liang *et al.*, 2011].

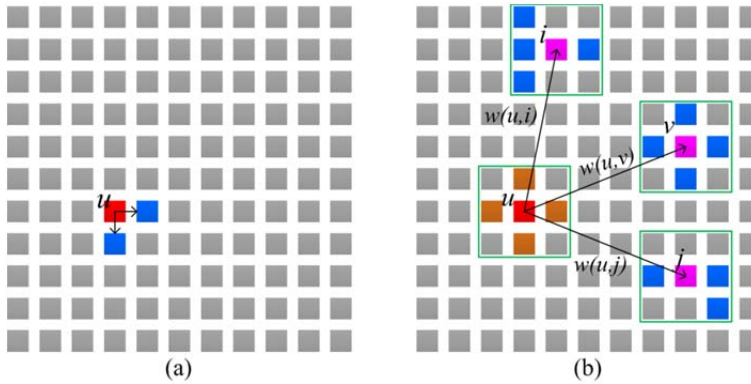


Fig. 5.1 The image gradient is calculated in (a) conventional TV regularization; and (b) NLTV regularization.

### 5.2.2 CS-MRI reconstruction using NLTV

The undersampled measurements  $b$  of the MR image  $x$  in k-space is then defined as:

$$b = F_u x \quad (5.4)$$

where  $F_u$  is a partial Fourier transform which can be expressed by  $F_u = PF$ , with  $F$  the Fourier transform and  $P$  the common undersampling pattern (mask).

For the undersampled case, that is, the number of measurements  $b$  is far fewer than that of pixels in  $x$ , without further information, it is, of course, impossible to recover  $x$  from  $b$  since Eq.(5.4) is highly underdetermined and has therefore an infinity of solutions. In order to find the optimal solution to this problem, additional constraints are introduced into the CS framework according to some prior knowledge.

By taking into account the above mentioned constraints, we formulate the CS image reconstruction method as:

$$\hat{x} = \arg \min_x \left\{ \frac{1}{2} \|F_u x - b\|_2^2 + \beta \|\Phi x\|_1 + \alpha \|x\|_{TV} + \gamma \|x\|_{NLTV} \right\} \quad (5.5)$$

with  $\Phi$  representing the wavelet transformation,  $\alpha$ ,  $\beta$ ,  $\gamma$  are positive constants.

Eq.(5.5) can be solved by the Fast Composite Splitting Algorithm (FCSA) [Huang *et al.*, 2011b], which means the problem can be divided into two subproblems: the regularization of TV-norm and  $l_1$ -norm. The former can be divided further into the regularized problems of local TV and nonlocal TV. Each subproblem is actually a convex function which can be solved by a proximal mapping operation  $prox(g)(x)$  [Beck *et al.*, 2009b].

$$prox_\rho(\phi)(x) = \arg \min_u \left\{ \phi(u) + \frac{1}{2\rho} \|u - x\|_2^2 \right\} \quad (5.6)$$

where  $\rho$  is the inverse of the Lipschitz constant  $L_f$  of  $\nabla f$ , and  $\nabla f$  is denoted as [Beck *et al.*, 2009b]:

$$\nabla f = \left( \frac{1}{2} \|F^u X - b\|_2^2 \right)' = (F^u)^T (F^u X - b) \quad (5.7)$$

where  $(F^u)^T$  indicating the inverse partial Fourier transform.

Defining that the solutions for the regularized problems of local TV, non-local TV and  $l_1$ -norm are  $x_{11}$ ,  $x_{12}$  and  $x_2$  respectively, the solution of Eq.(5.5) can be then obtained from the weighted average of  $x_{11}$ ,  $x_{12}$  and  $x_2$  in an iterative framework with an iteration stepsize of  $t^k$ .

The pseudocode of this algorithm is detailed as follows:

**Algorithm 1 CS-MRI-TV-NLTV**
**INPUT:**

$K$  : the maximum number of iterations;  
 $\alpha, \beta, \gamma$  : the regularization parameters;  
 $tol$  : the tolerance parameter.

**INIT:**  $\rho = 1/L$ ,  $t^1 = 1$ ,  $X^0 = r^1 = 0$ ,  $k = 0$ ;

**OUTPUT:**

$\hat{x}$  : the reconstructed MR image.

**REPEAT:**

$k = k + 1$ ;

$$x_g = r^k - \rho \nabla f(r^k);$$

$$x_{11} = prox_\rho(2\alpha \|x\|_{TV})(x_g);$$

$$x_{12} = prox_\rho(2\gamma \|x\|_{NLTV})(x_g);$$

$$x_1 = \frac{1}{2}(x_{11} + x_{12});$$

$$x_2 = prox_\rho(2\beta \|\Phi x\|_1)(x_g);$$

$$x^k = \frac{x_1 + x_2}{2};$$

$$t^{k+1} = \frac{1 + \sqrt{1 + 4(t^k)^2}}{2};$$

$$r^{k+1} = x^k + \frac{t^k - 1}{t^{k+1}}(x^k - x^{k-1});$$

**UNTIL**  $k > K$  **OR**  $\frac{\|x^{k-1} - x^k\|_2}{\|x^k\|_2} < tol$ .

To evaluate the performance of the method proposed in this sub-section, we compare it with several reconstruction approaches used in CS-MRI, including the FCSA [Huang *et al.*, 2011b] and NLTV\_FCSA [Junzhou *et al.*, 2012] methods. Two-dimensional (2D) brain and chest MR images with size of 256 x 256 are used (Note: data from Ref. [Junzhou *et al.*, 2012]) in this work. In Fig. 5.2(a) the k-space sampling mask is given, where the k-space data is sampled with a rate of 20% (i.e. keeping 20% of the complete k-space data) using the variable

density sampling pattern. Fig. 5.2(b) and Fig. 5.2(c) show the original MR images of brain and chest. In the experiments, the Daubechies wavelets with four decomposition levels are used. The parameter settings for each reconstruction method are given in Table 5-1. For fair comparison, the experimental setup for FCSA and NLTV\_FCSA methods follows the previous works [Huang *et al.*, 2011b] and [Junzhou *et al.*, 2012].

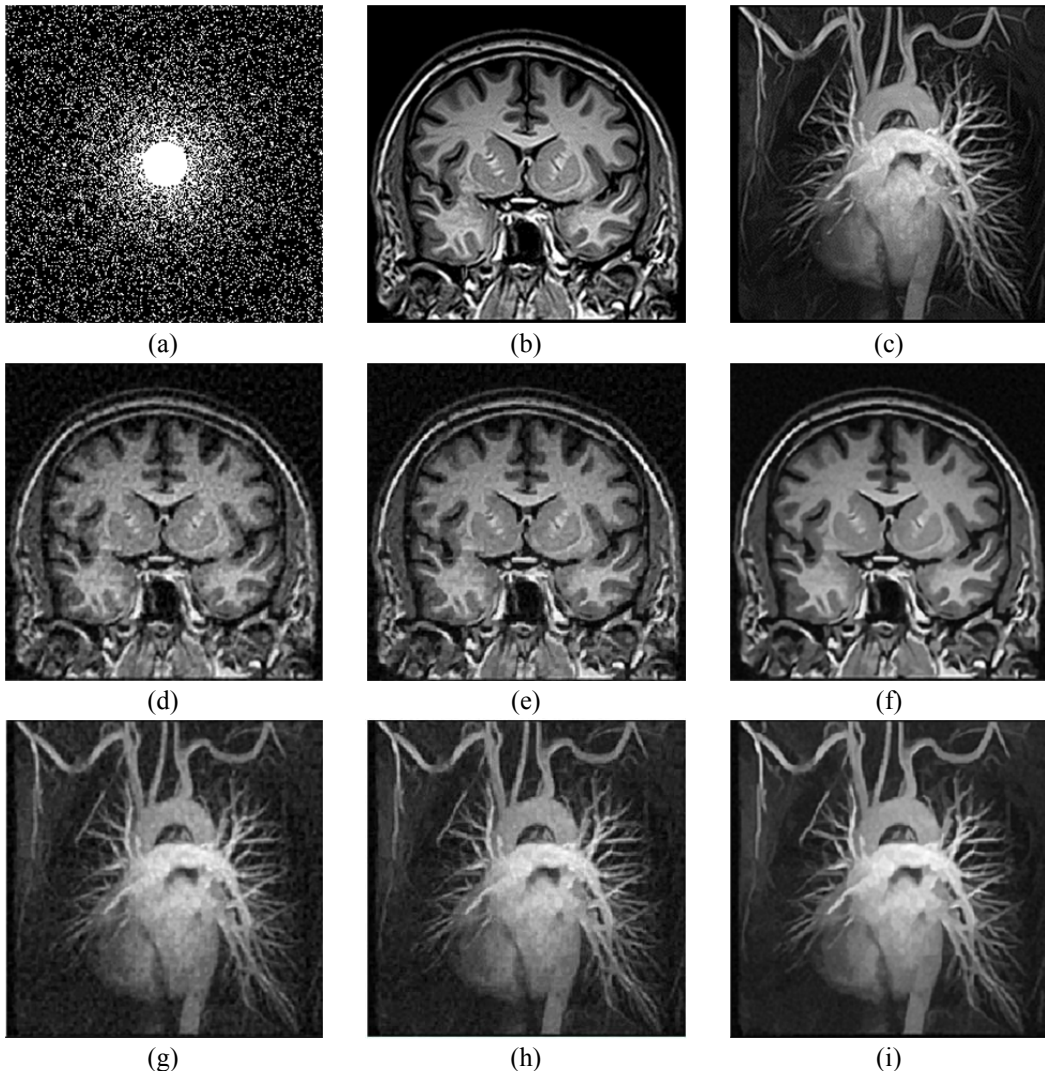


Fig. 5.2 Results of reconstruction on MR images using different methods. (a): k-space sampling mask. (b) and (c): Original MR images of brain and chest respectively. From (d) to (f): brain image reconstructed using FCSA, NLTV\_FSCA and the proposed method respectively. From (g) to (i): chest image reconstructed using FCSA, NLTV\_FSCA and the proposed method respectively.

Table 5-1 Parameter setting for different reconstruction methods

Parameters	FCSA	NLTV_FCSA	Proposed
$\alpha$	0.001	0.001	0.0005
$\beta$	0.035	0.035	0.035
$\gamma$	---	---	0.0025
$h$	---	0.025	0.025
$m$	---	2	2
$\delta$	---	5	5

The experiment results show that, there are many residual noise and artifacts in the images reconstructed with the FCSA, as shown in Fig. 5.2(d) and (g), and NLTV\_FCSA methods, see Fig. 5.2(e) and (h). Instead, the method proposed provides more satisfying results with clear contours, sharp edges and fine image details, as illustrated in Fig. 5.2(f) and (i).

To further compare these methods quantitatively, the mean square error (MSE), peak-signal-to-noise ratio (PSNR) and mean structural similarity (MSSIM) indices are calculated for the MR images of brain and chest reconstructed with different methods, as shown in Table 5-2. It can be observed that the proposed method improves the reconstruction performance in comparison with FCSA and NLTV\_FCSA, which has higher PSNRs, smaller MSEs, and greater MSSIMs.

In order to see the effects of the sampling rate on the reconstruction results, experiments were also performed with sampling rates of 0.1~0.5. The curve of PSNR, MSSIM and MSE versus different sampling rates for the MR images of brain reconstructed with FCSA, NLTV\_FCSA, and NLTV\_FCSA\_TV methods (our proposed method) are shown in Fig. 5.3.

The experimental results demonstrate that the local TV model and NL self-similarity constraint are complementary to each other, making the proposed approach highly effective in reducing noise and preserving image edges and details. Compared to existing CS reconstruction methods, the proposed reconstruction approach has higher PSNRs, smaller MSEs, and greater MSSIMs. In addition, the performance of our method changes relatively gently with the variation of the sampling rates, which verifies the robustness of the proposed method.

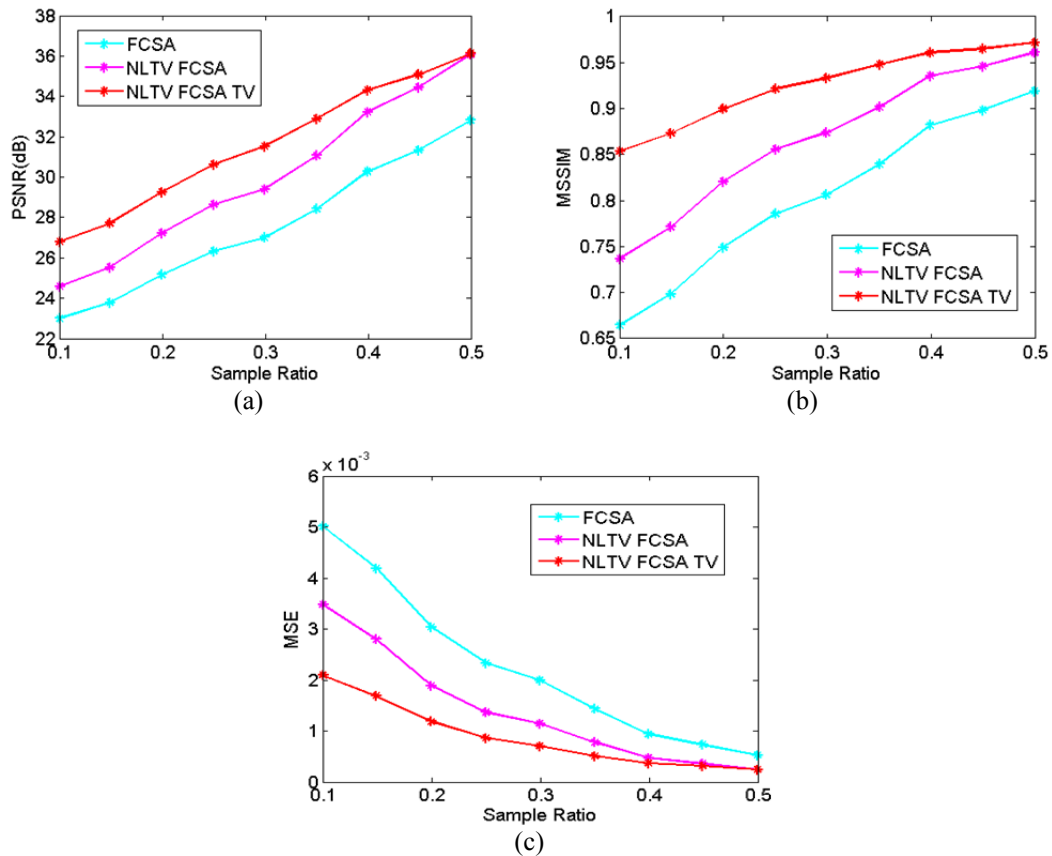


Fig. 5.3 Curve of PSNR (a), MSSIM (b) and MSE (c) versus different sampling rates for the MR images of brain reconstructed with FCSA, NLTV\_FCSA, and NLTV\_FCSA\_TV methods respectively.

Table 5-2 Comparison of the experiment results in terms of PSNR, MSSIM and MSE for various reconstruction methods. Bold font indicates the best performance with respect to PSNR, MSSIM, and MSE

Method	Brain			Chest		
	PSNR	MSSIM	MSE	PSNR	MSSIM	MSE
FCSA	24.8830	0.7404	0.0032	28.0662	0.7512	0.0016
NLTVA_FCSA	26.9024	0.8136	0.0020	29.8917	0.8157	0.0010
Proposed	<b>29.0811</b>	<b>0.8979</b>	<b>0.0012</b>	<b>31.3269</b>	<b>0.8684</b>	<b>0.0007</b>

### 5.2.3 CS DT-MR image reconstruction using low rank and TV model

Let  $x_l$  be a DW image with size  $m \times n$  and  $F_l^u$  is a partial Fourier transform for  $l$ th direction. Then the undersampled k-space data  $b_l$  of the DW image for each direction in k-space can be formulated as:

$$b_l = F_l^u x_l + \varepsilon_l \quad (5.8)$$

where,  $\varepsilon$  is the noise level, and diffusion direction  $l = 1, 2, \dots, L$ .

Let  $X$  be an aligned column vector of each 2D DW image (as shown in Eq.(5.9)). Since the DW images are correlated across the diffusion directions, the resulting matrix  $X$  is rank deficiency. The matrix  $X$  is low rank means that  $\text{rank}(X) \leq \min(mn, L)$ .

$$X_{mn \times L} = [x_1, x_2, \dots, x_L] = \begin{bmatrix} x_{1,1} & x_{1,2} & \cdots & x_{1,L} \\ x_{2,1} & x_{2,2} & \cdots & x_{2,L} \\ \vdots & \vdots & \ddots & \vdots \\ x_{mn,1} & x_{mn,2} & \cdots & x_{mn,L} \end{bmatrix} \quad (5.9)$$

As elaborated in chapter 4 and [Gao et al., 2014], the low rank model more suitable for dMR images reconstruction. This chapter proposes a new reconstruction method for DW images by combining low rank prior and total variation (TV) constrains together. The sampling multiple DW images can be formulated as follow:

$$b = \begin{bmatrix} b_1 \\ \vdots \\ b_l \\ \vdots \\ b_L \end{bmatrix} = \begin{bmatrix} F_1^u & 0 & 0 & 0 & 0 \\ 0 & \ddots & 0 & 0 & 0 \\ 0 & 0 & F_l^u & 0 & 0 \\ 0 & 0 & 0 & \ddots & 0 \\ 0 & 0 & 0 & 0 & F_L^u \end{bmatrix} \begin{bmatrix} x_1 \\ \vdots \\ x_l \\ \vdots \\ x_L \end{bmatrix} \quad (5.10)$$

Then, the reconstruction undersampling k-space data can be described as the following optimization problem:

$$\widehat{X} = \arg \min_X \left\{ \frac{1}{2} \|F^u X - b\|_2^2 + \alpha \cdot \|X\|_* + \beta \cdot \|X\|_{TV3D} \right\} \quad (5.11)$$

here,  $\|\bullet\|_*$  is the nuclear norm, which is the best convex approximation of the rank function;  $\|X\|_{TV3D}$  is the finite difference along  $x$ ,  $y$  and  $d$  (diffusion gradient direction), respectively;  $\alpha > 0$  and  $\beta > 0$  are two positive regularization parameters, respectively.

The Eq.(5.11) can be solved by the Fast Composite Splitting Algorithm (FCSA) [Huang *et al.*, 2011b]. Specifically, let  $f(X) = \frac{1}{2} \|F^u X - b\|_2^2$ , which is a convex and smooth function with the Lipschitz constant  $L_f$ ,  $g_1(X) = \alpha \cdot \|X\|_*$  and  $g_2(X) = \beta \cdot \|X\|_{TV3D}$ . Then, the  $g(X)$  can be obtained by a proximal mapping operation [Huang *et al.*, 2011b] as defined in Eq.(5.6):

The outline of the proposed method for problem (5.11) is detailed as shown in Algorithm 2.

By taking into account the advantage of NLTV constraints, we propose an improved CS reconstruction method by combining low rank, local TV regularization and nonlocal total variation (NLTV) constraint together. The outline of the proposed method for is detailed as shown in Algorithm 3. (Note that: The code for NL means filter can be download from the website <http://www.mathworks.com/matlabcentral/fileexchange/27395-fast-non-local-means-1d--2d-color-and-3d>.

### Algorithm 2 CS-DTMRI-LRTV

#### INPUT:

$K$  : the maximum number of iterations;

$\alpha, \beta$  : the regularization parameters;

$tol$  : the tolerance parameter.

**INIT:**  $\rho = 1/L$ ,  $t^1 = 1$ ,  $X^0 = r^1 = 0$ ,  $k = 0$ ;

#### OUTPUT:

$\widehat{X}$  : the reconstructed DW images.

#### REPEAT:

$k = k + 1$ ;

$$x_g = r^k - \rho \nabla f(r^k);$$

$$X_1^k = prox_{\rho}(2\alpha \|X\|_*)(x_g);$$

$$X_2^k = prox_{\rho}(2\beta \|X\|_{TV3D})(x_g);$$

$$X^k = \frac{X_1^k + X_2^k}{2};$$

$$t^{k+1} = \frac{1 + \sqrt{1 + 4(t^k)^2}}{2};$$

$$r^{k+1} = X^k + \frac{t^k - 1}{t^{k+1}}(X^k - X^{k-1});$$

**UNTIL**  $k > K$  **OR**  $\frac{\|X^{k-1} - X^k\|_2}{\|X^k\|_2} < tol$ .

---

**Algorithm 3 CS-DTMRI-LRTV-NLTV**
**INPUT:**

$K$  : the maximum number of iterations;  
 $\alpha, \beta$  : the regularization parameters;  
 $tol$  : the tolerance parameter.  
 $m$  : the radius of local patch.  
 $\delta$  : the radius of neighbourhood search window.  
 $h$  : the strength of the filtering

**INIT:**  $\rho = \frac{1}{L}, t^1 = 1, X^0 = r^1 = 0, k = 0;$

**OUTPUT:**

$\hat{X}$  : the reconstructed DW images.

**REPEAT:**

$k = k + 1;$

$$x_g = r^k - \rho \nabla f(r^k);$$

$$X_1^k = prox_{\rho}(2\alpha \|X\|_*)(x_g);$$

if  $\text{mod}(k, 20)$

$$X_2^k = prox_{\rho}(2\beta \|X\|_{TV3D})(x_g);$$

else

$$X_2^k = prox_{\rho}(2\beta \|X\|_{NLTV3D})(x_g);$$

end

$$X^k = \frac{X_1^k + X_2^k}{2};$$

$$t^{k+1} = \frac{1 + \sqrt{1 + 4(t^k)^2}}{2};$$

$$r^{k+1} = X^k + \frac{t^k - 1}{t^{k+1}}(X^k - X^{k-1});$$

**UNTIL**  $k > K$  **OR**  $\frac{\|X^{k-1} - X^k\|_2}{\|X^k\|_2} < tol$ .

---

## 5.3 Experimental Results

### 5.3.1 Data and sampling pattern

The experiments were carried out on both simulation and real human cardiac DTMR datasets. Simulated DW images were generated as proposed in [Wang *et al.*, 2012], which using physical measurements from polarized light imaging (PLI) to generate realistic DW images at different diffusion gradient directions. Simulated DTI data were obtained with diffusion gradient directions applied in 42 directions, the DW images were obtained with diffusion sensitivity  $b = 1000 \text{ s/mm}^2$ , and the image size of  $128 \times 128$ , as shown in Fig. 5.4(a).

The real data have been collected using ex-vivo samples of human heart [Helm *et al.*, 2005a, Helm *et al.*, 2005b, Helm *et al.*, 2006]. The corresponding acquisition parameters are the following: The the image size of  $256 \times 256 \times 134$ , the image spatial resolution is  $0.43 \times 0.43 \times 1.0 \text{ mm}^3$ , and 21 diffusion gradient direction. In the experiment of this chapter, we

chose slice 70. In Fig. 5.4(b) is shown the DW image in slice 70 and diffusion gradient direction 3. The dataset can be download from the website <http://cvrgrid.org/data/ex-vivo>.

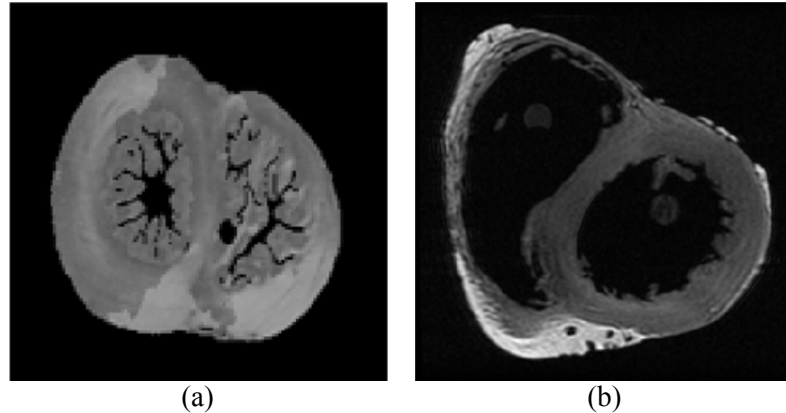


Fig. 5.4 Reference human cardiac DW images in one diffusion direction. (a) Simulated data; (b) real data.

### 5.3.2 Evaluation criteria

In DTI, the diffusion tensor  $D$  was used to describe the diffusion properties in each voxel, which is a  $3 \times 3$  symmetric and positive definite matrix. There are many measure indices derived from the diffusion tensor  $D$  to characterizing the water molecule diffusion quantitatively [Basser *et al.*, 1996, Pierpaoli *et al.*, 1996]. Mean diffusivity (MD) and Fractional anisotropy (FA) are two quantitative parameters commonly used in a clinical to assessing tissue microstructure, which characterize the mean diffusivity and regarding the diffusion anisotropy, respectively. The FA and MD are defined as follow:

$$MD = \frac{\lambda_1 + \lambda_2 + \lambda_3}{3} \quad (5.12)$$

$$FA = \sqrt{\frac{3 \cdot [(\lambda_1 - MD)^2 + (\lambda_2 - MD)^2 + (\lambda_3 - MD)^2]}{2 \cdot (\lambda_1^2 + \lambda_2^2 + \lambda_3^2)}} \quad (5.13)$$

On the other hand, for determine the orientation of a fiber, the helix angle (HA) (also called the inclination angle or fiber angle) and the transverse angle (TA) are among the most widely used, which can be drived from the eigensystem of diffusion tensor  $D$ . The helix angle was defined as the angle between the projection of the primary eigenvector onto the tangent plane and the imaging plane, and the transverse angle was defined as the angle between the projection of the primary eigenvector onto the imaging plane and the tangent plane [Streeter *et al.*, 1969, Scollan *et al.*, 1998, Chen *et al.*, 2003].

In this chapter, the root mean square errors (RMSE) of FA, MD, TA and HA were calculated to evaluate and compare the reconstruction performance. The RMSE defined as:

$$RMSE = \sqrt{\frac{\|\text{vec}(x_{rec}) - \text{vec}(x_{ref})\|_2^2}{N}} \quad (5.14)$$

where,  $x_{rec}$  and  $x_{ref}$  denoted the reconstructed signal and reference signal,  $N$  is the total number of signal.

### 5.3.3 Comparison with existing techniques

To evaluate the performance of the proposed method, comparison was performed with joint sparsity method [Wu *et al.*, 2014]. The observation measurement  $b$  is corrupted by complex Gaussian white noise  $\varepsilon$  with standard deviation  $\sigma_n$ . The latter is derived from the associated input SNR (ISNR) [Carrillo *et al.*, 2012], which is defined as  $\text{ISNR} = 20 \log_{10} \left( \frac{\sigma_x}{\sigma_n} \right)$ , where  $\sigma_x$  denotes the standard deviation of the DW images. The Daubechies wavelets with four decomposition levels are used; the ISNR is set to 30 dB. For the simulated cardiac DTI dataset, the regularization parameter  $\alpha$  and  $\beta$  are set to 0.1 and 0.0001, respectively. In algorithm 2, the radius of window size for the nonlocal neighbors  $\delta$  was chosen to be 3, the radius of local patch size  $m$  was chosen 3, and the strength of the filtering  $h$  is set to 0.005.

### 5.3.4 Effects of sampling rates

Comparisons of the reconstruction performance with sampling rates of 10%~50% and ISNR 30dB for simulated and real human cardiac data are illustrated in Fig. 5.5 and Fig. 5.6. From the figures, it can be seen that the proposed method based on low rank constraint achieves better reconstructions with lower RMSE of FA and MD compared with joint sparsity method. On the other hand, using low rank with NLTV constraint approach has lower reconstruction RMSE of FA and MD than using low rank with TV constraint, especially for the real human heart dataset.

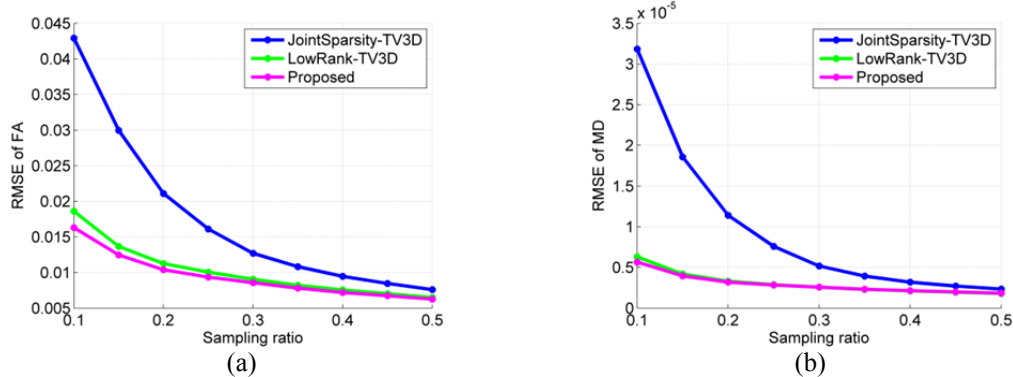


Fig. 5.5 Performance comparisons on simulated heart data with ISNR 30dB. (a) RMSE of FA; (b) RMSE of MD

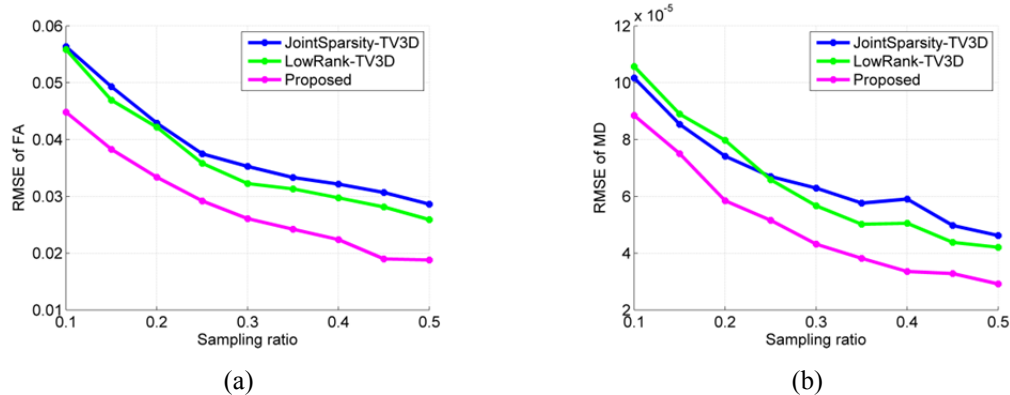


Fig. 5.6 Performance comparisons on real human heart data with ISNR 30dB. (a) RMSE of FA; (b) RMSE of MD

### 5.3.5 Maps of FA and MD

Fig. 5.7 and Fig. 5.8 illustrated the maps of FA and MD on simulated and real heart data with the sampling rate of 25% and ISNR 30dB. In these calculations, the involved diffusion tensors corresponding to the complete k-space were taken as the references. As shown in figures, the FA and MD maps with the proposed method are visually better than those obtained with joint sparsity with TV model.

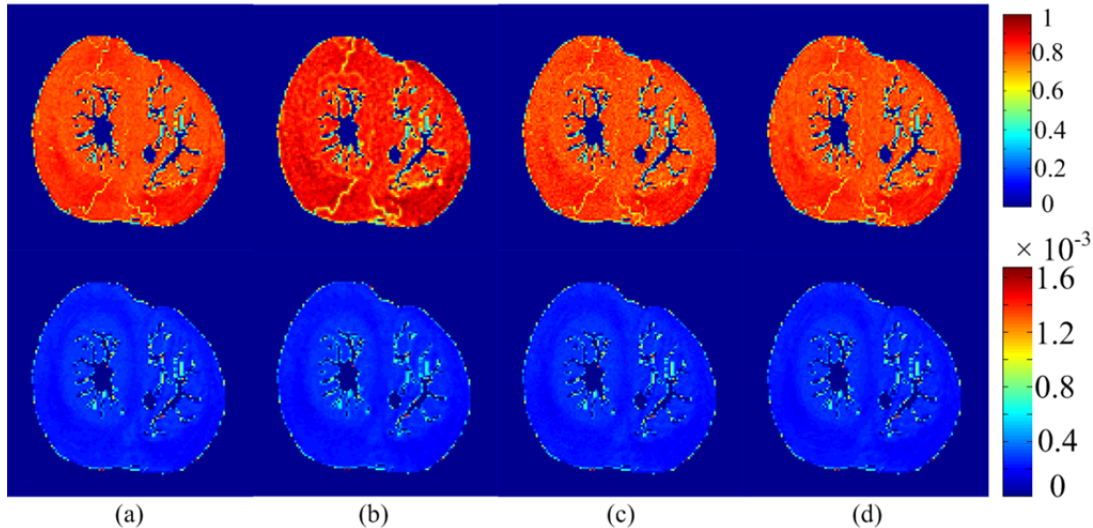


Fig. 5.7 Maps of FA (first row) and MD (second row) of the simulated human heart data with the sampling rate of 25% and ISNR 30dB. (a) Reconstruction from the complete k-space data; Reconstructions from undersampled k-space using (b) joint sparsity with TV; (c) low rank with TV; and (d) the low rank with NLTV methods.

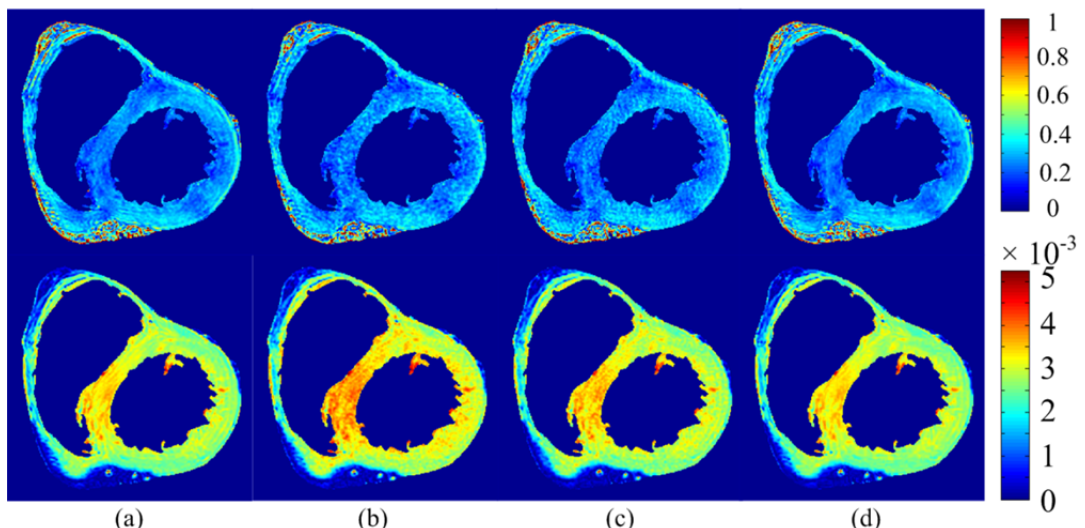


Fig. 5.8 Maps of FA (first row) and MD (second row) of the real human heart data with the sampling rate of 25% and ISNR 30dB. (a) Reconstruction from the complete k-space data; Reconstructions from undersampled k-space using (b) joint sparsity with TV; (c) low rank with TV; and (d) the low rank with NLTV methods.

### 5.3.6 Tensor fields visualization

Fig. 5.9 and Fig. 5.10 illustrated the reconstructed tensor fields obtained using the three methods (the Joint Sparsity with TV, the Low Rank with TV, and the Low Ran with NLTV) on simulated and real human cardiac data with sampling rates of 15% (approximation acceleration factors 6) and ISNR 30dB. From the figures, we can see that the reconstructed tensor fields of the proposed method gives greater the visual effects and visually comparable with the references.

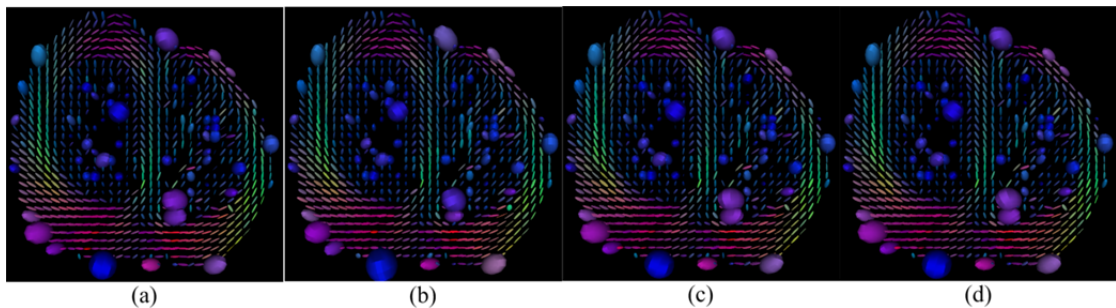


Fig. 5.9 The reconstruction tensor fields on simulated human heart data with sampling rates 15% and ISNR 30dB using the different methods. (a) Reconstruction from the complete k-space data; Reconstructions from undersampled k-space using (b) joint sparsity with TV; (c) low rank with TV; and (d) the low rank with NLTV methods.

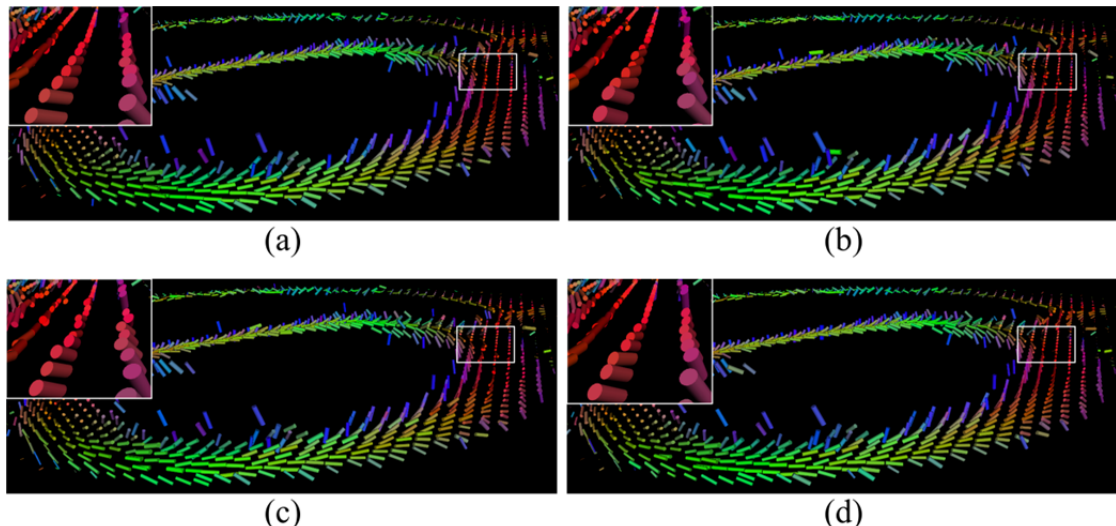


Fig. 5.10 The reconstruction tensor fields on real human heart data with sampling rates 15% and ISNR 30dB using the different methods. (a) Reconstruction from the complete k-space data; Reconstructions from undersampled k-space using (b) joint sparsity with TV; (c) low rank with TV; and (d) the low rank with NLTV methods.

### 5.3.7 Effects of regularization parameters

The regularization parameters  $\alpha$  and  $\beta$  were empirically determined for the proposed methods. Different values were tested for  $\beta$  (fixing  $\alpha=0.1$ ). As illustrated in Fig. 5.11 (a) and (b), the reconstruction RMSE of FA and MD on simulated data changed slightly when  $\beta$  was smaller than 1e-03. Based on these results,  $\alpha$  and  $\beta$  were set to 0.1 and 0.0001, respectively.

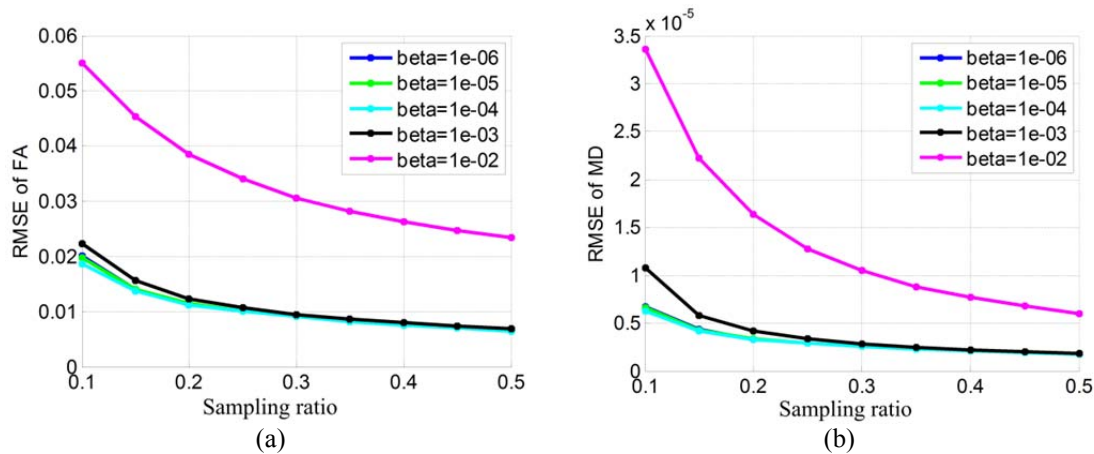


Fig. 5.11 Effects of regularization parameters. (a) RMSE of FA on simulated data; (b) RMSE of MD on simulated data.

## 5.4 Conclusion

This chapter proposed two efficient methods for reconstructing DTMR images from undersampled k-space data using compressed sensing. The proposed method exploits image correlation across diffusion directions via low rank regularization. The results on both simulated and real human cardiac DW images showed that the proposed method provides more accurate reconstructions and more accurate DTI indices compared with the state-of-the-art CS DTMR image reconstruction techniques.

## Chapter 6

# The influence of radial undersampling schemes on compressed sensing cardiac DTI

## Contents

---

Résumé en français.....	112
Abstract .....	113
6.1    Introduction.....	114
6.2    Experimental method .....	115
6.2.1 <i>Cardiac datasets and Evaluation criteria.</i> .....	115
6.2.2 <i>Sampling schemes</i> .....	116
6.3    Experimental results.....	117
6.3.1 <i>Effects of sampling rates</i> .....	117
6.3.2 <i>Maps of FA and MD</i> .....	117
6.3.3 <i>Tensor fields visualization</i> .....	120
6.4    Conclusion .....	122

---

## Résumé en français

Le sous-échantillonnage des données espace  $k$  fournit un moyen efficace pour réduire la quantité de données à acquérir tout en maintenant la qualité d'image. Le sous-échantillonnage purement aléatoire de l'espace  $k$  est généralement impossible en raison de considérations matérielles et physiologiques. Le sous-échantillonnage radial est le plus populaire parmi les échantillonnages de l'espace  $k$  non-cartésiens, parce qu'il a une sensibilité au mouvement plus faible par rapport aux trajectoires cartésiennes et les artefacts de reconstruction linéaire ressemblent plus au bruit. Par conséquent, l'imagerie radiale est une stratégie prometteuse de sous-échantillonnage pour accélérer l'acquisition. Ce chapitre vise à étudier différents schémas d'échantillonnage radial ainsi que la reconstruction de l'image en utilisant CS. En particulier, nous proposons deux schémas de sous-échantillonnage radial perturbés aléatoirement: angle d'or et angle aléatoire. Les méthodes proposées sont comparées avec les méthodes existantes, y compris l'angle uniforme, l'angle uniforme perturbé aléatoirement, l'angle d'or et l'angle aléatoire. Les résultats sur des images simulées et réelles pondérées en diffusion du cœur montrent que, pour la même quantité de données de l'espace  $k$ , un échantillonnage aléatoire autour d'une ligne radiale aléatoire génère une meilleure qualité de reconstruction en termes d'anisotropie fractionnelle (FA) et diffusivité moyenne (MD), et que le sous-échantillonnage de l'angle d'or perturbé aléatoirement donne les meilleurs résultats pour la reconstruction CS des images en imagerie du tenseur de diffusion (DTI) cardiaque.

## Abstract

Undersampling of k-space data provides an effective way to reduce the amount of data to acquire while maintaining image quality. Purely random undersampling of k-space is generally impractical due to hardware and physiological considerations. Radial undersampling is one of the most popular non-Cartesian k-space sampling schemes, because it has relatively lower sensitivity to motion than Cartesian trajectories and artifacts from linear reconstruction are more noise-like. Therefore, radial imaging is a promising strategy of undersampling to accelerate acquisitions. This chapter aims to investigate the various radial sampling schemes as well as reconstruction using CS. In particular, we propose two randomly perturbed radial undersampling schemes: golden-angle and random angle. The proposed methods are compared with existing radial undersampling methods: uniformity-angle, randomly perturbed uniformity-angle, golden-angle, random angle. The results on both simulated and real human cardiac DW images show that for the same amount of k-space data, randomly sampling around a random radial line results in better reconstruction quality in terms of fractional anisotropy (FA) and mean diffusivities (MD), and that the randomly perturbed golden-angle undersampling yields the best results for cardiac CS-DTMR image reconstruction.

## 6.1 Introduction

To date, almost all clinical MR imaging is performed by acquiring k-space along a Cartesian trajectory. Data are sampled line-by-line on a rectangular grid. However, k-space can also be sampled in an arbitrary non-Cartesian manner, and different sampling trajectories will have different properties and implications for the reconstructed image [Wright *et al.*, 2014]. Radial sampling is one of the most frequently non-Cartesian k-space sampling schemes, first proposed by Lauterbur in 1973 [Lauterbur, 1973], which sampling the k-space signal along spokes instead of line by line of k-space sampling. Radial acquisitions is very fast and is less susceptible to object motion and ghosting artifacts than Cartesian trajectories, it can be significantly undersampled [Block *et al.*, 2007, Lustig, 2008]. Radial sampling is by far the best suited practical and efficient sampling scheme, and is a promising strategy of undersampling to accelerate acquisitions [Lustig, 2008, Majumdar *et al.*, 2012]. In the Traditionally uniform radial sampling scheme, the k-space is sampled with equally spaced radial lines, which is restricted to a constant length of the acquisition window and requires a new scan for each desired temporal resolution. Therefore, the Golden Ratio based profile acquisition scheme were proposed to provides a nearly uniform profile distribution for an arbitrary number of profiles [Winkelmann *et al.*, 2007] and widely applied for MRI , dynamic volumetric MRI [Feng *et al.*, 2014], and . Other classical radial sampling strategies including bit-reversed [Chan *et al.*, 2012] and radial with random angles [El-Metwally *et al.*, 2008].

Undersampling of radial k-space data provides an effective way to reduce the amount of acquired data while keeping the image quality. In the radial sampling, the number of sample points in the center of k-space is much higher for the low spatial frequencies (in the central region) than the surrounding of k-space. It is means that sampling the low frequencies more densely than high frequencies [Block, 2008]. Hence, reconstruction from the radial sampling trajectories is more complicated that cannot be obtained by inverse 2D Fourier transform. Conventional image reconstruction from radial data using projection reconstruction algorithms [Lauterbur, 1973, Glover *et al.*, 1992, Peters *et al.*, 2000] or k-space interpolation schemes (e.g. gridding [Jackson *et al.*, 1991, Fessler *et al.*, 2003, Sha *et al.*, 2003, Block *et al.*, 2007, Fessler, 2007, Yang *et al.*, 2014]).

Recently, Compressed Sensing (CS) appeared as a new mathematical theory for accelerating data acquisitions with high quality from significantly under-sampled data via non-linear reconstruction algorithm [Candes *et al.*, 2006a, Donoho, 2006]. An essential ingredient of CS is incoherent sampling. Pure random undersampling of k-space simplify the mathematical proofs and in particular to guarantee a very high degree of incoherence. But, sampling a completely random subset of k-space is generally impractical due to hardware and physiological considerations [Lustig, 2008, Lustig *et al.*, 2008]. In radial sampling, undersampling k-space along spokes can be seen as an approximation of a random sampling scheme and also have a variety of significant non-random structures.

The effects of CS applied to different radial sampling schemes (e.g. uniform-angle, golden-angle, bit-reversed, and random sampling) has been investigated, and the experiments demonstrate that the Golden-angle sampling outperforms the other radial sampling schemes for the Breast MRI [Chan *et al.*, 2012] and for the myocardial perfusion MR imaging (MPI) [Lingala *et al.*, 2013]. Combination of compressed sensing, parallel imaging, and radial sampling provides a fast and flexible way to reduce the amount of acquired data while keeping the integrity of relevant data information. It has been rapidly gaining popularity in different areas of science, and shown to dramatically improve the quality of undersampled

images in MRI [Block *et al.*, 2007, Lustig, 2008], dynamic MRI [Xie *et al.*, 2010, Nam, 2012, Feng *et al.*, 2014], Myocardial Perfusion MRI [Adluru *et al.*, 2009, Lingala *et al.*, 2013],

Randomly perturbed uniform radial trajectories increase the incoherence in radial CS-MRI, significantly reduce the streaking artifacts and further improve image quality [A. Bilgin, 2008]. This chapter aims to investigate the radial sampling and various radial sampling schemes as well as reconstruction using CS. In particular, we propose two randomly perturbed radial undersampling schemes: golden-angle and random angle. The proposed methods are compared with existing radial undersampling methods: uniformity-angle, randomly perturbed uniformity-angle, golden-angle, random angle. The experiments are carried out on both simulated and real human cardiac DW images and reconstruction results are assessed in terms of fractional anisotropy (FA) and mean diffusivities (MD).

This chapter is organized as follows. Section 6.2 describes the experimental material and method, including datasets, sampling scheme and experiment condition. Section 6.3 demonstrates the undersampling scheme's performance using simulation and real human cardiac datasets; Finally the conclusion is drawn in Section 6.4.

## 6.2 Experimental method

### 6.2.1 Cardiac datasets and Evaluation criteria

The experiments were carried out on both simulation and real human cardiac DTMR datasets (see Fig. 6.1). Simulated DW images were generated as proposed in [Wang *et al.*, 2012], which using physical measurements from polarized light imaging (PLI) to generate realistic DW images at different diffusion gradient directions. Simulated DTI data were obtained with diffusion gradient directions applied in 42 directions, the DW images were obtained with diffusion sensitivity  $b = 1000 \text{ s/mm}^2$ , and the image size of  $128 \times 128$ , as shown in Fig. 6.1(a).

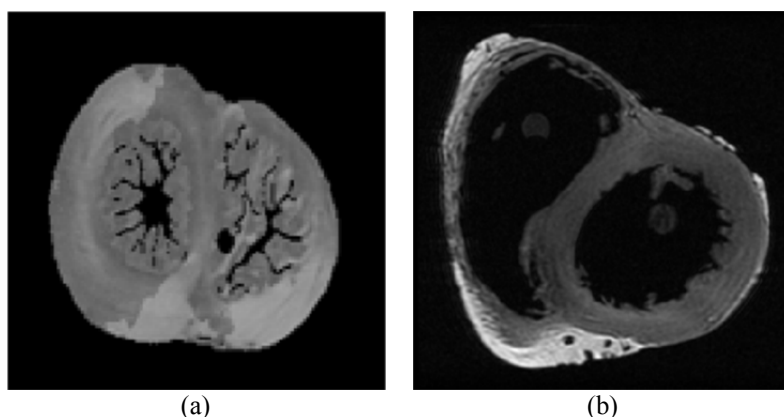


Fig. 6.1 Reference human cardiac DW images. (a) Simulated data; (b) real data.

The real data have been collected using ex-vivo samples of human heart [Helm *et al.*, 2005a, Helm *et al.*, 2005b, Helm *et al.*, 2006]. The corresponding acquisition parameters are the following: The image size of  $256 \times 256 \times 134$ , the image spatial resolution is  $0.43 \times 0.43 \times 1.0 \text{ mm}^3$ , and 21 diffusion gradient direction. In the experiment of this chapter, we chose slice 70. In Fig. 6.1(b) is shown the DW image in slice 70 and diffusion gradient direction 3th. The dataset can be downloaded from the website <http://cvrgrid.org/data/ex-vivo>.

To quantitatively compare different undersampling mask, the RMSE of FA, RMSE of MD are calculated as defined in Eq.(4.11) to Eq.(4.13) of chapter 4. The observation measurement  $b$  is corrupted by complex Gaussian white noise  $\varepsilon$  with standard deviation  $\sigma_n$ . The latter is derived from the associated input SNR (ISNR) [Carrillo *et al.*, 2012], which defined in as:

$ISNR = 20\log_{10}\left(\frac{\sigma_x}{\sigma_n}\right)$ , where  $\sigma_x$  denotes the standard deviation of the DW images. In the experiment, the ISNR is set to 30dB.

## 6.2.2 Sampling schemes

Radial lines are perturbed by adding slight random deviations taken from Guassian distribution with zero mean and varying variances, as demonstrated in Fig. 6.2. The six different radial k-space sampling schemes are shown in Fig. 6.3, that is uniformity-angle, golden-angle, random-angle sampling and the corresponding randomly perturbed sampling. The sampling ratio in k-space is set to be approximately 10% (i.e. keeping 10% of the complete k-space data).

- **Uniform-angle:** The angle between samples on neighboring spokes (or also called views or profiles) are incremented by the constant angle increment  $\Delta\phi = \frac{180}{K}$ ,  $K$  is the number of spokes. For a set of exactly spokes, this provides the most uniform azimuthal data distribution, as shown in Fig. 6.3(a).
- **Gloden-angle:** Radial projections are successively incremented by the golden angle  $\Delta\phi = \frac{\sqrt{5}-1}{2} \cdot 180 \approx 111.25^\circ$ . The Golden Ratio based profile acquisition scheme were proposed to provide a nearly uniform azimuthal profile distribution in k-space for an arbitrary number of profiles [Winkelmann *et al.*, 2007]. A relatively well-distributed set is shown in Fig. 6.3(b).
- **Random-angle:** In this case, spokess are generated from random angles that are uniformly distributed. A reference k-space sampling with sampling ratio approximate 10% is shown in Fig. 6.3(c). From the figure, we can see that the randomly placed sprokkes are clustered in certain regions.

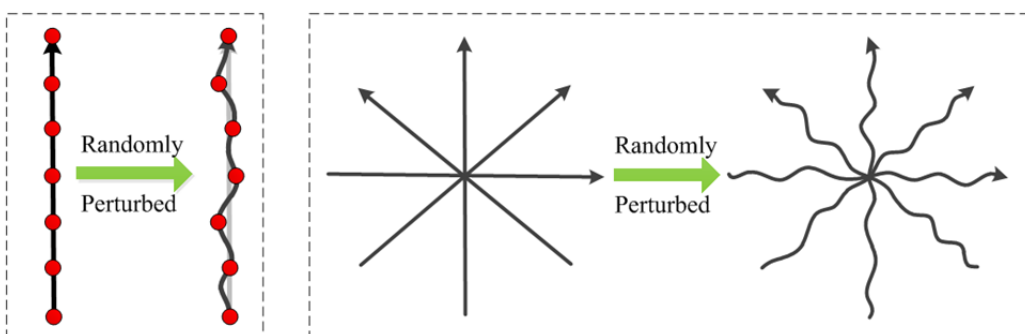


Fig. 6.2 Demonstrate the randomly perturbed radial lines.

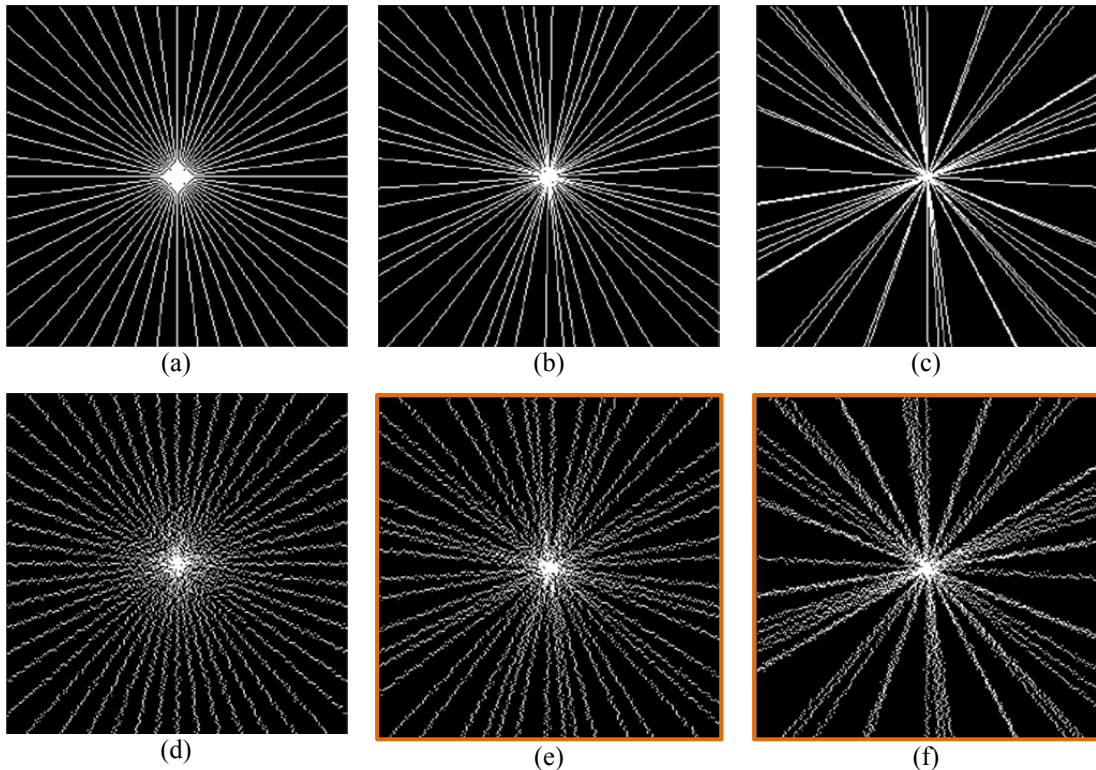


Fig. 6.3 Reference k-space sampling masks in one diffusion direction with sampling rate of 20%. (a) uniform-angle; (b) golden-angle; (c) random-angle; (d)-(f) randomly perturbed (a)-(c), respectively.

## 6.3 Experimental results

### 6.3.1 Effects of sampling rates

Fig. 6.4 and Fig. 6.5 (RP is the abbreviation of randomly perturbed) compare the reconstruction performance of the different radial sampling mask with sampling rates of 10%~50% for simulated and real human cardiac data. As illustrated in figures, the reconstruction of undersampled randomly perturbing the radial data resulted in significant reduction of reconstruction error compared to regular radial trajectories. On the other hand, the reconstruction error of the uniform-angle and golden-angle radial sampling was almost identical, and less than randomized-angle sampling.

### 6.3.2 Maps of FA and MD

Fig. 6.6 and Fig. 6.7 map FA and MD on simulated heart data with a 25% sampling rate, which corresponds to an acceleration factor of 4. In these calculations, the involved diffusion tensors corresponding to the complete k-space were taken as references. As shown in Fig. 6.6 and Fig. 6.7, the FA and MD maps with the uniform-angle and golden-angle undersampling scheme are visually better than those obtained with randomized-angle sampling scheme.

Fig. 6.8 and Fig. 6.9 map FA and MD on real heart data with a 25% sampling rate, which corresponds to an acceleration factor of 4. In these calculations, the involved diffusion tensors corresponding to the complete k-space were taken as references. As shown in Fig. 6.8 and Fig. 6.9, the FA and MD maps with the uniform-angle and golden-angle undersampling scheme are visually better than those obtained with randomized-angle sampling scheme.

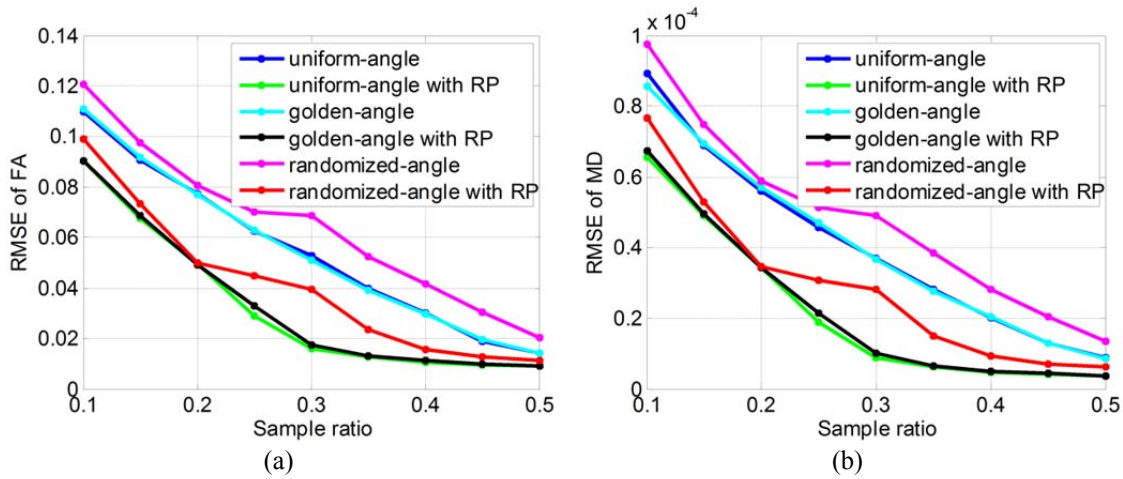


Fig. 6.4 Performance comparisons on simulated data with different sampling rates (RP is the abbreviation of randomly perturbed). (a) RMSE of FA; (b) RMSE of MD.

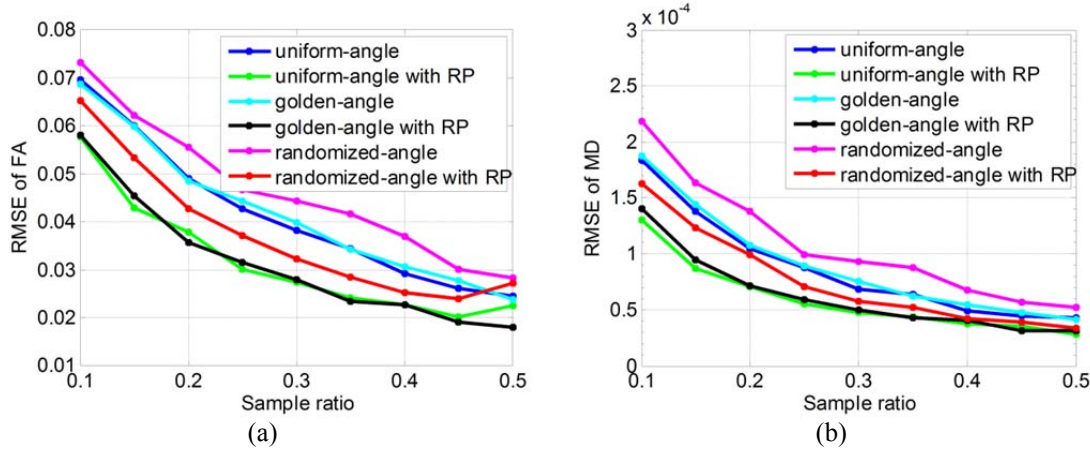


Fig. 6.5 Performance comparisons on real data with different sampling rates (RP is the abbreviation of randomly perturbed). (a) RMSE of FA; (b) RMSE of MD.

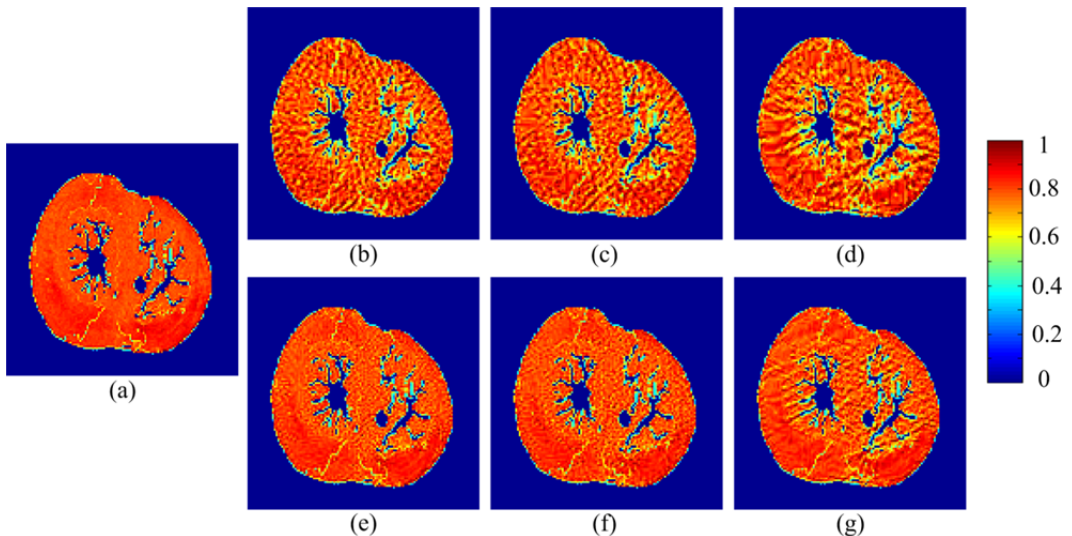


Fig. 6.6 Maps of FA of the simulated human heart data with 25% sampling rates. (a) Reconstruction from the complete k-space data. Reconstructions from undersampled k-space using (b) uniform-angle radial, (c) golden-angle radial, (d) random-angle radial, and (e)-(g) the corresponding randomly perturbed radial sampling of (b)-(d).

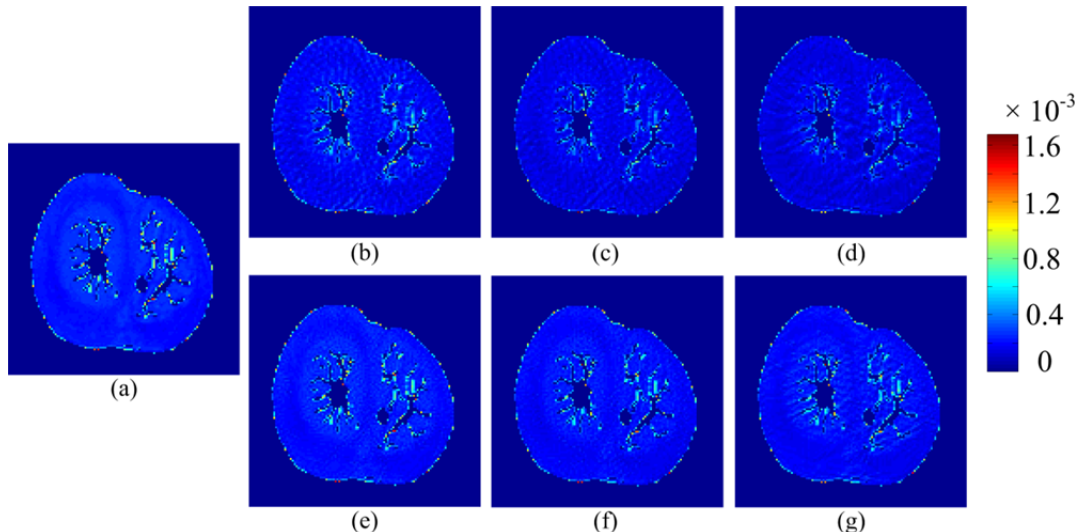


Fig. 6.7 Maps of MD of the simulated human heart data with 25% sampling rates. (a) Reconstruction from the complete k-space data. Reconstructions from undersampled k-space using (b) uniform-angle radial, (c) golden-angle radial, (d) random-angle radial, and (e)-(g) the corresponding randomly perturbed radial sampling of (b)-(d).

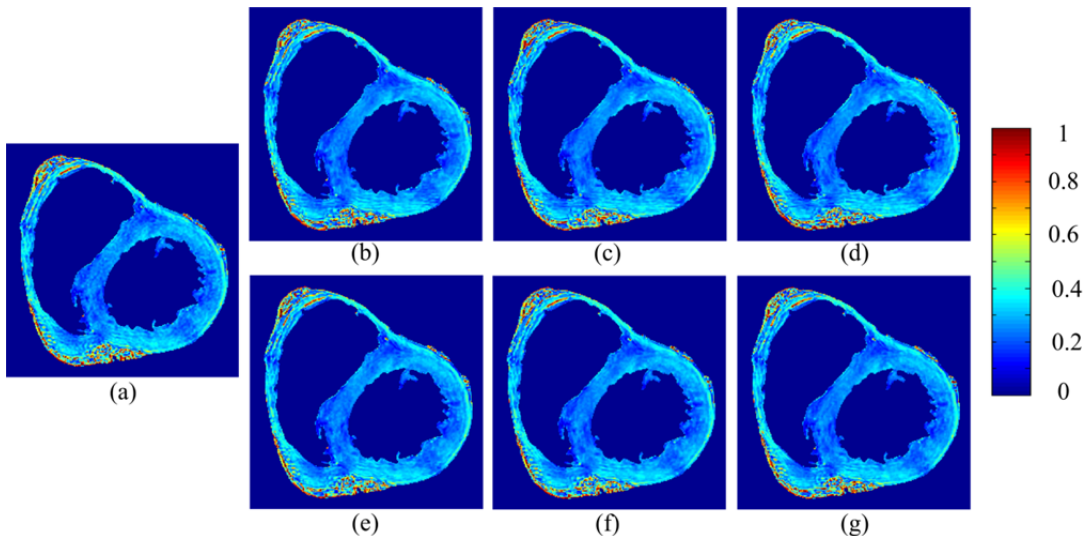


Fig. 6.8 Maps of FA of the real human heart data with 25% sampling rates. (a) Reconstruction from the complete k-space data. Reconstructions from undersampled k-space using (b) uniform-angle radial, (c) golden-angle radial, (d) random-angle radial, and (e)-(g) the corresponding randomly perturbed radial sampling of (b)-(d).

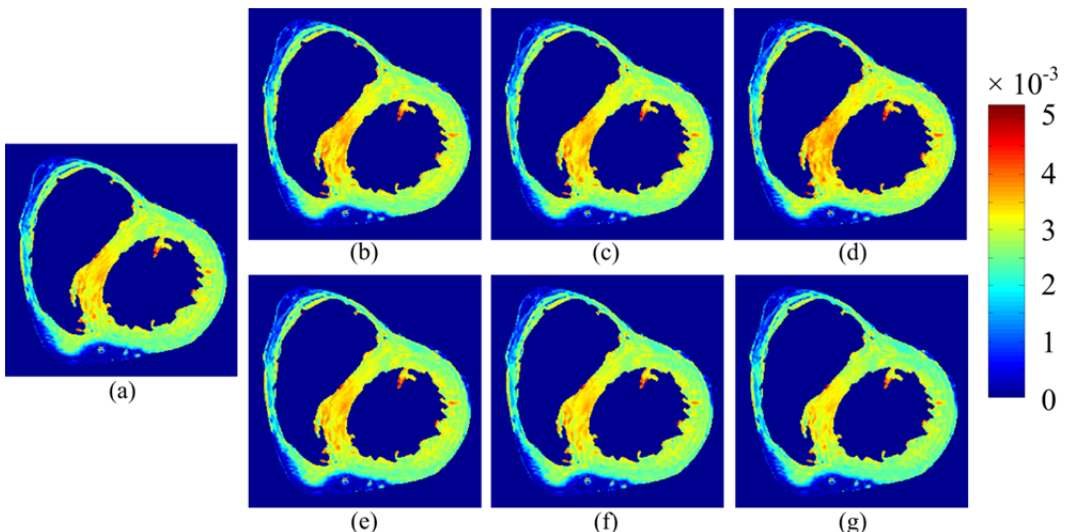


Fig. 6.9 Maps of MD of the real human heart data with 25% sampling rates. (a) Reconstruction from the complete k-space data. Reconstructions from undersampled k-space using (b) uniform-angle radial, (c) golden-angle radial, (d) random-angle radial, and (e)-(g) the corresponding randomly perturbed radial sampling of (b)-(d).

### 6.3.3 Tensor fields visualization

Fig. 6.10 and Fig. 6.11 shows the reconstructed tensor fields obtained using the six radial undersampling scheme (the uniformity-angle, golden-angle, random-angle sampling and the corresponding randomly perturbing the radial data resulted gives greater the visual effects compared to regular radial trajectories.

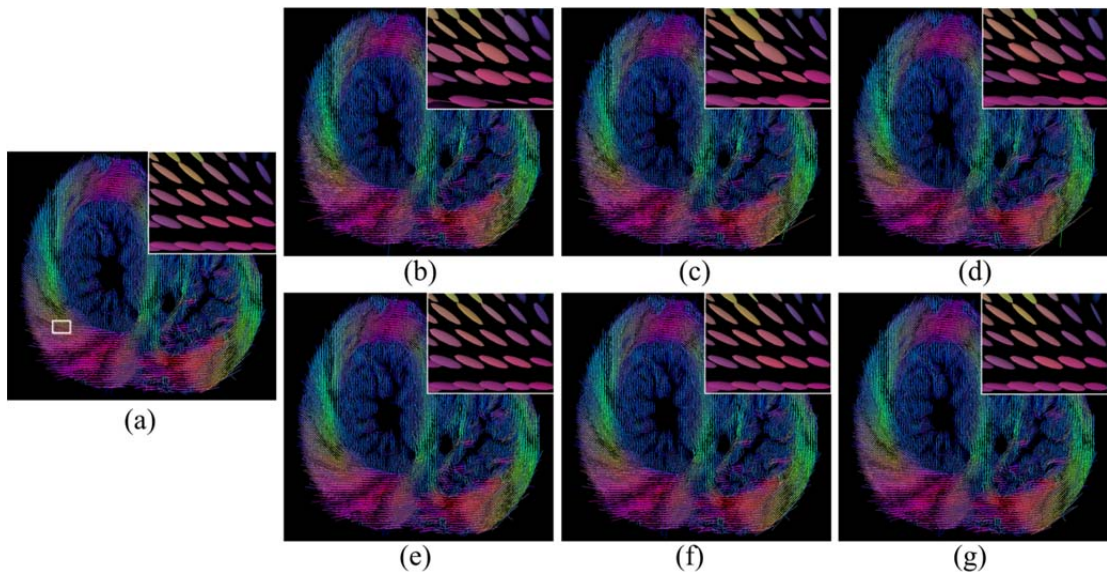


Fig. 6.10 The reconstruction tensor fields on simulated human heart data with sampling rates 25% and ISNR 30dB (Diffusion tensor field represented by arrows and ellipsoid. In order to enhance the orientation of the cardiac fibers, the tensor image is sampled with a ratio of 3 to 1, and shown on the top right corner of the each sub-figure). (a) Reconstruction from the complete k-space data. Reconstructions from undersampled k-space using (b) uniform-angle radial, (c) golden-angle radial, (d) random-angle radial, and (e)-(g) the corresponding randomly perturbed radial sampling of (b)-(d).

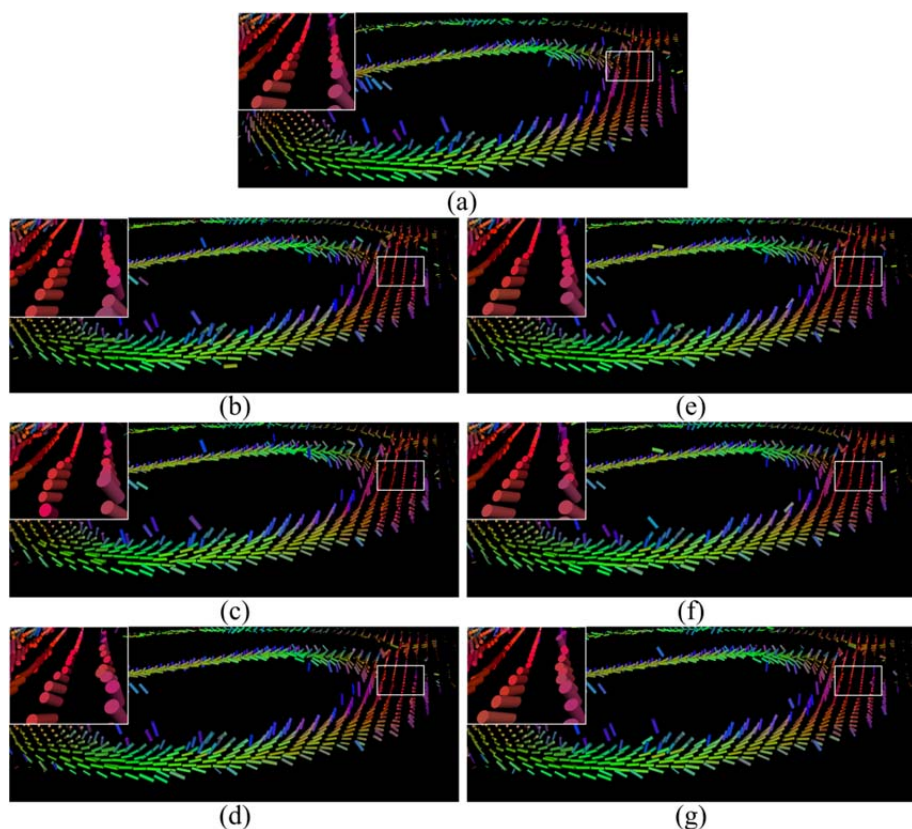


Fig. 6.11 The reconstruction tensor fields on real human heart data with sampling rates 25% and ISNR 30dB (Diffusion tensor field represented by arrows. In order to enhance the orientation of the cardiac fibers, the tensor image is sampled with a ratio of 3 to 1, and shown on the top right corner of the each sub-figure). (a) Reconstruction from the complete k-space data. Reconstructions from undersampled k-space using (b) uniform-angle radial, (c) golden-angle radial, (d) random-angle radial, and (e)-(g) the corresponding randomly perturbed radial sampling of (b)-(d).

## 6.4 Conclusion

This chapter proposed two randomly perturbed radial undersampling scheme for cardiac CS-DTMR imaging, that is randomly perturbed golden-angle and random-angle undersampling scheme. The effects of CS for cardiac DTMR imaging applied to several different radial k-space sampling schemes (uniformity-angle, golden-angle, random-angle sampling and the corresponding randomly perturbed sampling ). The results demonstrate that the experiments show that the choice of radial sampling pattern influences the reconstruction performance in CS-DTMR imaging. The CS reconstruction of undersampled randomly perturbing the radial data resulted in significant reduction of reconstruction error compared to regular radial trajectories. On the other hand, the uniformity-angle and golden-angle radial undersampling scheme more suitable for cardiac CS-DTMR image reconstruction.

## **PART III**

### **General Conclusion**

## Chapter 7

### General conclusions and perspectives

---

7.1 Contributions.....	125
7.2 Discussion and perspectives.....	126
7.3 Author's publications.....	126

---

## 7.1 Contributions

The research work presented in this thesis deals with the fast imaging techniques for MRI and more particularly for cardiac DTI based on the recent theory of CS.

Our first contribution is on the development of an improved CS reconstruction method for MR images by combining data-driven tight frame (data-driven TF) constraint and Total generalized variation (TGV) regularization together. The proposed reconstruction algorithm exploits data adaptive of data-driven TF and “selectively regularizes” of TGV to provide a better sparse approximation of images with varying content, and preserves sharp edges and fine structure of images. The experimental results demonstrate that the proposed approach improves the reconstruction performance, and preserves various image features (including edges and textures) in comparison with other commonly used sparsifying transforms for CS-MRI

Our second contribution concerns the study of a new CS reconstruction method that employs joint sparsity and rank deficiency prior to reconstructing cardiac DTMR images from the undersampled k-space data. Diffusion weighted images acquired in different diffusion directions are firstly stacked as columns to form the matrix. Such matrix is row sparse (i.e. few non-zero rows) in transform domain and also has a low rank. These two properties are then incorporated into the CS reconstruction framework. The experiments were carried out on both simulation and real human cardiac DTMR images. The results demonstrate that the proposed approach has lower reconstruction errors in terms of DTI indices, including fractional anisotropy (FA), mean diffusivities (MD), transverse angle and helix angle, compared to the existing CS-DTMR image reconstruction techniques.

Our third contribution is about the use of CS scheme with low rank constraint and total variation (TV) regularizations for reconstructing cardiac DTI images from highly undersampled k-space data. Two TV regularizations are considered: local TV (i.e. classical TV) and nonlocal TV (NLTv). The local TV constraint yields an effective removal of undersampling artifacts as well as an edge-preserving denoising of the image. The NLTv method can avoid blocking effects and preserve image details effectively. The experiments were carried out on both simulated and real human cardiac diffusion weightrd (DW) images. The results show that the proposed approaches present lower reconstruction errors compared to existing CS-DTI image reconstruction techniques, in terms of DTI indices such as fractional anisotropy (FA) and mean diffusivities (MD)

Our fourth contribution is on the investigation of various radial sampling schemes as well as reconstruction using CS. In particular, two randomly perturbed radial undersampling schemes (golden-angle and random angle) were proposed. The proposed methods were compared with existing radial undersampling methods such as uniformity-angle, randomly perturbed uniformity-angle, golden-angle, random angle. The results on both simulated and real human cardiac DW images show that for the same amount of k-space data, randomly sampling around a random radial line results in better reconstruction quality in terms of fractional anisotropy (FA) and mean diffusivities (MD), and that the randomly perturbed golden-angle undersampling yields the best results for cardiac CS-DTMR image reconstruction.

## 7.2 Discussion and perspectives

This present work proposed several efficient methods for reconstructing MRI and cardiac DTMR images from highly undersampled k-space data and investigated two radial undersampling schemes for cardiac DTMR based on the CS theory. The conducted experiments have demonstrated the effectiveness of our methods. In the light of these results, a number of interesting points can be formulated for future work:

- The results presented in this dissertation being on ex vivo heart, it would be interesting to apply the methods to in vivo cardiac DTI.
- The global low rank methods capture the global correlation among the whole images, but it completely ignores any local information. It would be interesting to use local low rank to improve reconstruction performance for cardiac CS-DTI.
- It is well known that parallel imaging technique can allow obtaining higher acceleration factors. Combining CS, parallel imaging and non-Cartesian trajectories may further speed up data acquisition and reduce cardiac motion artefacts for the DTI of the human heart.
- High Angular Resolution Diffusion Imaging (HARDI) has received recently intensive attention. It will be interesting to extend the proposed methods to HARDI.

## 7.3 Author's publications

- **Jianping Huang**, Wanyu Liu, Yanli Zhang, Isabelle E. Magnin, Yuemin Zhu. Cardiac Diffusion Tensor Imaging Based on Compressed Sensing Using Joint Sparsity and Low-Rank Approximation. *Journal of Medical Imaging and Health Informatics*, 1<sup>st</sup> round accepted.
- **Jianping Huang**, Lihui Wang, Chunyu Chu, Wanyu Liu, Isabelle E. Magnin and Yuemin Zhu. Compressed sensing MRI via data-driven tight frame and total generalized variation (TGV), *Physics in Medicine and Biology*, submitted.
- **Jianping Huang**, Wanyu Liu, Lihui Wang, and Yuemin Zhu. Combining total variation with nonlocal self-similarity constraint for compressed sensing MRI, 2014 IEEE 11th International Symposium on Biomedical Imaging (ISBI), 2014, pp. 1063-1066.
- **Jianping Huang**, Lihui Wang, Chuchun Yu, Yanli Zhang, Wanyu Liu, and Yuemin Zhu. Compressed sensing MR image reconstruction using data-driven tight frame, GRETSI 2015, Lyon, 4p, 2015.

## Bibliographies

- [A. Bilgin, 2008] T. P. T. A. Bilgin, A. F. Gmitro, and M. I. Altbach, "Randomly Perturbed Radial Trajectories for Compressed Sensing Mri," in ISMRM, Toronto, Canada, 2008.
- [Adluru *et al.*, 2007] G. Adluru, E. Hsu, and E. V. R. Di Bella, "Constrained Reconstruction of Sparse Cardiac Mr Dti Data," in Functional Imaging and Modeling of the Heart, Proceedings, Salt Lake, USA, 2007, pp. 91-99.
- [Adluru *et al.*, 2009] G. Adluru, C. McGann, P. Speier, E. G. Kholmovski, A. Shaaban, and E. V. R. DiBella, "Acquisition and Reconstruction of Undersampled Radial Data for Myocardial Perfusion Magnetic Resonance Imaging," *Journal of Magnetic Resonance Imaging*, vol. 29, no. 2, pp. 466-473, Feb, 2009.
- [Akcakaya *et al.*, 2011] M. Akcakaya, T. A. Basha, B. Goddu, L. A. Goepfert, K. V. Kissinger, V. Tarokh, W. J. Manning, and R. Nezafat, "Low-Dimensional-Structure Self-Learning and Thresholding: Regularization Beyond Compressed Sensing for Mri Reconstruction," *Magnetic Resonance in Medicine*, vol. 66, no. 3, pp. 756-767, Sep, 2011.
- [Assaf *et al.*, 2008] Y. Assaf, T. Blumenfeld-Katzir, Y. Yovel, and P. J. Basser, "Axcaliber: A Method for Measuring Axon Diameter Distribution from Diffusion Mri," *Magnetic Resonance in Medicine*, vol. 59, no. 6, pp. 1347-1354, Jun, 2008.
- [Assemlal *et al.*, 2011] H.-E. Assemlal, D. Tschumperle, L. Brun, and K. Siddiqi, "Recent Advances in Diffusion Mri Modeling: Angular and Radial Reconstruction," *Medical Image Analysis*, vol. 15, no. 4, pp. 369-396, Aug, 2011.
- [Bammer *et al.*, 2002] R. Bammer, M. Auer, S. L. Keeling, M. Augustin, L. A. Stables, R. W. Prokesch, R. Stollberger, M. E. Moseley, and F. Fazekas, "Diffusion Tensor Imaging Using Single-Shot Sense-Epi," *Magnetic Resonance in Medicine*, vol. 48, no. 1, pp. 128-136, Jul, 2002.
- [Bammer *et al.*, 2001] R. Bammer, S. L. Keeling, M. Augustin, K. P. Pruessmann, R. Wolf, R. Stollberger, H. P. Hartung, and F. Fazekas, "Improved Diffusion-Weighted Single-Shot Echo-Planar Imaging (Epi) in Stroke Using Sensitivity Encoding (Sense)," *Magnetic Resonance in Medicine*, vol. 46, no. 3, pp. 548-554, Sep, 2001.
- [Bao *et al.*, 2013] L. Bao, M. Robini, W. Liu, and Y. Zhu, "Structure-Adaptive Sparse Denoising for Diffusion-Tensor Mri," *Medical Image Analysis*, vol. 17, no. 4, pp. 442-457, May, 2013.
- [Baraniuk, 2007] R. G. Baraniuk, "Compressive Sensing," *Ieee Signal Processing Magazine*, vol. 24, no. 4, pp. 118, Jul, 2007.
- [Basser, 1995] P. J. Basser, "Inferring Microstructural Features and the Physiological State of Tissues from Diffusion-Weighted Images," *Nmr in Biomedicine*, vol. 8, no. 7-8, pp. 333-344, Nov-Dec, 1995.
- [Basser *et al.*, 1994a] P. J. Basser, J. Mattiello, and D. Lebihan, "Mr Diffusion Tensor Spectroscopy and Imaging," *Biophysical Journal*, vol. 66, no. 1, pp. 259-267, Jan, 1994a.
- [Basser *et al.*, 1994b] P. J. Basser, J. Mattiello, and D. Lebihan, "Estimation of the Effective Self-Diffusion Tensor from the Nmr Spin-Echo," *Journal of Magnetic Resonance Series B*, vol. 103, no. 3, pp. 247-254, Mar, 1994b.
- [Basser *et al.*, 1996] P. J. Basser, and C. Pierpaoli, "Microstructural and Physiological Features of Tissues Elucidated by Quantitative-Diffusion-Tensor Mri," *Journal of Magnetic Resonance Series B*, vol. 111, no. 3, pp. 209-219, Jun, 1996.
- [Beaulieu, 2002] C. Beaulieu, "The Basis of Anisotropic Water Diffusion in the Nervous System - a Technical Review," *Nmr in Biomedicine*, vol. 15, no. 7-8, pp. 435-455, Nov-Dec, 2002.

- [Beck *et al.*, 2009a] A. Beck, and M. Teboulle, "Fast Gradient-Based Algorithms for Constrained Total Variation Image Denoising and Deblurring Problems," *Ieee Transactions on Image Processing*, vol. 18, no. 11, pp. 2419-2434, Nov, 2009a.
- [Beck *et al.*, 2009b] A. Beck, and M. Teboulle, "A Fast Iterative Shrinkage-Thresholding Algorithm for Linear Inverse Problems," *Siam Journal on Imaging Sciences*, vol. 2, no. 1, pp. 183-202, 2009, 2009b.
- [Bernstein *et al.*, 2004] M. A. Bernstein, K. F. King, and X. J. Zhou, *Handbook of Mri Pulse Sequences*: Academic Press, 2004.
- [Beurling, 1938] A. Beurling, "Sur Les Intégrales De Fourier Absolument Convergentes Et Leur Applicationa Une Transformation Fonctionnelle." pp. 345-366.
- [Bilen, 2013] C. Bilen, "Compressed Sensing for Dynamic Parallel Magnetic Resonance Imaging," POLYTECHNIC INSTITUTE OF NEW YORK UNIVERSITY, 2013.
- [Blaimer *et al.*, 2004] M. Blaimer, F. Breuer, M. Mueller, R. M. Heidemann, M. A. Griswold, and P. M. Jakob, "Smash, Sense, Pils, Grappa: How to Choose the Optimal Method," *Topics in magnetic resonance imaging : TMRI*, vol. 15, no. 4, pp. 223-236, 2004-Aug, 2004.
- [Blink, 2004] E. J. Blink, "Mri: Physics," *Online PDF file*, 2004.
- [Bloch, 1946] F. Bloch, "Nuclear Induction," *Physical Review*, vol. 70, no. 7-8, pp. 460, 1946.
- [Block, 2008] K. T. Block, "Advanced Methods for Radial Data Sampling in Magnetic Resonance Imaging," Niedersächsische Staats-und Universitätsbibliothek Göttingen, 2008.
- [Block *et al.*, 2007] K. T. Block, M. Uecker, and J. Frahm, "Undersampled Radial Mri with Multiple Coils. Iterative Image Reconstruction Using a Total Variation Constraint," *Magnetic Resonance in Medicine*, vol. 57, no. 6, pp. 1086-1098, Jun, 2007.
- [Bredies *et al.*, 2010] K. Bredies, K. Kunisch, and T. Pock, "Total Generalized Variation," *Siam Journal on Imaging Sciences*, vol. 3, no. 3, pp. 492-526, 2010, 2010.
- [Brown *et al.*, 2014] R. W. Brown, Y.-C. N. Cheng, E. M. Haacke, M. R. Thompson, and R. Venkatesan, *Magnetic Resonance Imaging: Physical Principles and Sequence Design*: John Wiley & Sons, 2014.
- [Buades *et al.*, 2005] A. Buades, B. Coll, and J. M. Morel, "A Review of Image Denoising Algorithms, with a New One," *Multiscale Modeling & Simulation*, vol. 4, no. 2, pp. 490-530, 2005, 2005.
- [Buckberg *et al.*, 2008] G. Buckberg, J. I. E. Hoffman, A. Mahajan, S. Saleh, and C. Coghlan, "Cardiac Mechanics Revisited the Relationship of Cardiac Architecture to Ventricular Function," *Circulation*, vol. 118, no. 24, pp. 2571-2587, Dec 9, 2008.
- [Cai *et al.*, 2014] J.-F. Cai, H. Ji, Z. Shen, and G.-B. Ye, "Data-Driven Tight Frame Construction and Image Denoising," *Applied and Computational Harmonic Analysis*, vol. 37, no. 1, pp. 89-105, Jul, 2014.
- [Cai *et al.*, 2010] J.-F. Cai, and Z. Shen, "Framelet Based Deconvolution," *Journal of Computational Mathematics*, vol. 28, no. 3, pp. 289-308, May, 2010.
- [Callaghan, 1993] P. T. Callaghan, *Principles of Nuclear Magnetic Resonance Microscopy*: Oxford University Press, 1993.
- [Candes, 2008] E. J. Candes, "Sparsity and Incoherence in Compressive Sampling," *Comptes Rendus Mathematique*, vol. 346, no. 9-10, pp. 589-592, May, 2008.
- [Candes *et al.*, 2011] E. J. Candes, Y. C. Eldar, D. Needell, and P. Randall, "Compressed Sensing with Coherent and Redundant Dictionaries," *Applied and Computational Harmonic Analysis*, vol. 31, no. 1, pp. 59-73, Jul, 2011.
- [Candes *et al.*, 2006a] E. J. Candes, J. Romberg, and T. Tao, "Robust Uncertainty Principles: Exact Signal Reconstruction from Highly Incomplete Frequency Information," *Ieee Transactions on Information Theory*, vol. 52, no. 2, pp. 489-509, Feb, 2006a.
- [Candes *et al.*, 2006b] E. J. Candes, J. K. Romberg, and T. Tao, "Stable Signal Recovery from Incomplete and Inaccurate Measurements," *Communications on pure and applied mathematics*, vol. 59, no. 8, pp. 1207-1223, Aug, 2006b.

- [Candes *et al.*, 2005] E. J. Candes, and T. Tao, "Decoding by Linear Programming," *Ieee Transactions on Information Theory*, vol. 51, no. 12, pp. 4203-4215, Dec, 2005.
- [Candes *et al.*, 2006c] E. J. Candes, and T. Tao, "Near Optimal Signal Recovery from Random Projections: Universal Encoding Strategies?," *Ieee Transactions on Information Theory*, vol. 52, no. 12, pp. 5406-5425, Dec, 2006c.
- [Candes *et al.*, 2008] E. J. Candes, and M. B. Wakin, "An Introduction to Compressive Sampling," *Ieee Signal Processing Magazine*, vol. 25, no. 2, pp. 21-30, Mar, 2008.
- [Carmi *et al.*, 2014] A. Y. Carmi, L. Mihaylova, and S. J. Godsill, *Compressed Sensing & Sparse Filtering*: Springer, 2014.
- [Carrillo *et al.*, 2012] R. E. Carrillo, J. D. McEwen, and Y. Wiaux, "Sparsity Averaging Reweighted Analysis (Sara): A Novel Algorithm for Radio-Interferometric Imaging," *Monthly Notices of the Royal Astronomical Society*, vol. 426, no. 2, pp. 1223-1234, Oct, 2012.
- [Chan *et al.*, 2004] R. H. Chan, S. D. Riemenschneider, L. X. Shen, and Z. W. Shen, "Tight Frame: An Efficient Way for High-Resolution Image Reconstruction," *Applied and Computational Harmonic Analysis*, vol. 17, no. 1, pp. 91-115, Jul, 2004.
- [Chan *et al.*, 2012] R. W. Chan, E. A. Ramsay, E. Y. Cheung, and D. B. Plewes, "The Influence of Radial Undersampling Schemes on Compressed Sensing Reconstruction in Breast MRI," *Magnetic Resonance in Medicine*, vol. 67, no. 2, pp. 363-377, Feb, 2012.
- [Chen *et al.*, 2014] C. Chen, and J. Huang, "The Benefit of Tree Sparsity in Accelerated MRI," *Medical Image Analysis*, vol. 18, no. 6, pp. 834-842, Aug, 2014.
- [Chen *et al.*, 2003] J. J. Chen, S. K. Song, W. Liu, M. McLean, J. S. Allen, J. Tan, S. A. Wickline, and X. Yu, "Remodeling of Cardiac Fiber Structure after Infarction in Rats Quantified with Diffusion Tensor MRI," *American Journal of Physiology-Heart and Circulatory Physiology*, vol. 285, no. 3, pp. H946-H954, Sep, 2003.
- [Chen *et al.*, 2001] S. S. B. Chen, D. L. Donoho, and M. A. Saunders, "Atomic Decomposition by Basis Pursuit," *SIAM review*, vol. 43, no. 1, pp. 129-159, Mar, 2001.
- [Chen *et al.*, 2010] Y. Chen, X. Ye, and F. Huang, "A Novel Method and Fast Algorithm for Mr Image Reconstruction with Significantly under-Sampled Data," *Inverse Problems and Imaging*, vol. 4, no. 2, pp. 223-240, May, 2010.
- [Christodoulou *et al.*, 2014] A. G. Christodoulou, P. Kellman, and L. Zhi-Pei, "Accelerating Cardiovascular Magnetic Resonance Imaging: Signal Processing Meets Nuclear Spins," *Ieee Signal Processing Magazine*, vol. 31, no. 5, pp. 138-143, Sept., 2014.
- [Coifman *et al.*, 2001] R. Coifman, F. Geshwind, and Y. Meyer, "Noiselets," *Applied and Computational Harmonic Analysis*, vol. 10, no. 1, pp. 27-44, Jan, 2001.
- [Compton *et al.*, 2012] R. Compton, S. Osher, and L. Bouchard, "Hybrid Regularization for MRI Reconstruction with Static Field Inhomogeneity Correction," *2012 IEEE 9th International Symposium on Biomedical Imaging*, pp. 650-655, 01 01, 2012.
- [Constantinides, 2014] C. Constantinides, *Magnetic Resonance Imaging: The Basics*: CRC press, 2014.
- [Corno *et al.*, 2006] A. F. Corno, M. J. Kocica, and F. Torrent-Guasp, "The Helical Ventricular Myocardial Band of Torrent-Guasp: Potential Implications in Congenital Heart Defects," *European Journal of Cardio-Thoracic Surgery*, vol. 29, pp. S61-S68, Apr, 2006.
- [Coupe *et al.*, 2008] P. Coupe, P. Yger, S. Prima, P. Hellier, C. Kervrann, and C. Barillot, "An Optimized Blockwise Nonlocal Means Denoising Filter for 3-D Magnetic Resonance Images," *Ieee Transactions on Medical Imaging*, vol. 27, no. 4, pp. 425-441, Apr, 2008.
- [Dabov *et al.*, 2007] K. Dabov, A. Foi, V. Katkovnik, and K. Egiazarian, "Image Denoising by Sparse 3-D Transform-Domain Collaborative Filtering," *Ieee Transactions on Image Processing*, vol. 16, no. 8, pp. 2080-2095, Aug, 2007.

- [Daubechies *et al.*, 2003] I. Daubechies, B. Han, A. Ron, and Z. W. Shen, "Framelets: Mra-Based Constructions of Wavelet Frames," *Applied and Computational Harmonic Analysis*, vol. 14, no. 1, pp. 1-46, Jan, 2003.
- [DeVore, 1998] R. A. DeVore, "Nonlinear Approximation," *Acta Numerica*, vol. 7, pp. 51-150, 1998.
- [Dominguez-Rodriguez *et al.*, 2013] A. Dominguez-Rodriguez, and P. Abreu-Gonzalez, "Hypertrophic Cardiomyopathy," *Lancet*, vol. 381, no. 9876, pp. 1456-1457, Apr 27, 2013.
- [Donoho, 1995] D. L. Donoho, "De-Noising by Soft-Thresholding," *Ieee Transactions on Information Theory*, vol. 41, no. 3, pp. 613-627, May, 1995.
- [Donoho, 2006] D. L. Donoho, "Compressed Sensing," *Ieee Transactions on Information Theory*, vol. 52, no. 4, pp. 1289-1306, Apr, 2006.
- [Donoho *et al.*, 2001] D. L. Donoho, and X. M. Huo, "Uncertainty Principles and Ideal Atomic Decomposition," *Ieee Transactions on Information Theory*, vol. 47, no. 7, pp. 2845-2862, Nov, 2001.
- [Donoho *et al.*, 1989] D. L. Donoho, and P. B. Stark, "Uncertainty Principles and Signal Recovery," *SIAM Journal on Applied Mathematics*, vol. 49, no. 3, pp. 906-931, Jun, 1989.
- [Dou *et al.*, 2002] J. G. Dou, T. G. Reese, W. Y. I. Tseng, and V. J. Wedeen, "Cardiac Diffusion MRI without Motion Effects," *Magnetic Resonance in Medicine*, vol. 48, no. 1, pp. 105-114, Jul, 2002.
- [Dou *et al.*, 2003] J. G. Dou, W. Y. I. Tseng, T. G. Reese, and V. J. Wedeen, "Combined Diffusion and Strain MRI Reveals Structure and Function of Human Myocardial Laminar Sheets in Vivo," *Magnetic Resonance in Medicine*, vol. 50, no. 1, pp. 107-113, Jul, 2003.
- [Duarte *et al.*, 2013] M. F. Duarte, and R. G. Baraniuk, "Spectral Compressive Sensing," *Applied and Computational Harmonic Analysis*, vol. 35, no. 1, pp. 111-129, Jul, 2013.
- [Duarte *et al.*, 2011] M. F. Duarte, and Y. C. Eldar, "Structured Compressed Sensing: From Theory to Applications," *Ieee Transactions on Signal Processing*, vol. 59, no. 9, pp. 4053-4085, Sep, 2011.
- [Einstein, 1956] A. Einstein, *Investigations on the Theory of the Brownian Movement*: Courier Corporation, 1956.
- [El-Metwally *et al.*, 2008] S. M. El-Metwally, K. Z. Abd-Elmoniem, A. M. Youssef, and Y. M. Kadah, "Rapid Cardiac MRI Using Random Radial Trajectories," *Journal of Engineering and Applied Science*, vol. 55, no. 5, pp. 441-456, Oct., 2008.
- [Eldar, 2009] Y. C. Eldar, "Uncertainty Relations for Shift-Invariant Analog Signals," *Ieee Transactions on Information Theory*, vol. 55, no. 12, pp. 5742-5757, Dec, 2009.
- [Eldar *et al.*, 2012] Y. C. Eldar, and G. Kutyniok, *Compressed Sensing: Theory and Applications*: Cambridge University Press, 2012.
- [Eldar *et al.*, 2009] Y. C. Eldar, and T. Michaeli, "Beyond Bandlimited Sampling," *Ieee Signal Processing Magazine*, vol. 26, no. 3, pp. 48-68, May, 2009.
- [Elmaoğlu *et al.*, 2011] M. Elmaoğlu, and A. Çelik, *MRI Handbook: MRI Physics, Patient Positioning, and Protocols*: Springer, 2011.
- [Elmoataz *et al.*, 2008] A. Elmoataz, O. Lezoray, and S. Bougleux, "Nonlocal Discrete Regularization on Weighted Graphs: A Framework for Image and Manifold Processing," *Ieee Transactions on Image Processing*, vol. 17, no. 7, pp. 1047-1060, Jul, 2008.
- [Feng *et al.*, 2014] L. Feng, R. Grimm, K. T. Block, H. Chandarana, S. Kim, J. Xu, L. Axel, D. K. Sodickson, and R. Otazo, "Golden-Angle Radial Sparse Parallel MRI: Combination of Compressed Sensing, Parallel Imaging, and Golden-Angle Radial Sampling for Fast and Flexible Dynamic Volumetric MRI," *Magnetic Resonance in Medicine*, vol. 72, no. 3, pp. 707-717, Sep, 2014.
- [Feng, 1997] P. Feng, "Universal Spectrum Blind Minimum Rate Sampling and Reconstruction of Multiband Signals," PhD thesis, University of Illinois at Urbana-Champaign, 1997.

- [Fernandez-Miranda, 2013] J. C. Fernandez-Miranda, “Beyond Diffusion Tensor Imaging,” *Journal of Neurosurgery*, vol. 118, no. 6, pp. 1363-1365, Jun, 2013.
- [Fessler, 2007] J. A. Fessler, “On Nufft-Based Gridding for Non-Cartesian Mri,” *Journal of Magnetic Resonance*, vol. 188, no. 2, pp. 191-195, Oct, 2007.
- [Fessler *et al.*, 2003] J. A. Fessler, and B. P. Sutton, “Nonuniform Fast Fourier Transforms Using Min-Max Interpolation,” *Ieee Transactions on Signal Processing*, vol. 51, no. 2, pp. 560-574, Feb, 2003.
- [Filli *et al.*, 2015] L. Filli, M. Piccirelli, D. Kenkel, R. Guggenberger, G. Andreisek, T. Beck, V. M. Runge, and A. Boss, “Simultaneous Multislice Echo Planar Imaging with Blipped Controlled Aliasing in Parallel Imaging Results in Higher Acceleration a Promising Technique for Accelerated Diffusion Tensor Imaging of Skeletal Muscle,” *Investigative Radiology*, vol. 50, no. 7, pp. 456-463, Jul, 2015.
- [Foltz *et al.*, 2012] W. D. Foltz, and D. A. Jaffray, “Principles of Magnetic Resonance Imaging,” *Radiation Research*, vol. 177, no. 4, pp. 331-348, Apr, 2012.
- [Fornasier *et al.*, 2008] M. Fornasier, and H. Rauhut, “Iterative Thresholding Algorithms,” *Applied and Computational Harmonic Analysis*, vol. 25, no. 2, pp. 187-208, Sep, 2008.
- [Foucart *et al.*, 2013] S. Foucart, and H. Rauhut, *A Mathematical Introduction to Compressive Sensing*: Springer, 2013.
- [Frank, 2001] L. R. Frank, “Anisotropy in High Angular Resolution Diffusion-Weighted Mri,” *Magnetic Resonance in Medicine*, vol. 45, no. 6, pp. 935-939, Jun, 2001.
- [Frank, 2002] L. R. Frank, “Characterization of Anisotropy in High Angular Resolution Diffusion-Weighted Mri,” *Magnetic Resonance in Medicine*, vol. 47, no. 6, pp. 1083-1099, Jun, 2002.
- [Froeling *et al.*, 2014] M. Froeling, G. Strijkers, A. Nederveen, S. Chamuleau, and P. Luijten, “Diffusion Tensor Mri of the Heart – in Vivo Imaging of Myocardial Fiber Architecture,” *Current Cardiovascular Imaging Reports*, vol. 7, no. 7, pp. 1-11, 2014.
- [Gao *et al.*, 2014] H. Gao, L. Li, K. Zhang, W. Zhou, and X. Hu, “Pclr: Phase-Constrained Low-Rank Model for Compressive Diffusion-Weighted Mri,” *Magnetic Resonance in Medicine*, vol. 72, no. 5, pp. 1330-1341, Nov, 2014.
- [Gho *et al.*, 2010] S.-M. Gho, Y. Nam, S.-Y. Zho, E. Y. Kim, and D.-H. Kim, “Three Dimension Double Inversion Recovery Gray Matter Imaging Using Compressed Sensing,” *Magnetic Resonance Imaging*, vol. 28, no. 10, pp. 1395-1402, Dec, 2010.
- [Gilboa *et al.*, 2008] G. Gilboa, and S. Osher, “Nonlocal Operators with Applications to Image Processing,” *SIAM Multiscale Modeling and Simulation*, vol. 7, no. 3, pp. 1005-1028, 2008, 2008.
- [Glover *et al.*, 1992] G. H. Glover, and J. M. Pauly, “Projection Reconstruction Techniques for Reduction of Motion Effects in Mri,” *Magnetic Resonance in Medicine*, vol. 28, no. 2, pp. 275-289, Dec, 1992.
- [Go *et al.*, 2014] A. S. Go, D. Mozaffarian, V. L. Roger, E. J. Benjamin, J. D. Berry, M. J. Blaha, S. Dai, E. S. Ford, C. S. Fox, S. Franco, H. J. Fullerton, C. Gillespie, S. M. Hailpern, J. A. Heit, V. J. Howard, M. D. Huffman, S. E. Judd, B. M. Kissela, S. J. Kittner, D. T. Lackland, J. H. Lichtman, L. D. Lisabeth, R. H. Mackey, D. J. Magid, G. M. Marcus, A. Marelli, D. B. Matchar, D. K. McGuire, E. R. Mohler, III, C. S. Moy, M. E. Mussolini, R. W. Neumar, G. Nichol, D. K. Pandey, N. P. Paynter, M. J. Reeves, P. D. Sorlie, J. Stein, A. Towfighi, T. N. Turan, S. S. Virani, N. D. Wong, D. Woo, M. B. Turner, C. Amer Heart Assoc Stat, and S. Stroke Stat, “Heart Disease and Stroke Statistics-2014 Update a Report from the American Heart Association,” *Circulation*, vol. 129, no. 3, pp. E28-E292, Jan 21, 2014.
- [Goel *et al.*, 2013] N. S. Goel, and N. Richter-Dyn, *Stochastic Models in Biology*: Elsevier, 2013.
- [Gopi *et al.*, 2014] V. P. Gopi, P. Palanisamy, K. A. Wahid, and P. Babyn, “Mr Image Reconstruction Based on Framelets and Nonlocal Total Variation Using Split Bregman Method,” *International Journal of Computer Assisted Radiology and Surgery*, vol. 9, no. 3, pp. 459-472, May, 2014.

- [Gorodnitsky *et al.*, 1995] I. F. Gorodnitsky, J. S. George, and B. D. Rao, "Neuromagnetic Source Imaging with Focuss - a Recursive Weighted Minimum Norm Algorithm," *Electroencephalography and Clinical Neurophysiology*, vol. 95, no. 4, pp. 231-251, Oct, 1995.
- [Gorodnitsky *et al.*, 1997] I. F. Gorodnitsky, and B. D. Rao, "Sparse Signal Reconstruction from Limited Data Using Focuss: A Re-Weighted Minimum Norm Algorithm," *Ieee Transactions on Signal Processing*, vol. 45, no. 3, pp. 600-616, Mar, 1997.
- [Gorodnitsky *et al.*, 1992] I. F. Gorodnitsky, B. D. Rao, and J. George, *Source Localization in Magnetoencephalography Using an Iterative Weighted Minimum Norm Algorithm*, 1992.
- [Gossuin *et al.*, 2010] Y. Gossuin, A. Hocq, P. Gillis, and Q. L. Vuong, "Physics of Magnetic Resonance Imaging: From Spin to Pixel," *Journal of Physics D-Applied Physics*, vol. 43, no. 21, Jun 2, 2010.
- [Graff *et al.*, 2015] C. G. Graff, and E. Y. Sidky, "Compressive Sensing in Medical Imaging," *Applied Optics*, vol. 54, no. 8, pp. C23-C44, Mar 10, 2015.
- [Griswold *et al.*, 2002] M. A. Griswold, P. M. Jakob, R. M. Heidemann, M. Nittka, V. Jellus, J. M. Wang, B. Kiefer, and A. Haase, "Generalized Autocalibrating Partially Parallel Acquisitions (Grappa)," *Magnetic Resonance in Medicine*, vol. 47, no. 6, pp. 1202-1210, Jun, 2002.
- [Groot *et al.*, 1963] S. R. Groot, P. Mazur, and A. L. King, "Non-Equilibrium Thermodynamics," *American Journal of Physics*, vol. 31, no. 7, pp. 558-559, 1963.
- [Guo *et al.*, 2014] W. Guo, J. Qin, and W. Yin, "A New Detail-Preserving Regularization Scheme," *Siam Journal on Imaging Sciences*, vol. 7, no. 2, pp. 1309-1334, 2014, 2014.
- [Gupta *et al.*, 2012] A. Gupta, G. S. Gulati, S. Seth, and S. Sharma, "Cardiac MRI in Restrictive Cardiomyopathy," *Clinical Radiology*, vol. 67, no. 2, pp. 95-105, Feb, 2012.
- [Haacke *et al.*, 1999] E. M. Haacke, R. W. Brown, M. Thompson, and R. Venkatesan, "Magnetic Resonance Imaging: Physical Principles and Sequence Design," *Recherche*, vol. 67, pp. 02, 1999.
- [Hahn, 1950] E. L. Hahn, "Spin Echoes," *Physical Review*, vol. 80, no. 4, pp. 580, 1950.
- [Haldar *et al.*, 2013] J. P. Haldar, V. J. Wedeen, M. Nezamzadeh, G. Dai, M. W. Weiner, N. Schuff, and Z.-P. Liang, "Improved Diffusion Imaging through Snr-Enhancing Joint Reconstruction," *Magnetic Resonance in Medicine*, vol. 69, no. 1, pp. 277-289, Jan, 2013.
- [Hansen *et al.*, 1993] P. C. Hansen, and D. P. O'leary, "The Use of the L-Curve in the Regularization of Discrete Ill-Posed Problems," *Siam Journal on Scientific Computing*, vol. 14, no. 6, pp. 1487-1503, Nov, 1993.
- [Hao Gao *et al.*, 2013] Hao Gao, L. Li, and a. X. Hu, "Compressive Diffusion MRI- Part 1 Why Low-Rank."
- [He *et al.*, 2009] L. He, and L. Carin, "Exploiting Structure in Wavelet-Based Bayesian Compressive Sensing," *Ieee Transactions on Signal Processing*, vol. 57, no. 9, pp. 3488-3497, Sep, 2009.
- [Helm *et al.*, 2005a] P. Helm, M. F. Beg, M. I. Miller, and R. L. Winslow, "Measuring and Mapping Cardiac Fiber and Laminar Architecture Using Diffusion Tensor Mr Imaging," *Annals of the New York Academy of Sciences*, vol. 1047, no. 1, pp. 296-307, 2005a.
- [Helm *et al.*, 2005b] P. A. Helm, H. J. Tseng, L. Younes, E. R. McVeigh, and R. L. Winslow, "Ex Vivo 3d Diffusion Tensor Imaging and Quantification of Cardiac Laminar Structure," *Magnetic Resonance in Medicine*, vol. 54, no. 4, pp. 850-859, Oct, 2005b.
- [Helm *et al.*, 2006] P. A. Helm, L. Younes, M. F. Beg, D. B. Ennis, C. Leclercq, O. P. Faris, E. McVeigh, D. Kass, M. I. Miller, and R. L. Winslow, "Evidence of Structural

- Remodeling in the Dyssynchronous Failing Heart," *Circulation research*, vol. 98, no. 1, pp. 125-132, Jan 6, 2006.
- [Holdsworth *et al.*, 2009] S. J. Holdsworth, S. Skare, R. D. Newbould, and R. Bammer, "Robust Grappa-Accelerated Diffusion-Weighted Readout-Segmented (Rs)-Epi," *Magnetic Resonance in Medicine*, vol. 62, no. 6, pp. 1629-1640, Dec, 2009.
- [Hong *et al.*, 2011] M. Hong, Y. Yu, H. Wang, F. Liu, and S. Crozier, "Compressed Sensing Mri with Singular Value Decomposition-Based Sparsity Basis," *Physics in Medicine and Biology*, vol. 56, no. 19, pp. 6311-6325, Oct 7, 2011.
- [Hornak, 2008] J. P. Hornak, "The Basics of Mri, 2008," <https://www.cis.rit.edu/htbooks/mri/>, vol. 68, 2008.
- [Hsu *et al.*, 2001] E. W. Hsu, and C. S. Henriquez, "Myocardial Fiber Orientation Mapping Using Reduced Encoding Diffusion Tensor Imaging," *Journal of Cardiovascular Magnetic Resonance*, vol. 3, no. 4, pp. 339-347, 2001, 2001.
- [Huang *et al.*, 2014] J.-P. Huang, W.-Y. Liu, L.-H. Wang, and Y.-M. Zhu, "Combining Total Variation with Nonlocal Self-Similarity Constraint for Compressed Sensing Mri," in Biomedical Imaging (ISBI), 2014 IEEE 11th International Symposium on, 2014, pp. 1063-1066.
- [Huang *et al.*, 2015a] J.-P. Huang, W.-Y. Liu, Y.-L. Zhang, E. M. Isabelle, and Y.-M. Zhu, "Cardiac Diffusion Tensor Imaging Based on Compressed Sensing Using Joint Sparsity and Low-Rank Approximation," in The 4th International Conference on Biomedical Engineering and Biotechnology (ICBEB2015), Shanghai, China, 2015a.
- [Huang *et al.*, 2015b] J.-P. Huang, L.-H. Wang, C.-Y. Chu, Y.-L. Zhang, W.-Y. Liu, and Y.-M. Zhu, "Compressed Sensing Mr Image Reconstruction Using Data-Driven Tight Frame," in GRETSI 2015, Lyon, France, 2015b.
- [Huang *et al.*, 2015c] J. Huang, L. Guo, Q. Feng, W. Chen, and Y. Feng, "Sparsity-Promoting Orthogonal Dictionary Updating for Image Reconstruction from Highly Undersampled Magnetic Resonance Data," *Physics in Medicine and Biology*, vol. 60, no. 14, pp. 5359-5380, Jul 21, 2015c.
- [Huang *et al.*, 2011a] J. Huang, S. Zhang, H. Li, and D. Metaxas, "Composite Splitting Algorithms for Convex Optimization," *Computer Vision and Image Understanding*, vol. 115, no. 12, pp. 1610-1622, Dec, 2011a.
- [Huang *et al.*, 2011b] J. Huang, S. Zhang, and D. Metaxas, "Efficient Mr Image Reconstruction for Compressed Mr Imaging," *Medical Image Analysis*, vol. 15, no. 5, pp. 670-679, Oct, 2011b.
- [Huppi *et al.*, 2006] P. S. Huppi, and J. Dubois, "Diffusion Tensor Imaging of Brain Development," *Seminars in Fetal & Neonatal Medicine*, vol. 11, no. 6, pp. 489-497, Dec, 2006.
- [Jackson *et al.*, 1991] J. I. Jackson, C. H. Meyer, D. G. Nishimura, and A. Macovski, "Selection of a Convolution Function for Fourier Inversion Using Gridding," *Ieee Transactions on Medical Imaging*, vol. 10, no. 3, pp. 473-478, Sep, 1991.
- [Jacques *et al.*, 2011] L. Jacques, L. Duval, C. Chaux, and G. Peyre, "A Panorama on Multiscale Geometric Representations, Intertwining Spatial, Directional and Frequency Selectivity," *Signal Processing*, vol. 91, no. 12, pp. 2699-2730, Dec, 2011.
- [Jacques *et al.*, 2010] L. Jacques, and P. Vandergheynst, "Compressed Sensing: "When Sparsity Meets Sampling", " *Optical and Digital Image Processing*, pp. 507-527, 2010.
- [Jaermann *et al.*, 2004] T. Jaermann, G. Crelier, K. P. Pruessmann, X. Golay, T. Netsch, A. M. C. van Muiswinkel, S. Mori, P. C. M. van Zijl, A. Valavanis, S. Kollias, and P. Boesiger, "Sense-Dti at 3 T," *Magnetic Resonance in Medicine*, vol. 51, no. 2, pp. 230-236, Feb, 2004.
- [Jefferies *et al.*, 2010] J. L. Jefferies, and J. A. Towbin, "Dilated Cardiomyopathy," *Lancet*, vol. 375, no. 9716, pp. 752-762, Feb 27, 2010.
- [Jiang *et al.*, 2005] Y. Jiang, and E. W. Hsu, "Accelerating Mr Diffusion Tensor Imaging Via Filtered Reduced-Encoding Projection-Reconstruction," *Magnetic Resonance in Medicine*, vol. 53, no. 1, pp. 93-102, Jan, 2005.

- [Jing *et al.*, 2013] Q. Jing, and G. Weihong, "An Efficient Compressive Sensing Mr Image Reconstruction Scheme," *2013 IEEE 10th International Symposium on Biomedical Imaging: From Nano to Macro (ISBI 2013)*, pp. 306-309, 2013, 2013.
- [Johansen-Berg *et al.*, 2013] H. Johansen-Berg, and T. E. Behrens, *Diffusion Mri: From Quantitative Measurement to in Vivo Neuroanatomy*: Academic Press, 2013.
- [Jones, 2011] D. K. Jones, *Diffusion Mri Theory Methods and Applications*, p.^pp. 784: Oxford University Press, USA; 1 edition (December 6, 2010), 2011.
- [Jouk *et al.*, 2007] P.-S. Jouk, A. Mourad, V. Milisic, G. Michalowicz, A. Raoult, D. Caillerie, and Y. Usson, "Analysis of the Fiber Architecture of the Heart by Quantitative Polarized Light Microscopy. Accuracy, Limitations and Contribution to the Study of the Fiber Architecture of the Ventricles During Fetal and Neonatal Life," *European Journal of Cardio-Thoracic Surgery*, vol. 31, no. 5, pp. 915-921, May, 2007.
- [Jouk *et al.*, 1995] P. S. Jouk, Y. Usson, G. Michalowicz, and F. Parazza, "Mapping of the Orientation of Myocardial-Cells by Means of Polarized-Light and Confocal Scanning Laser Microscopy," *Microscopy Research and Technique*, vol. 30, no. 6, pp. 480-490, Apr 15, 1995.
- [Junzhou *et al.*, 2012] H. Junzhou, and Y. Fei, "Compressed Magnetic Resonance Imaging Based on Wavelet Sparsity and Nonlocal Total Variation," *2012 IEEE 9th International Symposium on Biomedical Imaging*, pp. 968-971, 01 01, 2012.
- [Ker, 2014] J. Ker, "A New Phenotypic Marker of Hypertrophic Cardiomyopathy," *Lancet*, vol. 384, no. 9956, pp. 1731-1731, Nov 15, 2014.
- [Kieren Grant, 2015] H. Kieren Grant, "Reducing Acquisition Time in Clinical Mri by Data Undersampling and Compressed Sensing Reconstruction," *Physics in Medicine and Biology*, vol. 60, no. 21, pp. R297, 2015.
- [Knoll *et al.*, 2011a] F. Knoll, K. Bredies, T. Pock, and R. Stollberger, "Second Order Total Generalized Variation (Tgv) for Mri," *Magnetic Resonance in Medicine*, vol. 65, no. 2, pp. 480-491, Feb, 2011a.
- [Knoll *et al.*, 2011b] F. Knoll, C. Clason, C. Diwoky, and R. Stollberger, "Adapted Random Sampling Patterns for Accelerated Mri," *Magnetic Resonance Materials in Physics Biology and Medicine*, vol. 24, no. 1, pp. 43-50, Feb, 2011b.
- [Knoll *et al.*, 2012] F. Knoll, G. Schultz, K. Bredies, D. Gallichan, M. Zaitsev, J. Hennig, and R. Stollberger, "Reconstruction of Undersampled Radial Patloc Imaging Using Total Generalized Variation," *Magnetic Resonance in Medicine*, pp. n/a-n/a, 2012.
- [Knoll *et al.*, 2010] F. Knoll, M. Unger, C. Diwoky, C. Clason, T. Pock, and R. Stollberger, "Fast Reduction of Undersampling Artifacts in Radial Mr Angiography with 3d Total Variation on Graphics Hardware," *Magnetic Resonance Materials in Physics Biology and Medicine*, vol. 23, no. 2, pp. 103-114, Apr, 2010.
- [Kocica *et al.*, 2006] M. J. Kocica, A. F. Corno, F. Carreras-Costa, M. Ballester-Rodes, M. C. Moghbel, C. N. C. Cueva, V. Lackovic, V. I. Kanjuh, and F. Torrent-Guasp, "The Helical Ventricular Myocardial Band: Global, Three-Dimensional, Functional Architecture of the Ventricular Myocardium," *European Journal of Cardio-Thoracic Surgery*, vol. 29, pp. S21-S40, Apr, 2006.
- [Kopf *et al.*, 1996] M. Kopf, C. Corinth, O. Haferkamp, and T. F. Nonnenmacher, "Anomalous Diffusion of Water in Biological Tissues," *Biophysical Journal*, vol. 70, no. 6, pp. 2950-2958, Jun, 1996.
- [Kotelnikov, 1933] V. A. Kotelnikov, "On the Carrying Capacity of the Ether and Wire in Telecommunications."
- [Kowalski *et al.*, 2013] M. Kowalski, K. Siedenburg, and M. Doerfler, "Social Sparsity! Neighborhood Systems Enrich Structured Shrinkage Operators," *Ieee Transactions on Signal Processing*, vol. 61, no. 10, pp. 2498-2511, May, 2013.
- [Landau, 1967] H. Landau, "Necessary Density Conditions for Sampling and Interpolation of Certain Entire Functions," *Acta Mathematica*, vol. 117, no. 1, pp. 37-52, 1967.
- [Larkman *et al.*, 2007] D. J. Larkman, and R. G. Nunes, "Parallel Magnetic Resonance Imaging," *Physics in Medicine and Biology*, vol. 52, no. 7, pp. R15-R55, Apr 7, 2007.

- [Lau *et al.*, 2015] A. Z. Lau, E. M. Tunnicliffe, R. Frost, P. J. Koopmans, D. J. Tyler, and M. D. Robson, "Accelerated Human Cardiac Diffusion Tensor Imaging Using Simultaneous Multislice Imaging," *Magnetic Resonance in Medicine*, vol. 73, no. 3, pp. 995-1004, Mar, 2015.
- [Lauterbur, 1973] P. C. Lauterbur, "Image Formation by Induced Local Interactions: Examples Employing Nuclear Magnetic Resonance," *Nature*, vol. 242, no. 5394, pp. 190-191, 16 March, 1973.
- [Le Bihan, 2003] D. Le Bihan, "Looking into the Functional Architecture of the Brain with Diffusion MRI," *Nature Reviews Neuroscience*, vol. 4, no. 6, pp. 469-480, Jun, 2003.
- [Le Bihan, 2013] D. Le Bihan, "Apparent Diffusion Coefficient and Beyond: What Diffusion MR Imaging Can Tell Us About Tissue Structure," *Radiology*, vol. 268, no. 2, pp. 318-322, Aug, 2013.
- [Le Bihan *et al.*, 2001] D. Le Bihan, J. F. Mangin, C. Poupon, C. A. Clark, S. Pappata, N. Molko, and H. Chabriat, "Diffusion Tensor Imaging: Concepts and Applications," *Journal of Magnetic Resonance Imaging*, vol. 13, no. 4, pp. 534-546, Apr, 2001.
- [Lebihan *et al.*, 1986] D. Lebihan, E. Breton, D. Lallemand, P. Grenier, E. Cabanis, and M. Lavaljeantet, "MR Imaging of Intravoxel Incoherent Motions - Application to Diffusion and Perfusion in Neurologic Disorders," *Radiology*, vol. 161, no. 2, pp. 401-407, Nov, 1986.
- [LeGrice *et al.*, 1997] I. J. LeGrice, P. J. Hunter, and B. H. Smaill, "Laminar Structure of the Heart: A Mathematical Model," *American Journal of Physiology-Heart and Circulatory Physiology*, vol. 272, no. 5, pp. H2466-H2476, May, 1997.
- [Legrice *et al.*, 1995] I. J. Legrice, B. H. Smaill, L. Z. Chai, S. G. Edgar, J. B. Gavin, and P. J. Hunter, "Laminar Structure of the Heart: Ventricular Myocyte Arrangement and Connective Tissue Architecture in the Dog," *American Journal of Physiology-Heart and Circulatory Physiology*, vol. 269, no. 2, pp. H571-H582, Aug, 1995.
- [Liang *et al.*, 2011] D. Liang, H. Wang, Y. Chang, and L. Ying, "Sensitivity Encoding Reconstruction with Nonlocal Total Variation Regularization," *Magnetic Resonance in Medicine*, vol. 65, no. 5, pp. 1384-1392, May, 2011.
- [Liang *et al.*, 2014] J. Liang, J. Ma, and X. Zhang, "Seismic Data Restoration Via Data-Driven Tight Frame," *Geophysics*, vol. 79, no. 3, pp. V65-V74, May-Jun, 2014.
- [Liang *et al.*, 2000] Z. P. Liang, and P. C. Lauterbur, *Principles of Magnetic Resonance Imaging: A Signal Processing Perspective*: "The" Institute of Electrical and Electronics Engineers Press, 2000.
- [Lingala *et al.*, 2013] S. G. Lingala, E. DiBella, G. Adluru, C. McGann, and M. Jacob, "Accelerating Free Breathing Myocardial Perfusion MRI Using Multi Coil Radial K-T Slr," *Physics in Medicine and Biology*, vol. 58, no. 20, pp. 7309-7327, Oct 21, 2013.
- [Lou *et al.*, 2010] Y. Lou, X. Zhang, S. Osher, and A. Bertozzi, "Image Recovery Via Nonlocal Operators," *Journal of Scientific Computing*, vol. 42, no. 2, pp. 185-197, Feb, 2010.
- [Luna *et al.*, 2012] A. Luna, R. Ribes, and J. A. Soto, *Diffusion MRI Outside the Brain: A Case-Based Review and Clinical Applications*: Springer, 2012.
- [Luo *et al.*, 2012] J. Luo, Y. Zhu, W. Li, P. Croisille, and I. E. Magnin, "MRI Reconstruction from 2d Truncated K-Space," *Journal of Magnetic Resonance Imaging*, vol. 35, no. 5, pp. 1196-1206, May, 2012.
- [Lustig, 2008] M. Lustig, "Sparse MRI," Stanford University, United States -- California, 2008.
- [Lustig *et al.*, 2007] M. Lustig, D. Donoho, and J. M. Pauly, "Sparse MRI: The Application of Compressed Sensing for Rapid MR Imaging," *Magnetic Resonance in Medicine*, vol. 58, no. 6, pp. 1182-1195, Dec, 2007.
- [Lustig *et al.*, 2008] M. Lustig, D. L. Donoho, J. M. Santos, and J. M. Pauly, "Compressed Sensing MRI," *Ieee Signal Processing Magazine*, vol. 25, no. 2, pp. 72-82, Mar, 2008.

- [Lustig *et al.*, 2010] M. Lustig, and J. M. Pauly, "Spirit: Iterative Self-Consistent Parallel Imaging Reconstruction from Arbitrary K-Space," *Magnetic Resonance in Medicine*, vol. 64, no. 2, pp. 457-471, Aug, 2010.
- [Majumdar *et al.*, 2012] A. Majumdar, and R. K. Ward, "Calibration-Less Multi-Coil Mr Image Reconstruction," *Magnetic Resonance Imaging*, vol. 30, no. 7, pp. 1032-1045, Sep, 2012.
- [Mallat *et al.*, 1993] S. G. Mallat, and Z. F. Zhang, "Matching Pursuits with Time-Frequency Dictionaries," *Ieee Transactions on Signal Processing*, vol. 41, no. 12, pp. 3397-3415, Dec, 1993.
- [Marvasti, 2000] F. Marvasti, *Nonuniform Sampling, Theory and Practice*, New York: Kluwer Academic/Plenum Publishers, 2000.
- [McGibney *et al.*, 1993] G. McGibney, M. R. Smith, S. T. Nichols, and A. Crawley, "Quantitative Evaluation of Several Partial Fourier Reconstruction Algorithms Used in Mri," *Magnetic Resonance in Medicine*, vol. 30, no. 1, pp. 51-59, Jul, 1993.
- [McRobbie *et al.*, 2006] D. W. McRobbie, E. A. Moore, M. J. Graves, and M. R. Prince, *Mri from Picture to Proton*: Cambridge university press, 2006.
- [Merlet *et al.*, 2013] S. Merlet, E. Caruyer, A. Ghosh, and R. Deriche, "A Computational Diffusion Mri and Parametric Dictionary Learning Framework for Modeling the Diffusion Signal and Its Features," *Medical Image Analysis*, vol. 17, no. 7, pp. 830-843, Oct, 2013.
- [Mori *et al.*, 1999] S. Mori, and P. B. Barker, "Diffusion Magnetic Resonance Imaging: Its Principle and Applications," *Anatomical Record*, vol. 257, no. 3, pp. 102-109, Jun 15, 1999.
- [Mori *et al.*, 2002] S. Mori, and P. C. M. van Zijl, "Fiber Tracking: Principles and Strategies - a Technical Review," *Nmr in Biomedicine*, vol. 15, no. 7-8, pp. 468-480, Nov-Dec, 2002.
- [Mozaffarian *et al.*, 2015] D. Mozaffarian, E. J. Benjamin, A. S. Go, D. K. Arnett, M. J. Blaha, M. Cushman, S. de Ferranti, J.-P. Despres, H. J. Fullerton, V. J. Howard, M. D. Huffman, S. E. Judd, B. M. Kissela, D. T. Lackland, J. H. Lichtman, L. D. Lisabeth, S. Liu, R. H. Mackey, D. B. Matchar, D. K. McGuire, E. R. Mohler, III, C. S. Moy, P. Muntner, M. E. Mussolini, K. Nasir, R. W. Neumar, G. Nichol, L. Palaniappan, D. K. Pandey, M. J. Reeves, C. J. Rodriguez, P. D. Sorlie, J. Stein, A. Towfighi, T. N. Turan, S. S. Virani, J. Z. Willey, D. Woo, R. W. Yeh, M. B. Turner, C. Amer Heart Assoc Stat, and S. Stroke Stat, "Heart Disease and Stroke Statistics-2015 Update a Report from the American Heart Association," *Circulation*, vol. 131, no. 4, pp. E29-E322, Jan 27, 2015.
- [Nam, 2012] S. H. Nam, "Accelerated Cardiovascular Magnetic Resonance Imaging Using Radial Acquisition with Compressed Sensing," Engineering Sciences, Harvard University, 2012.
- [Naumova *et al.*, 2014] A. V. Naumova, and V. L. Yarnykh, "Assessment of Heart Microstructure from Mouse to Man," *Circulation*, vol. 129, no. 17, pp. 1720-1722, Apr 29, 2014.
- [Nesterov, 1983] Y. Nesterov, "A Method of Solving a Convex Programming Problem with Convergence Rate O (1/K<sup>2</sup>).", pp. 372-376.
- [Nesterov, 2013] Y. Nesterov, "Gradient Methods for Minimizing Composite Functions," *Mathematical Programming*, vol. 140, no. 1, pp. 125-161, Aug, 2013.
- [Nesterov *et al.*, 2013] Y. Nesterov, and A. Nemirovski, "On First-Order Algorithms for L(1)/Nuclear Norm Minimization," *Acta Numerica*, vol. 22, pp. 509-575, 2013, 2013.
- [Nicholas *et al.*, 2015] M. Nicholas, N. Townsend, P. Scarborough, and M. Rayner, "Cardiovascular Disease in Europe 2014: Epidemiological Update," *European Heart Journal*, vol. 36, no. 13, pp. 794-794, Apr 1, 2015.
- [Nichols *et al.*] M. Nichols, N. Townsend, P. Scarborough, and M. Rayner, "European Cardiovascular Disease Statistics 2012," European Heart Network, Brussels, European Society of Cardiology, Sophia Antipolis, page P118.

- [Nielles-Vallespin *et al.*, 2013] S. Nielles-Vallespin, C. Mekkaoui, P. Gatehouse, T. G. Reese, J. Keegan, P. F. Ferreira, S. Collins, P. Speier, T. Feiweier, R. de Silva, M. P. Jackowski, D. J. Pennell, D. E. Sosnovik, and D. Firmin, "In Vivo Diffusion Tensor Mri of the Human Heart: Reproducibility of Breath-Hold and Navigator-Based Approaches," *Magnetic Resonance in Medicine*, vol. 70, no. 2, pp. 454-465, Aug, 2013.
- [Nyquist, 1928] H. Nyquist, "Certain Topics in Telegraph Transmission Theory," *American Institute of Electrical Engineers, Transactions of the*, vol. 47, no. 2, pp. 617-644, 1928.
- [Ozarslan *et al.*, 2006] E. Ozarslan, T. M. Shepherd, B. C. Vemuri, S. J. Blackband, and T. H. Mareci, "Resolution of Complex Tissue Microarchitecture Using the Diffusion Orientation Transform (Dot)," *Neuroimage*, vol. 31, no. 3, pp. 1086-1103, Jul 1, 2006.
- [Parikh *et al.*, 2013] N. Parikh, and S. Boyd, "Proximal Algorithms," *Foundations and Trends in Optimization*, vol. 1, no. 3, pp. 123-231, 2013.
- [Pati *et al.*, 1993] Y. C. Pati, R. Rezaifar, and P. S. Krishnaprasad, "Orthogonal Matching Pursuit: Recursive Function Approximation with Applications to Wavelet Decomposition," *Conference Record of The Twenty-Seventh Asilomar Conference on Signals, Systems and Computers (Cat. No.93CH3312-6)*, pp. 40-44 vol.41, 1993, 1993.
- [Pennebaker *et al.*, 1993] W. B. Pennebaker, and J. L. Mitchell, *Jpeg Still Image Data Compression Standard*: Springer, 1993.
- [Perrin *et al.*, 2005] M. Perrin, C. Poupon, B. Rieul, P. Leroux, A. Constantinesco, J. F. Mangin, and D. LeBihan, "Validation of Q-Ball Imaging with a Diffusion Fibre-Crossing Phantom on a Clinical Scanner," *Philosophical Transactions of the Royal Society B-Biological Sciences*, vol. 360, no. 1457, pp. 881-891, May 29, 2005.
- [Peters *et al.*, 2000] D. C. Peters, F. R. Korosec, T. M. Grist, W. F. Block, J. E. Holden, K. K. Vigen, and C. A. Mistretta, "Undersampled Projection Reconstruction Applied to Mr Angiography," *Magnetic Resonance in Medicine*, vol. 43, no. 1, pp. 91-101, Jan, 2000.
- [Pierpaoli *et al.*, 1996] C. Pierpaoli, and P. J. Basser, "Toward a Quantitative Assessment of Diffusion Anisotropy," *Magnetic Resonance in Medicine*, vol. 36, no. 6, pp. 893-906, Dec, 1996.
- [Pruessmann *et al.*, 1999] K. P. Pruessmann, M. Weiger, M. B. Scheidegger, and P. Boesiger, "Sense: Sensitivity Encoding for Fast Mri," *Magnetic Resonance in Medicine*, vol. 42, no. 5, pp. 952-962, Nov, 1999.
- [Qaisar *et al.*, 2013] S. Qaisar, R. M. Bilal, W. Iqbal, M. Naureen, and S. Lee, "Compressive Sensing: From Theory to Applications, a Survey," *Journal of Communications and Networks*, vol. 15, no. 5, pp. 443-456, Oct, 2013.
- [Qu *et al.*, 2012] X. Qu, D. Guo, B. Ning, Y. Hou, Y. Lin, S. Cai, and Z. Chen, "Undersampled Mri Reconstruction with Patch-Based Directional Wavelets," *Magnetic Resonance Imaging*, vol. 30, no. 7, pp. 964-977, 2012-Sep, 2012.
- [Qu *et al.*, 2014] X. Qu, Y. Hou, F. Lam, D. Guo, J. Zhong, and Z. Chen, "Magnetic Resonance Image Reconstruction from Undersampled Measurements Using a Patch-Based Nonlocal Operator," *Medical Image Analysis*, vol. 18, no. 6, pp. 843-856, Aug, 2014.
- [Qu *et al.*, 2010] X. Qu, W. Zhang, D. Guo, C. Cai, S. Cai, and Z. Chen, "Iterative Thresholding Compressed Sensing Mri Based on Contourlet Transform," *Inverse Problems in Science and Engineering*, vol. 18, no. 6, pp. 737-758, 2010, 2010.
- [Rao *et al.*, 1998] B. D. Rao, and Ieee, "Signal Processing with the Sparseness Constraint," *Proceedings of the 1998 Ieee International Conference on Acoustics, Speech and Signal Processing, Vols 1-6*, International Conference on Acoustics Speech and Signal Processing (Icassp), pp. 1861-1864, 1998.
- [Ravishankar *et al.*, 2011] S. Ravishankar, and Y. Bresler, "Mr Image Reconstruction from Highly Undersampled K-Space Data by Dictionary Learning," *Ieee Transactions on Medical Imaging*, vol. 30, no. 5, pp. 1028-1041, May, 2011.

- [Rivenson *et al.*, 2013] Y. Rivenson, A. Stern, and B. Javidi, “Overview of Compressive Sensing Techniques Applied in Holography,” *Applied Optics*, vol. 52, no. 1, pp. A423-A432, Jan 1, 2013.
- [Ron *et al.*, 1997] A. Ron, and Z. W. Shen, “Affine Systems in L-2(R-D): The Analysis of the Analysis Operator,” *Journal of Functional Analysis*, vol. 148, no. 2, pp. 408-447, Aug 15, 1997.
- [Ross *et al.*, 1979] A. A. Ross, and D. D. Streeter, Jr., “Myocardial Fiber Disarray,” *Circulation*, vol. 60, no. 6, pp. 1425-1426, 1979-Dec, 1979.
- [Rubinstein *et al.*, 2010] R. Rubinstein, A. M. Bruckstein, and M. Elad, “Dictionaries for Sparse Representation Modeling,” *Proceedings of the IEEE*, vol. 98, no. 6, pp. 1045-1057, Jun, 2010.
- [Rudin *et al.*, 1992a] L. I. Rudin, S. Osher, and E. Fatemi, “Nonlinear Total Variation Based Noise Removal Algorithms,” *Physica D: Nonlinear Phenomena*, vol. 60, no. 1-4, pp. 259-268, Nov 1, 1992a.
- [Rudin *et al.*, 1992b] L. I. Rudin, S. Osher, and E. Fatemi, “Nonlinear Total Variation Based Noise Removal Algorithms,” *Physica D: Nonlinear Phenomena*, vol. 60, no. 1-4, pp. 259-268, 1992b.
- [Santosa *et al.*, 1986] F. Santosa, and W. W. Symes, “Linear Inversion of Band-Limited Reflection Seismograms,” *SIAM Journal on Scientific and Statistical Computing*, vol. 7, no. 4, pp. 1307-1330, Oct, 1986.
- [Scollan *et al.*, 1998] D. F. Scollan, A. Holmes, R. Winslow, and J. Forder, “Histological Validation of Myocardial Microstructure Obtained from Diffusion Tensor Magnetic Resonance Imaging,” *American Journal of Physiology-Heart and Circulatory Physiology*, vol. 275, no. 6, pp. H2308-H2318, Dec, 1998.
- [Sha *et al.*, 2003] L. W. Sha, H. Guo, and A. W. Song, “An Improved Gridding Method for Spiral MRI Using Nonuniform Fast Fourier Transform,” *Journal of Magnetic Resonance*, vol. 162, no. 2, pp. 250-258, Jun, 2003.
- [Shannon, 1949] C. E. Shannon, “Communication in the Presence of Noise,” *Proceedings of the IRE*, vol. 37, no. 1, pp. 10-21, 1949.
- [Shi *et al.*, 2014] X. Shi, X. Ma, W. Wu, F. Huang, C. Yuan, and H. Guo, “Parallel Imaging and Compressed Sensing Combined Framework for Accelerating High-Resolution Diffusion Tensor Imaging Using Inter-Image Correlation,” *Magnetic Resonance in Medicine*, 2014.
- [Soares *et al.*, 2013] J. M. Soares, P. Marques, V. Alves, and N. Sousa, “A Hitchhiker’s Guide to Diffusion Tensor Imaging,” *Frontiers in Neuroscience*, vol. 7, 2013.
- [Sodickson *et al.*, 1997] D. K. Sodickson, and W. J. Manning, “Simultaneous Acquisition of Spatial Harmonics (Smash): Fast Imaging with Radiofrequency Coil Arrays,” *Magnetic Resonance in Medicine*, vol. 38, no. 4, pp. 591-603, Oct, 1997.
- [Sosnovik *et al.*, 2009] D. E. Sosnovik, R. Wang, G. Dai, T. G. Reese, and V. J. Wedeen, “Diffusion MR Tractography of the Heart,” *Journal of Cardiovascular Magnetic Resonance*, vol. 11, Nov 13, 2009.
- [Stejskal *et al.*, 1965] E. O. Stejskal, and J. E. Tanner, “Spin Diffusion Measurements: Spin Echoes in the Presence of a Time-Dependent Field Gradient,” *The journal of chemical physics*, vol. 42, pp. 288, 1965.
- [Streeter, 1979] D. D. Streeter, “Gross Morphology and Fiber Geometry of the Heart,” *Handbook of physiology: The cardiovascular system*, vol. 1, pp. 61-112, 1979.
- [Streeter *et al.*, 1969] D. D. Streeter, Jr., H. M. Spotnitz, D. P. Patel, J. Ross, Jr., and E. H. Sonnenblick, “Fiber Orientation in the Canine Left Ventricle During Diastole and Systole,” *Circulation research*, vol. 24, no. 3, pp. 339-347, 1969-Mar, 1969.
- [Strohmer, 2012] T. Strohmer, “Measure What Should Be Measured: Progress and Challenges in Compressive Sensing,” *IEEE Signal Processing Letters*, vol. 19, no. 12, pp. 887-893, Dec, 2012.
- [Taubman *et al.*, 2002] D. S. Taubman, M. W. Marcellin, and M. Rabbani, “Jpeg2000: Image Compression Fundamentals, Standards and Practice,” *Journal of Electronic Imaging*, vol. 11, pp. 286, 2002.

- [Torrent-Guasp, 1973] F. Torrent-Guasp, "The Cardiac Muscle," *Madrid, Juan March Foundation*, 1973.
- [Torrent-Guasp *et al.*, 2001] F. Torrent-Guasp, G. D. Buckberg, C. Clemente, J. L. Cox, H. C. Coghlan, and M. Gharib, "The Structure and Function of the Helical Heart and Its Buttress Wrapping. I. The Normal Macroscopic Structure of the Heart," *Seminars in thoracic and cardiovascular surgery*, vol. 13, no. 4, pp. 301-319, 2001-Oct, 2001.
- [Torrey, 1956] H. C. Torrey, "Bloch Equations with Diffusion Terms," *Physical Review*, vol. 104, no. 3, pp. 563, 1956.
- [Tournier *et al.*, 2011] J.-D. Tournier, S. Mori, and A. Leemans, "Diffusion Tensor Imaging and Beyond," *Magnetic Resonance in Medicine*, vol. 65, no. 6, pp. 1532-1556, Jun, 2011.
- [Toussaint *et al.*, 2010] N. Toussaint, M. Sermesant, C. T. Stoeck, S. Kozerke, and P. G. Batchelor, "In Vivo Human 3d Cardiac Fibre Architecture: Reconstruction Using Curvilinear Interpolation of Diffusion Tensor Images," *Medical Image Computing and Computer-Assisted Intervention - Miccai 2010, Pt I*, Lecture Notes in Computer Science T. Jiang, N. Navab, J. P. W. Pluim and M. A. Viergever, eds., pp. 418-425, 2010.
- [Toussaint *et al.*, 2007] N. Toussaint, J.-C. Souplet, and P. Fillard, "Medinria: Medical Image Navigation and Research Tool by Inria."
- [Tropp *et al.*, 2007] J. A. Tropp, and A. C. Gilbert, "Signal Recovery from Random Measurements Via Orthogonal Matching Pursuit," *Ieee Transactions on Information Theory*, vol. 53, no. 12, pp. 4655-4666, Dec, 2007.
- [Tropp *et al.*, 2010a] J. A. Tropp, J. N. Laska, M. F. Duarte, J. K. Romberg, and R. G. Baraniuk, "Beyond Nyquist: Efficient Sampling of Sparse Bandlimited Signals," *Ieee Transactions on Information Theory*, vol. 56, no. 1, pp. 520-544, Jan, 2010a.
- [Tropp *et al.*, 2010b] J. A. Tropp, and S. J. Wright, "Computational Methods for Sparse Solution of Linear Inverse Problems," *Proceedings of the IEEE*, vol. 98, no. 6, pp. 948-958, Jun, 2010b.
- [Tsao *et al.*, 2012] J. Tsao, and S. Kozerke, "Mri Temporal Acceleration Techniques," *Journal of Magnetic Resonance Imaging*, vol. 36, no. 3, pp. 543-560, 2012-Sep, 2012.
- [Tuch, 2004] D. S. Tuch, "Q-Ball Imaging," *Magnetic Resonance in Medicine*, vol. 52, no. 6, pp. 1358-1372, Dec, 2004.
- [Tuch *et al.*, 1999] D. S. Tuch, R. Weisskoff, J. Belliveau, and V. Wedeen, "High Angular Resolution Diffusion Imaging of the Human Brain."
- [Unser, 2000] M. Unser, "Sampling-50 Years after Shannon," *Proceedings of the IEEE*, vol. 88, no. 4, pp. 569-587, Apr, 2000.
- [Vetterli *et al.*, 2002] M. Vetterli, P. Marziliano, and T. Blu, "Sampling Signals with Finite Rate of Innovation," *Ieee Transactions on Signal Processing*, vol. 50, no. 6, pp. 1417-1428, Jun, 2002.
- [Vishal M. Patel *et al.*, 2013] Vishal M. Patel, and R. Chellappa, "Sparse Representations and Compressive Sensing for Imaging and Vision," 2013.
- [Wang *et al.*, 2011] G. Wang, Y. Bresler, and V. Ntziachristos, "Compressive Sensing for Biomedical Imaging," *Ieee Transactions on Medical Imaging*, vol. 30, no. 5, pp. 1013-1016, May, 2011.
- [Wang, 2013] L. Wang, "Modeling and Simulation of Diffusion Magnetic Resonance Imaging for Cardiac Fibers," INSA de Lyon, 2013.
- [Wang *et al.*, 2012] L. Wang, Y. Zhu, H. Li, W. Liu, and I. E. Magnin, "Multiscale Modeling and Simulation of the Cardiac Fiber Architecture for Dmri," *Ieee Transactions on Biomedical Engineering*, vol. 59, no. 1, pp. 16-19, Jan, 2012.
- [Wang *et al.*, 2004] Z. Wang, A. C. Bovik, H. R. Sheikh, and E. P. Simoncelli, "Image Quality Assessment: From Error Visibility to Structural Similarity," *Ieee Transactions on Image Processing*, vol. 13, no. 4, pp. 600-612, Apr, 2004.
- [Wedeen *et al.*, 2005] V. J. Wedeen, P. Hagmann, W. Y. I. Tseng, T. G. Reese, and R. M. Weisskoff, "Mapping Complex Tissue Architecture with Diffusion Spectrum

- Magnetic Resonance Imaging," *Magnetic Resonance in Medicine*, vol. 54, no. 6, pp. 1377-1386, Dec, 2005.
- [Wei *et al.*, 2015] H. Wei, M. Viallon, B. M. A. Delattre, K. Moulin, F. Yang, P. Croisille, and Y. Zhu, "Free-Breathing Diffusion Tensor Imaging and Tractography of the Human Heart in Healthy Volunteers Using Wavelet-Based Image Fusion," *Ieee Transactions on Medical Imaging*, vol. 34, no. 1, pp. 306-316, Jan, 2015.
- [Wei *et al.*, 2013] H. Wei, M. Viallon, B. M. A. Delattre, L. Wang, V. M. Pai, H. Wen, H. Xue, C. Guetter, P. Croisille, and Y. Zhu, "Assessment of Cardiac Motion Effects on the Fiber Architecture of the Human Heart in Vivo," *Ieee Transactions on Medical Imaging*, vol. 32, no. 10, pp. 1928-1938, Oct, 2013.
- [Welsh *et al.*, 2013] C. L. Welsh, E. V. R. DiBella, G. Adluru, and E. W. Hsu, "Model-Based Reconstruction of Undersampled Diffusion Tensor K-Space Data," *Magnetic Resonance in Medicine*, vol. 70, no. 2, pp. 429-440, Aug, 2013.
- [Westbrook *et al.*, 2011] C. Westbrook, and C. K. Roth, *Mri in Practice*, 4th Ed ed.: Wiley-Blackwell, 2011.
- [WIIITAKER, 1915] E. WIIITAKER, "On the Functions Which Are Represented by the Expansions of the Interpolatory Theory." pp. 181-194.
- [Winkelmann *et al.*, 2007] S. Winkelmann, T. Schaeffter, T. Koehler, H. Eggens, and O. Doessel, "An Optimal Radial Profile Order Based on the Golden Ratio for Time-Resolved Mri," *Ieee Transactions on Medical Imaging*, vol. 26, no. 1, pp. 68-76, Jan, 2007.
- [Wright *et al.*, 2014] K. L. Wright, J. I. Hamilton, M. A. Griswold, V. Gulani, and N. Seiberlich, "Non-Cartesian Parallel Imaging Reconstruction," *Journal of Magnetic Resonance Imaging*, vol. 40, no. 5, pp. 1022-1040, Nov, 2014.
- [Wu *et al.*, 2006] M.-T. Wu, W.-Y. I. Tseng, M.-Y. M. Su, C.-P. Liu, K.-R. Chiou, V. J. Wedeen, T. G. Reese, and C.-F. Yang, "Diffusion Tensor Magnetic Resonance Imaging Mapping the Fiber Architecture Remodeling in Human Myocardium after Infarction - Correlation with Viability and Wall Motion," *Circulation*, vol. 114, no. 10, pp. 1036-1045, Sep 5, 2006.
- [Wu *et al.*, 2014] Y. Wu, Y.-J. Zhu, Q.-Y. Tang, C. Zou, W. Liu, R.-B. Dai, X. Liu, E. X. Wu, L. Ying, and D. Liang, "Accelerated Mr Diffusion Tensor Imaging Using Distributed Compressed Sensing," *Magnetic Resonance in Medicine*, vol. 71, no. 2, pp. 763-772, Feb, 2014.
- [Xie *et al.*, 2010] J. Xie, P. Lai, F. Huang, Y. Li, and D. Li, "Cardiac Magnetic Resonance Imaging Using Radial K-Space Sampling and Self-Calibrated Partial Parallel Reconstruction," *Magnetic Resonance Imaging*, vol. 28, no. 4, pp. 495-506, May, 2010.
- [Yang *et al.*, 2010] J. Yang, Y. Zhang, and W. Yin, "A Fast Alternating Direction Method for Tvl1-L2 Signal Reconstruction from Partial Fourier Data," *Ieee Journal of Selected Topics in Signal Processing*, vol. 4, no. 2, pp. 288-297, Apr, 2010.
- [Yang *et al.*, 2014] Z. Yang, and M. Jacob, "Mean Square Optimal Nufft Approximation for Efficient Non-Cartesian Mri Reconstruction," *Journal of Magnetic Resonance*, vol. 242, pp. 126-135, 2014-May, 2014.
- [Yanjie *et al.*, 2012] Z. Yanjie, W. Yin, Z. Yuanjie, E. X. Wu, L. Ying, and L. Dong, "A Model-Based Method with Joint Sparsity Constraint for Direct Diffusion Tensor Estimation," *2012 IEEE 9th International Symposium on Biomedical Imaging*, pp. 510-513, 01 01, 2012.
- [Zangwill *et al.*, 2009] S. Zangwill, and R. Hamilton, "Restrictive Cardiomyopathy," *Pacing and Clinical Electrophysiology*, vol. 32, pp. S41-S43, Jul, 2009.
- [Zhang *et al.*, 2014] J. Zhang, D. Zhao, and W. Gao, "Group-Based Sparse Representation for Image Restoration," *Ieee Transactions on Image Processing*, vol. 23, no. 8, pp. 3336-3351, Aug, 2014.
- [Zhang *et al.*, 2010a] S. Zhang, J. A. Crow, X. Yang, J. Chen, A. Borazjani, K. B. Mullins, W. Chen, R. C. Cooper, R. M. McLaughlin, and J. Liao, "The Correlation of 3d Dt-Mri Fiber Disruption with Structural and Mechanical Degeneration in Porcine

- Myocardium," *Annals of Biomedical Engineering*, vol. 38, no. 10, pp. 3084-3095, Oct, 2010a.
- [Zhang *et al.*, 2010b] X. Zhang, M. Burger, X. Bresson, and S. Osher, "Bregmanized Nonlocal Regularization for Deconvolution and Sparse Reconstruction," *Siam Journal on Imaging Sciences*, vol. 3, no. 3, pp. 253-276, 2010, 2010b.
- [Zhang *et al.*, 2013] Y.-L. Zhang, W.-Y. Liu, I. E. Magnin, and Y.-M. Zhu, "Feature-Preserving Smoothing of Diffusion Weighted Images Using Nonstationarity Adaptive Filtering," *Ieee Transactions on Biomedical Engineering*, vol. 60, no. 6, pp. 1693-1701, Jun, 2013.
- [Zhao *et al.*, 2014] D. Zhao, H. Du, Y. Han, and W. Mei, "Compressed Sensing Mr Image Reconstruction Exploiting Tgv and Wavelet Sparsity," *Computational and Mathematical Methods in Medicine*, vol. 2014, 2014.
- [Zhukov *et al.*, 2003] L. Zhukov, and A. H. Barr, *Heart-Muscle Fiber Reconstruction from Diffusion Tensor Mri*, 2003.

**FOLIO ADMINISTRATIF**  
**THÈSE SOUTENUE DEVANT L'INSTITUT NATIONAL**  
**DES SCIENCES APPLIQUÉES DE LYON**

**NOM :** Huang

**DATE de SOUTENANCE :** 13 décembre 2015

**Prénoms :** Jian-Ping

**TITRE :** Etude de l'imagerie de tenseur de diffusion en utilisant l'acquisition Comprimée

**NATURE :** Doctorat

**Numéro d'ordre :** 2015-ISAL-0136

**Ecole doctorale :** École Doctorale Électronique, Électrotechnique, Automatique

**Spécialité :** Image et System

**RESUME :**

L'étude de la structure microscopique des fibres du cœur offre une nouvelle approche pour expliquer les maladies du cœur et pour trouver des moyens de thérapie efficaces. L'imagerie de tenseur de diffusion par résonance magnétique (DTMR) ou l'imagerie de tenseur de diffusion (DTI) fournit actuellement un outil unique pour étudier les structures tridimensionnelles (3D) de fibres cardiaques *in vivo*. Cependant, DTI est connu pour souffrir des temps d'acquisition longs, ce qui limite considérablement son application pratique et clinique. Les méthodes traditionnelles pour l'acquisition et la reconstruction de l'image ne peuvent pas résoudre ce problème. La motivation principale de cette thèse est alors d'étudier des techniques d'imagerie rapide en reconstruisant des images de haute qualité à partir des données fortement sous-échantillonnées. La méthode adoptée est basée sur la nouvelle théorie de l'acquisition compressée (CS). Plus précisément, nous étudions l'utilisation de la théorie de CS pour l'imagerie par résonance magnétique (IRM) et DTI cardiaque.

Tout d'abord, nous formulons la reconstruction de l'image par résonance magnétique (MR) comme un problème d'optimisation avec les contraintes de trames ajustées guidées par les données (TF) et de variation totale généralisée (TGV) dans le cadre de CS, dans lequel, le TF guidé par les données est utilisé pour apprendre de manière adaptative un ensemble de filtres à partir des données fortement sous-échantillonnées afin d'obtenir une meilleure approximation parcimonieuse des images, et le TGV est dédié à régulariser de façon adaptative les régions d'image et à réduire ainsi les effets d'escalier. Ensuite, nous proposons une nouvelle méthode CS qui emploie conjointement la parcimonie et la déficience de rang pour reconstruire des images de DTMR cardiaques à partir des données de l'espace k fortement sous-échantillonnées. Puis, toujours dans le cadre de la théorie CS, nous introduisons la contrainte de rang faible et la régularisation de variation totale (TV) dans la formulation de la reconstruction par CS. Deux régularisations TV sont considérées: TV locale (i.e. TV classique) et TV non locale (NLTV). Enfin, nous proposons deux schémas de sous-échantillonnage radial aléatoire (angle d'or et angle aléatoire) et une méthode d'optimisation avec la contrainte de faible rang et la régularisation TV pour traiter des données espace k fortement sous-échantillonnées en DTI cardiaque. Enfin, nous comparons nos méthodes avec des stratégies existantes de sous-échantillonnage radial telles que l'angle uniforme, l'angle uniforme perturbé aléatoirement, l'angle d'or et l'angle aléatoire.

**MOTS-CLÉS :** diffusion MRI, DTI, compressed sensing, k-space undersampling, reconstruction.

**Laboratoire (s) de recherche :** Creatis (CNRS UMR 5520, INSERM U630)

**Directeur de thèse:** Yue-Min ZHU

**Co-directeur de thèse :** Wan-Yu LIU

**Président de jury :** Isabelle E. MAGNIN

**Composition du jury :** Nicole VINCENT, Jin LI, Ping LI, Isabelle E. MAGNIN, Yue-Min ZHU, Wan-Yu LIU